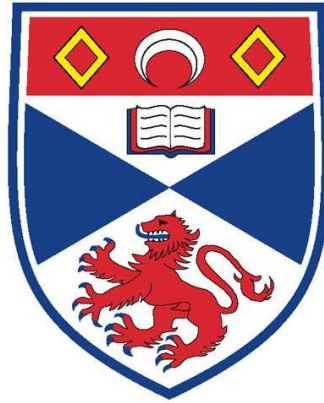THE UNIVERSITY OF ST. ANDREWS

Compact Objects in Active Galactic Nuclei and X-ray Binaries

Edward M. Cackett

Submitted for the degree of Ph.D.

4 August 2006

DECLARATION

I, Edward Cackett, hereby certify that this thesis, which is approximately 50,000 words in length, has been written by me, that it is the record of work carried out by me and that it has not been submitted in any previous application for a higher degree.

Date   Signature of candidate

I was admitted as a research student in October 2003 and as a candidate for the degree of Ph.D in October 2004; the higher study for which this is a record was carried out in the University of St Andrews between 2003 and 2006.

Date   Signature of candidate

In submitting this thesis to the University of St Andrews I understand that I am giving permission for it to be made available for use in accordance with the regulations of the University Library for the time being in force, subject to any copyright vested in the work not being affected thereby. I also understand that the title and abstract will be published, and that a copy of the work may be made and supplied to any bona fide library or research worker, that my thesis will be electronically accessible for personal or research use, and that the library has the right to migrate my thesis into new electronic forms as required to ensure continued access to the thesis. I have obtained any third-party copyright permissions that may be required in order to allow such access and migration.

Date   Signature of candidate

I hereby certify that the candidate has fulfilled the conditions of the Resolution and Regulations appropriate for the degree of Ph.D in the University of St Andrews and that the candidate is qualified to submit this thesis in application for that degree.

Date   Signature of supervisor

Acknowledgements

First, and foremost, I would like to thank my inspirational supervisors Keith Horne and Rudy Wijnands. Their enthusiasm, help, advice and insight (the list could easily continue) has been paramount to me enjoying astronomy research so much.

The continual love and support of my parents and family throughout my education has always been much appreciated. Catríona, thank you for your love, support and friendship, it means the world to me.

Thanks also to all my collaborators for insightful, and enjoyable discussions on many aspects of this work, especially Mike Goad, Kirk Korista, Hartmut Winkler, Craig Heinke and Dave Pooley.

I would like to thank Sidney Harris (http://://www.sciencecartoonsplus.com), for kind permission to reprint his cartoons in this thesis.

Finally, thanks have to go to all my office mates who have put up with me over the years, but especially Nick and John - you were always there to provide distractions when I needed it (and even when I really didn't!).

Preface

This thesis is based on all the first author papers listed below. Additionally, Chapter 3 will shortly be submitted as a paper to MNRAS.

[1] Cackett, E. M., Wijnands, R., Linares, M., Miller, J. M, Homan, J., Lewin, W. H. G.
2006, MNRAS, 372, 479

[2] Cackett, E. M, Wijnands, R. & Remillard, R.
2006, MNRAS, 369, 1965

[3] Cackett, E. M., Wijnands, R., Heinke, C. O., Edmonds, P. D., Lewin, W. H. G.,
Pooley, D., Grindlay, J. E., Jonker, P. G., Miller, J. M.
2006, MNRAS, 369, 407

[4] Cackett, E. M., Horne, K.
2006, MNRAS, 365, 1180

[5] Cackett, E. M., Wijnands, R., Heinke, C. O., Edmonds, P. D., Lewin, W. H. G.,
Pooley, D., Grindlay, J. E., Jonker, P. G., Miller, J. M.
2005, ApJ, 620, 922

THE UNIVERSITY OF ST. ANDREWS

Compact Objects in Active Galactic Nuclei and X-ray Binaries

Submitted for the degree of Ph.D.

4 August 2006

Edward M. Cackett

ABSTRACT

In this thesis I study the inner-most regions of Active Galactic Nuclei (AGN) using the reverberation mapping technique, and neutron star low-mass X-ray binaries in quiescence using X-ray observations.

Using the 13-year optical monitoring data for the AGN NGC 5548, the luminosity-dependence of the Hβ emitting radius was modelled using a delay map, finding that the radius scales with luminosity as predicted by recent theoretical models. Time-delays between the continuum at different wavelengths in AGN can be used to probe the accretion disc. Here, continuum time-delays in a sample of 14 AGN were used to measure the radial temperature profile of the accretion discs, determine the nuclear extinction, and measure distances to the objects. However, the distances measured correspond to a value for Hubble's constant that is a factor of ~ 2 lower than the accepted value. The implications of this on the thermal disc reprocessing model are discussed.

I present two *Chandra* observations of the neutron star transient in the globular cluster NGC 6440 in quiescence, where the power-law component to the spectrum is seen to be variable between the observations, suggesting that there is ongoing residual accretion. From a *Chandra* observation of the globular cluster Terzan 1, I have identified the likely quiescent counterpart to a transient previously observed in outburst, and discuss the other sources within the cluster. Using *Chandra* and *XMM-Newton* monitoring observations of two neutron star transients (KS 1731−260 and MXB 1659−29) in quiescence I have found that the neutron star crusts in both sources have now returned to thermal equilibrium with the core. These observations also indicate that the crusts in both sources may have a high thermal conductivity and that enhanced neutrino emission may be occurring in the core. Finally, the discovery of an X-ray transient with *XMM-Newton* is presented, and the other sources in this observation discussed.

CONTENTS

LIST OF FIGURES

LIST OF TABLES

CHAPTER 1

Introduction

"It's black, and it looks like a hole.
I'd say it's a black hole."

One of the most efficient ways of releasing gravitational potential energy is by the accretion of mass. In our Universe accretion onto compact objects is seen on a wide range of scales. The masses of the compact objects range from of order a solar mass in X-ray binary systems in our own Galaxy, to millions to billions of solar masses for supermassive black holes in Active Galactic Nuclei (AGN) (see Fig. 1.1). Gravitational potential energy is converted into radiation via viscous dissipation in an accretion disc, where angular momentum gets transferred outwards, as gas spirals in onto the compact object. The reader is referred to the excellent book by Frank, King & Raine (2002) for a full in-depth discussion on accretion.
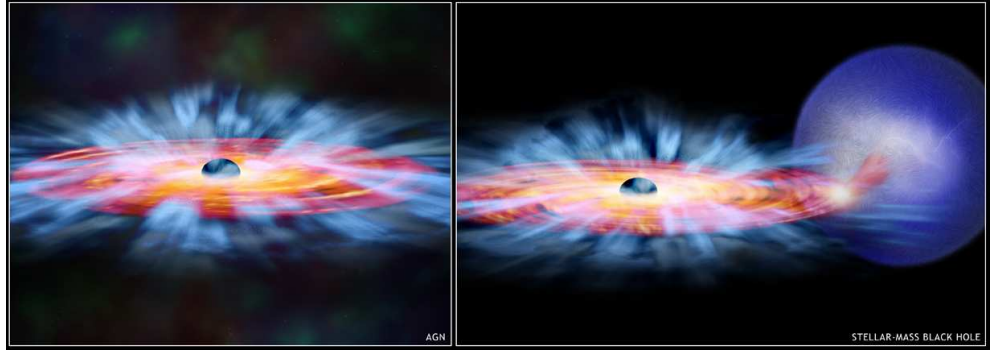
Figure 1.1: An artist's impression of the an accretion disc around a supermassive black hole in an Active Galactic Nucleus (left), and a stellar-mass black hole in an low-mass X-ray binary (right). While the mass scales are wildly different, the same physical process is thought to be powering both. Credit: NASA/CXC/M.Weiss

Due to the different size scales, the temperatures of accretion discs in binary systems peak in the X-rays, whereas accretion discs in AGN peak in the EUV/UV and have significant emission in the optical (though AGN discs also emit in the X-ray and X-ray binary discs emit in the UV and optical too). The timescales in the two classes of objects are also different, with X-ray binaries varying on much shorter timescales (as fast as milliseconds in some cases as opposed to days in AGN). Studying accretion in both X-ray binaries in our Galaxy and AGN may lead to the scaling of properties with mass between the two. Of course, if we can understand what is going on in one type of system, it could improve our understanding of the other and help to build one coherent picture of accretion in strong fields on all scales.

AGN are some of the most luminous objects in the Universe and can be seen to significant redshifts where the Universe was only a fraction of the age it is now. If AGN can be used as a standard candle, they provide a very attractive way to probe cosmology to high redshifts, much further than can be seen with current supernovae methods.

From the point of view of stellar evolution, X-ray binaries are interesting in their own right, however they also, provide an opportunity to study strong gravity and dense matter. One advantage of studying X-ray binaries (as opposed to AGN) is that it is possible, at least in principle, to determine what characteristics are unique for black hole systems via comparison with neutron star systems and which properties are common to both. The study of the neutron star systems leads to constraints on the properties of the

ultra-dense matter that makes up these stars.

In this thesis I study the inner-most regions of AGN, and demonstrate the potential of using AGN accretion discs as standard candles to probe cosmology. I also focus on the study of neutron star low-mass X-ray binaries in quiescence and discuss the implications of these observations on the properties of the neutron stars in these systems.

1.1   Active Galactic Nuclei

Active Galactic Nuclei (AGN) refers to the central region of a galaxy, known as the galactic nucleus, that is observed to be particularly energetic, in many cases outshining the rest of the galaxy. In 1943 Carl Seyfert noted that a reasonable proportion (up to a few percent) of spiral galaxies have high central surface brightnesses that are point-like and as bright as the rest of the galaxy (Seyfert, 1943). Radio astronomers in the 1950's performed large radio surveys of the sky and discovered many AGN. For example, a bright radio source associated with Cygnus A, a galaxy faint in the optical, was found and later revealed to be two huge radio lobes extending to a quarter of a million light years either side of the nucleus to which it is connected by jets (collimated outflows travelling close to the speed of light). Further radio surveys in the 1960's observed other strong radio signals that were found to come from star-like objects exhibiting strong broad emission lines. Although at the time the nature of these quasi-stellar radio sources, or quasars, was very confusing, we now know them to be the extremely bright centres of galaxies.

While there is a veritable smorgasbord of different AGN subclasses (for example Seyferts, quasars, blazars), they all show most, if not all, of the following properties: nuclei with small angular size (so small that they cannot be spatially resolved), a high luminosity ($\sim 10^{42-48}$ erg s^{-1}), broad-band continuum emission from the radio to hard X-rays, strong optical and UV emission lines, and variability in the continuum and emission lines.

The extremely high luminosity of AGN from such a small region initially caused problems explaining the the source of the energy. However, it is now widely accepted that the central source in AGN is a supermassive black hole surrounded by a hot accretion disc (the arguments for a supermassive black hole rather than other models such as dense star clusters are reviewed by Rees, 1984). The Eddington luminosity limit (the luminosity

at which the gravitational force acting on the gas is balanced by the outward force of radiation) for AGN provides a lower limit for the masses of the central supermassive black holes, and indicates they may be around $M = 10^{6-9}$ M$_\odot$. This makes the study of AGN particularly important as they are the only place to study black holes on this scale. As AGN are bright, they are seen over a wide range of redshifts and so also provide a way of studying the evolution of supermassive black holes.

1.1.1 Emission Lines

A particular feature of most AGN is their strong emission lines in the optical and UV. A wide number of emission lines are observed, but they can be split into broad lines and narrow lines, where broad lines are those that are seen to have 'broad' profiles with widths corresponding to velocities between 10^3 and 10^4 km s^{-1} and narrow lines are those that have 'narrow' profiles with widths corresponding to velocities of several hundred km s^{-1}. An example of broad emission lines is shown in the UV spectrum of NGC 5548 (Fig. 1.2).

There are many broad emission lines found in AGN spectra but some of the stronger lines include Lyα, Hα, Hβ, HeII $\lambda1640$ and CIV $\lambda1549$. Importantly, only permitted broad emission lines are seen. The absence of forbidden broad emission lines indicates that the broad-line gas must exceed a minimum density. In contrast, forbidden narrow emission lines are seen (e.g. [OIII] $\lambda4959, 5007$, [OII] $\lambda3727$, [NII] $\lambda6583$, [OI] $\lambda6300$, and [SII] $\lambda6724$), as well as some permitted narrow emission lines, indicating the gas responsible is less dense than the broad-line gas.

The mechanism behind the formation of these emission lines is photoionization by the continuum. Evidence for this includes the correlated continuum and emission-line fluctuations (see section 1.2 for more details). Also, in some nearby AGN the narrow-line region is seen to occupy a triangular projection on the sky, known as an 'ionization cone' (e.g. Pogge, 1988; Tadhunter & Tsvetanov, 1989). These ionization cones can be explained by photoionization excitation where the ionizing radiation has been collimated close to the nucleus (e.g., Bland-Hawthorn, Cackett and Maloney 2006, in preparation).

Many AGN are classified based on their emission line characteristics. For example, Seyfert galaxies (the low redshift, lower luminosity AGN that have a quasar-like nucleus but where the host galaxy is also easily observable) are classified into type 1 and type
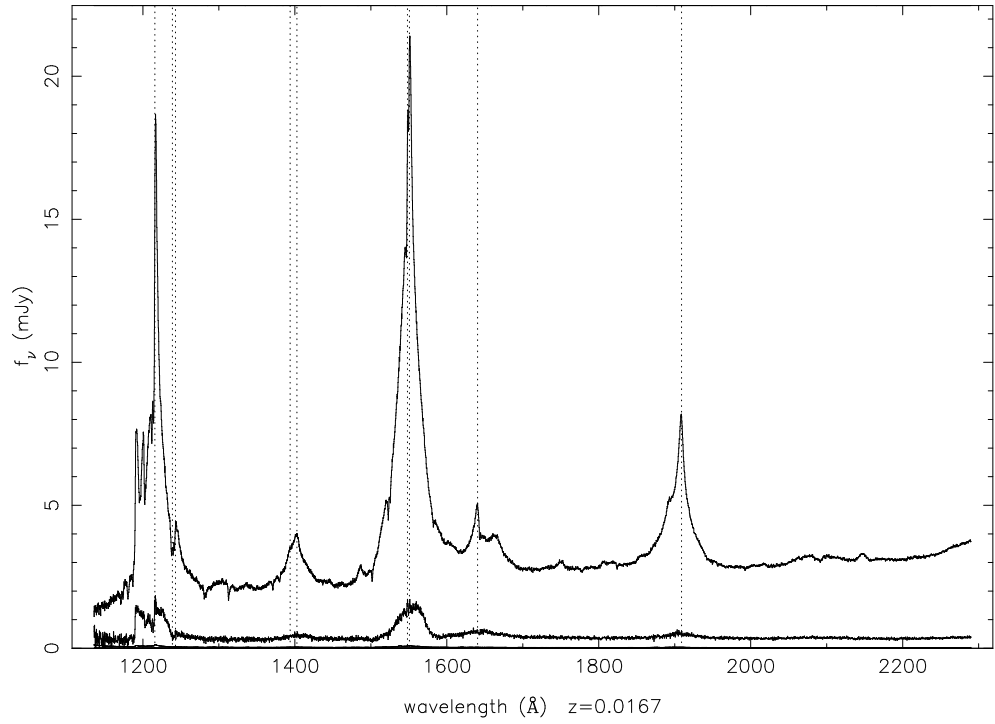
Figure 1.2: The UV spectrum of Seyfert 1 galaxy NGC 5548. Data from the HST 1993 monitoring campaign (Korista et al., 1995). The mean spectrum of 39 observations has been taken, shifted to the rest wavelength (z = 0.0167). The lower line is the rms spectrum which shows the variable component of the spectrum. The position of the most prominent broad emission lines are marked with dashed lines. In increasing rest wavelength they are: Lyα λ1216, N V λ1240, Si IV $\lambda\lambda$1394, 1403+ O IV] λ1402, C IV λ1549, He II λ1640 and C III] λ1909.

2 (Khachikian & Weedman, 1974). Type 1 Seyferts have both narrow emission lines and broad emission lines present. However, Seyfert type 2 galaxies do not exhibit broad emission lines and only narrow emission lines are present. The continuum in Seyfert 2's is also observed to be weaker.

1.1.2 Variability

Variability is a property observed in many AGN on timescales of days to months with little variability seen on timescales shorter than a few days. Variability has been observed in all wavebands, and in the broad emission lines as well as the continuum (see Fig.1.3). The observed rapid variability implies that the size of the continuum-emitting region is of the order of light days - if an object varies with a timescale, t, then the radius of the varying region must be $R \leq ct$ otherwise the light time travel would smooth out the time variations.

Although periodic behaviour has not been identified in AGN variations, the variability can be characterised. For example, one can look at the mean fractional variation, which is typically around 10-20% in the optical continuum on timescales of about a month. Another useful way to characterize the variability is to look at the power-density spectrum - the product of the Fourier transform of the light curve and its complex conjugate. This indicates the power-density in the variations per unit frequency. AGN are seen to have a broken power-law like power-density spectrum, $P(f) \propto f^{-\alpha}$, typically with $\alpha \sim 2$ above the break frequency and flattening off at low frequencies to $\alpha \sim 1$, with the break frequency seemingly scaled with mass, though other parameters such as the mass accretion rate likely provide the large scatter in this relationship (e.g., Markowitz et al., 2003; McHardy et al., 2004, 2005). Optical and UV continuum variability is understood to be due to reprocessing by the accretion disc of varying EUV/X-ray ionizing radiation, whereas the variable broad lines are due to the heating and reprocessing of the ionizing radiation in the broad line gas.

1.1.3 The current AGN paradigm

The current AGN paradigm is a unified model that combines the various different types of AGN (e.g. Antonucci, 1993; Urry & Padovani, 1995). In these unified models AGN
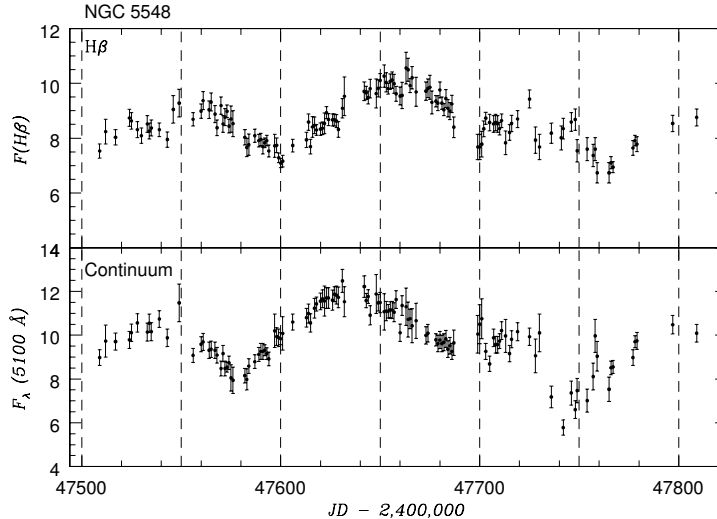
Figure 1.3: Optical continuum at 5100 Å (bottom panel) and the Hβ (top panel) lightcurves of NGC 5548 from the first year of monitoring by the *AGN Watch* collaboration. The continuum fluxes are in units of 10^{-15} ergs s^{-1} cm^{-2} Å^{-1} and the Hβ fluxes are in units of 10^{-13} ergs s^{-1} cm^{-2} Å^{-1}. Data is from *AGN Watch* NGC 5548 observing campaign (Peterson et al., 2002, and references therein).

are all intrinsically identical with the observed differences explained simply by differing luminosities and/or viewing angles. The basic components of this model are a supermassive black hole and accretion disc, high velocity gas clouds close to the nucleus giving rise to the broad lines, a region of low velocity gas clouds further away from the nucleus giving rise to the narrow lines and a dusty torus that obscures the nucleus from some viewing angles.

The primary energy source for the AGN is accretion onto a supermassive black hole. Although AGN accretion discs have not been resolved spatially the 'big blue bump' (Malkan & Sargent, 1982) is widely accepted as a spectral signature of it. The thermal nature of this continuum emission has been confirmed by the detection of the Balmer edge in the polarized light from several quasars (Kishimoto et al., 2003, 2004). In addition, the composite difference spectra (that is the difference between two spectra taken at different epochs) of over 300 quasars from the Sloan Digital Sky Survey can be fit well by an accretion disc model where the accretion rate has changed between the observations (Pereyra et al., 2006). The use of difference spectra isolates the variable part of the spectrum, therefore removing constant contributions to emission from starlight. The Keplerian motion of
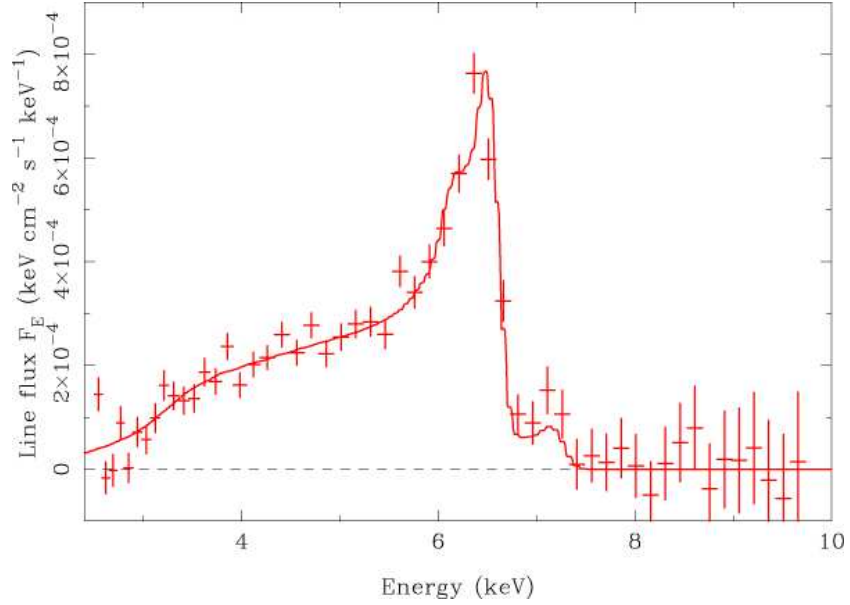
Figure 1.4: Relativistic iron line profile in the AGN MCG$-6-30-15$ from a 325-ks observation with the *XMM-Newton* X-ray telescope. The line has a broadened asymmetric profile with most of the line flux redshifted from its rest energy of 6.4 keV. Taken from Fabian et al. (2002).

water maser emission in NGC 4258 with 0.13 pc of a massive object (Miyoshi et al., 1995) supports the accretion disc idea. Further strong evidence for AGN accretion discs is given by the gravitationally redshifted Fe K-α emission line that has been observed in the X-ray spectra of several AGN (Tanaka et al., 1995). The broad, asymmetric profiles with most of the line flux redshifted indicates that the line arises from a region several Schwarzschild radii from a supermassive black hole. See Fig. 1.4 for an example of the relativistic iron line in the AGN MCG$-6-30-15$ and Reynolds & Nowak (2003) for a review of this topic.

The broad emission lines have widths corresponding to high velocities and the absence of forbidden broad lines indicates the gas is of high density. This suggests that the broad line region (BLR) must be close into the nucleus (we discuss reverberation mapping observations of the BLR in §1.3). The narrow line region (NLR) is a lower density, lower velocity gas and is the smallest scale that can be spatially resolved in even the nearest AGNs. The IR emission seems to arise from warm dust grains which must form in a region that is cooler than the dust sublimation temperature.

The IR emission is important in AGN unification theories. The orientation argument

for unification is based on the idea that there is obscuration of the nucleus by optically thick dust along some lines of sight. Whether the dust is in a molecular torus (e.g. Krolik & Begelman, 1988; Pier & Krolik, 1992a,b, 1993) or is the outer edges of a warped accretion disc (e.g. Sanders et al., 1989) or something else is unclear, however, it is still generally referred to as being a dusty torus, whatever its nature. Recent deep multiwavelength surveys have discovered a significant population of obscured AGN (where the obscuration is due to a dusty torus) by comparing X-ray and IR observations, as predicted by AGN unification, with 3 times as many obscured AGN as unobscured (Treister et al., 2004, 2006).

The simplistic general unified model is shown in Fig. 1.5. From this it is clear that by changing the viewing angle, one would observe different properties. For instance, if viewing close to edge-on the obscuring dusty torus would prevent the nucleus and BLR from being viewed directly and only the narrow lines would be present in the spectrum, hence the AGN would be classed as a Seyfert 2. Alternatively, viewing close to face-on would allow the nucleus and BLR to be seen and the AGN would be classed as a Seyfert 1. The fact that the continuum is weaker in Seyfert 2's than in Seyfert 1's is also explained by the obscuring of the nucleus. Only light from the nucleus scattered or reflected by dust or free electrons reaches an observer that is edge-on. Evidence for this has been seen in the polarized spectrum of the nearby Seyfert 2 galaxy NGC 1068 (Antonucci & Miller, 1985; Miller et al., 1991) and some other nearby Seyfert 2 galaxies (Miller & Goodrich, 1990). In this case, weak broad emission lines have been detected in the polarized spectrum indicating that Seyfert 1 and 2 galaxies are intrinsically identical, in at least a handful of sources.

1.2   Reverberation Mapping

The observed variability of AGN helps with the understanding of their structure and kinematics. For instance, time-delays are observed between broad emission line lightcurves and continuum lightcurves. The emission line - continuum time delays are interpreted as the light travel time within the system between the central source of ionizing radiation (continuum) and the BLR where the emission lines are formed. Variations in ionizing radiation from the central source causes spherical waves of heating to propagate outwards
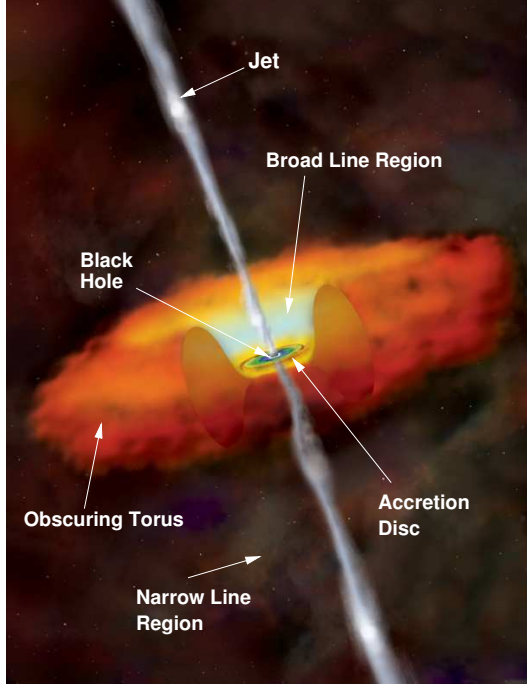
Figure 1.5: Schematic diagram showing the simplistic unified model of AGN. A Seyfert 1 will be observed when viewing close to face-on, whereas when viewing edge-on the dusty torus obscures the nucleus and BLR so a Seyfert 2 is observed. Credit: CXC/M. Weiss

through the disc and gas at the speed of light. The incident ionizing radiation is then absorbed by the gas and reprocessed into emission-line photons. As the reprocessing time is insignificant compared to the light travel time, the light travel time dominates the observed time delay. Changes in the ionizing radiation (peaks or dips in the lightcurve) have the knock-on effect of causing changes in the reprocessed emission at observable time delays. This causes the emission-line light curve to be delayed and smeared compared to the continuum light curve. Reverberation (or 'echo') mapping (Blandford & McKee, 1982) uses these observable time delays to indirectly determine information on the kinematics and geometry of the accretion disc and BLR.

1.2.1 Time Delays

Surfaces of constant time delay (iso-delay surfaces) are given by ellipsoids with one focus at the central source and the other at the observer. As the distance between the source and the observer are so large, this is approximated well by a paraboloid (see Fig 1.6) given
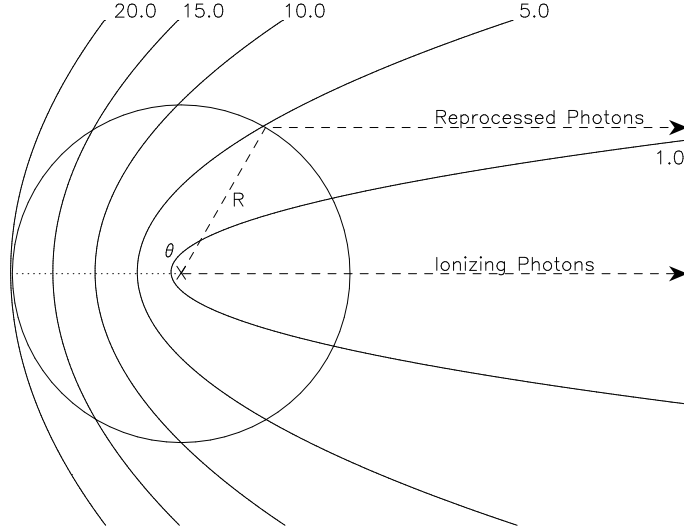
Figure 1.6: Schematic view of the BLR modelled as a thin spherical shell with isodelay paraboloids indicated. The different path length for radiation travelling directly from the compact nucleus to the observer and the radiation that travels to the BLR and then to the observer leads to an observable time delay given by $\tau = R/c\,(1 + \cos\theta)$ where R is the radius and θ is the azimuth angle measured to be $0°$ along the line of site on the far-side of the nucleus and $180°$ on the near side. At any time, τ the observer sees reprocessed photons at the intersection of an isodelay paraboloid and the BLR.

by:

$$\tau = \frac{R}{c}\,(1 + \cos\theta) \tag{1.1}$$

where τ is the observed time delay between the arrival of light straight from the nucleus and the arrival of light from a reprocessing site a distance R from the nucleus and azimuthal angle θ. Gas on the near side of the nucleus along the line of sight has a delay of $\tau = 0$ ($\theta = 180°$) and the maximum delay is given by gas on the far side of the nucleus which has a delay of $\tau = 2R/c$ ($\theta = 0°$). In the very much simplified example of a single δ-function like outburst from a central source surrounded by a thin spherical shell of gas, it can be seen that at any time after the outburst is observed, the part of the gas that is seen is the intersection of the appropriate iso-delay surface and the thin spherical shell.

1.2.2 Transfer Functions

The most simple linearized model of the emission line light curve, $L(t)$, driven by continuum variations, $C(t)$ is given by:

$$L(t) = \bar{L} + \int_0^\infty \Psi(\tau) \left(C(t - \tau) - \bar{C} \right) d\tau \qquad (1.2)$$

where $\bar{C}$ is the background continuum flux, $\bar{L}$ is the constant background line flux that would be produced if the continuum were constant at $\bar{C}$ and $\Psi(\tau)$ is the transfer function or delay map. In these 1-dimensional terms, the time delay map, $\Psi(\tau)$, is effectively a map of the strength of the emission line region response along the iso-delay surface for time delay, τ. Most analyses of current AGN data have concentrated on solving this 1D case, however, it is possible to use more of the information available to do a 2D analysis. For example, determining a velocity-delay map getting velocity information from the line width (e.g., Horne et al., 1991; Welsh & Horne, 1991; Horne, 1994), or determining a luminosity-delay map to see how the size of the broad-line region changes with luminosity (this is the topic of investigation in Chapter 2).

1.2.3 Techniques for analysing the variability

The most commonly used technique is cross-correlation. Although this method is simple, it does not give much more information than the mean time delay. A more detailed discussion of cross-correlation analysis follows below. Several practical methods have been developed to determine the transfer functions. Although Blandford & McKee (1982) originally suggested using Fourier transform techniques this is not practical when the data are noisy and sparse and so is not used. The other methods are the Regularized Linear Inversion (RLI) method (Vio et al., 1994; Krolik & Done, 1995), the Subtractive Optimally-Localized Averages (SOLA) method (Pijpers & Wanders, 1994) and the Maximum Entropy Method (MEM) (Horne et al., 1991; Horne, 1994). The most widely used of these is MEM. MEM is a generalisation of maximum likelihood techniques, such as least-squares and χ^2 minimisation. In MEM the 'simplest' (maximum entropy) model that fits the data is selected, balancing simplicity (entropy) and realism (e.g., χ^2) (Horne, 1994).

Cross-correlation

Cross-correlation is the most commonly used technique, largely because it is easy to implement. Cross-correlation of the continuum and emission line light curves is a simple way to determine the mean response time for an individual emission line. It allows a linear shift in time between the two light curves when determining the correlation. The cross correlation function (CCF) is the convolution integral of the line light curve with the continuum light curve (e.g., Peterson, 1993),

$$\mathrm{CCF}(\tau) = \int_{-\infty}^{\infty} L(t)C(t-\tau)\,\mathrm{d}t \ . \tag{1.3}$$

We have previously defined $L(t)$ in Eq. 1.2 which then gives

$$
\begin{aligned}
\mathrm{CCF}(\tau) &= \int_{-\infty}^{\infty} C(t-\tau) \int_{-\infty}^{\infty} \Psi(\tau')C(t-\tau')\,\mathrm{d}\tau'\,\mathrm{d}t \\
&= \int_{-\infty}^{\infty} \Psi(\tau') \int_{-\infty}^{\infty} C(t-\tau')C(t-\tau)\,\mathrm{d}t\,\mathrm{d}\tau' \ .
\end{aligned}
\tag{1.4}
$$

The autocorrelation function (ACF) is defined as being the cross-correlation of the continuum light curve with itself, i.e.,

$$\mathrm{ACF}(\tau) = \int_{-\infty}^{\infty} C(t)C(t-\tau)\,\mathrm{d}t \ . \tag{1.5}$$

It is then possible to write the CCF in terms of the convolution integral of the delay map with the continuum ACF,

$$\mathrm{CCF}(\tau) = \int_{-\infty}^{\infty} \Psi(\tau')\mathrm{ACF}(\tau-\tau')\,\mathrm{d}\tau' \tag{1.6}$$

Thus, the time-delay, or 'lag', for a particular emission line is just given by the peak or centroid of the CCF. Importantly, the lag measured depends not only on the delay-map but also on the nature of the continuum lightcurve, given by the ACF. The lag will occur at the mean time delay for the system, i.e. at $\tau = R/c$ for a thin spherical shell of radius R or a thin ring of radius R. Thus, from the time-delay, the size of the BLR can be determined.

AGN data are unfortunately rarely evenly spaced in time and so to perform a cross-correlation practically this has to be dealt with. The two most common methods of doing this are the interpolation method (Gaskell & Sparke, 1986; Gaskell & Peterson, 1987; White & Peterson, 1994), and the discrete correlation function method (Edelson & Krolik, 1988; White & Peterson, 1994). In this thesis I use the interpolation method described below, though it should be noted that, if the sampling is sufficient, both methods get similar results (e.g., Peterson, 2001).

Interpolation Method

We use the interpolation method in the modified version of Gaskell & Peterson (1987) by White & Peterson (1994). In this method each emission line data point, $L(t_i)$, is paired with a linearly interpolated continuum value at $C(t_i - \tau)$ and the CCF determined for a wide range of time delays, τ using:

$$\text{CCF}(\tau) = \frac{1}{N} \sum_{i=1}^{N} \frac{[L(t_i) - \bar{L}][C(t_i - \tau) - \bar{C}]}{\sigma_c \sigma_L} \ , \qquad (1.7)$$

where there are N data points, $\bar{L}$ and σ_L are the mean and standard deviation of the emission line flux data points, $L(t_i)$, and $\bar{C}$ and σ_C are the mean and standard deviation of the continuum flux data points, $C(t_i)$. All points outside the time series ($t_i - \tau < t_1$ or $t_i - \tau > t_N$) are excluded. This is then repeated but pairing the continuum data points, $C(t_i)$, with linearly interpolated emission line values at $L(t_i + \tau)$ and the average of the two cross-correlation functions taken. The advantage of the interpolation method is that it can give results from just a few data points. However, if the interpolation of the data points is not a good representation of the true light curve the results can be misleading and thus a well-sampled lightcurve is required.

1.3 Previous Observational Results

1.3.1 Size and Radial Structure of the BLR

Previous observations have focused on determining the size of the BLR by measuring the lags of different emission lines compared to the continuum. The *International AGN Watch*[1] collaboration undertook a 13-year ground based campaign for the Seyfert 1 galaxy NGC 5548, one of the best studied AGN (see Peterson et al., 2002, and references therein) as well as obtaining UV data with IUE and HST (Korista et al., 1995). The typical time delay between the continuum and the Hβ emission line is found to be around 20 days, indicating that the distance from the central source that the Hβ line response is most significant is around 20 light days. This collaboration also monitored the variability in other AGNs in the UV and optical (see the AGN Watch webpage for references and further

---

[1]See http://www.astronomy.ohio-state.edu/∼agnwatch for more information on the International AGN Watch collaboration

details). Kaspi et al. (2000) obtained lags for several dozen Seyfert 1s and low-luminosity quasars, as did Wandel et al. (1999). These observations made several important findings. Firstly, the continuum emission in the UV and optical were found to vary with a lag of only a couple of days (see Continuum Variability section below for a discussion). Secondly, it was found that the highest ionization emission lines have the shortest time delays and largest Doppler widths. This implies that there is ionization stratification in the BLR, as expected for ionization by the continuum emission.

The 13-year campaign of NGC 5548 also allows the study of time delay with changing luminosity. As the luminosity increases, one would expect the region that is ionized to increase in size and hence the time delay increase. It is seen that the emission line lag is longer when the continuum source is brighter (Peterson et al., 2002). In Chapter 2 we model this change in size in terms of a luminosity-delay map.

A recent monitoring campaign of a handful of Seyfert galaxies by the MAGNUM collaboration (Suganuma et al., 2004; Minezaki et al., 2004; Suganuma et al., 2006) in the optical and near-infrared wavebands has found lags between the optical V and near-IR K lightcurves ranging from around 10 to 90 days. Other monitoring by Glass (2004) has found lags between the optical and IR of tens to hundreds of days also. These lags are interpreted as thermal dust reverberation from the inner edge of the dusty torus. From these results it appears that the size of the inner edge of the dust torus is well outside the size of the BLR determined by the optical/UV emission line lags for each of the objects.

1.3.2 Black Hole Masses

The mass of supermassive black holes in the cores of many normal galaxies have been determined using stellar dynamics (e.g., Kormendy & Richstone, 1995) and Miyoshi et al. (1995) determined the mass of the central object in Seyfert galaxy NGC 4258 by observing the line-of-sight velocities for water masers in the central regions of the galaxy. Reverberation mapping also provides a method for determining the black hole mass. Assuming that the velocities of the line-emitting gas are dominated by gravity, the size (from time delays) and velocity (from line widths) can be combined to estimate the mass. From the virial theorem,

$$M \quad = \quad \frac{f \, r \, \sigma^2}{G}$$

$$= \frac{f\,\tau c\,\sigma^2}{G} \tag{1.8}$$

where, f is a dimensionless factor of order unity that depends on the geometry and kinematics of the BLR, σ is the emission line velocity dispersion and $r = \tau c$ is the size of the emitting region using the time delay, τ, and speed of light, c. The virial hypothesis predicts that lines formed at different radii in the same object should follow $\tau \propto \sigma^{-2}$, and this anti-correlation is seen (Peterson & Wandel, 1999, 2000; Onken & Peterson, 2002; Kollatschny, 2003), providing evidence that these reverberation based masses are reasonably accurate measurement of the black hole mass. It has also been found that mass estimates using different emission lines in the same object are consistent with each other (Peterson & Wandel, 1999, 2000), again supporting the accuracy of the mass estimates. Additionally, the relationship between the central black hole mass and the velocity dispersion in the bulge (the so-called $M - \sigma$ relation, Ferrarese & Merritt, 2000; Gebhardt et al., 2000) that was found in quiescent galaxies is seen to hold for AGN (see Onken et al., 2003, 2004, and references therein). Using reverberation mapping, masses ranging from 10^6 to 10^9 M$_\odot$ have been determined for many AGNs (e.g., Wandel et al., 1999; Kaspi et al., 2000; Peterson, 2004; Peterson et al., 2004, 2005).

The masses determined by reverberation mapping have been used to calibrate the radius-luminosity relationship where the radius of the broad line region increases with luminosity like $R \propto L^{0.5}$ (Kaspi et al., 2000, 2005; Bentz et al., 2006). This important relationship has been used to determine the mass of a black hole from a single measurement of luminosity and line width, allowing mass estimations for large populations of AGN (Wandel et al., 1999; Vestergaard, 2002, 2004; McLure & Jarvis, 2002; Vestergaard & Peterson, 2006).

1.4   Continuum Variability

Whilst the observable, variable, continuum is seen to be driving the emission line variations, and the time delay between the two leads to important details about the size of the BLR, the relationship between the continuum at different wavelengths is also very important. The optical and UV continuum is highly correlated, and they vary nearly simultaneously - the time-delay between the UV and optical continua from the AGN Watch campaigns is found to be less than a couple days (Wanders et al., 1997; Collier et al., 1998;

Peterson et al., 1998). This suggests that the continuum variations cannot be due to disc instabilities or variable accretion rate as time delays of the order of hundreds of days (i.e. on the viscous timescale) would be expected for these models. It has been proposed that the continuum flux variations are due to reprocessing of variable high-energy (soft X-ray/ EUV) flux (Collin-Souffrin, 1991; Krolik et al., 1991; Clavel et al., 1992). In fact, Krolik et al. (1991) note that as the variations in optical and UV fluxes are almost simultaneous this would require a radial speed for temperature fluctuations within the accretion disc of greater than $c/10$, strongly suggesting reprocessing.

In the reprocessing model, ionizing photons are produced above the disc plane near the centre and irradiate the disc, heating it, and causing it to produce thermal emission in excess of that resulting from the local viscous dissipation within the disc (Rokaki & Magnan, 1992; Chiang & Blaes, 2003). The accretion disc reprocesses high energy continuum photons from near the central black hole into UV/optical continuum photons, with the hot inner regions of the accretion disc emitting mainly UV photons and the cool outer regions emitting mainly optical photons. Variability in the high-energy driving continuum results in wavelength-dependent time-delays which are set by the light travel times to different disc regions.

More specifically, the observed delays between different continuum wavelengths depend on the disc's radial temperature distribution $T(R)$, its accretion rate, $\dot{M}$, and the mass, M, of the central black hole. A disc surface with $T \propto R^{-b}$ will reverberate with a delay spectrum $\tau \propto \lambda^{-1/b}$. For the temperature distribution of a steady-state externally irradiated disc, $T(R) \propto R^{-3/4}$, the wavelength-dependent continuum time delays should follow

$$\tau = \frac{R}{c} \propto (M\dot{M})^{1/3} T^{-4/3} \propto (M\dot{M})^{1/3} \lambda^{4/3} \,. \tag{1.9}$$

Spectroscopically, wavelength-dependent continuum time-delays have been identified in two objects, NGC 7469 and Akn 564, and appear to follow the predicted relation (Wanders et al., 1997; Collier et al., 1998, 1999, 2001). More recently, Sergeev et al. (2005) have shown that these wavelength-dependent continuum time-delays can be measured by photometric monitoring of AGN. Importantly, in *all* the 14 nearby Seyferts studied the time-delays are present and show an increase in time delay with increasing wavelength. The timescales of the detected delays are consistent with standard disc models and the delays increase with greater absolute luminosity of the AGN as predicted by reprocessed

disc models.

The current observational evidence for reprocessing between the X-rays and the optical is confusing. Correlated short-term V-band and X-ray flux variations in NGC 5548 are found with a delay of 1 or 2 days, indicating the thermal reprocessing of X-ray emission by the central accretion flow (Suganuma et al., 2006). In NGC 4051, correlations between the X-ray and optical on timescales of months have been seen (Peterson et al., 2000), as well as short-term UV/optical correlations (Mason et al., 2002). A tentative correlation between X-rays and the UV/optical was also observed in Akn 564 (Shemmer et al., 2001). However, there are several observations that present problems for the reprocessing of X-ray emission. No correlation has been found between the X-ray and optical lightcurves of NGC 3516 (Edelson et al., 2000; Maoz et al., 2002), or NGC 7469 (Nandra et al., 1998). Further monitoring of NGC 7469 showed the X-ray spectral index to be correlated with the UV flux, suggesting that the EUV/soft X-rays are reprocessed into the UV/optical, and up-scattered into the X-ray band. Chiang (2002) proposes a model that explains how the uncorrelated optical/UV and X-ray light curves in NGC 3516 and NGC 7469 can be explained by variations in the size, shape, and temperature of a hot central Comptonizing plasma. Long-term X-ray and optical monitoring of NGC 5548 (Uttley et al., 2003) has shown that it is correlated, however, the amplitude of the optical variability is larger than that of the X-ray variability on timescales, the opposite of what would be expected by reprocessing of X-rays to produce the optical emission. One possibility is that the hidden EUV is strongly variable and drives the optical/UV variations, or that the optical emission region in NGC 5548 is much closer in due to a low accretion rate and high mass leading to a lower disc temperature (Uttley et al., 2003). However, reprocessing, whether it be by soft X-rays or by EUV photons, must be present to provide the near simultaneous correlated emission seen in the optical and UV.

1.4.1   Continuum reverberations and cosmology

Collier et al. (1999) showed that measuring continuum time-delays provides a promising method of determining the distance to AGN. With the temperature profile of the disc measured from the wavelength-dependent time delays, the disc's absolute flux can be calculated, and the distance to the source determined by comparison with the observed

flux. To illustrate, summing up blackbodies over disc annuli gives

$$
\begin{aligned}
f_\nu(\lambda) &= \int B_\nu(T(R), \lambda) \frac{2\pi R \, \mathrm{d}R \, \cos i}{D^2} \\
&= 11.2\mathrm{Jy} \left(\frac{\tau}{\mathrm{days}}\right)^2 \left(\frac{D}{\mathrm{Mpc}}\right)^{-2} \left(\frac{\lambda}{10^4 \text{\AA}}\right)^{-3} \left(\frac{X}{4}\right)^{-8/3} \cos i \,, \qquad (1.10)
\end{aligned}
$$

where the second expression is for the steady state disc. Solving for distance gives

$$
D = 3.3\mathrm{Mpc} \left(\frac{\tau}{\mathrm{days}}\right) \left(\frac{\lambda}{10^4 \text{\AA}}\right)^{-3/2} \left(\frac{f_\nu / \cos i}{\mathrm{Jy}}\right)^{-1/2} \left(\frac{X}{4}\right)^{-4/3} \,, \qquad (1.11)
$$

where X is a constant determined by the shape of the blackbody distribution.

Thus, by measuring the wavelength dependent time-delays and disc flux a distance to the AGN can be determined. If distances to a large number of AGN can be determined, this provides a promising method of probing cosmology, particularly as AGN can be seen way past the redshift horizon of supernovae ($z \sim 2$), which provide the current best method. This is discussed in more detail in Chapter 3, though we briefly discuss some alternative cosmological methods below.

1.4.2 Alternative cosmological methods

One approach to determining the expansion, and the ultimate fate, of the Universe, is to measure the distance to astronomical objects over a range of redshifts. This involves knowing the intrinsic brightness of an object, and then measuring its redshift and apparent brightness (the 'standard candle' method). A major problem has been that objects that have an accurate way of measuring distances to them are often not bright enough to observe over cosmologically significant scales. This led to the concept of the 'distance ladder', where the distances to more faraway objects are calibrated on the distance to closer objects. In such a way, the Hubble Space Telescope key project measured accurate distances to many Cepheid variables using the Cepheid period-luminosity relation. The distances to other objects were then calibrated using these distances and other independent methods such as the Tully-Fisher relation (which relates a galaxies luminosity and its rotational velocity), and Type Ia supernovae (discussed in more detail below). In this way the key project measured distances to objects from 60-400 Mpc, and determined Hubble's constant (the current expansion rate of the Universe) to be $H_0 = 72 \pm 8$ km s^{-1} Mpc^{-1} (Freedman et al., 2001).
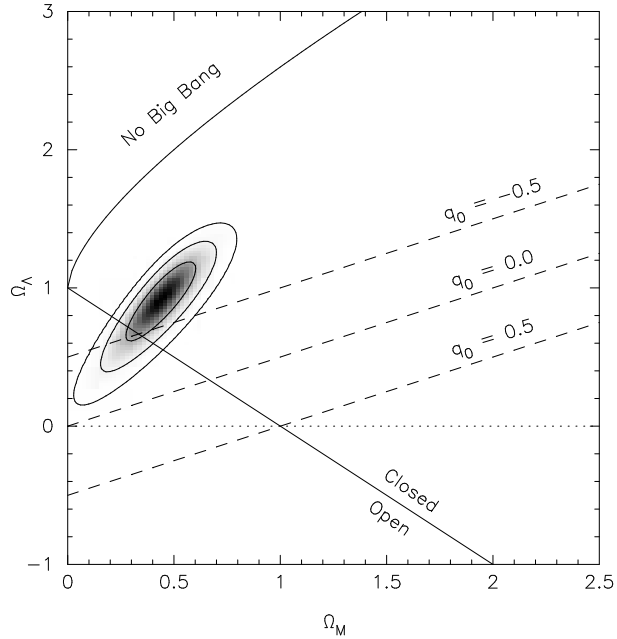
Figure 1.7: Constraints on Ω_M and Ω_Λ from SNe Ia observations. 1, 2 and 3-σ confidence limits are indicated on the χ^2 probability map. Data from Riess et al. (2004).

While it was known that the Universe contains a significant amount of ordinary matter that causes the expansion of the Universe to decelerate, the presence of other forms of energy, such as Einstein's vacuum energy, the so-called 'cosmological constant', were unknown, until observations of distant type Ia supernovae (SNe Ia) showed that the expansion of the Universe was accelerating (Riess et al., 1998; Perlmutter et al., 1999), requiring a non-zero cosmological constant, or dark energy. By measuring the redshifts and apparent brightness of SNe Ia with known intrinsic brightness, the distances to these objects can be determined. It was found that the distances of the highest redshift SNe Ia are, on average, $10\%-15\%$ further than expected in a low mass density universe without a cosmological constant. It is the energy density of matter, Ω_M, and the energy density of dark energy, Ω_Λ, that determine the nature of the expansion of the Universe, and the current best measurements from SNe Ia, assuming a flat Universe, is $\Omega_M = 0.29^{+0.05}_{-0.03}$ (and $\Omega_\Lambda = 0.71$ correspondingly) (Riess et al., 2004). Current constraints on Ω_M and Ω_Λ are shown in Fig. 1.7. However, very few SNe Ia have been observed at redshifts past $z = 1$, yet it is at redshifts greater than this that a $\Omega_M = 0.3$, $\Omega_\Lambda = 0.7$ universe varies significantly from other cosmologies (see Fig. 1.8). This is where it is advantageous to try to find alternative methods to measure distances to objects at higher redshifts, especially ones that are direct methods, not requiring calibration to the distance ladder.
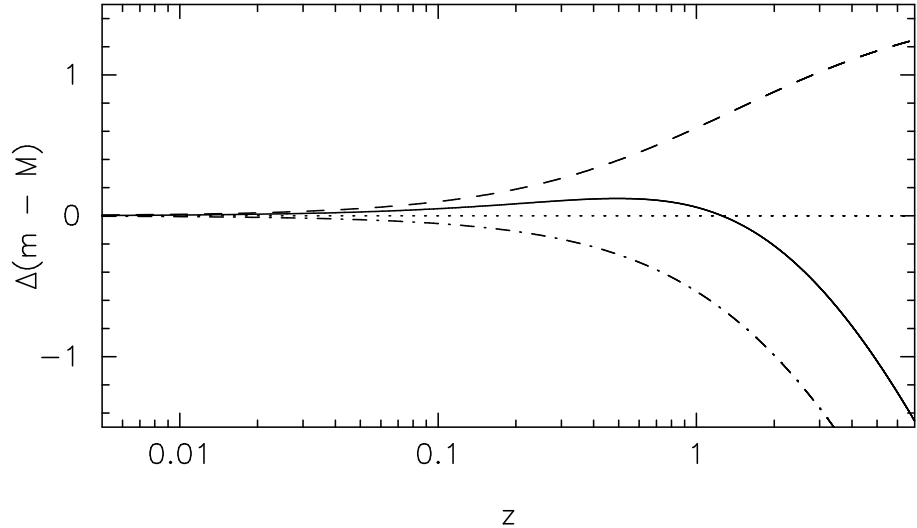
Figure 1.8: The magnitude difference between the distance modulus of 3 different cosmologies and an empty cosmology (i.e., $\Omega = 0.0$, dotted line) as a function of redshift, z. Solid line has $\Omega_M = 0.3$, $\Omega_\Lambda = 0.7$. Dashed line has $\Omega_M = 0.0$, $\Omega_\Lambda = 1.0$. Dashed-dotted line has $\Omega_M = 1.0$, $\Omega_\Lambda = 0.0$.

Two of these direct methods include using the Sunyaev-Zeldovich effect (Sunyaev & Zeldovich, 1972; Silk & White, 1978; Sunyaev & Zeldovich, 1980) and using gravitational lens systems (Refsdal, 1964). The Sunyaev-Zeldovich (SZ) effect is the decrease in brightness temperature of the cosmic microwave background (CMB) due to the presence of hot gas in galaxy clusters. To determine a distance to the cluster, X-ray observations are used to determine the temperature and surface-brightness distribution of the cluster gas, where-as radio/sub-mm observations are used to determine the cooling of the CMB in the cluster direction. A combination of both observations, with some assumptions about the spatial distribution of the gas, leads to a measurement of the angular diameter distance to the cluster. This has been used to determine Hubble's constant. Schmidt et al. (2004), for example, have found $H_0 = 69 \pm 8$ km s^{-1} Mpc^{-1} assuming $\Omega_M = 0.d3$ and $\Omega_\Lambda = 0.7$, whereas Bonamente et al. (2005) combine observations of 38 galaxy clusters to determine $74 < H_0 < 78$ km s^{-1} Mpc^{-1}, with the range of values due to different assumed gas models. In the gravitational lens method, a measurement of the time delay between two gravitationally lensed images of an intrinsically variable quasar leads to a determination of H_0, provided there is a good model for the mass distribution of the lensing galaxy. The time delay is due to the different optical path lengths brought about by the foreground lens galaxy. The time delay depends on the mass distribution of the galaxy, the position of the source, and distances to the lens and to the source (for a review see Schechter, 2005, and

references therein). Typical time delays are of the order of 30-100 days. A simple average of H_0 values determined by this method gives $H_0 = 61 \pm 7$ km s^{-1} Mpc^{-1} (Courbin, 2003). The use of AGN accretion discs as a way of determining H_0 and putting constraints on Ω_M and Ω_Λ provides another direct method that is independent on the distance ladder (see Chapter 3 for further discussion).

1.5   X-ray Binaries

X-ray binaries (see Fig 1.1) are binary systems where the donor star accretes onto a compact object (either a neutron star or a black hole) and, when actively accreting, are the brightest persistent X-ray sources in the sky. They provide an ideal laboratory to study strong gravitational fields - the inner accretion flow onto stellar mass black holes and low-magnetic field neutron stars is only at a few Schwarzschild radii ($R_S = 2GM/c^2$) where spacetime is strongly curved. They also allow an opportunity to constrain the equation of state of ultradense matter at the core of neutron stars, which leads to an understanding of the properties and behaviour of matter under extreme densities, through studying their fundamental properties such as the radius and mass.

X-ray binaries are split into two groups - low-mass X-ray binaries (LMXBs) and high-mass X-ray binaries (HMXBs). In the LMXBs the compact object (either a neutron star or a black hole) accretes matter from a low-mass companion star whose mass is less than that of the compact object, whereas the compact objects in HMXBs accrete from high-mass companion stars (blue O or B stars with $M > 10$ M$_\odot$). There are no intermediate mass X-ray binaries, as Roche-lobe overflow is unstable when the companion star is more massive than the compact object, and intermediate mass companions are not luminous enough to have significant enough stellar winds. In LMXBs accretion occurs via Roche-lobe overflow when the orbits are close enough or companion star has evolved enough, that the companion fills its Roche-lobe allowing mass transfer through the inner Lagrangian point to occur. LMXBs are significantly brighter in X-rays than in the optical, and the optical emission is mainly from reprocessing of X-rays in the disc (though the companion is more prominent in evolved LMXBs). In HMXBs the outflowing stellar wind from the companion star is captured by the neutron star or black hole, thus the companion star must be massive enough to drive a strong stellar wind. Alternatively, if the high-mass

star is a Be star, which possesses a circumstellar disc, and the compact object has a highly elliptical orbit, then as the compact object passes through the circumstellar disc it will accrete matter and emit X-rays. In HMXBs, the massive star dominates the emission of optical light, whereas accretion onto the compact object is the dominant source of X-rays. The O/B stars are luminous and therefore easily detected in the optical. The evolution of the high-mass companions in HMXBs determines their lifetime, which is short ($10^5 - 10^7$ yr), and therefore they are distributed along the Galactic plane (as young stellar populations do). In contrast, the lifetime of LMXBs is much longer ($10^7 - 10^9$ yr) and they tend to be concentrated towards the Galactic centre and in globular clusters. See fig. 1 of Grimm et al. (2002) for an illustration of the distribution of the LMXB and HMXB populations within the Galaxy. For a recent detailed review of accreting neutron stars and black holes the reader is referred to the book by Lewin & van der Klis (2006).

Further evidence for a difference in the age of the HMXB and LMXB populations comes from the presence of X-ray pulsations, or lack thereof. Interestingly, almost all HMXBs show X-ray pulsations indicating that compact object is a strongly magnetized neutron star with field strengths a few times 10^{12} G (e.g., Pringle & Rees, 1972; Bildsten et al., 1997). In these systems, material from the accretion disc is channelled onto the neutron star magnetic poles. If the magnetic and rotational axes are aligned differently, then pulsations in the X-ray lightcurve will be seen at the neutron star spin frequency as the magnetic poles rotate through the line of sight. LMXBs, on the other hand, rarely show X-ray pulsations, which is explained by the fact that the neutron stars in HMXBs are young, and therefore are strongly magnetized and rapidly rotating. In contrast, neutron stars in LMXBs are generally significantly older. Whilst they will have initially spun-down as energy is radiated at the expense of stored rotational energy, once accretion begins, they become spun up again. This leaves a weakly magnetized neutron star with $B \sim 10^8$ G, although the process of the decrease in magnetic field is not understood (Bhattacharya & Srinivasan, 1995). However, the discovery of a millisecond X-ray pulsar in the LMXB SAX J1808.4−3658 (Wijnands & van der Klis, 1998), showed that over time, accretion onto the neutron star in LMXBs can lead to it being spun-up to millisecond periods, leaving a weakly-magnetized, rapidly rotating neutron star, which once accretion halts becomes a millisecond radio pulsar.

Of course, when studying X-ray binaries it is important to be able to determine whether the compact object is a black hole or a neutron star. Obviously, this can be done

by determining the mass of the compact object (neutron stars should not be heavier than around 3 $M_\odot$, see below) through optical radial-velocity data of the companion star. Even with only the mass function for the companion determined (through the orbital period and absorption-line velocity amplitude), this puts a lower limit on the mass of the compact object, and hence can determine whether or not it can be a neutron star. Black holes can be ruled out easily if a property that can be associated with a neutron star is seen, for instance, X-ray pulsations or type I X-ray bursts (thermonuclear flashes on the surface of a neutron star, Lewin, van Paradijs & Taam, 1995; Bildsten, 1998). Unfortunately, however, there are no such clean-cut distinctive characteristics that are only seen in black hole binaries.

1.5.1 Transient Low-mass X-ray Binaries

While many of the LMXBs are persistent sources and always actively accreting, there is a group of LMXBs that are transient. These transients spend the vast majority of their time in a quiescent state, during which very little or no accretion onto the compact object occurs. Occasionally, however, these systems go into outburst, which usually last weeks to months, throughout which they increase greatly (by a factor of around 10^4, though it can be as much as 10^9) in brightness. Such outbursts arise due to a significant increase in the mass-accretion rate onto the compact object (for reviews of neutron star and black hole transients see, e.g., Chen et al., 1997; Campana et al., 1998a). These transient systems allow for the study of accretion onto neutron stars and black holes over a wide range of accretion rates and luminosities. It is believed that the increase in mass-accretion rate during outburst is caused by a thermal-viscous instability in the accretion disc, similar to the dwarf-novae instability (see Lasota, 2001, for a review of disc instabilities). In the disc instability model a steady-state accretion flow is stable if hydrogen is ionized everywhere. But, if the temperature or mass accretion rate is low enough that the disc is cool enough for hydrogen to recombine, the disc then becomes thermally and viscously unstable, changing from a hot, ionized state in outburst, to a cold, neutral state in quiescence. However, to match the properties of low-mass X-ray binaries the disc-instability model becomes a little more complicated, with the need for irradiation of the disc to quench the instability by keeping a lot, or all, of the disc above the hydrogen ionization temperature (van Paradijs, 1996; Dubus, Hameury & Lasota, 2001).

During outburst the optical spectra of LMXBs show a few emission lines, especially Balmer lines, due to reprocessing of X-rays in the disc which dominates over the viscous heating within the disc. Usually, the companion star is not observable (unless the companion star is evolved), and the optical spectrum is totally unlike an ordinary star. However, when in a quiescent state optical emission in the system is dominated by the companion star rather than by X-ray heating of the accretion disc, which is not important in this state (e.g., van Paradijs & McClintock, 1995; van Paradijs, 1998).

The work on X-ray binaries in this thesis focuses on the quiescent emission from neutron star X-ray binaries. We therefore review the emission processes involved, and compare with black hole quiescent emission. Before discussing quiescent emission from neutron star X-ray binaries, it is relevant to briefly outline the structure of a neutron star and their formation, as the various components play an important part in the quiescent emission.

1.5.2   Neutron stars

Neutron stars are very small (radius $\sim$10 - 20 km), dense, stars with masses between about 1.4 and 3.0 $M_\odot$, with the core composed of degenerate neutron gas, or more exotic forms of matter. They are one of the few possible endpoints of stellar evolution. Neutron stars cannot be more massive than around 3.0 $M_\odot$ (this limit is not known well due to the lack of knowledge of the equation of state for neutron-degenerate matter) as gravitational forces would overcome the degenerate neutron gas pressure, causing gravitational collapse, and the formation of a black hole (Srinivasan, 2002). Stars formed at the end of stellar evolution with a mass lower than about 1.4 $M_\odot$ are white dwarfs and are supported by degenerate electron gas pressure rather than a degenerate neutron gas. The neutron star radius depends on the mass, with more massive neutron stars having smaller radii. The high density of neutron stars leads to a high surface gravity and a substantial gravitational redshift for light emitted from the surface.

The structure of a neutron star is still not well-understood, though the currently accepted theoretical picture is outlined here (see Fig. 1.9). For detailed discussions see, for example Lattimer & Prakash (2001) or Yakovlev & Pethick (2004). The outer-most region is a thin *atmosphere* several centimetres deep, which is mainly hydrogen and helium, as heavier elements quickly sink under the strong gravity of the neutron star. The next

hundred metres down is the *outer crust* consisting of atomic nuclei and electrons. The electrons form a degenerate gas, whereas the nuclei are solid in most of the outer crust. At the base of the outer crust we get to the 'neutron drip' layer where it becomes energetically favourable for neutrons to drip out of the nuclei and move around freely forming a neutron gas between the nuclei. This 'neutron drip' layer marks the boundary between the inner and outer crust. The next 1 km or so down is the *inner crust* which consists of electrons, free neutrons and neutron-rich atomic nuclei (Haensel, 2003). As the depth (and therefore density) increases, the fraction of free neutrons also increases.

Below the inner crust is the stellar *core* where all the constituents are strongly degenerate and it is here where the neutron star structure is least certain. The outer core consists of mainly neutrons with several percent being protons, electrons and maybe muons. The size and content of the inner core, which could be as big as several kilometres, has a number of (exotic) possibilities. It could contain nucleon matter, basically the same as the outer core. Other possibilities include hyperonic matter, a pion condensate, a kaon condensate or even a quark fluid. The state of the matter in the core is important for neutron star cooling, as it determines the rate of neutrino emission - an important process in neutron star cooling. A good understanding of the cooling of neutron stars can therefore lead to a greater understanding of the deep interior of neutron stars (Yakovlev & Pethick, 2004).

The temperature at the surface of the neutron star is dependent on the temperature of the core and on the composition of the outer 100 m of the neutron star - the atmosphere and the outer crust (Brown, Bildsten & Chang, 2002). In accretion-heated neutron stars (the ones that are relevant to this thesis) the temperature of the core is around 10^8 K, and is constant for timescales of $\leq 10^4$ yr (Brown, Bildsten & Rutledge, 1998), whereas the temperature of the surface is around 10^6 K. As mentioned above, the relationship between the core and surface temperature is dependent on the equation of state and thermal conductivity of this outer envelope. The core contains practically all the mass and thermal energy of the neutron star. The outer and inner crust together occupy around 1 km and contain only about 0.01 $M_\odot$ (Brown, 2000). The core and inner crust, where the densities are $\gg 10^{10}$ g cm^{-3} are almost isothermal, and it is only in the outer envelope (the least dense region of the star) where there is an appreciable temperature gradient (Gudmundsson, Pethick & Epstein, 1983; Potekhin, Chabrier & Yakovlev, 1997). The temperature profile is dependent on the radiative and conduction opacities which change

Inner crust (~1km) Increasing amounts of free neutrons

Atmosphere (~few cm) H and He

Core (~9 km) superfluid of degenerate neutrons, or something more exotic?

Outer crust (~100m) atomic nuclei and degenerate e⁻
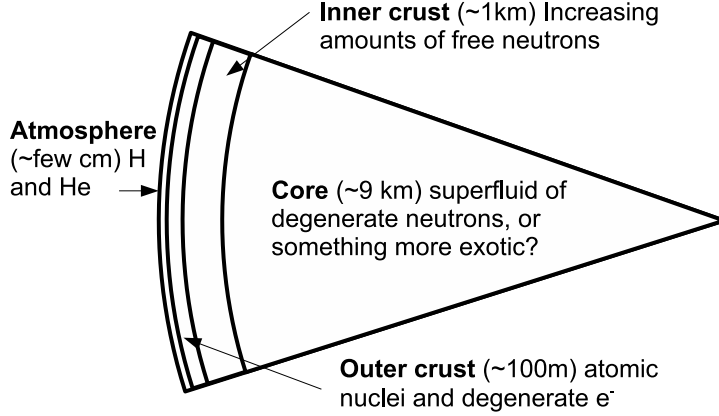
Figure 1.9: A diagram outlining the structure of a neutron star (not to scale).

significantly as the density (and temperature) increases and the structure of the star changes from containing degenerate electrons in the outer crust to increasing amounts of free neutrons from the inner crust to the core (Gudmundsson et al., 1983). Whilst the core temperature is constant for timescales of $\leq 10^4$ yr, the outer envelope can change temperature on timescales of days (Brown et al., 2002). Energy given to the outer envelope of the neutron star during accretion is generally radiated away due to the steep thermal gradient. However, when nuclear reactions are ignited in the inner crust due to compression by accreted material the core can be heated (Brown et al., 1998, see the section below on quiescent emission from neutron stars).

1.5.3 Neutron Star Formation in Low-Mass X-ray Binaries

Neutron stars are formed in supernovae explosions at the end of stellar evolution (see, e.g. Janka, 2004; Fryer & Hungerford, 2005, for a review of the mechanisms). There are several formation paths for neutron stars: accretion induced collapse of a heavy white dwarf, or, collapse of star between about $\sim 8 - 20$ M$_\odot$ (though collapse of heavier stars to neutron stars is also possible, see e.g., Muno et al., 2006). In the accretion induced collapse, a heavy white dwarf collapses after having gained mass via accretion pushing its mass over the Chandrasekhar limit and leading to a supernovae type Ia. The fraction of neutron stars formed in this manner is at least 100 to 1000 times lower than the other formation scenario (Fryer, 1999), though accretion induced collapse may be important in the formation of neutron stars in globular clusters.

The origin of a binary with a low mass companion and a neutron star is initially a little perplexing - one might quite reasonably expect that it would difficult to keep the companion bound to the binary in a supernovae explosion because more than half the mass of the binary will be lost in the explosion. Also, the current orbits of LMXBs are too small to have accommodated the progenitor to the neutron star. Three basic solutions to this problem are: (i) the supernova explosion was relatively quiet, resulting from accretion induced collapse of a white dwarf, (ii) the neutron star was born outside the binary and captured (this most likely applies to the formation of LMXBs in globular clusters), and (iii) the binary loses most of its initial mass and angular momentum during a 'spiral-in' phase. In the last case, as the neutron star progenitor (the more massive star in the binary) evolves it will expand and engulf the companion forming a common envelope. The friction from the common envelope causes the orbits to shrink, which in turn can cause the ejection of the common envelope. Thus, this common envelope phase will reduce both the mass of the progenitor and the size of the orbit. Finally, the remaining core continues to evolve and turn into a supernova. See Verbunt & van den Heuvel (1995) for a detailed review of the formation and evolution of neutron stars in X-ray binaries. We leave further discussion of the formation of LMXBs in globular clusters to the next section.

1.5.4   Low-Mass X-ray Binaries in Globular Clusters

It has long been noted that there is an over-abundance of LMXBs found in Galactic globular clusters (gravitationally bound systems of about a million or so stars in the Galactic halo) compared to in the rest of the Galaxy (Clark, 1975), and in recent years, hundreds more LMXBs and low-luminosity X-ray sources have been discovered using *Chandra* and, to a lesser- extent, *XMM-Newton* X-ray observations (see Heinke et al., 2003b; Pooley et al., 2003, and references therein). For example, using the excellent spatial resolution of *Chandra*, Heinke et al. (2005) recently detected over 300 X-ray sources within the half-mass radius (the radius within which half the mass of the cluster is contained) of the globular cluster 47 Tuc alone (see Fig. 1.10). Galactic globular clusters provide an ideal location to study these types of sources - the distance to host clusters can usually be determined more accurately than for the Galactic X-ray binaries. Distances to globular clusters can be determined by comparing the apparent magnitude of a group of stars in the horizontal branch in the cluster colour-magnitude diagram with the absolute magnitude of stars in
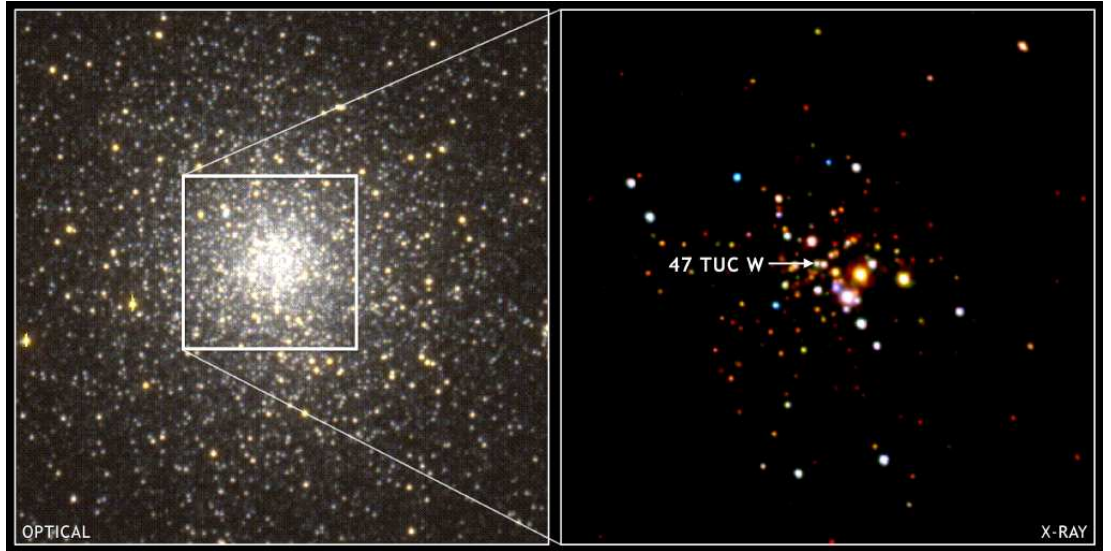
Figure 1.10: Optical and X-ray images of the globular cluster 47 Tucanae. The *Chandra* X-ray image is false colour - with red indicating soft X-rays, and blue hard X-rays. The optical image of the globular cluster 47 Tuc was taken with the European Southern Observatory's Danish 1.54-m Telescope at La Silla, Chile. Credit: X-ray: NASA/CXC/CfA/J.Grindlay & C.Heinke; Optical: ESO/Danish 1.54-m/W.Keel et al.

this phase. The known distance and reddening allows accurate luminosities to be derived and removes the distance uncertainty from the properties. All the low-luminosity X-ray sources in globular clusters (at least to current detection levels) are binary systems (active binaries, CVs, LMXBs). Thus, studying globular clusters in X-rays allows us to study the binary content of globular clusters and how that might evolve in time.

The high incidence of compact binaries in globular clusters suggests that the higher stellar density in globular clusters, particularly in the cluster core, significantly increases the formation rate of LMXBs. The high densities increase the likelihood of close encounters of stars and binaries with each other. For instance, the tidal capture of neutron stars by main-sequence stars can occur (Fabian, Pringle & Rees, 1975). In this process, energy is taken out of the orbital motion by the tidal wave caused on the main-sequence star due to the very close (~ 3 stellar radii) passing of a neutron star, which binds the two together as a binary. Similarly giants can capture neutron stars. Another possibility, is the formation of binaries via exchange encounters (e.g. Verbunt & Hut, 1987; Hut, Murphy & Verbunt, 1991). Here, the neutron star encounters an existing binary, temporarily forming a triple system. However, this system will be unstable, and the lightest star gets ejected, leaving a neutron star binary. Finally, ultracompact systems may be formed via direct collisions of
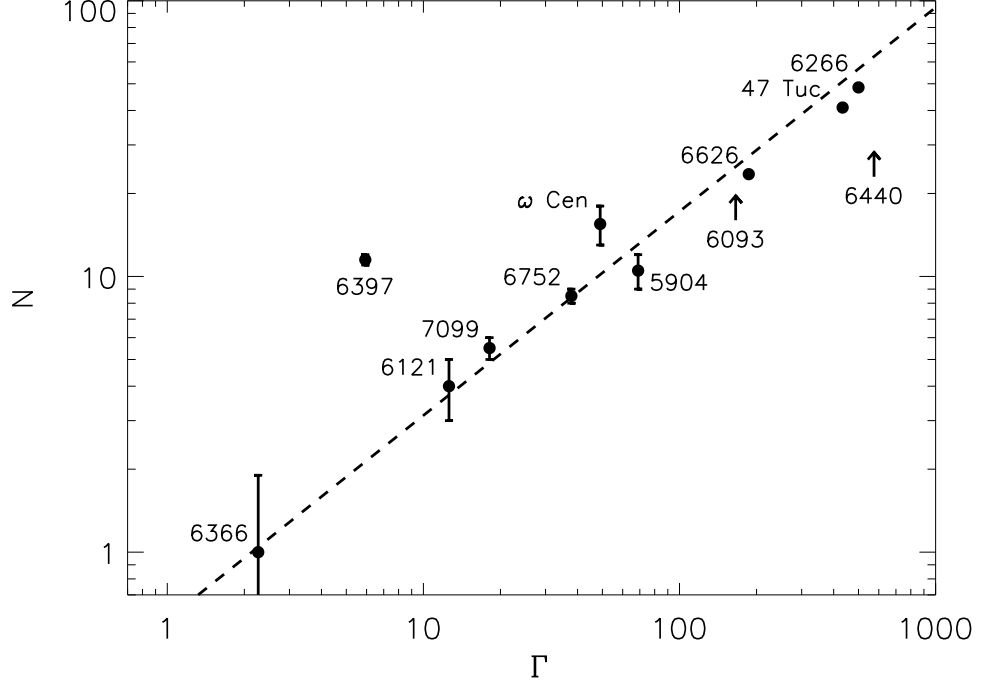
Figure 1.11: Number of globular cluster X-ray sources (N) with $L_X \geq 4 \times 10^{30}$ ergs s^{-1} vs. the normalised encounter rate, Γ of the cluster. An arrow indicates a globular cluster for which the *Chandra* observation did not reach the required sensitivity. The dashed line indicates the best-fit $N \propto \Gamma^{0.74}$. From Pooley et al. (2003), courtesy of Dave Pooley.

a neutron star with a red giant, followed by orbital decay (Sutantyo, 1975; Ivanova et al., 2005). As the neutron star enters the giant's atmosphere, it is slowed down. If it leaves the giant's atmosphere with a velocity less than the escape velocity, $(2GM_{tot}/R)^{1/2}$, then it will be captured in a close binary orbit. The passage of the neutron star through the red giant's atmosphere will cause the common envelope to be disrupted, hence, these collisions produce tight, eccentric neutron star-white dwarf binaries (Rasio & Shapiro, 1991).

Recently, there has been observational evidence that it is the case that higher densities in the globular cluster cores increases binary formation - Pooley et al. (2003) show that the number of X-ray sources in globular clusters is closely linked with stellar encounter rate for that cluster (see Fig. 1.11), far more so than with the mass. This has also been shown for the CV population in globular clusters (Pooley & Hut, 2006). In Chp. 5, we compare the observed number of X-ray sources in Terzan 1 with what would be expected from this relationship.

1.6 Quiescent Emission from Neutron Stars

Well over a dozen neutron star X-ray transient systems have been detected in quiescence as well as in outburst. The quiescent luminosity of these neutron star systems is typically $10^{32} - 10^{34}$ erg s^{-1} (though some are fainter) compared to typical outburst luminosities in the range $10^{36} - 10^{38}$ erg s^{-1}. One way to investigate the source of this emission, is to study the X-ray spectra. The X-ray spectra of these quiescent neutron star systems are generally characterised by two components: a soft component (which dominates the spectra below a few keV), equivalent to a blackbody temperature of $kT \sim 0.1 - 0.3$ keV, and a hard power-law tail (which dominates the spectra above a few keV).

The mechanism most often used to explain the thermal X-ray emission from neutron star transients in quiescence is that in which the emission is due to the cooling of a hot neutron star which has been heated during outburst (van Paradijs et al., 1987; Brown et al., 1998). In the Brown, Bildsten & Rutledge (1998) model, during each outburst the neutron star core is heated by nuclear reactions occurring deep in the crust that are induced by compression of matter during accretion. After a period of around 10^4 years, the core is heated to a steady state, and is maintained at temperatures around 10^8 K by recurrent outbursts. This hot neutron star then emits thermally during quiescence. The temperature of the neutron star core and surface in quiescence is set by the time-averaged (over the neutron star thermal timescale) mass accretion rate, such that the quiescent luminosity is given by (Brown et al., 1998; Rutledge et al., 2002b)

$$L_q = 8.7 \times 10^{33} \left(\frac{\langle \dot{M} \rangle}{10^{-10} \ M_\odot \ \mathrm{yr}^{-1}} \right) \frac{Q}{1.45 \ \mathrm{MeV}} \ \mathrm{ergs \ s^{-1}} \ , \quad (1.12)$$

where $\langle \dot{M} \rangle$ is the time-averaged mass accretion rate onto the neutron star and Q is the amount of heat deposited in the crust per accreted nucleon and when assuming standard neutron star core cooling model. For an accretion flux onto the neutron star, $F_{\mathrm{acc}} = \epsilon \dot{M} c^2 / (4\pi D^2)$, the 'rock bottom' quiescent flux due to deep crustal heating is then

$$F_q \approx \frac{\langle F_{\mathrm{acc}} \rangle}{135} \frac{Q}{1.45 \ \mathrm{MeV}} \frac{0.2}{\epsilon} \quad (1.13)$$

where $\langle F_{\mathrm{acc}} \rangle$ is the time-averaged accretion flux, and the accretion efficiency $\epsilon = 0.2$ for an accretion luminosity of $GM\langle \dot{M} \rangle / R$.

If the distance, D, to an object is known, and the emission is blackbody-like, the emitting area of object, R, can be determined. As $f = L/4\pi D^2$ and $L = 4\pi R^2 \sigma T^4$, then

$f = (R/D)^2 \sigma T^4$, where the flux, f, and the temperature T, can be measured from X-ray spectral fitting. One criticism of the thermal emission hypothesis had been that blackbody spectral fits to quiescent spectra vastly underestimated the emitting area, with $R \approx 1$ km (Rutledge et al., 2000, and references therein). However, when realistic neutron star atmosphere model spectra are used (for example the model by Zavlin, Pavlov & Shibanov, 1996) realistic emitting areas of around 10 km are found (e.g., Rutledge et al., 1999, 2000). The neutron star atmosphere models used are for a pure hydrogen atmosphere and for a weakly magnetized neutron star (with $B < 10^{10}$ G, as expected for neutron stars in LMXBs). The atmosphere is expected to be nearly pure hydrogen as the accreting metals will gravitationally settle faster than they are supplied. The reason for the difference in measured emitting area between blackbody and neutron star atmosphere models is due to a slight difference in shape of the spectra. The opacity in the hydrogen atmosphere is dominated by free-free absorption, which is highly frequency dependent ($\propto \nu^{-3}$). Therefore, higher energy (frequency) photons escape from deeper (and thus hotter) regions in the atmosphere than the less energetic photons (Pavlov & Shibanov, 1978; Rajagopal & Romani, 1996; Zavlin et al., 1996). This makes the spectrum harder than a blackbody, and so any attempted blackbody fit will result in a systematically higher temperature and lower emission radii.

When published, the Brown et al. (1998) model was able to explain the luminosities of the majority of quiescent neutron-star transients, however, there are some exceptions, such as Cen X−4 (Rutledge et al., 2001b) that are cooler than expected given their known accretion histories. This is generally explained by assuming that enhanced core cooling processes (as opposed to the standard processes assumed by Brown et al., 1998) occur. We leave further discussion of this to Chapters 4, 5 and 6 where we investigate and discuss quiescent neutron-star transient luminosities further. However, at this point, it is worth briefly mentioning the difference between 'standard' and 'enhanced' core cooling processes. The difference is due to the level of neutrino emission from the core. Neutrinos carry away energy, and provide an efficient way of cooling warm neutron stars. The dominant neutrino cooling reactions are known as Urca processes[2] (see, e.g., Yakovlev & Pethick, 2004; Lattimer & Prakash, 2004). In this process thermally excited particles alternatively undergo

---

[2]'Urca' is, quite surprisingly, not another astronomical acronym, but the name of a casino in Rio de Janeiro at which George Gamow commented to Mario Schoenberg "the energy disappears in the nucleus of the supernova as quickly as the money disappeared at that roulette table." (Gamow & Schoenberg, 1941)

beta and inverse-beta decays, with each reaction producing a neutrino or antineutrino. The most efficient Urca process is the direct Urca process involving nucleons:

$$n \rightarrow p + e^- + \bar{\nu}_e \,, \qquad p \rightarrow n + e^+ + \nu_e \,. \qquad (1.14)$$

This can only occur if both energy and momentum are conserved simultaneously. If this is not possible, then the modified Urca process can take place, in which a bystander baryon absorbs momentum:

$$n + (n, p) \rightarrow p + (n, p) + e^- + \bar{\nu}_e \,, \qquad p + (n, p) \rightarrow n + (n, p) + e^+ + \nu_e \,. \qquad (1.15)$$

In standard cooling models, the modified Urca process is the neutrino emission that takes place. However, in enhanced cooling models, where the level of neutrino emissions is higher, the direct Urca process is usually invoked. Enhanced cooling via the direct Urca process requires that the neutron star is more massive than the canonical value of 1.4 $M_\odot$, with a mass around 1.7 $M_\odot$ (Colpi et al., 2001). There are, however, other processes that increase neutrino emissions such as the breaking of nucleonic Cooper pairs (e.g., Flowers et al., 1976; Gusakov et al., 2004), or processes similar to the direct Urca process, but involving pion or kaon condensates, or quark matter (Yakovlev & Pethick, 2004).

Nevertheless, back to the discussion on the thermal emission from neutron stars. Whilst the cooling of an accretion-heated neutron star is the most widely accepted model for the thermal emission, there are alternative models that have been proposed (see Campana et al., 1998a, for a detailed review of the possibilities). For instance, continued accretion onto the neutron star surface at a low level during quiescence can produce a thermal-like spectrum (Zampieri et al., 1995). Another possibility is low-level accretion down to the magnetospheric radius (Menou et al., 1999; Menou & McClintock, 2001) where accretion onto the surface is prevented due to the propeller effect - when the magnetosphere is beyond the co-rotation radius, centrifugal force prevents material from entering the magnetosphere, and thus accretion onto magnetic poles ceases (Pringle & Rees, 1972; Lamb et al., 1973).

As mentioned above, there is sometimes a power-law component present in the quiescent spectra of neutron star transients. The origin of the power-law component is poorly understood, and cannot be explained by the neutron star cooling model. In some cases it is not present, whereas in other systems it completely dominates the emission (e.g. EXO 1745−248 in the globular cluster Terzan 5, Wijnands et al., 2005a). Jonker

et al. (2004b) found that the power-law contribution is low only when the source quiescent luminosity is close to $\sim 1 - 2 \times 10^{33}$ erg s^{-1}, and that both at lower values the power-law contribution to the 0.5-10 keV luminosity increases. Possible mechanisms for the emission of this power-law component include residual accretion onto the neutron star magnetosphere (as mentioned above) or a putative pulsar wind colliding with infalling matter from the companion star (Tavani, 1991; Campana et al., 1998a). Whilst the 'rock-bottom' flux may be set by the cooling neutron star, additional residual accretion may cause the power-law component. This can explain some variability seen in quiescence (this will be discussed in detail in Chp. 4).

Finally, some X-ray transients (the quasi-persistent transients) spend an unusually long time in outburst, with outbursts lasting years to decades rather than the more common weeks to months. During outbursts, the crust of the neutron star is heated to a point beyond thermal equilibrium with the stellar interior. Once accretion falls to quiescent levels, the crust cools thermally, emitting X-rays, until it reaches equilibrium again with the core (e.g., Wijnands et al., 2002a; Rutledge et al., 2002b). Whilst in 'normal' transients the crust and core reach thermal equilibrium in days, it can take months to years for the quasi-persistent sources. These sources allow us to probe the cooling mechanisms at work in neutron stars, and set limits on the structure of the core. These sources are the focus of Chp. 6.

1.6.1   Quiescent Emission from Black Holes

While the results presented in this thesis focus on the quiescent emission from neutron stars, it is interesting to note the differences between quiescent emission from black holes and neutron stars. In general, black hole transients in quiescence are usually seen to be intrinsically fainter than the quiescent neutron star transients (e.g., see fig. 5 of Tomsick et al., 2005), with quiescent luminosities of $< 10^{31}$ ergs s^{-1}, though there are some exceptions. This difference has been proposed as evidence for advection of energy across a black hole event horizon (Narayan et al., 1997; Garcia et al., 2001; Kong et al., 2002), where there is continued low-level accretion during quiescence in an advection-dominated accretion flow (ADAF). In this model the accreting gas reaches the compact object with a large amount of thermal energy. If the compact object is a black hole, then thermal energy will disappear though the event horizon, if it is neutron star, then it will hit the surface

and be radiated away from there. However, such a model over predicts the neutron star luminosities, and requires that accretion rate onto the neutron star has to be systematically lower than in quiescent black hole transients, for instance by having accretion onto the neutron star prevented by the propeller effect (Menou et al., 1999). Fender, Gallo & Jonker (2003) present another possible model for quiescent emission where in quiescence the binaries are in a 'jet-dominated' state, in which the majority of the liberated accretion power is in the form of a radiatively inefficient jet and not dissipated as X-rays in the accretion flow. In this model, based on empirical scaling relations at higher luminosities, black hole transients are more 'radio-loud' than neutron star transients, leading to lower quiescent X-ray luminosities.

Whatever the nature of the quiescent emission in black hole transients, any residual accretion during quiescence in neutron star transients should be on-top of the base flux set by the emission from the accretion heated neutron star.

1.7   X-ray Astronomy

I now discuss X-ray astronomy, in particular, the important features of the *Chandra* and *XMM-Newton* X-ray telescopes, and X-ray spectral analysis.

As the Earth's atmosphere is opaque to X-rays, X-ray telescopes have to be placed in space. The first extra-terrestrial X-rays (apart from the Sun) were detected in 1962 from the source Scorpius X-1, which turned out to be a low-mass X-ray binary, by using a Geiger counter on a sounding rocket and at the same time the X-ray background (a background source of X-rays from all over the sky) was detected (Giacconi et al., 1962). Since then, many X-ray telescopes have been sent into orbit around the Earth. In the late 1990s, two of the most sophisticated X-ray telescopes yet were launched - NASA's *Chandra* X-ray Observatory and ESA's *XMM-Newton*.

The X-ray data presented in this thesis are from both *Chandra* and *XMM-Newton*. I utilise the imaging-spectrometry mode in both these satellites, where the arrival time, position and energy of each photon that arrives at the Charge-Coupled Device (CCD) is known, allowing for broad-band X-ray spectroscopy. Photoelectric absorption of an X-ray in silicon within the CCD results in the liberation of a proportional number of electrons. A higher energy X-ray liberates more charge, allowing a determination of the energy of
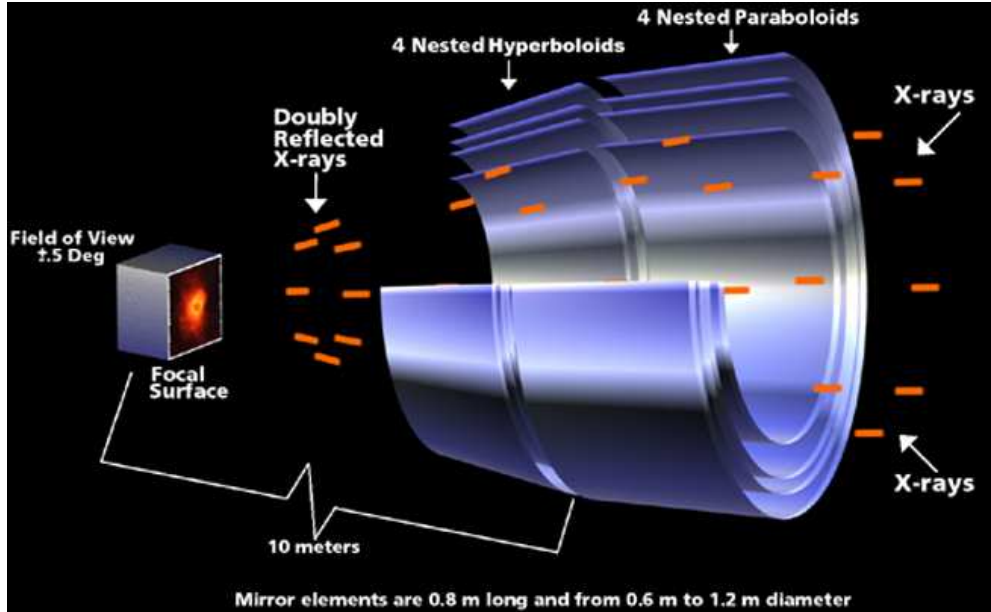
Figure 1.12: Diagram of the design of the *Chandra* mirrors. Credit: CXC/D. Berry

the incident X-ray. The position of the incident X-ray is determined by the CCD pixel that it hits, whereas the arrival time is determined from the time of the exposure when it arrived. This can cause a problem, however, if a source is very bright, as more than one photon may arrive during a single exposure. This 'pile-up' causes the count rate to be underestimated as the two or more events are counted as one. It also distorts the energy spectrum as the apparent energy is approximately the sum of the energies of the two (or more) photons. The CCDs are also sensitive to optical and UV photons as well as X-rays and so an optical blocking filter has to be placed in front of the detectors.

Another feature of X-ray telescopes that differs from optical telescopes is the mirrors used. In optical telescopes a large primary mirror focuses the light onto a smaller secondary mirror and then onto the detector/instruments. However, the critical angle for external reflection of X-rays from materials composed of heavy elements is only around $1°$ for X-rays with energies of a few keV (Aschenbach, 1985). Obviously, this leads to a much different design for the mirrors! Both *Chandra* and *XMM-Newton* use Wolter type I mirrors where the reflections occur off the inside of a paraboloid surface followed by a hyperboloid surface. Such a system allows several mirrors to be nested inside one another, vastly increasing the total collecting area of the telescope (see Fig. 1.12 for a diagram of the *Chandra* mirror set-up). I now briefly describe the features of each telescope, with a focus of the instruments that are used in this thesis.

1.7.1 Chandra X-ray Observatory

NASA's *Chandra* X-ray Observatory is in an elliptical high-earth orbit which allows uninterrupted observing intervals of more than 48 hours in length and it is sensitive to X-rays in the energy range from 0.2 keV to 10 keV. The mirror consists of four pairs of nested reflecting surfaces with the largest having a diameter of 1.2 m. The focal length of the mirrors is 10 m. The spatial on-axis resolution is $0\rlap{.}''5$ and is limited by the pixel size, rather than the mirrors. It has two instruments at the focal plane of the mirrors - the high resolution camera (HRC), and the Advanced CCD Imaging Spectrometer (ACIS). I will only discuss the ACIS. The ACIS can operate in several modes, when used on its own it can provide high resolution imaging, with medium resolution spectra (this is the mode that I utilise), however, it can also be used in conjunction with the High Energy Transmission Grating (HETG) or Low Energy Transmission Grating (LETG) to obtain higher resolution spectra.

The ACIS instrument is comprised of two arrays of CCDs arranged in two configurations, as an imaging array (ACIS-I) and a spectroscopy array (ACIS-S). The ACIS-S is comprised of 4 front-illuminated and 2 back-illuminated CCDs. The back-illuminated CCDs are more sensitive to lower energies than the front-illuminated CCDs, which are more efficient at higher energies. However, the drawback to the back-illuminated CCDs is that they have a higher background. The ACIS-I has 4 front-illuminated CCDs.

When used in the basic default full-frame mode, the active CCDs are exposed for ~ 3.2s, and at the end of the exposure, the charge in the active region is quickly (~ 41 ms) transferred into the frame store (which is shielded from incident X-rays), allowing the next exposure to begin whilst the last is read-out. If the source is particularly bright, a read-out streak will appear on the image, where photons have hit the CCD in the ~ 41 ms that the source is transferred to the frame store. In addition, there are more complicated operating modes allowing timing and continuous clocking mode (for extremely bright sources), that are not discussed here.

1.7.2 XMM-Newton

The European Space Agency's X-ray Multi-Mirror telescope, *XMM-Newton*, carries three X-ray telescopes which are sensitive to X-rays in the energy range 0.1 - 15 keV. They each

contain 58 concentric nested mirrors, which offers a larger collecting area than *Chandra*. The mirrors are 0.3m to 0.7m in diameter and 0.6m in length and have a focal length of 7.5m with an on-axis spatial resolution of $5''$ and field of view of $30'$. It has three different scientific instruments - the three European Photon Imaging Cameras (EPIC), two Reflection Grating Spectrometers (RGS) and an Optical Monitor (OM), co-aligned with the main X-ray telescope. I will only briefly discuss the EPIC cameras here.

One EPIC camera is located at the prime focus of each of the three telescopes. Two of the cameras employ metal oxide semi-conductors (MOS) CCDs that are comprised of 7 individual CCDs in a mosaic (Turner et al., 2001), while the third uses the PN CCD which comprises 12 silicon CCDs (Strüder et al., 2001). The MOS detectors are more sensitive to the 'soft' X-rays, whereas the PN gives better response to the 'hard' X-rays. As with the *Chandra* ACIS instrument, there are a variety of operating modes allowing for timing etc.

1.7.3   X-ray spectral analysis

The shape of the X-ray spectra are generally fitted with simple physically-motivated models in order to tell us about the X-ray emitting source. Changes in the shape of the X-ray spectra can be interpreted in terms of changes in the source. However, unfortunately, it is often found that spectra can be fit equally well with different models, or combinations of models. Nevertheless, it is often the best that can be done, for instance due to the limited number of photons from faint sources. Throughout this thesis I have used the X-ray spectral fitting package `XSPEC` (see Arnaud, 1996, for details, though I summarise the important points below).

In `XSPEC` a model is convolved with the instrument response function (which effectively gives the probability that an incident photon of particular energy will be detected) to give the predicted counts spectrum. This is then compared with the observed background-subtracted counts spectrum by means of a 'goodness-of-fit' statistic. The model parameters are then varied to find the best-fitting parameters when the goodness-of-fit statistic is optimum. Generally, if there are enough counts in the spectrum to allow the spectrum to be binned into a least 15 counts per bin, then the χ^2 fit-statistic is used as defined by:

$$\chi^2 = \sum (C(I) - C_p(I))^2/(\sigma(I))^2 \qquad (1.16)$$

where $C(I)$ are the observed counts in detector channel I, $\sigma(I)$ is the error for channel I (usually estimated by $\sqrt{C(I)}$) and $C_p(I)$ are the predicted model counts in channel I.

Once the value of χ^2 has been minimized, one can determine whether a good fit has been found by calculating the reduced-$\chi^2 = \chi^2/\nu$, where ν is the number of degrees of freedom. Ideally, one would like $\chi^2 = \nu$, and so the reduced-$\chi^2 = 1.0$. Values much greater than 1.0 indicate that the model is not a good representation of the observed data, whereas a value much lower than one indicates that the errors have been over-estimated. Once a good-fit has been achieved, the errors in the model parameters can be determined by varying each parameter in turn until χ^2 has changed from the minimum value by a fixed amount. This amount depends on the required confidence interval and on the number of parameters whose confidence space is being calculated. For example, for 1-σ errors (or, equivalently a 68% confidence limit) and 1 parameter, $\Delta\chi^2 = 1.0$, or, for 90% confidence limit and 1 parameter, $\Delta\chi^2 = 2.71$.

Of course, when observing faint objects, such as quiescent X-ray transients, it is often the case that there are not that many (< 50) counts in the spectrum. χ^2 statistics cannot be used in these cases because the χ^2 statistic requires that there is a sufficient number of counts such that the deviation of the observed number from the expected number has a Gaussian distribution to good approximation. Instead, the spectrum is left unbinned, and the C-statistic (Cash, 1979) can be used when the background is very low, and the W-statistic (Wachter et al., 1979) when the background is significant. Both allow the determination of confidence intervals in the same way as χ^2 statistics, however, they do not provide a goodness-of-fit like the reduced-χ^2 that is easy to interpret. However, a Monte Carlo simulation can be used to provide this by calculating the percentage of simulated spectra based on the best-fit model that have a fit statistic less than that for the data. If the observed spectrum was produced by the model then this number should be around 50%.

1.8   Thesis Outline

The first part of this thesis is focused on my AGN research, where-as in the second part, I present my work on X-ray binaries. In chapter 2, I investigate the change in the size of the broad-line region with luminosity in NGC 5548 over a 13-year campaign. I use

a luminosity-dependent transfer function to model the Hβ lightcurve, and compare the results to recent theoretical models. I also discuss the implications of the residuals from this model fit on the gas distribution of the broad-line region.

Chapter 3 uses observed wavelength-dependent time delays in 14 AGN to test the accretion disc thermal reprocessing model and the use of AGN accretion discs as a standard candle.

Chapter 4 presents *Chandra* X-ray observations of a quiescent neutron star X-ray transient in the globular cluster NGC 6440 at two epochs, investigating the source of observed variability between the two epochs and the implications for quiescent neutron star emission models.

In chapter 5 I use *Chandra* X-ray observations of the globular cluster Terzan 1 to search for the quiescent counterpart of a transient previously only observed in outburst. The nature of the other X-ray sources in the cluster are investigated, and the number of sources observed is compared with those predicted from the cluster stellar encounter rate.

In chapter 6 I present *Chandra* and *XMM-Newton* X-ray observations of 2 quasi-persistent neutron stars whose crusts have been heated out of equilibrium with the stellar interior. The observations track the cooling of the crust, and put important constraints on the cooling timescale, and hence the dominant cooling processes.

Chapter 7 presents the discovery of an X-ray transient with *XMM-Newton* whilst doing an archival search for faint accreting X-ray sources from the *ASCA* Galactic Plane Survey. The results of the search are discussed, as well as the nature of the transient.

Finally, in chapter 8 the main conclusions from this thesis are summarised, and possible directions for related work in the future discussed.

CHAPTER 2

Photoionized Hβ Emission in NGC 5548: it breathes!

The AGN Watch collaboration monitored around a dozen AGN during the 1990s. The longest monitoring campaign was of NGC 5548, which has an optical lightcurve spanning 13 years. Such a dataset allows us to look at changes in the size of the broad line region with luminosity. Here we explore this.

This chapter is based on a paper published in the Monthly Notices of the Royal Astronomical Society by E. M. Cackett & K. Horne (2006, MNRAS, 365, 1180).

2.1   Introduction

Photoionization models predict the sizes of Strömgren zones for H II regions and planetary nebulae ionized by hot stars of various luminosities and spectral types. Higher luminosity can maintain a larger mass of ionized gas. Dynamical tests of photoionization models are rare. The ionizing stars evolve in luminosity at rates too slow for humans to directly observe changes in radius. However, active galacic nuclei (AGN) vary on much shorter time-scales (days to months). Rapid variations in the ionizing luminosity emerging from an AGN should cause the photoionized region to expand and contract. This 'breathing' of the emission-line region is an interesting test of photoionization models.

Although the time-scales of the variations are convenient to human observers, unfortunately, the angular sizes of the broad emission-line regions are too small to be resolved directly. A nebula 100 light days across at distance of 100 Mpc spans only 180 microarcseconds. Fortunately, light travel times within the nebula introduce time delays for any changes in the line emission. The ionizing radiation from the innermost regions of an

AGN is reprocessed by gas in the surrounding broad line region (BLR). As the central source varies, spherical waves of heating and ionization, cooling and recombination, expand at the speed of light through the BLR. A change in ionization causes a corresponding change in the reprocessed emission. In AGNs, the recombination timescales of the gas in the BLR is very short compared to the light travel time, so the delay seen by a distant observer is dominated by the light travel time. Hence, we see line emission correlated with the continuum but with a time delay, τ. A gas cloud 1 light day behind the ionizing source will be seen to brighten 2 days after the ionizing source flux rises. Thus, we can use light travel time delays to measure the size of the region that is responding to variations in the ionizing flux, where the reverberation radius is $\langle R \rangle \approx \langle \tau \rangle c$. Echo mapping, or reverberation mapping (Blandford & McKee, 1982), aims to use this correlated variability to determine the kinematics and structure of the BLR, as well as the mass of the central supermassive black hole (e.g. Peterson, 1993; Peterson et al., 2004, and references therein).

The nearby ($z = 0.017$) Seyfert 1 galaxy NGC 5548 has been intensively monitored in the optical range for 13 years (1989-2001) by the international *AGN Watch*[1] consortium (e.g. Peterson et al., 2002). Those data spanning the source in a wide range of luminosity states are ideal for searching for this 'breathing' effect. In this chapter, we investigate the luminosity dependence of the Hβ emission and present two methods of fitting the data, accounting for the 'breathing' using (i) parameterized models and (ii) the reverberation mapping code `MEMECHO` (Horne, Welsh & Peterson, 1991; Horne, 1994). Although previous work by Peterson et al. (1999, 2002); Gilbert & Peterson (2003); Goad et al. (2004) has studied the luminosity dependence of the Hβ emission in NGC 5548, this study applies alternative techniques to characterise the 'breathing'. In §2.2 we describe the echo mapping technique and discuss the luminosity dependence of the emission-line lightcurve. In §2.3 we present the luminosity dependent parameterized models followed by the `MEMECHO` method in §2.4. The results of these methods of fitting the data, and their implications, are discussed in §2.5 and we summarise the main findings in §2.6.

---

[1]http://www.astronomy.ohio-state.edu/∼agnwatch/

2.2 Echo Mapping

The emission line flux, $F_l(t)$, that we see at each time, t, is driven by the continuum variations, $F_c(t)$, and arises from a range of time delays, τ. The emission line lightcurve is therefore a delayed and blurred version of the continuum lightcurve. In the usual linearized echo model the line lightcurve is modelled as

$$F_c(t) = \bar{F}_c + \Delta F_c(t) \tag{2.1}$$

$$F_l(t) = \bar{F}_l + \int_0^{\tau_{\max}} \Psi(\tau)\,\Delta F_c(t-\tau)d\tau \ . \tag{2.2}$$

where $\Psi(\tau)$ is the transfer function, or delay map. We can adopt a continuum background level $\bar{F}_c$, somewhat arbitrarily, at the median of the observed continuum fluxes. $\bar{F}_l$ is then a constant background line flux that would be produced if the continuum level were constant at $\bar{F}_c$.

A simple way of determining the size of the emission-line region is to determine the time delay (or 'lag') between the line and continuum lightcurves using cross-correlation. Taking the centroid of the cross-correlation function (CCF) as the lag gives a luminosity-weighted radius for the BLR (Robinson & Perez, 1990). However, the cross-correlation function is a convolution of the delay map, $\Psi(\tau)$, with the auto-correlation function (ACF) of the driving continuum lightcurve. It is therefore possible that changes in the measured cross-correlation lag arise from changes in the continuum auto-correlation function rather than in the delay map (e.g. Robinson & Perez, 1990; Perez, Robinson & de La Fuente, 1992; Welsh, 1999). If the continuum variations become slower, a sharp peak at low time-delay in the delay distribution will be blurred by the broader auto-correlation function and the peak of the cross-correlation function will be shifted to larger delays (Netzer & Maoz, 1990). A typical delay map may have a rapid rise to a peak at small lag, and a long tail to large lags. The asymmetric peak in $\Psi(\tau)$, will shift toward its longer wing when blurred by the auto-correlation function. Thus the lag measured by cross-correlation analysis depends not only on the delay distribution, $\Psi(\tau)$, but also on the characteristics (ACF) of the continuum variations.

Previous analysis of the *AGN Watch* data for NGC 5548 by Peterson et al. (2002) determined the Hβ emission-line lag relative to the optical continuum, on a year by year basis, using cross-correlation. These authors find that the lag increases with increasing mean continuum flux. To improve upon the CCF analysis we use the echo mapping

43

technique to fit the lightcurves in detail. However, the linearized echo model (Eq. 2.2) is appropriate only when the delay map is independent of time (static). In this chapter we extend the model to search for changes in the delay map with luminosity.

2.2.1   Luminosity-Dependent Delay Map

The above linearized echo model (Eq. 2.2) assumes that the line emissivity and continuum flux can be related by a linear function and thus is appropriate only for responses that are static. In principle, the delay map may change with time, for example, due to motion, or changes in quantity, of line-emitting gas within the system. The delay map may also change with luminosity. In the "local optimally emitting clouds" (LOC) model (Baldwin et al., 1995) at each time delay there is a variety of gas clouds with differing properties, and those most efficient at reprocessing tend to dominate the line flux emerging from the region. A change in ionizing luminosity induces a change in the efficiency of reprocessing at each place in the region and so the time delay at which the line emission is dominant will change. When a cloud is partially ionized its response may initially be large so that increasing luminosity increases the depth of the ionized zone on the face of the cloud. Once the cloud becomes completely ionized, however, further increases in ionizing flux are less effectively reprocessed. The line flux saturates, and may even decrease with increasing ionizing flux due to either ionization or decline in the recombination coefficients caused by an increase in gas temperature (O'Brien, Goad & Gondhalekar, 1995).

To account for these effects, we generalise the echo model by allowing the delay map to be luminosity-dependent, $\Psi(\tau, F_c)$. The response we see at time t from a parcel of emission-line gas located at time delay τ is set by the luminosity of the nucleus that we saw at the earlier time $t - \tau$. Thus,

$$F_l(t) = \bar{F_l} + \int_0^{\tau_{\max}} \Psi\left[\tau, F_c(t - \tau)\right] \Delta F_c(t - \tau) d\tau \ . \tag{2.3}$$

2.2.2   Luminosity dependence of Hβ flux

A well-established correlation between continuum and emission-line properties is the 'Baldwin' effect (Baldwin, 1977; Osmer, Porter & Green, 1994) where, in different AGN, broad emission-line equivalent width is observed to decrease with increasing continuum level. The relationship between the line luminosity, L_l, and the continuum luminosity, L_c, can

be described by

$$L_l \propto L_c^\alpha \ . \tag{2.4}$$

Kinney, Rivolo & Koratkar (1990) find that $\alpha \approx 0.83$ for CIV, and $\alpha \approx 0.88$ for Lyα.

Within a single source, various studies have shown that emission lines have a nonlinear response to continuum variations (e.g. Pogge & Peterson, 1992; Dietrich & Kollatschny, 1995). This 'intrinsic Baldwin effect' (Kinney et al., 1990; Krolik et al., 1991; Pogge & Peterson, 1992; Korista & Goad, 2004) where the Hβ emission-line response to variations in the continuum decreases with increasing continuum level has been observed for NGC 5548 (Gilbert & Peterson, 2003; Goad, Korista & Knigge, 2004). In terms of the continuum flux, F_c, and the line flux, F_l, the intrinsic Baldwin effect is described by

$$F_l \propto F_c^\alpha \ . \tag{2.5}$$

This nonlinearity can be seen by simply examining the 13-year lightcurves (Fig. 2.1). In the lowest state (1992), the trough in the Hβ lightcurve is deeper than in the continuum lightcurve, whereas in the highest state (1998), the Hβ peak is not as pronounced as the continuum. This argument neglects that light travel time delay smears out the emission-line response, but this should happen to both the peak and the trough.

The relation between the optical continuum flux at 5100Å and the Hβ line flux is examined in Fig. 2.2 (a), where a power-law (Eq. 2.5) with $\alpha = 0.63$ gives a good fit. Here we corrected the optical continuum flux at 5100 Å, F_{opt}, for the background host galaxy contribution, F_{gal}, where we take $F_{gal} = 3.4 \times 10^{-15}$ erg s^{-1} cm^{-2} Å^{-1} as determined by Romanishin et al. (1995). The narrow-line component of the Hβ line has also been removed, and we use $F_{H\beta}(narrow) = 6.7 \times 10^{-14}$ erg s^{-1} cm^{-2} determined by Gilbert & Peterson (2003). We included a time delay of 17.5 days between the continuum flux and Hβ flux to remove reverberation effects which was determined by cross-correlation of the full 13-year lightcurves. This time delay was subtracted from the times of each of the Hβ data points and the continuum flux at this new time determined via linear interpolation. Gilbert & Peterson (2003) do a more detailed analysis allowing for the different time delays observed each year, and when adopting the same galaxy continuum background and Hβ narrow-line component, determine $\alpha = 0.65 \pm 0.02$. Goad et al. (2004) find that the slope of this relation is not constant, but decreases as the continuum flux increases, an effect which is predicted by the photoionization models of Korista & Goad (2004). However, the driving ionizing continuum maybe closer to that observed in the UV at 1350 Å, and
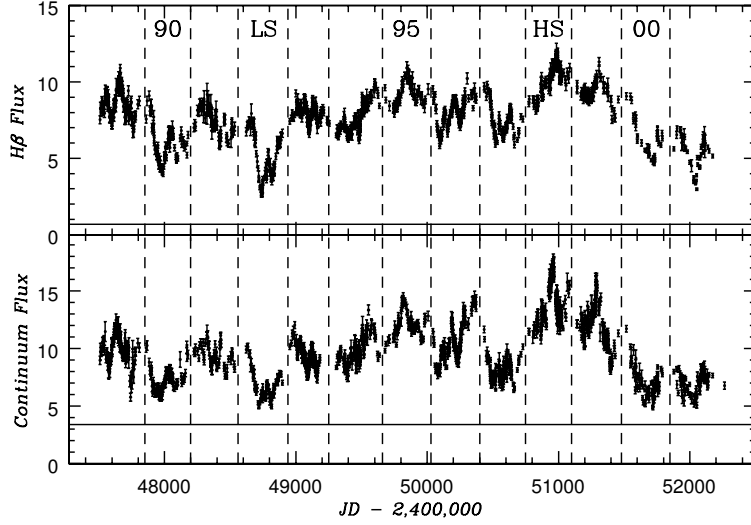
Figure 2.1: Lightcurves for optical continuum flux (10^{-15} erg s^{-1} cm^{-2}Å^{-1}, at 5100 Å) and Hβ emission line flux (10^{-13} erg s^{-1} cm^{-2}) from the 1989-2001 *AGN Watch* data on NGC 5548. LS and HS marks the lowest (1992) and highest (1998) states of the lightcurves respectively. Solid lines mark the galaxy contribution to the continuum flux (Romanishin et al., 1995) and the narrow-line contribution to the Hβ flux (Gilbert & Peterson, 2003). Dashed lines separate the observing seasons.

so previous observations of NGC 5548 at this wavelength by the *AGN Watch* using IUE and HST (Clavel et al., 1991; Korista et al., 1995) can be used to correct the relationships determined by the optical continuum. Using the IUE data Peterson et al. (2002) finds a relation $F_{opt} \propto F_{UV}^{0.56}$, while Gilbert & Peterson (2003) find a relation of $F_{opt} \propto F_{UV}^{0.67}$. Combining both IUE and HST data, we find a relation $F_{opt} \propto F_{UV}^{0.53\pm0.02}$ (see Fig. 2.2 (b)) assuming no time delay between the optical and UV continuum and linearly interpolating to get the optical continuum at the required times. From this result, we get a relationship between the Hβ flux and the ionizing UV flux of $F_{H\beta} \propto F_{UV}^{0.31}$. However, the UV flux can be combined directly with the $H\beta$ flux to determine this relationship. Including cross-correlation time delays for the relevant years (19.7 days for the 1989 data and 13.6 days for the 1993 data), we determine this relation directly to be $F_{H\beta} \propto F_{UV}^{0.26\pm0.01}$ (see Fig. 2.2 (c)).

46
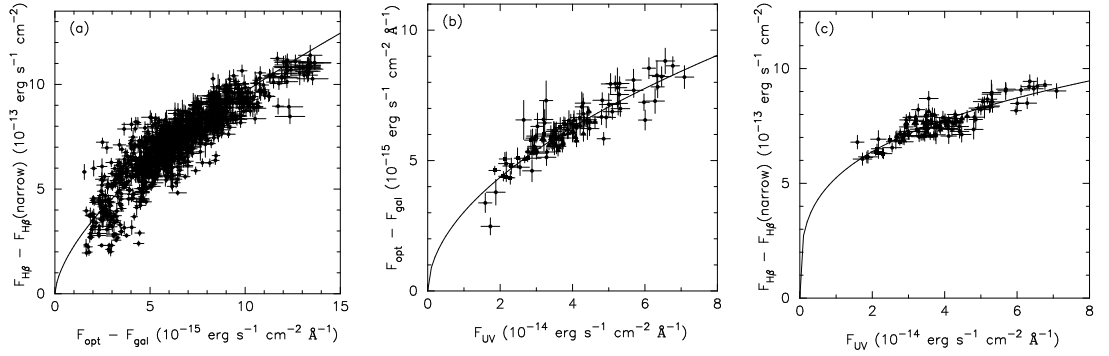
Figure 2.2: (a) Narrow-line subtracted Hβ flux vs. optical continuum flux at 5100Å (F_{opt}), with the host galaxy continuum flux removed (F_{gal}) for the 13-year data set. The solid line indicates $F_{H\beta} \propto F_{opt}^{0.63}$. A time delay between the continuum and Hβ fluxes of 17.5 days is included. (b) UV continuum flux at 1350Å vs. F_{opt} - F_{gal}. UV data are taken from the IUE campaigns in 1989 (circles; Clavel et al., 1991) and 1993 (squares) as well as the HST campaign in 1993 (triangles; Korista et al., 1995). The solid line indicates the best fit of $F_{opt} \propto F_{UV}^{0.53\pm0.02}$. (c) Narrow-line subtracted Hβ flux vs. UV continuum flux at 1350Å (symbols as in (b)). A time delay between the Hβ and UV fluxes has been added with the Hβ fluxes from 1989 19.7 days behind the UV and for the 1993 data the delay is 13.6 days. The solid line indicates the best fit of $F_{H\beta} \propto F_{UV}^{0.28\pm0.01}$.

2.2.3 Luminosity dependence of time delay

As the ionizing luminosity varies we expect the size of the photoionized region to expand and contract - a larger luminosity should ionize gas to a greater distance. We now consider a couple of simple theoretical predictions for this effect. If the BLR acts as a simple Strömgren sphere with uniform gas density, then one would predict that $R \propto L^{1/3}$. If instead we assume that the response in an emission line will be greatest at some density, n, and ionization parameter, $\Gamma \propto L/R^2 n$, then it is easy to show this predicts $R \propto L^{1/2}$ (for a particular value of the product Γn) (Peterson et al., 2002). More detailed photoionization modelling (using the LOC model) by Korista & Goad (2004) predicts a responsivity-weighted radius scaling as $R \propto L^{0.23}$ for Hβ. Photoionization models by O'Brien et al. (1995) and also Korista & Goad (2004) both come to the conclusion that a relationship between emission-line lag and incident continuum level is due to a non-linear emission-line response.

Peterson et al. (1999) and more recently Peterson et al. (2002) used a year by year cross-correlation analysis of the *AGN Watch* data for NGC 5548 to show that the Hβ emission-line lag (relative to the optical continuum) is correlated with the mean optical continuum flux (at 5100Å). As the mean optical continuum flux increases, the lag, and hence the size of the Hβ emitting region, is seen to increase. Using the full 13-year lightcurves for NGC 5548, Peterson et al. (2002) find $\tau \propto F_{opt}^{0.95}$, though with much scatter. They argue, however, that the UV continuum (at 1350Å) is much closer to the driving ionizing continuum than the optical continuum used. Correcting for the relationship between the optical and UV continuum (using $F_{opt} \propto F_{UV}^{0.53}$) leads to $\tau \propto F_{UV}^{0.50}$ as predicted assuming that the emission will be greatest at some particular gas density and ionization parameter.

To test the predictions, using more complex methods than cross-correlation, we have fitted the data allowing for these breathing effects. Firstly, we present our parameterized models and then the `MEMECHO` fits to the 13-year (1989-2001) *AGN Watch* optical continuum and Hβ lightcurves for NGC 5548 before discussing these results, their findings and implications.

2.3   Parameterized models

In this method we model the delay map and include parameters to allow it to be luminosity dependent. We choose to model the delay map as a Gaussian in $\ln \tau$,

$$\Psi\left(\tau\right) = \frac{\Psi_0}{A} \exp\left(-\frac{1}{2}\left[\frac{\ln(\tau/\tau_0)}{\Delta\ln\tau}\right]^2\right) \tag{2.6}$$

where τ_0 is the peak of the Gaussian and $\Delta\ln\tau$ is the width of the Gaussian. Ψ_0 scales the strength of the delay map. We include a normalisation factor, $1/A$, chosen so that $\Psi_0 = \int \Psi\left(\tau\right)d\tau$, where,

$$\begin{aligned} A &= \int_0^\infty \exp\left(-\frac{1}{2}\left[\frac{\ln(\tau/\tau_0)}{\Delta\ln\tau}\right]^2\right)d\tau \\ &= \sqrt{2\pi}\left(\Delta\ln\tau\right)\tau_0 \exp\left[(\Delta\ln\tau)^2/2\right] \ . \end{aligned} \tag{2.7}$$

We select this model as it ensures causality ($\Psi\left(\tau\right) = 0$ for $\tau < 0$) while allowing parameters τ_0 and $\Delta\ln\tau$ to control the centroid and width of the delay distribution.

We introduce three 'breathing' parameters to allow the delay map to be luminosity dependent. To account for the two effects discussed in §2.2.2 and §2.2.3, we introduce α to model the 'intrinsic Baldwin effect', so that $F_{H\beta} \propto F_{opt}^\alpha$, and β to allow the mean time delay of the delay map to depend on the continuum flux i.e., $\tau \propto F_{opt}^\beta$. A further parameter, γ, is introduced to allow the width of the delay map, $\Delta\ln\tau$, to depend on the continuum flux, so that $\Delta\ln\tau \propto F_{opt}^\gamma$. Fig. 2.3 illustrates how these parameters affect the delay map as the continuum flux increases. A linear line response corresponds to $\alpha = 1.0$, whereas $\beta = 0.0$ means that there is no dependence of time-delay with luminosity, and $\gamma = 0.0$ ensures $\Delta\ln\tau$ is constant. A positive value for β indicates that the time delay is increasing with increasing continuum flux, and similarly, a positive value for γ indicates that the width of the delay map is increasing with increasing continuum flux.

One complication is the host galaxy's contribution, F_{gal}, to the observed optical continuum flux $F_{opt}(t)$. We treat this by defining the normalised lightcurve (with the background galaxy contribution subtracted) as

$$X(t) = \frac{F_{opt}(t) - F_{gal}}{\overline{F_{opt}} - F_{gal}}, \tag{2.8}$$

where F_{gal} is the background galaxy continuum flux and $\overline{F_{opt}}$ is the mean continuum flux, so that $X = 1$ when $F_{opt} = \overline{F_{opt}}$, and $X = 0$ when $F_{opt} = F_{gal}$. In all fits we adopt a
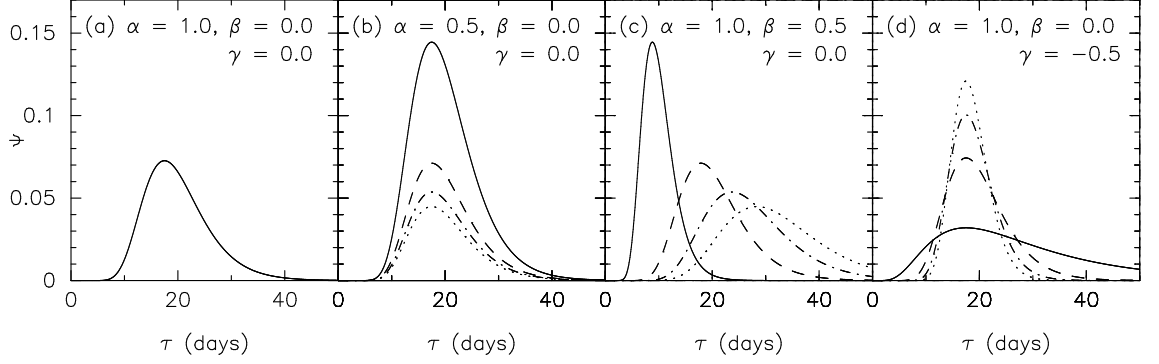
Figure 2.3: Delay maps for different values of the 'breathing' parameters α, β and γ. Different lines indicate different continuum fluxes where $F_{opt} = 5.0$ (solid), 10.0 (dashed), 15.0 (dot-dashed) and 20.0 (dotted) $\times 10^{-15}$ erg s^{-1} cm^{-2} Å^{-1}. $\overline{\tau_0} = 17.5$ days and $\overline{\Delta \ln \tau} = 0.3$ throughout.

background galaxy continuum flux, $F_{gal} = 3.4 \times 10^{-15}$ erg s^{-1} cm^{-2} Å^{-1} as determined by Romanishin et al. (1995).

We include the three 'breathing' parameters (α, β and γ) to our model as follows,

$$\Psi_0 \;=\; \overline{\Psi_0} \; [X(t-\tau)]^{\alpha-1} \tag{2.9}$$

$$\tau_0 \;=\; \overline{\tau_0} \; [X(t-\tau)]^{\beta} \tag{2.10}$$

$$\Delta \ln \tau \;=\; \overline{\Delta \ln \tau} \; [X(t-\tau)]^{\gamma} \;, \tag{2.11}$$

where $\overline{\Psi_0}$, $\overline{\tau_0}$ and $\overline{\Delta \ln \tau}$ are just the values of Ψ_0, τ_0 and $\Delta \ln \tau$ at the mean optical continuum flux, $\overline{F_{opt}}$. The Hβ lightcurve is then just given by

$$F_{H\beta}(t) = \overline{F_{H\beta}} + \int_0^{\tau_{\max}} \Psi\left[\tau, X(t-\tau)\right] \Delta F_{opt}(t-\tau) d\tau \;, \tag{2.12}$$

where,

$$F_{opt}(t) = \overline{F_{opt}} + \Delta F_{opt}(t) \;. \tag{2.13}$$

As the delay map is Gaussian in $\ln \tau$, not τ, the delay map is asymmetric and has a long tail to high time delays (unless $\Delta \ln \tau \ll 1$). Although we have parameterized the delay map in terms of τ_0, the lag at which the delay map peaks, it is useful to characterise the delay map in terms of the median lag, τ_{med}, and the mean lag, $\langle \tau \rangle$, as these values are more directly comparable to the cross-correlation lags. We define these quantities as

$$\frac{1}{2} = \frac{\int_0^{\tau_{med}} \Psi(\tau) \, d\tau}{\int_0^{\infty} \Psi(\tau) \, d\tau} \;, \tag{2.14}$$

and

$$\langle \tau \rangle = \frac{\int_0^\infty \tau \Psi(\tau) \, d\tau}{\int_0^\infty \Psi(\tau) \, d\tau} \ . \tag{2.15}$$

We now present tests of a series of models allowing the delay map to vary in different ways with continuum flux. The models are detailed in sections 2.3.1 to 2.3.5 with Fig. 2.7 showing the luminosity-dependent delay maps recovered from these models. The parameters found from the fits are detailed in Table 2.2. Initially, the delay map is made to be static.

2.3.1 Static (S)

The importance of allowing the delay map to be luminosity-dependent is highlighted when fitting the data with a static delay map. In this static model the delay map is independent of continuum level, thus we fix $\alpha = 1.0$, $\beta = 0.0$ and $\gamma = 0.0$. The free parameters are $\overline{\Psi_0}$, $\overline{\tau_0}$, $\overline{\Delta \ln \tau}$ and $\overline{F_{H\beta}}$, which are adjusted to give the best fit, determined by minimizing χ^2. The uncertainties are derived by $\Delta \chi^2 = \chi^2_{min}/N$. The delay map is convolved with the continuum lightcurve to give the predicted line lightcurve (see Eq. 2.12) with $\tau_{\max} = 100$ days. However, we need to know the continuum lightcurve at all times, and so we linearly interpolate between the continuum data points for this purpose. In all the parameterized model fits to the 13-year data set we take $\overline{F_{opt}} = 9.73 \times 10^{-15}$ erg s^{-1} cm^{-2} Å^{-1}, the mean of the optical continuum flux from this data. Not surprisingly, this static model fits the 13-year Hβ lightcurve poorly, with $\chi^2/1248 = 9.6$ (where 1248 is the number of Hβ data points). Table 2.2 gives the best fitting values of the parameters for this model and the delay map is shown in Fig. 2.7.

We examine how the delay map changes with continuum flux by fitting this static model to the data on a year by year basis (see Table 2.1). When fitting the static model to the separate years, it was found that there was often not enough information to clearly determine $\overline{\Delta \ln \tau}$, therefore we fix $\overline{\Delta \ln \tau} = 0.66$, the value that is determined from the global fit to the 13-year data set. Fig. 2.4 shows the change in the delay map between the lowest state ($\overline{F_{opt}} = 6.7 \times 10^{-15}$ erg s^{-1} cm^{-2} Å^{-1} in 1992) and the highest state ($\overline{F_{opt}} = 13.5 \times 10^{-15}$ erg s^{-1} cm^{-2} Å^{-1} in 1998). The delay peak increases by a factor of ~ 3 from 5.7d to 18.0d in time delay, while the height of the peak drops a factor of ~ 5 from 0.1 to 0.02. Thus, the Hβ response (the area under the curve) decreases by a factor

Table 2.1: Parameters for fits of the Static model to the yearly Hβ lightcurves of NGC 5548 between 1989-2001 as well as the global fit to all 13-years of data. From the global fit we determine $\overline{\Delta \ln \tau} = 0.66$. In the static fits we fix $\overline{\Delta \ln \tau}$ to this value.

Year	$\overline{F_{opt}}$	$\overline{\tau_0}$	τ_{med}	$\langle \tau \rangle$	$\overline{F_{H\beta}}$	$\overline{\Psi_0}$	χ^2/dof
1989	9.92 ± 1.26	12.7 ± 0.8	19.6 ± 1.2	24.3 ± 1.5	8.56 ± 0.03	0.78 ± 0.08	$198/132 = 1.5$
1990	7.25 ± 1.00	11.4 ± 0.7	17.7 ± 1.1	22.0 ± 1.4	5.69 ± 0.04	1.14 ± 0.10	$278/94 = 3.0$
1991	9.40 ± 0.93	11.2 ± 1.1	17.2 ± 1.7	21.4 ± 2.1	7.22 ± 0.05	1.16 ± 0.12	$88/65 = 1.4$
1992	6.72 ± 1.17	5.7 ± 0.7	8.8 ± 1.1	10.9 ± 1.4	4.80 ± 0.06	1.15 ± 0.16	$464/83 = 5.6$
1993	9.04 ± 0.90	7.0 ± 1.2	10.8 ± 1.8	13.4 ± 2.3	7.78 ± 0.03	0.41 ± 0.09	$386/142 = 2.7$
1994	9.76 ± 1.10	10.9 ± 1.0	16.8 ± 1.6	20.9 ± 2.0	7.68 ± 0.03	0.88 ± 0.09	$324/128 = 2.5$
1995	12.09 ± 1.00	10.8 ± 1.9	16.7 ± 2.9	20.7 ± 3.6	9.35 ± 0.04	0.59 ± 0.11	$234/78 = 3.0$
1996	10.56 ± 1.64	9.4 ± 0.5	14.5 ± 0.8	18.1 ± 1.0	8.08 ± 0.04	0.61 ± 0.09	$592/144 = 4.1$
1997	8.12 ± 0.91	12.5 ± 0.6	19.3 ± 0.9	23.9 ± 1.2	7.06 ± 0.04	1.01 ± 0.10	$384/95 = 4.0$
1998	13.47 ± 1.45	18.0 ± 1.2	27.7 ± 1.9	34.2 ± 2.3	10.09 ± 0.03	0.65 ± 0.09	$242/119 = 2.0$
1999	11.83 ± 1.82	16.6 ± 1.3	25.6 ± 2.0	31.7 ± 2.5	9.21 ± 0.03	0.55 ± 0.08	$99/86 = 1.2$
2000	6.98 ± 1.20	6.0 ± 1.9	9.3 ± 2.9	11.6 ± 3.6	5.94 ± 0.07	0.81 ± 0.19	$292/37 = 7.9$
2001	7.03 ± 0.86	10.6 ± 2.0	16.4 ± 3.0	20.4 ± 3.8	5.29 ± 0.09	1.31 ± 0.26	$668/45 = 14.8$
Global	9.73 ± 2.44	11.4 ± 0.6	17.6 ± 1.0	21.9 ± 1.2	7.67 ± 0.02	0.79 ± 0.01	$12016/1248 = 9.6$

$\sim \frac{3}{5}$. In this figure the cross-correlation function (CCF) and continuum auto-correlation functions (ACF) are shown for both of these years for comparison with the delay map. The CCF peak is close to the median of the delay map. In calculating the CCF and ACF we used the White & Peterson (1994) implementation of the interpolation cross-correlation method (Gaskell & Sparke, 1986; Gaskell & Peterson, 1987).

Fig. 2.5 shows how the time delay increases with increasing continuum flux. We have plotted τ_{med} as this is less biased by long asymmetric tail of the delay map. Fitting a power-law of the form $\tau_{med} \propto F_{opt}^{\beta}$ to this gives $\beta = 0.92 \pm 0.16$. This is similar to the Peterson et al. (2002) findings where the lag was determined from cross-correlation and the resulting slope, $\beta = 0.95$ (see their Fig. 3). Thus, we confirm that the time delay increases with mean continuum flux.

2.3.2   B1

In this model we allow two of the 'breathing' parameters, α and β to be free, while still fixing $\gamma = 0.0$. The delay map is now luminosity dependent - the strength of the Hβ response and the time delay can vary with continuum flux. The free parameters in this
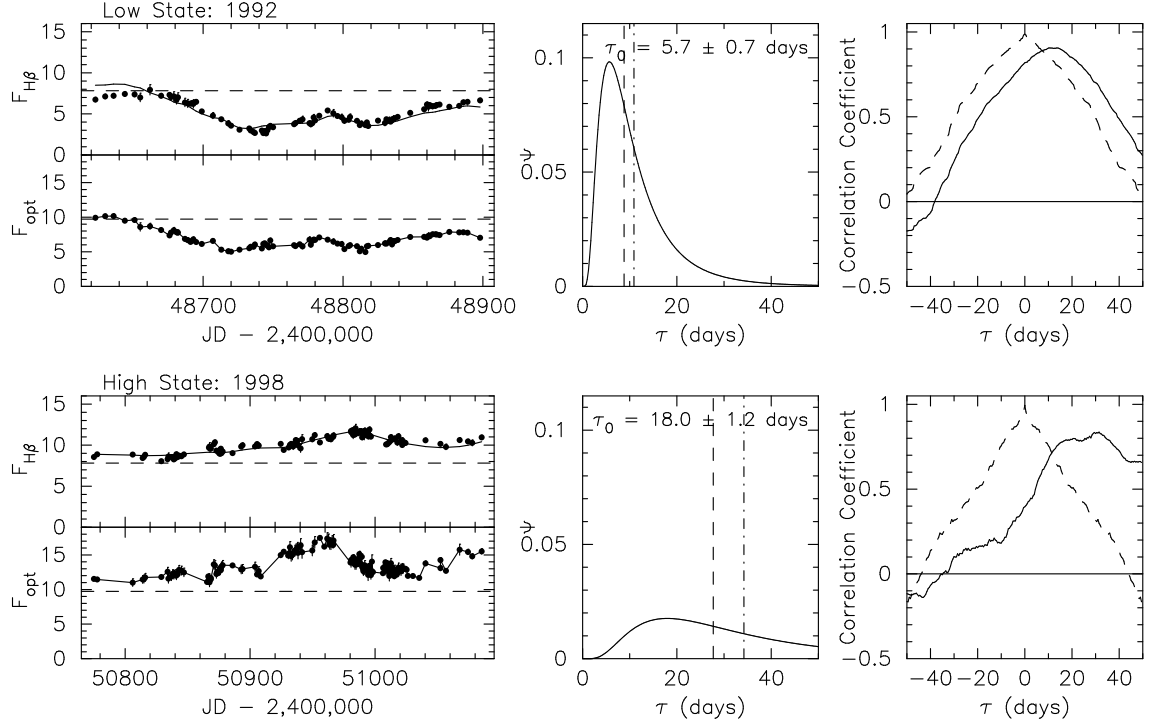
Figure 2.4: Static delay map fit to the low state (1992, upper panels) and the high state (1998, lower panels). The central plots show the delay maps, where the median and mean time delays are marked by dashed and dot-dashed lines respectively. The mean time delay of the delay map in the high state is clearly larger, and the total response (the area under the curve) is lower, than in the low state. In these fits $\overline{\Delta \ln \tau} = 0.66$. On the lightcurves (lefthand plots), the dashed lines indicate the mean continuum and Hβ fluxes for the 13-year data set. Also shown (right) is the cross-correlation function (solid line) and continuum auto-correlation function (dashed line) for these years.
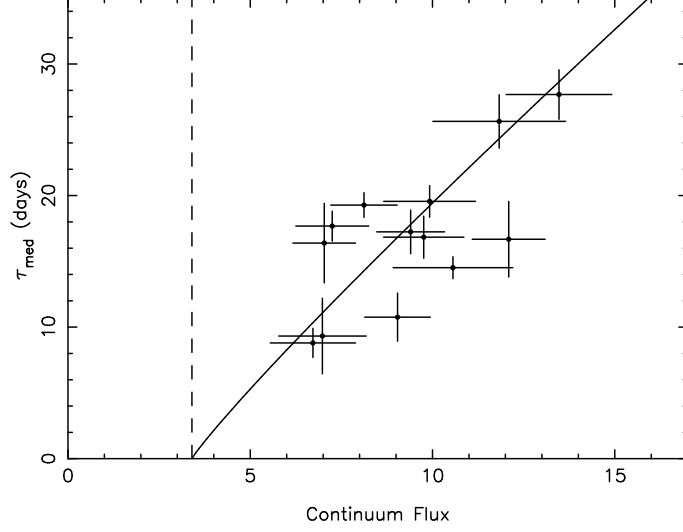
Figure 2.5: τ_{med} vs. mean optical continuum flux for static delay map fit to yearly data. τ_{med} (see Eq. 2.14) is the median of the delay map. Solid line shows best fitting power-law to the data with $\tau_{med} \propto F_{opt}^{0.92\pm0.16}$. Dashed line indicates host galaxy continuum flux (Romanishin et al., 1995).

model are $\alpha, \beta, \overline{\Psi_0}, \overline{\tau_0}, \overline{\Delta \ln \tau}$ and $\overline{F_{H\beta}}$. As in the static model, we linearly interpolate the continuum lightcurve to get the continuum flux at the required times. This model fits the data significantly better than the static model with $\chi^2/1248 = 6.0$ (Table 2.2). The delay map (Fig. 2.7) clearly shows an increase in the time delay and a decrease in the Hβ response with increasing continuum flux. We find $\alpha = 0.66 \pm 0.03$ and $\beta = 0.28 \pm 0.05$ for this model. It is interesting to note that β is lower than the value determined by fitting the static delay map to the yearly data (Fig. 2.5).

2.3.3 B2

In an attempt to improve on model B1 we allow the width of the Gaussian delay map to vary as a function of continuum flux, letting γ be a free parameter in the fit. Again, the continuum lightcurve is linearly interpolated to get the continuum flux at the required times. This extra parameter resulted in a slight improvement of the fit, with $\chi^2/1248 = 5.9$. Again, the delay map (Fig. 2.7) clearly shows an increase in the time delay and a decrease in the Hβ response with increasing continuum flux. $\alpha = 0.57 \pm 0.02$ and $\beta = 0.41 \pm 0.08$ for this model. $\gamma = -0.20 \pm 0.06$ allowing there to be a wider range of delays at lower continuum flux than at higher continuum flux.

2.3.4 B3

The residuals of the B2 fit (Fig. 2.6), exhibit slow trends (timescale $\sim$1 year) that are not fit by our model. There is no obvious correlation of these slow line variations with continuum flux, suggesting that they are due to a process that is independent of the reverberation effects. These trends may indicate a violation of the assumption that the distribution of the line-emitting gas in the BLR is constant over the timescale of the data. However, as the dynamical timescale for the Hβ-emitting gas, with $R \sim \tau c \sim 20$ light days and $\Delta v \sim 5000$ km s^{-1}, is ~ 3 years, changes in the gas distribution may well occur over the timespan of the observations. To allow for this in model B3 we fit a spline (with 26 nodes) to the residuals. Physically, this allows the background line flux to evolve with time e.g. accounting for different amounts of line-emitting gas in the system. However, Goad et al. (2004) find that the index of the intrinsic Baldwin effect, α changes on these sorts of timescales and therefore these residuals might instead be interpreted as a consequence of that effect. Allowing the line background flux to vary improves the fit significantly, yielding $\chi^2/1248 = 3.1$. The parameters of the fit are similar to the B2 model (see Table 2.2), with $\alpha = 0.58 \pm 0.03$, $\beta = 0.46 \pm 0.07$ and $\gamma = -0.24 \pm 0.06$.

Fig. 2.8 shows the continuum and Hβ lightcurves for 1991-1992 and 1998-1999 and demonstrates how well the Static, B2, and B3 models fit the Hβ lightcurve. Particularly clear in this figure is the failure of the static model (dot-dashed line) to fit the deepest trough and largest peak.

2.3.5 B4

In the models so far we have used linear interpolation to determine the continuum flux at all the required times. This, however, can lead to unphysical lightcurves in the gaps between the data points. It also takes no account of the noise in the data, so a wider delay map could be being recovered in an attempt to blur out the jagged continuum lightcurve. The reverberation mapping code MEMECHO that we also use to determine the luminosity dependent delay map (see § 2.4) uses maximum entropy methods to fit both the continuum and Hβ lightcurves. In this model we make use of the MEMECHO continuum fit to determine the continuum flux between the data points. The line background flux is still allowed to vary in the fit. The extra degrees of freedom allowed in the MEMECHO fit to
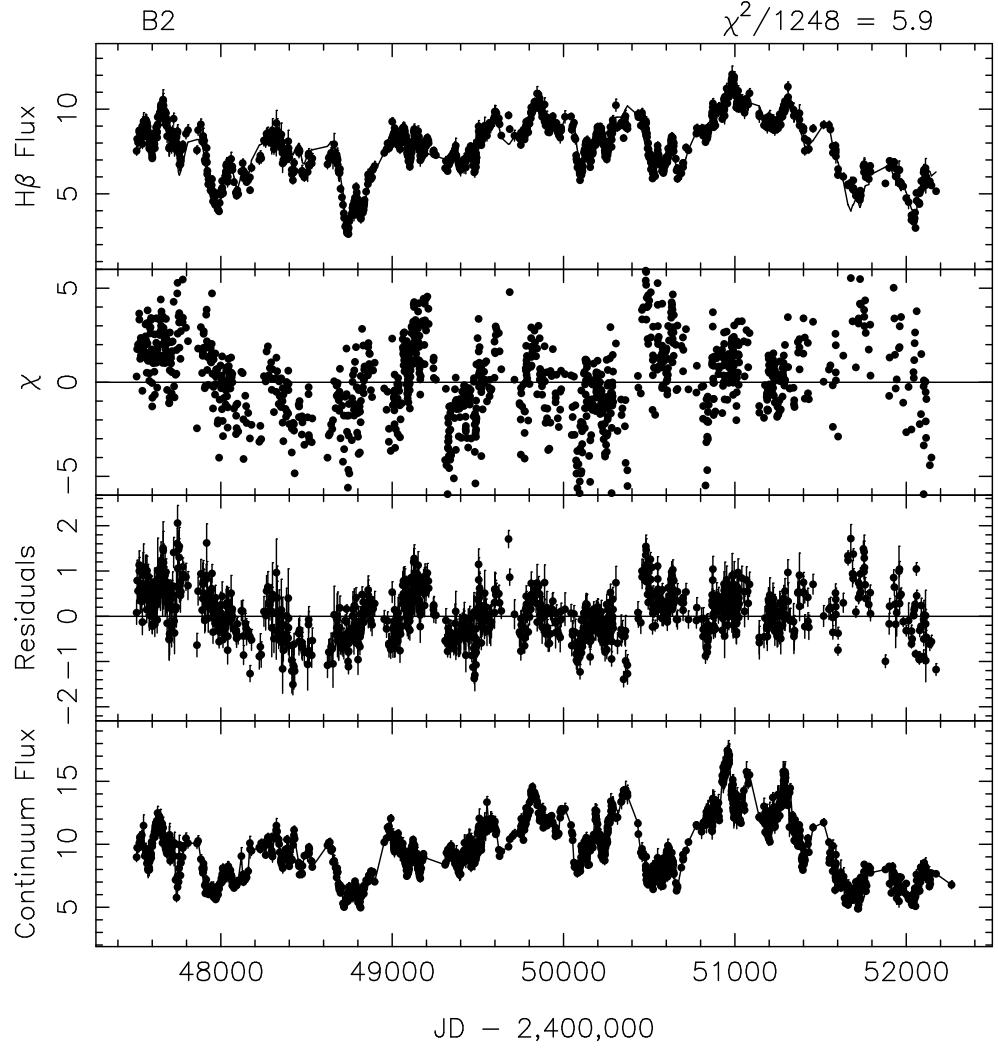
Figure 2.6: Hβ and continuum lightcurves (top and bottom, respectively) and residuals for B2 model fit to the 1989-2001 Hβ lightcurve (two middle panels). Two tupes of residuals plotted are: $(data - model)$, and $\chi = (data - model)/\sigma$.

Table 2.2: Parameters for fits to 1989-2001 Hβ lightcurve of NGC 5548. In all models the mean optical continuum level $\overline{F_{opt}} = 9.73 \times 10^{-15}$ erg s^{-1} cm^{-2} Å^{-1}.

	$\chi^2/1248$	α	β	γ	$\overline{\tau_0}$	$\overline{\Delta \ln \tau}$	$\overline{F_{H\beta}}$	$\overline{\Psi_0}$
S	9.6	1.0	0.0	0.0	11.4 ± 0.6	0.66 ± 0.05	7.67 ± 0.02	0.79 ± 0.01
B1	6.0	0.66 ± 0.03	0.28 ± 0.05	0.0	12.9 ± 1.0	0.70 ± 0.07	7.98 ± 0.02	0.77 ± 0.05
B2	5.9	0.57 ± 0.02	0.41 ± 0.08	-0.20 ± 0.06	13.9 ± 0.8	0.56 ± 0.05	7.98 ± 0.02	0.68 ± 0.01
B3	3.1	0.58 ± 0.03	0.46 ± 0.07	-0.24 ± 0.06	12.3 ± 0.7	0.58 ± 0.04	7.97 ± 0.01	0.68 ± 0.01
B4	1.2	0.64 ± 0.01	0.10 ± 0.01	0.46 ± 0.05	16.4 ± 0.3	0.32 ± 0.02	8.05 ± 0.01	0.68 ± 0.01

the continuum has again improved the fit, with $\chi^2/1248 = 1.2$. The width of the delay map from this model is seen to be thinner than the previous models (Fig. 2.7) because the MEMECHO continuum lightcurve is smoother than the linearly interpolated continuum lightcurve. This has affected the value of γ, which is is now positive (see Table.2.2), and allows the width of the delay map to increase with increasing flux, the opposite to what was seen from the previous model fits. The physical interpretation of a negative value of γ is not obvious, and negative values of γ found in B2 and B3 could be an artifact of using a linearly interpolated continuum model - a wider delay map at low continuum fluxes may be needed to smear out the jagged linearly interpolated continuum model. However, in the B4 model the time delay still increases with increasing continuum flux, though the relationship is flatter ($\beta = 0.10 \pm 0.01$). α remains similar to previous fits.

2.4 MEMECHO fit to the NGC 5548 AGN Watch 1989-2001 lightcurves

The echo mapping computer code MEMECHO (see Horne et al., 1991; Horne, 1994, for technical details) can allow luminosity-dependent delay maps to be made by means of a maximum-entropy deconvolution of Eq. 2.3. The maximum-entropy method finds the simplest positive image that fits the data, balancing simplicity, measured by entropy, and realism, measured, in this case, by χ^2 (Horne, 1994).

The optical continuum lightcurve, $F_{opt}(t)$, must thread through the measured continuum fluxes, and the predicted Hβ emission-line lightcurve, $F_{H\beta}(t)$, must similarly fit the measured line fluxes. In our fit to the data points we adjust the line background flux $\overline{F_{H\beta}}$, the continuum variations $F_{opt}(t)$, and the delay map $\Psi(\tau, F_{opt})$, we take $\overline{F_{opt}}$ as the
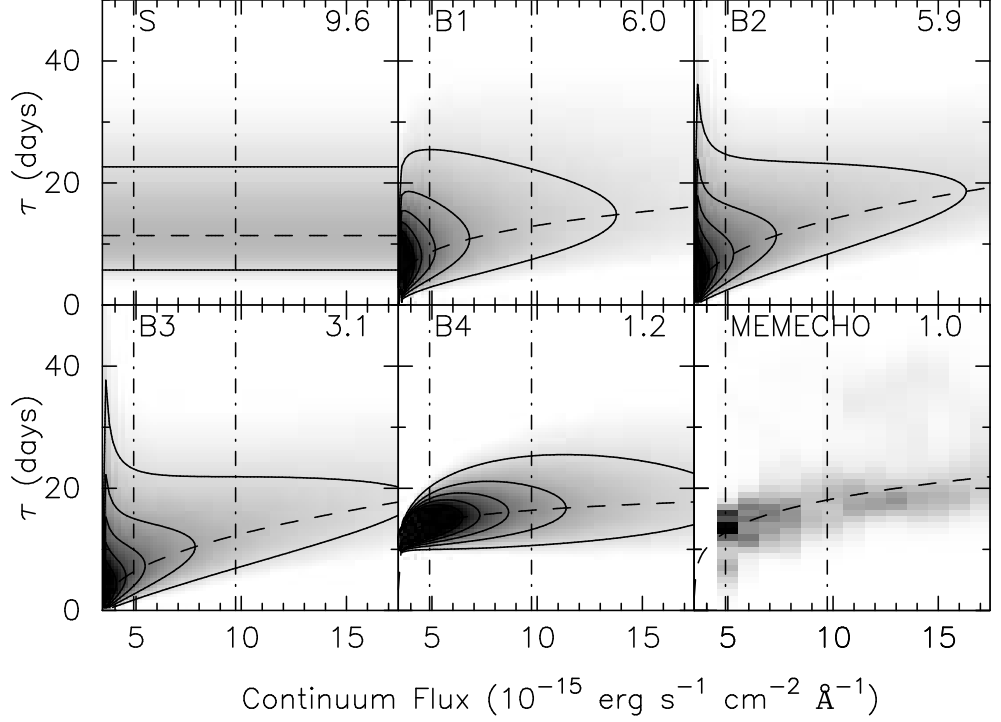
Figure 2.7: Luminosity-dependent delay maps for the 5 parameterized models as well as the `MEMECHO` recovered delay map. The greyscale indicates the value of the delay map (Ψ) at each time-delay and continuum flux. The reduced χ^2 value of each fit is indicated. For the parameterized models, the dashed line indicates the dependence of the peak of the delay map on the continuum flux. For the `MEMECHO` model the dashed line indicates the best fit power-law, $\tau \propto F_{opt}^{\beta}$ to the delay map. The dot-dashed lines indicate the minimum and mean continuum flux of the 13-year data, and the upper-limit of the plots is the maximum continuum flux. The lower limit of the plots is the background continuum flux. Solid lines mark the contours of the delay map. The parameters for each model are shown in Table 2.2.
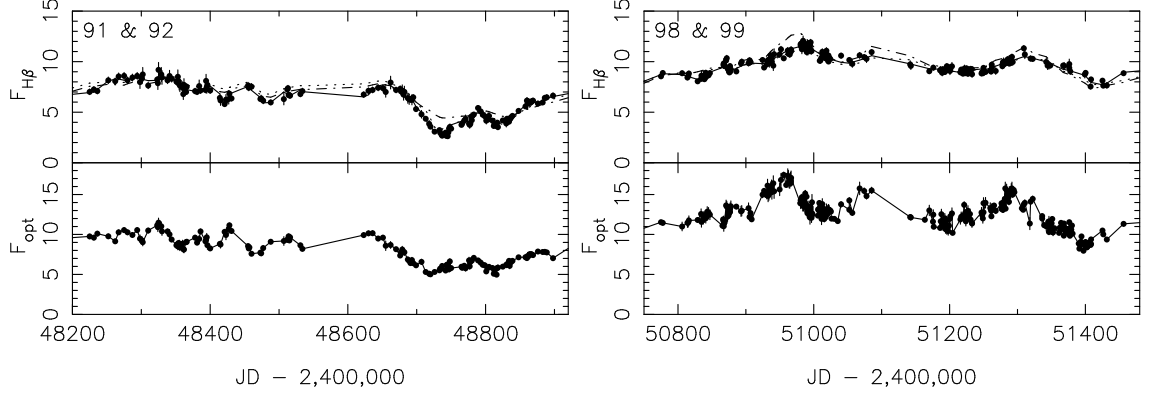
Figure 2.8: Continuum (F_{opt}) and Hβ ($F_{H\beta}$) lightcurves for 1991 - 1992 (left) and 1998 - 1999 (right). The linearly interpolated continuum flux model is marked with a solid line. The fit to the Hβ lightcurve can be seen for 3 of the different models (B3 (solid line), B2 (dotted line) and S (dot-dashed line)).

median of the continuum data. The fit is required to have a reduced $\chi^2/N = 1 \pm \sqrt{2/N}$, where N is the number of data points. We require this to hold for the line flux measurements, and also for the continuum flux measurements. The continuum is split into several flux levels (indicated in the lower panel of Fig. 2.9), and delay maps corresponding to each level are determined. When computing the convolution (Eq. 2.3) we linearly interpolate between these continuum levels to find the delay map that applies to the continuum flux at time $t - \tau$. Such an approach allows for fully non-linear line responses. Further details of this can be found in Horne (1994).

Fig. 2.9 shows the measured lightcurves and the MEMECHO fit. The greyscale (middle panel) shows the delay map at each time. Fig. 2.10 shows the luminosity-dependent delay map $\Psi(\tau, F_{opt})$ (greyscale) reconstructed from the observed lightcurves at each continuum level. The crosses indicate the median of the delay map and the dots indicate the upper and lower quartiles (see Tab. 2.3). The lower left panel projects the delay map along the time delay axis and thus indicates that the amplitude of the line response decreases with rising continuum level. The upper right panel gives the luminosity-averaged one-dimensional transfer function. At each continuum luminosity the range of delays is relatively narrow compared to the one-dimensional transfer function. As the luminosity rises, the mean delay increases. At minimum light the median delay is ~ 13 days, and this rises to ~ 23 days at maximum light. Fitting a power-law of the form $\tau \propto F_{opt}^{\beta}$ (with the galaxy background continuum removed) to the median time delay leads to $\beta = 0.24 \pm 0.08$.

59

Table 2.3: Time delay at the median, lower and upper quartile of the `MEMECHO` luminosity-dependent delay map for each continuum flux.

Continuum Flux $(10^{-15}$ erg s^{-1} cm^{-2} Å^{-1})	Median delay (days)	Lower quartile (days)	Upper quartile (days)
5.	13.	11.	15.
6.	15.	12.	17.
7.	16.	13.	18.
8.	16.	14.	19.
9.	17.	15.	20.
10.	19.	16.	22.
11.	19.	17.	24.
12.	20.	17.	25.
13.	20.	18.	28.
14.	20.	18.	29.
15.	20.	18.	26.
16.	21.	18.	26.
17.	23.	19.	28.

In order to understand how robust the `MEMECHO` recovered luminosity-dependent delay map is we ran a short Monte-Carlo simulation. We generated ten sets of continuum and Hβ lightcurves with the data points shifted by a Gaussian random number with a mean of zero and standard deviation equal to the uncertainty on that data point. Ten different delay maps were then recovered using these lightcurves. The delay maps recovered are all close to the original. Fig. 2.11 shows the ten realisations of the delay maps when the continuum flux is at the average of the low and high states (7.0 and 13.0 $\times 10^{-15}$ erg s^{-1} cm^{-2} Å^{-1} respectively). This shows the possible range of uncertainties expected in the delay map.

2.5   Discussion

Both the parameterized fit and the `MEMECHO` fit to the 13-year continuum and Hβ lightcurves for NGC 5548 show that Hβ reverberations depend upon the continuum state in such a way that greater time delays occur for higher continuum states. From the parameterized
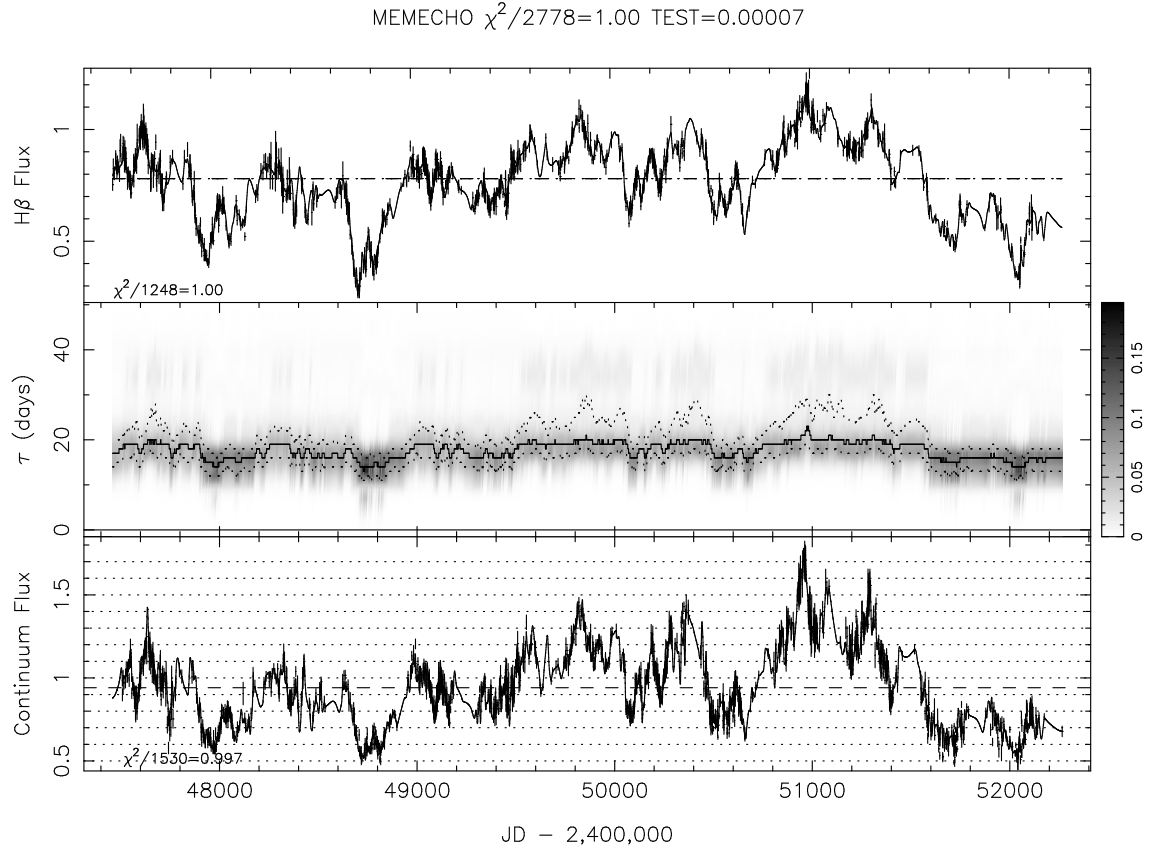
Figure 2.9: Lightcurves for optical continuum (bottom) and Hβ emission line flux (top) from the 1989-2001 *AGN Watch* data on NGC 5548. The `MEMECHO` fit is the smoothest model that achieves $\chi^2/N = 1 \pm \sqrt{2/N}$ for both lightcurves. In the middle panel, the greyscale shows the delay map at each time, the solid line marks the median of the delay map, where as the dotted lines mark the lower and upper quartiles. The horizontal dotted lines in the bottom panel show the flux levels at which each delay map is determined.
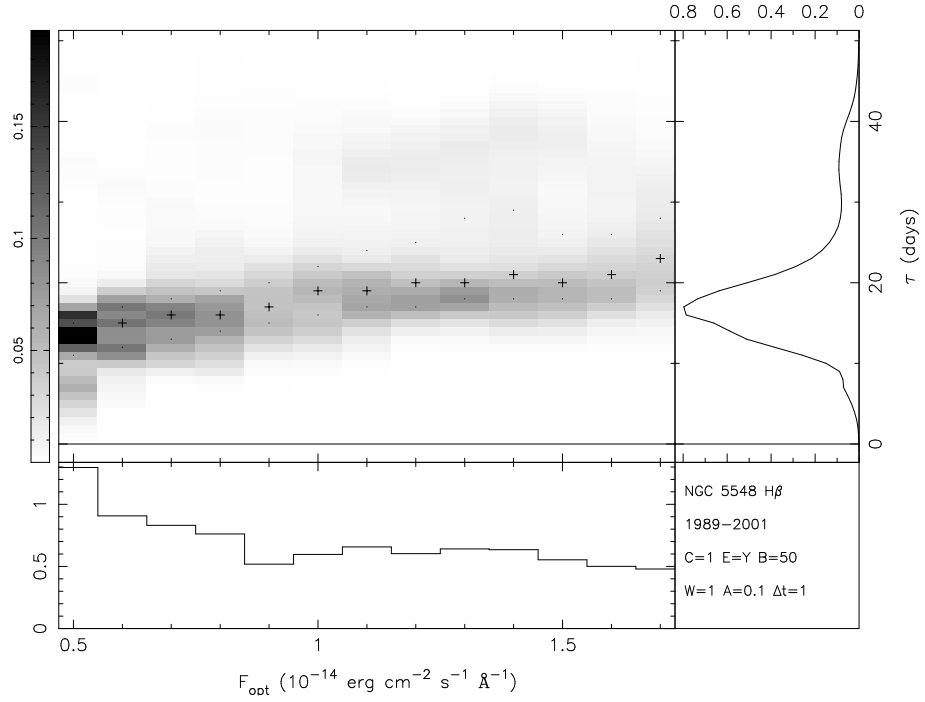
Figure 2.10: The greyscale shows luminosity-dependent delay map $\Psi(\tau, F_{opt})$ from the MEMECHO fit to the 1989-2001 *AGN Watch* data on NGC 5548. The bottom panel shows the luminosity-dependent delay map compressed in time-delay axis, and the righthand side panel shows the delay map compressed in the continuum flux axis.
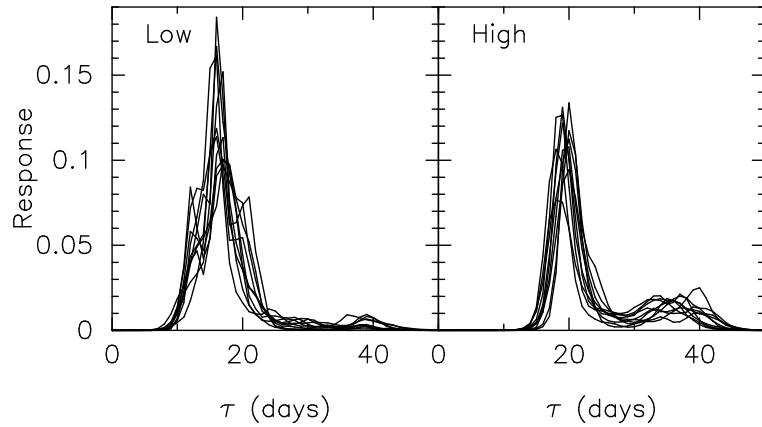
Figure 2.11: 10 realisations of the MEMECHO recovered delay map at low (left) and high (right) continuum levels (7.0 and 13.0×10^{-15} erg s^{-1} cm^{-2} Å^{-1} respectively) from Monte-Carlo simulations.

breathing models we find that $\tau \propto F_{opt}^{\beta}$ with β in the range 0.1 to 0.46, depending on the specific model, with the continuum at 5100 Å corrected for the galaxy contribution. However, as noted in §2.2.2, the driving ionizing continuum may be closer to that observed at 1350 Å. Using our relationship that $F_{opt} \propto F_{UV}^{0.53}$, the luminosity-dependent lag scales like $\tau \propto F_{UV}^{0.05-0.24}$. The MEMECHO fit gives $\tau \propto F_{opt}^{0.24}$, or $\tau \propto F_{UV}^{0.13}$ with respect to the UV continuum. This would appear to be in contrast with both the results of the Static model fits to the separate years, where we find $\tau \propto F_{opt}^{0.93}$, and the findings of Peterson et al. (2002) where they find that CCF centroid lag scales as $F_{opt}^{0.95}$. Our values from the breathing models are closer to that predicted by the photoionization models of Korista & Goad (2004) who find that the responsivity weighted radius, $R \propto F_{c}^{0.23}$, although they noted that the power-law slope should differ somewhat in high (flatter) and low (steeper) continuum states.

Peterson et al. (2002) determine the lag on a yearly basis using cross-correlation. As mentioned in § 2.2, the CCF is the convolution of the delay map with the ACF. Thus, it is clear that the time delay between the line and continuum light curves determined via cross-correlation depends on the shape of both the delay map and the ACF of the continuum. If the ACF is a delta function, then the CCF is identical to the delay map. Generally the ACF is broad and the delay map is asymmetric, thus the peak of the CCF will not necessarily occur at the same time delay as in the delay map (e.g. Welsh, 1999). The continuum variability properties of NGC 5548 vary from year to year leading to a change in ACF, and as an artifact of this, a change in lag could be measured without there being a change in the delay map. It is also the case that the accuracy of the CCF centroid depends on the length of the sampling window, the sampling rate, the continuum variability characteristics and the data quality (Perez et al., 1992). Throughout the 13-year monitoring campaign of NGC 5548 the mean sampling rate has varied, which could lead to a change in the determined lag. However, our results from the Static fits to the yearly data produce similar lags (when comparing our τ_{med} with the centroid lag) and a similar slope to Peterson et al. (2002), suggesting that the cross-correlation results may be measuring the true lags.

Both the parameterized breathing fits and the MEMECHO fit to the full 13-year data show a much flatter dependence of the lag on the luminosity than the year-by-year analysis shows. There is scatter within the results from the yearly analysis. For example, there is a wide range of delay ($\sim 9 - 18$ days) when the continuum is in a low state with

$F_{opt} \sim 7 \times 10^{-15}$ erg s^{-1} cm^{-2} Å^{-1}, and there is also a wide range of continuum fluxes (7 - 12×10^{-15} erg s^{-1} cm^{-2} Å^{-1}) that have a lag of approximately 17 days. A wide range of delays at low continuum flux and also the same lag at a wide range of fluxes favours a flatter relationship. It could be that these features dominate over the two years with the largest lag when fitting to the full 13-year data set. The tail to long delays on the delay maps determined by the parameterized models and the MEMECHO fits may also allow a flatter relationship. The difference in slope is certainly interesting and merits further investigation.

From both the parameterized models and the MEMECHO fits, we also find that the amplitude of the Hβ response declines with increasing continuum luminosity, in other words, the change in Hβ flux relative to changes in the continuum is greater in lower continuum states. Detailed photoionization calculations by Korista & Goad (2004) predict this, and Gilbert & Peterson (2003) and Goad et al. (2004) find the same general result. From our parameterized fits to the data, we find $F_{H\beta} \propto F_{opt}^{\alpha}$ with $0.57 < \alpha < 0.66$, which is consistent with that found by Gilbert & Peterson (2003). Correcting our relationship to be relative to the UV continuum gives $F_{H\beta} \propto F_{UV}^{0.30-0.35}$, which is close to the relationship shown in Fig 2.2 (c). Goad et al. (2004) find a range in this parameter (relative to the optical continuum) of $0.41 < \alpha < 1.0$, that correlates with the optical continuum flux with a high degree of statistical confidence. Korista & Goad (2004) find this to be a natural result, given that the Hβ equivalent width drops with increasing incident photon flux. Their model predicts slightly higher values for the responsivity to the ionizing flux ($F_{H\beta} \propto F_{ion}^{0.54-0.77}$) than we observe from the parameterized fits.

The MEMECHO recovered delay map (Fig. 2.7, panel (f) and Fig. 2.10) and the delay map from the B4 model (Fig. 2.7, panel (e)) seem similar, which is not surprising as they are both driven by the same continuum lightcurve model. However, the B4 model differs from the B1, B2, and B3 models, particularly in its value for β, because of the differing continuum models used. MEMECHO allows the continuum model to have more freedom between the data points (compared to the linear interpolation used in models B1 - B3) resulting in a delay map with a smaller width at shorter time delays as less blurring of the continuum lightcurve is required. Nevertheless, the α parameter does not vary too much between the different models. It is also interesting to note that the residuals in B4 are very flat, even without the spline fit, the long term trends seen in the residuals to B2 have
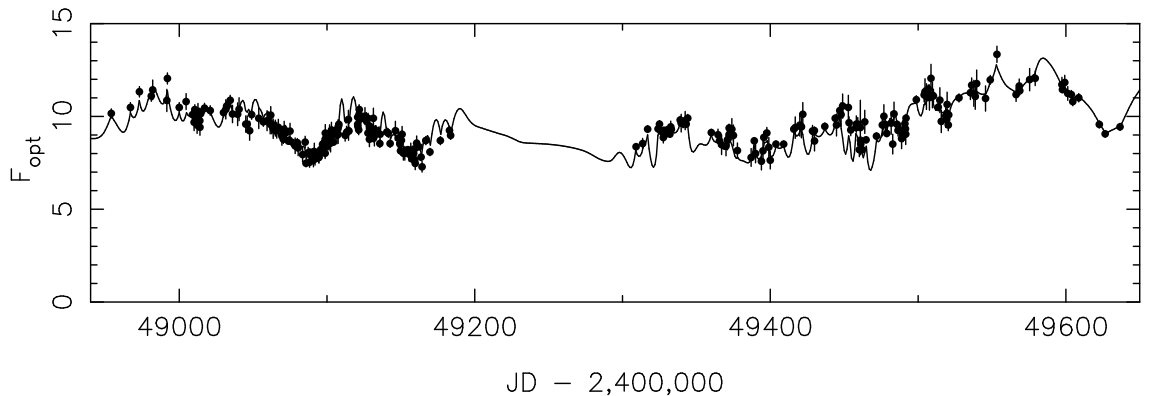
Figure 2.12: A section of the MEMECHO fit to the continuum lightcurve covering the observing campaign in 1993 and 1994.

disappeared. On close inspection of the MEMECHO fit to the continuum (see Fig. 2.12), it can be seen that between the data points the continuum model sometimes shows unphysical dips and peaks. For instance, if the model constantly dips down between the data points, the lag between the continuum and the line lightcurves can be shifted without altering the delay map. In this way it seems that MEMECHO accounts for the long timescale variations that cannot be described by the delay map in the B2 model. Although these spurious dips mean that the MEMECHO result may not be completely reliable, it is clear that the recovered lag luminosity relationship is much flatter than found by the cross-correlation method and thus is an important independent check of the parameterized models.

For the B3 and B4 models we allowed a spline fit to the residuals to account for slowly varying trends (timescale $\sim$ 1 year, see Fig. 2.6). We suggest that these long timescale variations are not due to reverberation effects, but due to slow changes of the BLR gas distribution. In a study of the line profile variability of the first five years of the *AGN Watch* data on NGC 5548, Wanders & Peterson (1996) find that although the Hβ emission line flux tracks the continuum flux, the Hβ emission line profile variations do not, and therefore are not reverberation effects within the BLR. In Fig. 2.13 we compare the line profile 'shapes' determined by Wanders & Peterson (1996) for the first five years of data with our residuals from the B2 model. Wanders & Peterson (1996) define these emission-line 'shapes' to describe the relative prominence of features in the emission-line profile. Each profile is split into its red wing, core and blue wing and the 'shape' for each determined. A positive number for the shape indicates that it is more prominent
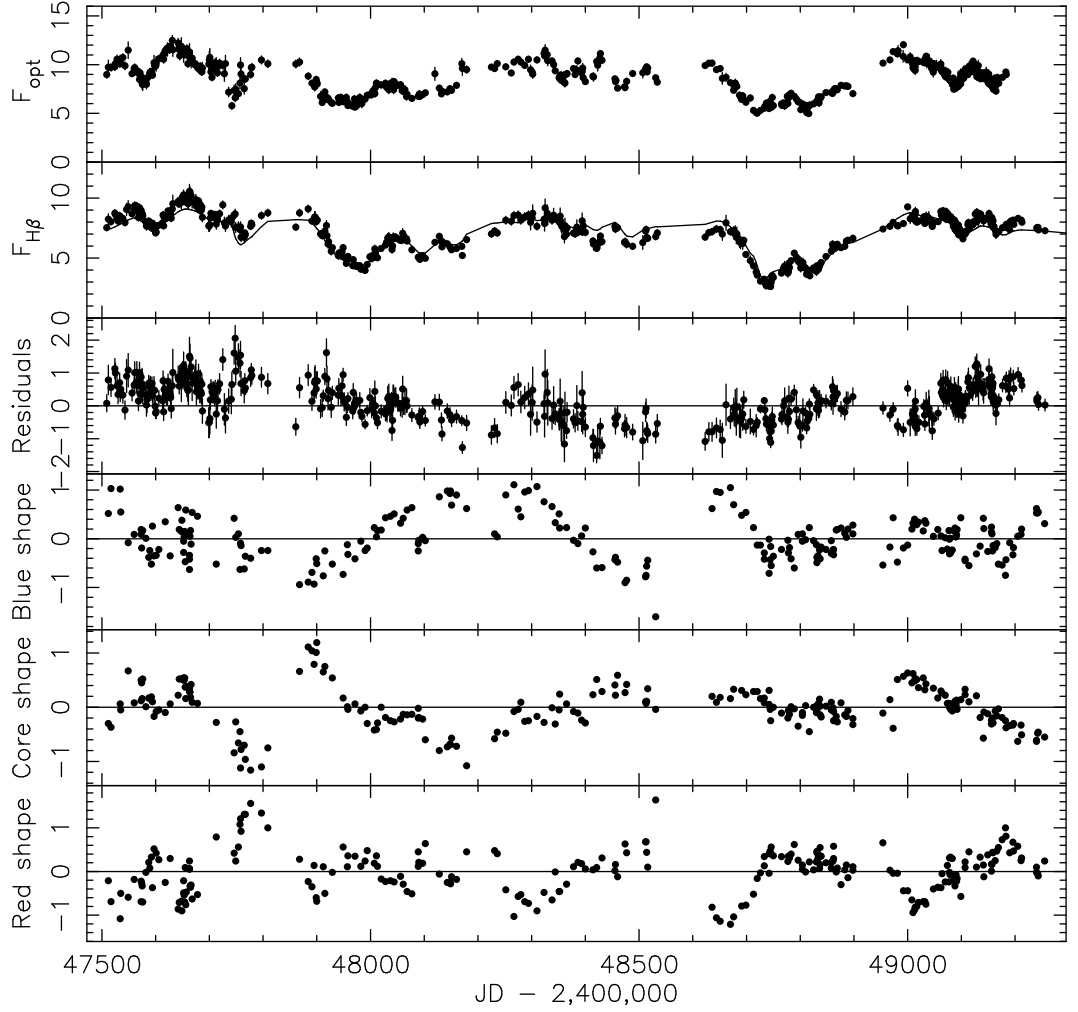
Figure 2.13: A comparison of the 'shapes' of the red wing, blue wing and core of the Hβ line profile as calculated by Wanders & Peterson (1996) with the residuals of the B2 parameterized model, and the continuum and Hβ flux with the B2 model shown.

than on average, whereas a negative number indicates that it is less prominent than on average. Although the shapes vary on similar timescales to the residuals, there is no obvious correlation with the profile shape variations. A comparison of the profile variability for the full 13-year data with our residuals warrants further study.

2.6   Conclusion

Our analysis of 13 years of optical spectrophotometric monitoring of the Seyfert 1 galaxy NGC 5548 from 1989 through 2001 reveals that the size of the Hβ emission-line region

increases as the continuum increases. We also find that the strength of the Hβ response decreases with increasing continuum flux. We have fit the Hβ emission-line lightcurve using both parameterized models and the echo-mapping code `MEMECHO`, both methods show these effects.

In our parameterized models, we allow the delay map to be luminosity-dependent. Our model is parameterized such that the Hβ emission can respond non-linearly to the optical continuum variations, i.e., $F_{H\beta} \propto F_{opt}^{\alpha}$. From our fits to the data we determine $0.57 < \alpha < 0.66$ which is consistent with previous findings of Gilbert & Peterson (2003) and Goad et al. (2004). However, the ionizing continuum is likely to be closer to the UV continuum (F_{UV}) than the optical continuum. Correcting for this ($F_{opt} \propto F_{UV}^{0.53}$) gives $F_{H\beta} \propto F_{UV}^{0.30-0.35}$. In addition, we allow the peak of the delay map, τ_0, to be luminosity-dependent, $\tau_0 \propto F_{opt}^{\beta}$, and find $0.10 < \beta < 0.46$. Correcting to be with respect to the UV continuum gives $\tau_0 \propto F_{UV}^{0.05-0.24}$. `MEMECHO` fits to the lightcurves also show these effects, and fitting a power-law of the form $\tau \propto F_{opt}^{\beta}$ to the luminosity-dependent delay map gives $\tau \propto F_{opt}^{0.24}$, or $\tau \propto F_{UV}^{0.13}$. The values we determine for β (corrected to be relative to the UV continuum) are not consistent with the simple Strömgren sphere ($\beta = 1/3$) and ionization parameter ($\beta = 1/2$) arguments and have a flatter slope than the $\beta = 0.95$ result from the cross-correlation analysis of Peterson et al. (2002). However, they are close to the prediction of Korista & Goad (2004) whose more detailed photoionization models predict $\beta = 0.23$.

In our parameterized models we find slowly vary residuals (timescale $\sim$ 1 year) which we suggest are not reverberation effects, but indicate changes in the gas distribution. Comparison of these residuals with velocity profile changes from the first five years of the data (Wanders & Peterson, 1996) are inconclusive. In future work we will examine velocity profile changes of the full 13-year lightcurves.

Testing thermal reprocessing in AGN accretion discs
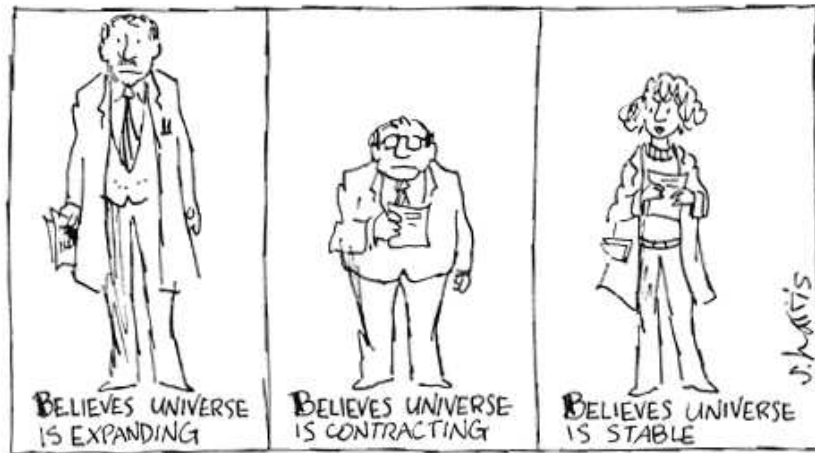
In this chapter we explore wavelength-dependent time delays in a sample of 14 AGN and use the method of Collier et al. (1999) to determine distances to these objects. The implications for the reprocessing model are discussed.

The work in this chapter will form the basis of a paper to be submitted to Monthly Notices of the Royal Astronomical Society.

3.1 Introduction

Echo mapping, or reverberation mapping, (Blandford & McKee, 1982; Peterson, 1993) uses light travel time to measure spatial separations within a distant accretion flow. Ionizing photons produced close to the compact object irradiate the surrounding gas which reprocesses this into UV/optical continuum and emission lines. As the ionizing radiation varies erratically, so do the reprocessed components but with time delays due to light

travel time within the system - the light travel time from source to reprocessing site to observer is longer than that on the direct path from source to observer. These observable delays provide indirect information on the size and structure of the surrounding accretion flows. This technique is a powerful probe of accretion flows on timescales of days to months in AGN. The micro-arcsecond resolution that can be achieved by echo mapping is unreachable by any other technique - 1 light day across at 100 Mpc is $\sim$2 micro-arcsecond.

It has long been known that the optical and UV continuum in AGN are highly correlated and vary nearly simultaneously. Initial attempts at measuring the time-delay (or lag) between the optical and UV continuum found it to be less than a couple of days, though in most cases, the uncertainties in the lags determined were as big as the lag itself. However, higher time-sampling by later spectroscopic monitoring campaigns have allowed for the measurement of wavelength-dependent continuum time-delays in two objects (NGC7469 & Akn564), and appear to follow the predicted relation for an irradiated accretion disc (Wanders et al., 1997; Collier et al., 1998, 2001), with the lags being of the order of 1-2 days. Such small lags can only be explained in terms of AGN reprocessing as disc instabilities should produce time delays of the order of the viscous timescale (the timescale on which the local surface density changes) which is at least hundreds of days in AGN (Krolik et al., 1991).

Recently, from photometric monitoring, Sergeev et al. (2005) found significant lags between optical lightcurves in 14 AGN, with the lags between the lightcurves determined by standard cross-correlation techniques. Their measured lags range from tenths of a day to several days, and with the lag increasing with wavelength, as is predicted by reprocessing in an accretion disc, where the inner hotter regions see the ionizing source before the outer cooler regions. They also find that the delay is systematically greater for greater absolute nuclear luminosity, following $\tau \propto L^b$ where $b \approx 0.4-0.5$, consistent with a disc reprocessing model. The lags are interpreted in terms of the light-travel time from an ionizing source above the disc to the region in the disc where the ionizing radiation is reprocessed into optical continuum emission. Thus, the brighter the source, the greater the light-travel time to the region emitting the optical continuum.

Collier et al. (1999) showed how measuring time-delays between the optical/UV continuum in an AGN accretion disc and the flux from the disc, the distance to an AGN can be measured, and hence be used as standard candles to determine the current expansion

rate of the Universe, Hubble's constant, H_0. From measurements of the wavelength-dependent time-delays in NGC 7469, these authors determine $H_0 = 42 \pm 9$ km s^{-1} Mpc^{-1} assuming an inclination of $45°$. However, this is at odds with other determinations of H_0. Over the past decade, several methods have been employed to determine H_0 (as discussed in Chp. 1), with all methods now converging to a value of around 72 km s^{-1} Mpc^{-1}. The method using AGN accretion discs does not rely on the distance ladder calibration, and thus provides another independent check on these results. One distinct advantage of this method, compared to other methods, is that AGN are common in the Universe, and can be found over a wide range of redshifts. As they are some of the most energetic sources in the Universe, AGN can be seen to redshifts greater than the supernova horizon, and thus potentially can set tight constraints on Ω_M and Ω_Λ - it is at redshifts greater than $z \sim 1$ where large differences are seen between differing cosmological models (see Fig. 1.8 in Chp. 1). In this work, we re-analyse the Sergeev et al. (2005) lightcurves, also in terms of thermal reprocessing in an AGN disc, in an attempt to extend the method of Collier et al. (1999) to use AGN accretion discs as a cosmological probe.

3.2 AGN lightcurves

Here we use the published optical lightcurves for 14 AGN from Sergeev et al. (2005) in the B, V, R, R1 and I bands. However, the filters used are non-standard filters (Doroshenko et al., 2005a,b), though the B, V, and R are close to Johnson filters, the R1 is close to the Johnson I filter and the I filter is close to the Cousins I filter. The published lightcurves are given as relative fluxes with respective to comparison stars. However, the magnitudes of the comparison stars are only given in the standard B, V, R, I bands, rather than the non-standard bandpasses used. For this work, we require the absolute fluxes of the AGN, rather than the relative fluxes, and therefore require the magnitudes of the comparison stars in the filters used. To calculate these we use Xcal, an interactive synthetic photometry program, developed by Keith Horne[1]. Xcal computes predicted count rates from target spectra in standard or non-standard passbands, allowing stellar spectra to be fit to the comparison star magnitudes in the standard Johnson-Cousins filters. Spectra of main sequence stars from the Bruzual-Persson-Gunn-Stryker atlas (Gunn & Stryker, 1983) were individually scaled to fit the observed magnitudes, and the star with lowest χ^2 was adopted to model

---

[1]available from http://star-www.st-and.ac.uk/~kdh1

Table 3.1: Fluxes (in mJy) for the comparison stars used by Sergeev et al. (2005) for each of the 14 AGN in their B, V, R, R1 and I filters.

Object	B	V	R	R1	I
1E 0754.6+3928	5.83	10.89	14.04	15.11	15.34
Akn 120	4.50	10.19	14.97	17.08	17.51
MCG+8-11-11	6.27	19.21	36.71	48.02	50.94
Mrk 335	8.02	13.61	16.93	18.06	18.32
Mrk 509	24.99	40.66	49.16	51.41	51.82
Mrk 6	3.46	5.91	7.53	8.01	8.05
Mrk 79	22.04	37.64	47.93	51.02	51.28
NGC 3227	15.24	28.46	36.70	39.50	40.11
NGC 3516	10.05	15.63	18.67	19.38	19.37
NGC 4051	5.11	7.91	9.31	9.70	9.76
NGC 4151	8.67	26.58	50.79	66.43	70.47
NGC 5548	5.97	11.14	14.37	15.47	15.71
NGC 7469	26.49	55.18	77.24	87.97	90.24
3C 390.3	3.80	6.99	9.02	9.89	10.03

the spectrum of the comparison star. Once the best-fitting stellar spectrum has been determined, the magnitudes in the non-standard filters are determined by computing the count rate of the best-fitting spectrum within the bandpasses of these filters. In this way, we determined the fluxes of the comparison stars in the B, V, R, R1 and I filters used by Sergeev et al. (2005) and are therefore able to get the fluxes of the AGN lightcurves. The fluxes we determine for the comparison stars are given in Table 3.1.

All 14 AGN show significant variability over the approximately 3 year period that they were monitored. In Fig. 3.1 we show the B-band lightcurves for all of these AGN over the entire monitoring period. The median temporal sampling for the lightcurves is 2 to 3 days (see Sergeev et al., 2005, for sampling rates for each AGN). As an example of the strong correlations between the lightcurves in the different wavebands, all 5 lightcurves for NGC 5548 and NGC 7469, with the cross-correlation functions (see section 1.2.3 for a definition) are shown in Figs. 3.2 and 3.3. We have determined the lags between the lightcurves (relative to the B-band lightcurve) for each AGN using the interpolation cross-correlation method, and find the delays to be the same as determined by (Sergeev et al.,

2005). For the sake of completeness, the lags determined are reproduced here, in Table 3.2. We compare the time delays determined from the peak and centroid of the CCF in Fig. 3.4. The peak time delay is generally smaller than the centroid time delay, though in many cases they are consistent within the uncertainties. The maximum and minimum fluxes of each of the lightcurves are also given in Table 3.3 as these are used in the model which we describe later.

Table 3.2: Time-delays relative to the B-band determined by cross-correlation. After Sergeev et al. (2005). τ_{peak} is the lag determined by the peak of the CCF, τ_{cent} is the lag determined from the centroid of the CCF.

Object	Filter	τ_{peak} (days)	τ_{cent} (days)
1E 0754.6+3928	V	$9.4^{+7.2}_{-6.6}$	13.2 ± 3.9
$z = 0.096$	R	$11.2^{+9.6}_{-1.5}$	$19.6^{+3.5}_{-3.7}$
	R1	$12.4^{+6.3}_{-2.3}$	$20.6^{+3.6}_{-4.6}$
	I	$12.9^{+7.6}_{-4.7}$	$17.4^{+4.6}_{-5.3}$
Akn 120	V	$0.55^{+0.93}_{-1.23}$	$1.32^{+2.01}_{-0.82}$
$z = 0.032$	R	$2.79^{+0.81}_{-1.27}$	$2.13^{+2.49}_{-0.93}$
	R1	$2.87^{+1.75}_{-1.20}$	$3.30^{+2.27}_{-1.25}$
	I	$3.04^{+1.33}_{-1.81}$	$3.79^{+2.52}_{-1.64}$
MCG+8-11-11	V	$0.35^{+0.42}_{-0.76}$	$0.93^{+0.43}_{-0.64}$
$z = 0.020$	R	$3.60^{+1.20}_{-0.51}$	$4.73^{+1.06}_{-0.60}$
	R1	$3.18^{+1.99}_{-0.57}$	$5.08^{+1.12}_{-0.98}$
	I	$3.48^{+2.69}_{-0.31}$	$5.87^{+1.04}_{-1.36}$
Mrk 335	V	$0.43^{+0.83}_{-0.81}$	$0.86^{+0.56}_{-0.97}$
$z = 0.026$	R	$2.36^{+0.74}_{-0.85}$	$2.44^{+0.67}_{-1.07}$
	R1	$2.30^{+0.44}_{-1.76}$	$1.45^{+0.94}_{-1.26}$
	I	$2.33^{+0.30}_{-1.86}$	$1.74^{+0.78}_{-1.25}$
Mrk 509	V	$0.27^{+0.36}_{-1.04}$	$-0.84^{+0.55}_{-1.30}$
$z = 0.034$	R	$5.62^{+0.75}_{-3.86}$	$6.07^{+1.32}_{-1.54}$
	R1	$5.56^{+2.79}_{-2.02}$	$7.45^{+1.67}_{-1.92}$
	I	$7.51^{+3.05}_{-1.54}$	$9.05^{+1.83}_{-2.45}$
Mrk 6	V	$0.43^{+0.37}_{-1.05}$	$0.98^{+1.02}_{-0.98}$
$z = 0.019$	R	$0.71^{+1.50}_{-0.12}$	$3.28^{+0.72}_{-1.20}$

Table 3.2 – continued from previous page

Object	Filter	τ_{peak} (days)	τ_{cent} (days)
	R1	$2.33^{+1.24}_{-0.84}$	$4.11^{+0.80}_{-1.09}$
	I	$2.27^{+1.36}_{-0.84}$	$4.24^{+0.91}_{-1.21}$
Mrk 79	V	$0.35^{+0.34}_{-0.08}$	$1.11^{+0.63}_{-0.85}$
$z = 0.022$	R	$3.52^{+0.25}_{-2.05}$	$2.64^{+2.64}_{-1.03}$
	R1	$2.54^{+1.75}_{-1.07}$	$4.32^{+2.61}_{-0.97}$
	I	$3.66^{+1.41}_{-1.09}$	$5.07^{+2.84}_{-1.40}$
NGC 3227	V	$0.19^{+0.21}_{-0.64}$	$-0.17^{+0.27}_{-0.51}$
$z = 0.004$	R	$0.49^{+0.27}_{-0.11}$	$1.44^{+0.38}_{-0.69}$
	R1	$0.55^{+0.82}_{-0.11}$	$1.49^{+0.53}_{-0.73}$
	I	$0.61^{+0.91}_{-0.15}$	$1.51^{+0.70}_{-0.65}$
NGC 3516	V	$0.38^{+0.28}_{-0.90}$	$0.00^{+0.62}_{-0.55}$
$z = 0.009$	R	$1.53^{+0.85}_{-0.98}$	$1.92^{+0.91}_{-0.72}$
	R1	$1.63^{+0.78}_{-1.04}$	$1.39^{+1.10}_{-1.00}$
	I	$0.53^{+1.99}_{-1.01}$	$1.60^{+0.93}_{-0.98}$
NGC 4051	V	$0.24^{+0.20}_{-0.62}$	$-0.16^{+0.44}_{-0.49}$
$z = 0.002$	R	$0.30^{+0.22}_{-0.76}$	$0.40^{+0.39}_{-0.57}$
	R1	$0.41^{+0.26}_{-0.85}$	$0.80^{+0.60}_{-0.80}$
	I	$0.41^{+1.03}_{-0.79}$	$1.41^{+0.55}_{-1.03}$
NGC 5548	V	$0.43^{+0.39}_{-0.95}$	$0.94^{+1.24}_{-1.04}$
$z = 0.017$	R	$7.68^{+3.02}_{-0.90}$	$11.0^{+1.48}_{-0.87}$
	R1	$4.55^{+2.27}_{-0.33}$	$8.76^{+1.56}_{-1.15}$
	I	$6.68^{+2.76}_{-1.23}$	$10.43^{+2.15}_{-0.98}$
NGC 7469	V	$-0.35^{+0.80}_{-0.24}$	$-0.29^{+0.38}_{-0.40}$
$z = 0.016$	R	$1.23^{+0.33}_{-0.62}$	$1.49^{+0.60}_{-0.55}$
	R1	$1.28^{+0.32}_{-0.64}$	$1.72^{+0.69}_{-0.67}$
	I	$1.56^{+1.71}_{-0.81}$	$2.51^{+0.76}_{-0.67}$
3C 390.3	V	$0.35^{+0.75}_{-1.02}$	$0.98^{+0.89}_{-0.98}$
$z = 0.056$	R	$3.48^{+3.09}_{-1.85}$	$7.88^{+1.43}_{-1.89}$
	R1	$3.87^{+5.46}_{-0.15}$	$9.20^{+1.47}_{-1.94}$
	I	$3.59^{+9.82}_{-0.32}$	$9.15^{+1.44}_{-2.69}$
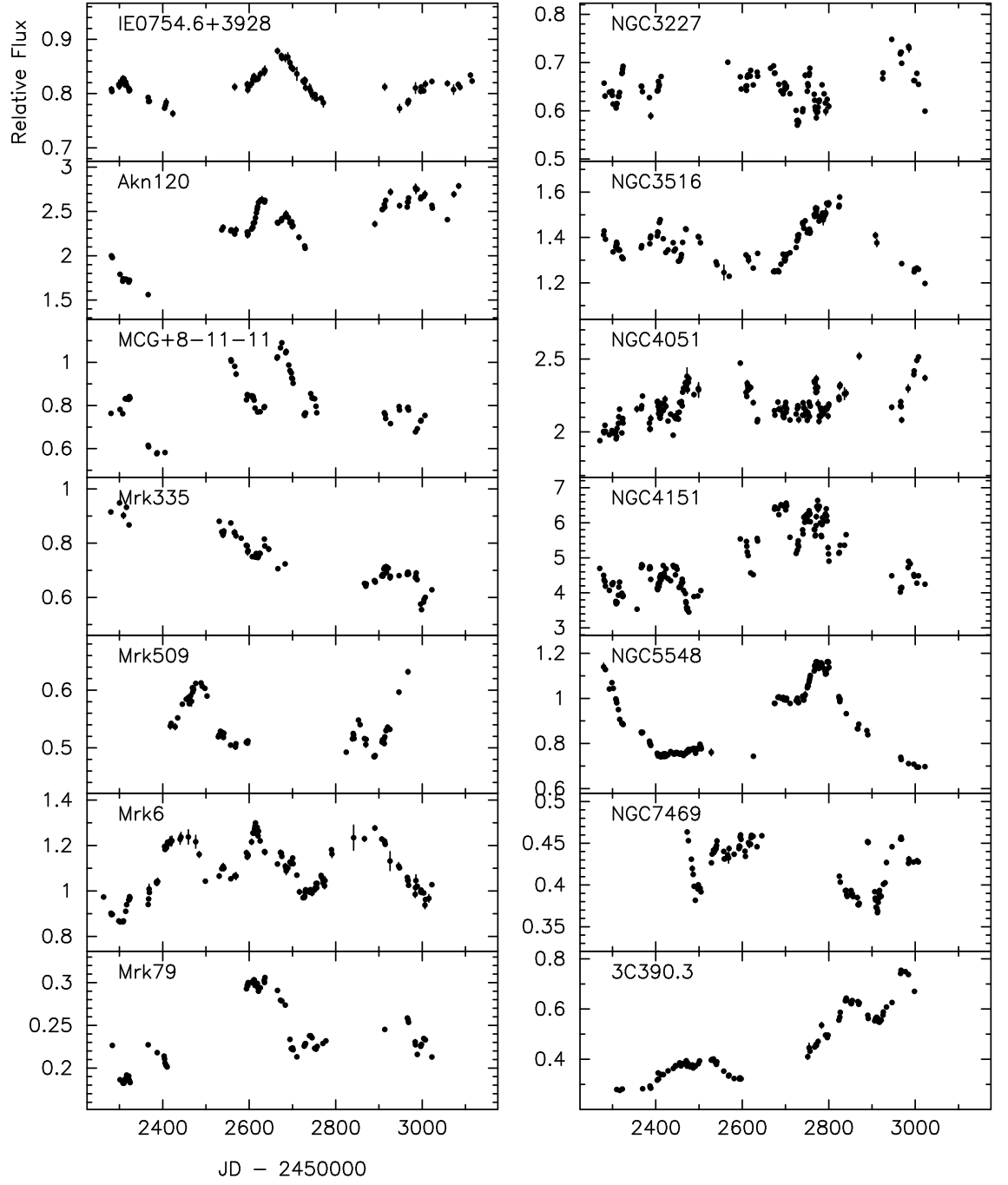
Figure 3.1: Lightcurves for the 14 AGN in the Sergeev et al. B filter. Fluxes are relative to a comparison star. Error bars are 1σ uncertainties. After Sergeev et al. (2005).

74
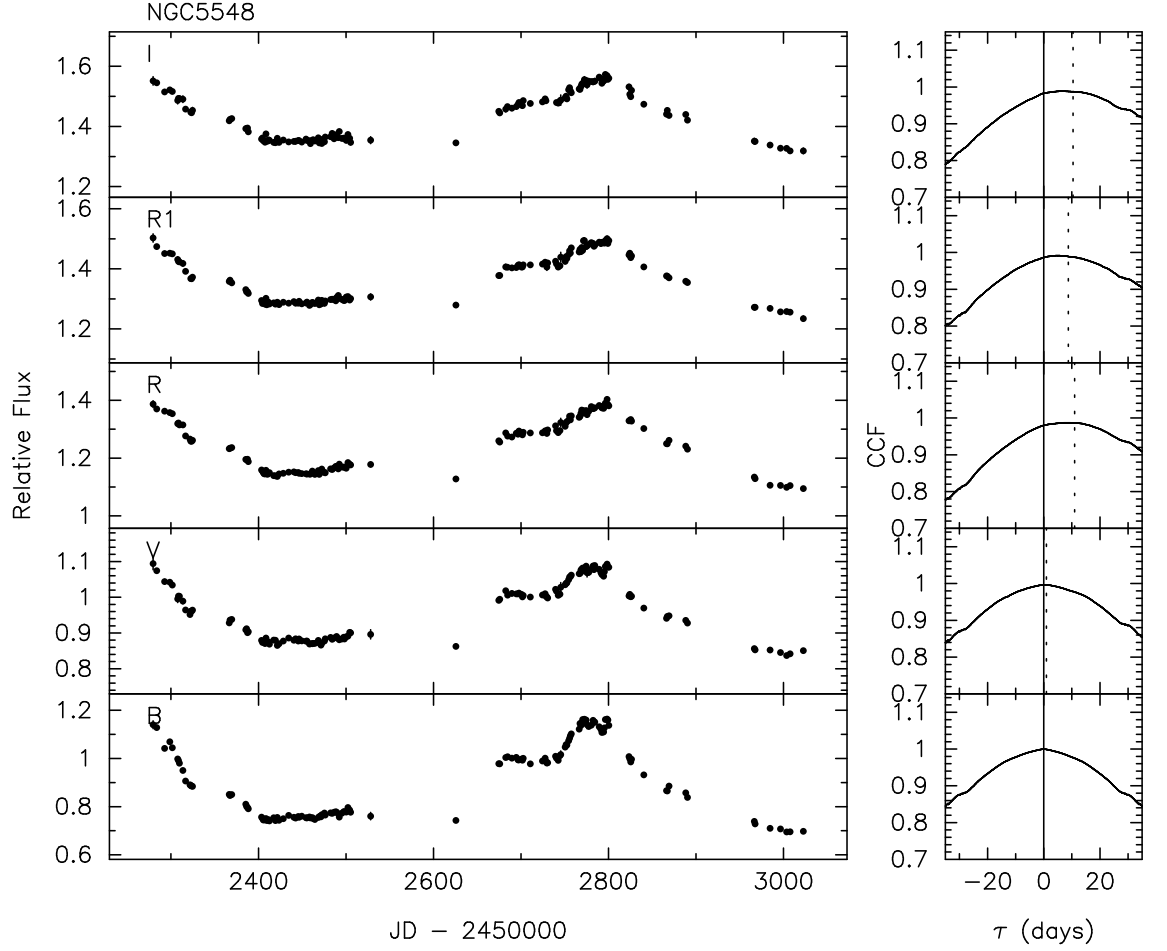
Figure 3.2: *Left:* Lightcurves for NGC 5548 in all 5 bands. *Right:* Corresponding cross-correlation functions (CCF) for the lightcurves with respect to the B-band. In the B-band the auto-correlation function is plotted. Solid line indicates a time-delay, $\tau = 0.0$ d, and the dotted line shows the centroid of the CCF.
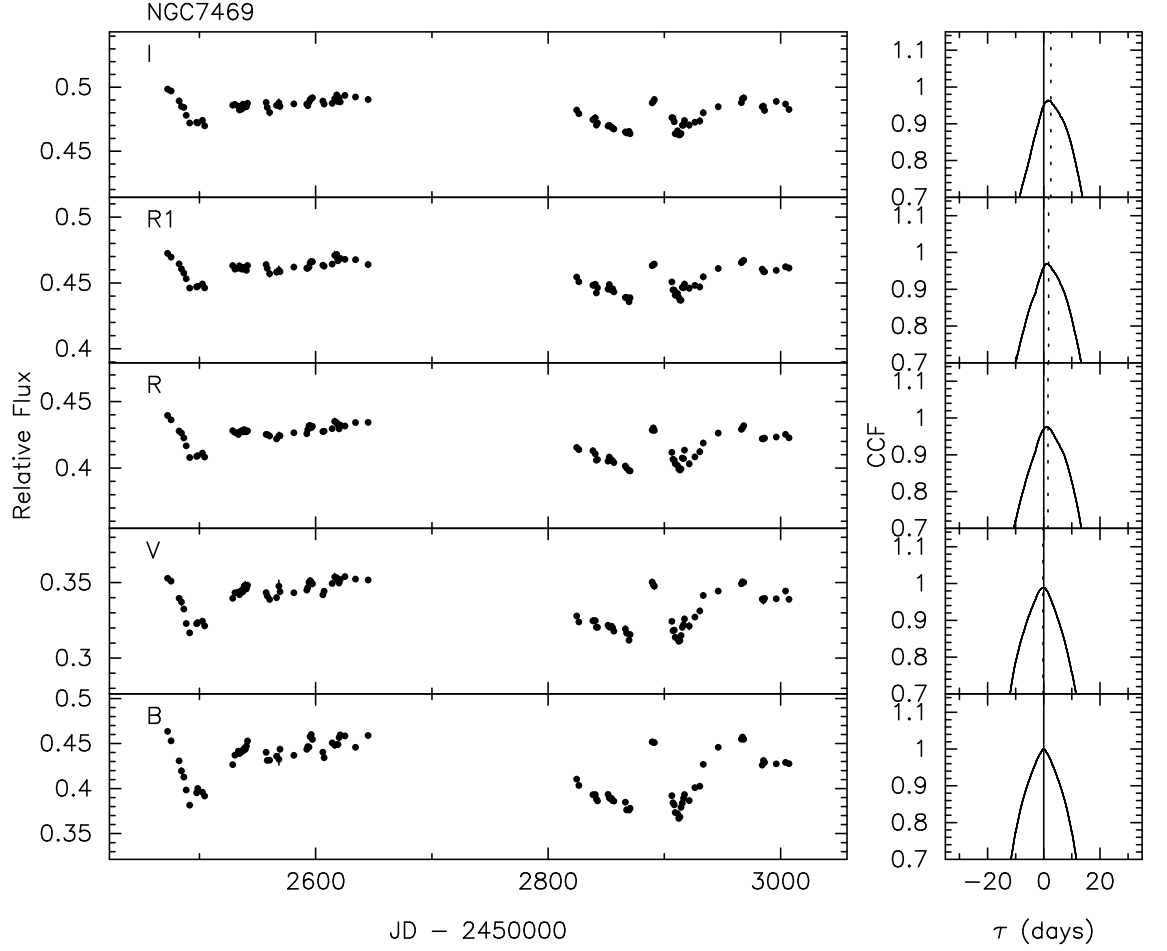
Figure 3.3: *Left:* Lightcurves for NGC 7469 in all 5 bands. *Right:* Corresponding cross-correlation functions (CCF) for the lightcurves with respect to the B-band. In the B-band the auto-correlation function is plotted. Solid line indicates a time-delay, $\tau = 0.0$ d, and the dotted line shows the centroid of the CCF.
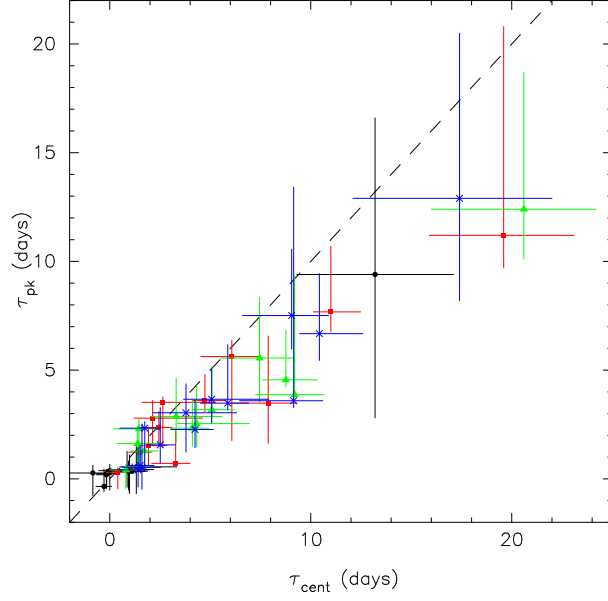
Figure 3.4: Comparison of τ_{pk} and τ_{cent} for each of the different filters. Black circles indicate the V band delays, red squares the R band delays, green triangles the R1 band delays, and blue crosses the I band delays. Dashed line is $\tau_{pk} = \tau_{cent}$.

Table 3.3: Maximum and minimum fluxes (mJy) from the AGN lightcurves

Object	Filter	Maximum flux (mJy)	Minimum flux (mJy)
1E 0754.6+3928	B	5.12 ± 0.03	4.45 ± 0.03
	V	6.87 ± 0.04	6.33 ± 0.06
	R	8.33 ± 0.05	7.62 ± 0.04
	R1	9.40 ± 0.06	8.58 ± 0.05
	I	8.81 ± 0.05	8.11 ± 0.06
Akn 120	B	12.55 ± 0.13	7.032 ± 0.10
	V	16.37 ± 0.13	10.60 ± 0.08
	R	23.55 ± 0.13	16.00 ± 0.09
	R1	24.02 ± 0.15	17.04 ± 0.09
	I	25.02 ± 0.16	18.06 ± 0.10
MCG+8-11-11	B	6.83 ± 0.04	3.61 ± 0.03
	V	10.60 ± 0.05	7.08 ± 0.05

Table 3.3 – continued from previous page

Object	Filter	Maximum flux (mJy)	Minimum flux (mJy)
	R	19.61 ± 0.08	14.98 ± 0.07
	R1	22.51 ± 0.09	17.53 ± 0.08
	I	24.44 ± 0.10	19.16 ± 0.09
Mrk 335	B	7.61 ± 0.06	4.45 ± 0.02
	V	8.90 ± 0.06	6.04 ± 0.04
	R	12.67 ± 0.07	9.00 ± 0.04
	R1	12.09 ± 0.07	8.74 ± 0.04
	I	12.58 ± 0.08	9.10 ± 0.05
Mrk 509	B	15.79 ± 0.11	12.11 ± 0.09
	V	18.07 ± 0.11	15.02 ± 0.11
	R	25.40 ± 0.12	22.24 ± 0.11
	R1	23.57 ± 0.13	20.76 ± 0.12
	I	24.47 ± 0.14	21.71 ± 0.12
Mrk 6	B	4.50 ± 0.03	2.99 ± 0.02
	V	9.42 ± 0.06	7.25 ± 0.04
	R	17.05 ± 0.09	13.45 ± 0.06
	R1	19.07 ± 0.11	15.50 ± 0.08
	I	20.26 ± 0.10	16.44 ± 0.09
Mrk 79	B	6.74 ± 0.05	4.02 ± 0.02
	V	9.65 ± 0.08	6.87 ± 0.04
	R	15.12 ± 0.09	11.50 ± 0.05
	R1	16.22 ± 0.12	12.67 ± 0.06
	I	16.96 ± 0.13	13.32 ± 0.08
NGC 3227	B	11.41 ± 0.07	8.69 ± 0.05
	V	22.84 ± 0.13	19.53 ± 0.10
	R	41.02 ± 0.20	36.95 ± 0.18
	R1	51.03 ± 0.26	46.72 ± 0.23
	I	54.54 ± 0.27	50.11 ± 0.52
NGC 3516	B	15.85 ± 0.10	12.03 ± 0.06

Table 3.3 – continued from previous page

Object	Filter	Maximum flux (mJy)	Minimum flux (mJy)
	V	31.00 ± 0.13	27.33 ± 0.13
	R	52.15 ± 0.22	46.25 ± 0.20
	R1	62.06 ± 0.39	56.58 ± 0.46
	I	65.25 ± 0.36	59.74 ± 0.30
NGC 4051	B	12.89 ± 0.12	9.92 ± 0.05
	V	21.46 ± 0.16	18.22 ± 0.08
	R	34.23 ± 0.19	29.71 ± 0.16
	R1	41.31 ± 0.27	36.55 ± 0.20
	I	43.42 ± 0.30	38.94 ± 0.24
NGC 4151	B	57.53 ± 0.54	29.93 ± 0.29
	V	74.97 ± 0.35	49.07 ± 0.27
	R	117.93 ± 0.49	84.37 ± 0.34
	R1	125.98 ± 0.54	91.60 ± 0.38
	I	133.10 ± 0.56	97.44 ± 0.43
NGC 5548	B	6.94 ± 0.05	4.15 ± 0.02
	V	12.20 ± 0.19	9.33 ± 0.04
	R	20.17 ± 0.11	15.73 ± 0.09
	R1	23.24 ± 0.21	19.09 ± 0.13
	I	24.71 ± 0.10	20.71 ± 0.15
NGC 7469	B	12.28 ± 0.06	9.72 ± 0.04
	V	19.53 ± 0.09	17.16 ± 0.07
	R	33.95 ± 0.14	30.73 ± 0.13
	R1	41.56 ± 0.17	38.33 ± 0.16
	I	44.99 ± 0.18	41.76 ± 0.17
3C 390.3	B	2.86 ± 0.02	1.05 ± 0.01
	V	4.12 ± 0.02	2.19 ± 0.01
	R	6.30 ± 0.03	3.74 ± 0.02
	R1	6.77 ± 0.04	4.25 ± 0.03
	I	7.13 ± 0.05	4.53 ± 0.03

3.3 Accretion disc model

Sergeev et al. (2005) successfully modelled the lag-luminosity relation in these sources with a disc reprocessing model, where interband time-delays exist due to different light travel times from the ionizing source and the different continuum emitting regions. Here we take this further, by simultaneously fitting the interband lag distribution and spectral energy distribution (SED) in terms of a disc reprocessing model. In this model we fit the SED at the maximum and minimum points in the lightcurve, interpreting the change in brightness as a change in the luminosity of the ionizing source driving the reprocessing in the disc, and hence a change in disc temperature. Simultaneously we fit the lags with the same model.

We assume that there is a highly variable source of ionizing radiation near the disc axis that illuminates the disc, driving optical/UV variability and leading to wavelength-dependent time-delays. The hot inner regions which emit mainly UV photons 'see' the driving ionizing photons before the cool outer regions which emit mainly optical photons. Thermal radiation from a disc annulus at temperature $T(R)$ emerges with a range of wavelengths, centred at $\lambda \sim hc/kT(R)$. Roughly speaking, each wavelength picks out a different temperature zone and the time delay $\tau = R/c$ measures the corresponding radius. Thus, shorter wavelengths sense disc annuli at higher temperatures.

In this model there is heating due to irradiation as well as viscous heating in the disc. For viscous heating alone, when the radius is much greater than the inner most stable orbit, the disc temperature profile should follow

$$T(R) = \left(\frac{3GM\dot{M}}{8\pi R^3 \sigma} \right)^{1/4} \tag{3.1}$$

where M is the mass of the black hole, and $\dot{M}$ the mass accretion rate. In the case of irradiation of the disc from a height H_x above the disc, the temperature profile is a combination of the temperature due to irradiation and the temperature due to viscous heating,

$$T(R) = \left[\left(\frac{3GM\dot{M}}{8\pi R^3 \sigma} \right) + \left(\frac{AL_x}{4\pi \sigma R_*^2} \right) \cos\theta_x \right]^{1/4} , \tag{3.2}$$

where L_x is the luminosity of the irradiating source, A is the disc albedo, R_* is the distance from the illuminating source to the surface element of the disc, and θ_x is the angle between the disc surface normal and a unit vector from the surface element to the variable central source. This leads to $T(R) \propto (L_x H_x)^{1/4} R^{-3/4}$, for $R \gg H_x$ and provided the disc thickness is $H \ll H_x$ (e.g. Frank et al., 2002). Thus, in both cases, we expect $T(R) \propto R^{-3/4}$. As the time delay goes as $\tau = R/c$ and the wavelength goes like $\lambda \propto 1/T$, then this predicts that wavelength-dependent time-delay profile goes like $\tau \propto \lambda^{4/3}$.

With the temperature profile determined from the wavelength-dependent time-delays, the predicted spectrum can be determined by summing up blackbodies over disc annuli, and comparing this with the observed spectrum leads to a determination of the distance to the source (Collier et al., 1999). In this way the predicted spectrum is given by

$$f_\nu = \int_{R_{in}}^{R_{out}} B_\nu \, \mathrm{d}\Omega = \int_{R_{in}}^{R_{out}} \frac{2hc}{\lambda^3} \frac{1}{e^{hc/\lambda kT} - 1} \frac{2\pi R \, \mathrm{d}R \cos i}{D^2} \tag{3.3}$$

with B_ν the Planck function, $\mathrm{d}\Omega$ the solid angle subtended by the disc annuli, R_{in} and R_{out} the inner and outer disc radii, i the inclination angle of the disc, and D the distance. Following Collier (1998), we assume a general temperature profile for the disc of $T = T_0 y^{-b}$ with $y = R/R_0$ (T_0 is the temperature at radius R_0), and $s_0 = hc/\lambda kT_0$ such that $s = s_0 y^b$ and $\mathrm{d}y = y \, \mathrm{d}s/bs$. Over a range of wavelengths that are well within those corresponding to the inner and outer disc radii, this leads to

$$f_\nu = \frac{4\pi R_0^2 \cos i}{D^2} (hc)^{1-(2/b)} \lambda^{(2/b)-3} (kT_0)^{2/b} \frac{I_2(b)}{b} \ , \tag{3.4}$$

where

$$I_n(b) = \int_0^\infty \frac{s^{(n/b)-1} \, \mathrm{d}s}{e^s - 1} \ . \tag{3.5}$$

$I_n(b)$ is a numerical function, and we calculate $I_2(3/4) = 1.93$ and $I_3(3/4) = 6.49$.

AGN spectra, however, do not match the classical thin-disc spectrum $f_\nu \propto \nu^{1/3}$. This is due to contributions from stars and dust. Nevertheless, the disc spectrum can be isolated by taking difference spectra, and Collier et al. (1999) found that the *variable* component of AGN light in NGC 7469 does have $\Delta f_\nu \propto \nu^{1/3}$. For this reason we choose to model the difference spectra of the AGN by using a disc transfer function, described below.

3.3.1 Disc Transfer Function

We choose to model the AGN wavelength-dependent time-delay distribution and spectrum by using a disc transfer function $\Psi_\nu(\tau, \lambda)$ to describe the response of the disc to changes at a given wavelength and time delay, as outlined by Collier (1998) in his Ph.D. thesis. The disc transfer function is defined as

$$
\begin{aligned}
\Psi_\nu(\tau, \lambda) &= \int_{R_{in}}^{R_{out}} \frac{\partial B_\nu}{\partial T} \frac{\partial T}{\partial L_x} \delta\left(\tau - \frac{R}{c}(1 + \sin i \cos \theta)\right) d\Omega & (3.6) \\
&= \int_{R_{in}}^{R_{out}} \int_0^{2\pi} \frac{\partial B_\nu}{\partial T} \frac{\partial T}{\partial L_x} \frac{R \, dR \, d\theta \cos i}{D^2} \delta\left(\tau - \frac{R}{c}(1 + \sin i \cos \theta)\right), & (3.7)
\end{aligned}
$$

where L_x is the driving ionizing luminosity. The δ-function ensures that only radii corresponding to the specific time delay contribute to the transfer function. As we are fitting the maximum and minimum SED of the AGN with this model, we treat the disc as having temperature T_B at R_0 during the bright state and T_F at R_0 during the faint state. Hence,

$$
\frac{\partial B_\nu}{\partial T} \frac{\partial T}{\partial L_x} = B_\nu(T_2) - B_\nu(T_1) \tag{3.8}
$$

and $T_2 = T_B(R/R_0)^{-b}$, $T_1 = T_F(R/R_0)^{-b}$, and we take $R_0 = 1$ light-day. Examples of the transfer function are given in Fig. 3.5.

3.3.2 Time-delays

The centroid of the transfer function is equivalent to the centroid of the CCF which is used as a measure of the luminosity-weighted radius of the reprocessing region (Koratkar & Gaskell, 1991), however, see Robinson & Perez (1990) and Welsh (1999) for limitations. Hence, knowing the transfer function, allows us to determine an analytical formula for the centroid of the time delay from

$$
\langle \tau \rangle = \frac{\int \tau \Psi_\nu(\tau, \lambda) \, d\tau}{\int \Psi_\nu(\tau, \lambda) \, d\tau} , \tag{3.9}
$$

which becomes

$$
\langle \tau \rangle = \frac{\int_{R_{in}}^{R_{out}} [B_\nu(T_2) - B_\nu(T_1)](R^2/c) \, dR}{\int_{R_{in}}^{R_{out}} [B_\nu(T_2) - B_\nu(T_1)] R \, dR} . \tag{3.10}
$$

Continuing to follow Collier (1998), this reduces to

$$
\langle \tau \rangle = \frac{R_0}{c} \left(\frac{\lambda k T_B}{hc}\right)^{1/b} \frac{I_3(b)}{I_2(b)} \frac{1 - \varepsilon^{3/2}}{1 - \varepsilon} , \tag{3.11}
$$
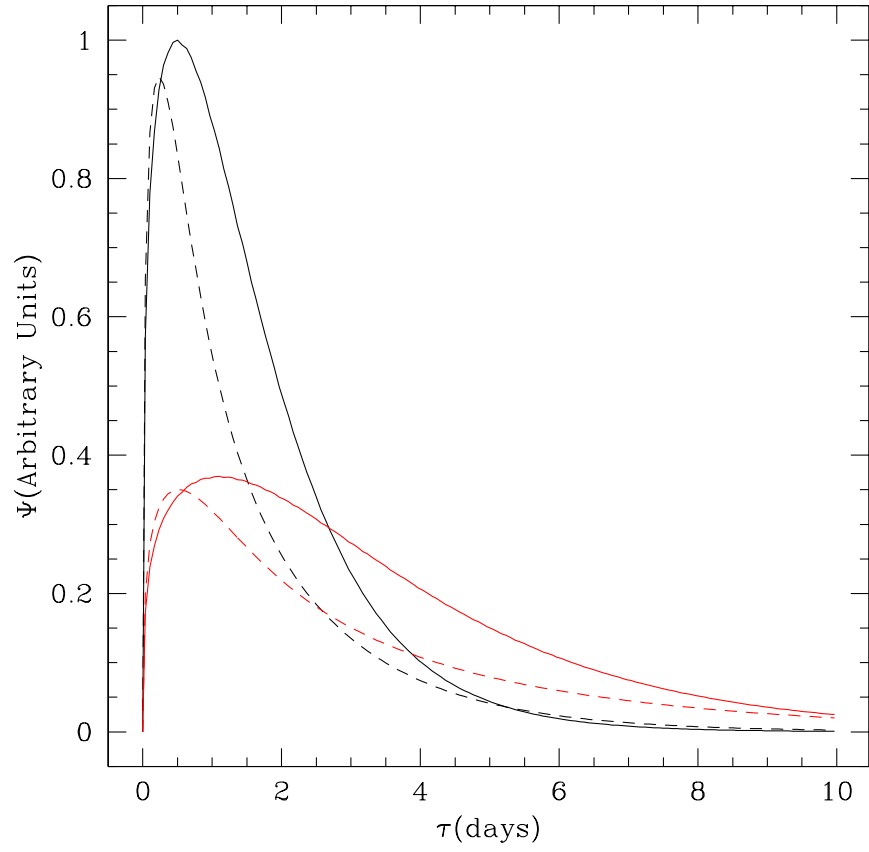
Figure 3.5: Irradiated accretion disc transfer functions for 4400Å (black) and 8000Å (red) and disc inclinations of 0° (solid) and 45° (dashed). $T_B = 15000$ K and $T_F = 12000$ K.

where $\varepsilon = (T_F/T_B)^{2/b}$. Rearranging the above equation for kT_B and substituting into Eq. 3.4, the bright state disc spectrum is given in terms of the measured lag:

$$f_\nu^B = \frac{4\pi \cos i}{D^2} hc^3 \lambda^{-3} \langle \tau \rangle^2 \frac{I_2(b)^3}{bI_3(b)^2} \left(\frac{1-\varepsilon}{1-\varepsilon^{3/2}}\right)^2 . \tag{3.12}$$

Similarly, it can be shown that the faint state spectrum is just given by $f_\nu^F = \varepsilon f_\nu^B$ and the difference spectrum between the bright and faint state is given by $\Delta f_\nu = f_\nu^B - f_\nu^F = (1-\varepsilon)f_\nu^B$. As here we will always use $b = 3/4$ (as is appropriate for a classical thin accretion disc), we evaluate Eq. 3.11 and 3.12 for $b = 3/4$ below:

$$\langle \tau \rangle = 0.62 \text{ days} \left(\frac{\lambda}{10^4\text{Å}}\right)^{4/3} \left(\frac{T_B}{10^4\text{K}}\right)^{4/3} \frac{1-\varepsilon^{3/2}}{1-\varepsilon} , \tag{3.13}$$

$$f_\nu^B = 40.1 \text{ Jy} \left(\frac{\tau}{\text{days}}\right)^2 \left(\frac{\lambda}{10^4\text{Å}}\right)^{-3} \left(\frac{D}{\text{Mpc}}\right)^{-2} \cos i \left(\frac{1-\varepsilon}{1-\varepsilon^{3/2}}\right)^2 . \tag{3.14}$$

Therefore, if the bright and faint state fluxes and interband time delays are measured from monitoring observations of an AGN, then the distance to the AGN can be determined. We describe how this model is applied to the Sergeev et al. data below.

3.3.3 Applying this model to the Sergeev et al. data

With interband time delays and long-term monitoring lightcurves for 14 AGN, the Sergeev et al. (2005) data offers an opportunity to test this reprocessing model and to determine distances to a sample of 14 AGN. The first thing to check when applying this model is whether the difference spectra (between the maximum and minimum points on the lightcurves) for these AGN do indeed show $f_\nu \propto \nu^{1/3}$ as expected for a classical thin accretion disc. However, we find that only in one case the difference spectrum has a slope of $\nu^{1/3}$. We attribute the difference in slope as extinction due to dust, with contributions from the Galaxy, of course, as well as internal nuclear reddening within the AGN. Therefore, as part of the model, we include $E(B-V)$ as a free parameter (we discuss this assumption below). The free parameters in the fit to the data are the bright state temperature, T_B, the faint state temperature, T_F, the extinction $E(B-V)$, the distance to the AGN, D, and the host galaxy fluxes in the V, R, R1 and I bands. For a lower limit on the distance (and hence an upper limit on H_0), we set the host galaxy contribution in the B band to zero. Whilst this is clearly an incorrect assumption, without it, a fit would be degenerate since a fainter disc can be offset by a brighter galaxy. Independent measurements of the host galaxy in the bands, would constrain the nuisance parameters to reduce or remove

this degeneracy. In the model we assume that the accretion disc inclination angle, $i = 45°$, as would be expected for type I AGN, where the broad emission lines are visible, from unified AGN theories (J. Krolik and M. Urry, private communication, Antonucci, 1993). However, the affect on the distance determined is small as $D \sim (\cos i)^{1/2}$.

3.3.4   Extinction within the central regions of AGN

Two of the assumptions made when applying this model are that the difference in slope between the difference spectra and a $\nu^{1/3}$ slope is due to extinction, from our own Galaxy and within the central regions of the AGN, and also that the variable component of the AGN spectra does not change shape between the bright and the faint state. To test these assumptions, we use the flux variation gradient method of Winkler et al. (1992) and Winkler (1997). In this method, when comparing the flux through one filter with the flux through another filter at corresponding times, a very strong linear relationship is seen. We show a couple of examples of 'flux-flux' diagrams in Fig. 3.6 from the Sergeev et al. data. Firstly, as the relationship is so close to linear, it demonstrates that the variable component has a constant flux distribution, thereby confirming our assumption that this is the case. If the spectrum did, in fact, change shape, the relationship in the flux-flux diagram would curve rather than be linear.

The slopes of the best-fit lines give the ratios of the variable component of the fluxes and hence the SED of the inner nucleus, as viewed from outside that galaxy. Of course, the intrinsic SED of this region will differ due to extinction from dust in the outer parts of the nucleus. Assuming some standard colours for the nuclear SED, the extinction can then be calculated by comparison of the standard colours with the colours determined from the flux-flux diagrams. Initially, we correct for the extinction in our Galaxy, $E(B - V)_g$, using values from Schlegel, Finkbeiner & Davis (1998). Next, we correct for extinction within the nucleus of the AGN. Assuming that the intrinsic SED for the nuclear region of an AGN follows $f_\nu \propto \nu^{1/3}$ in the optical, as expected for a classical thin accretion disc, we adjust the nuclear extinction, $E(B - V)_n$, so that the reddened model matches the observations.

This, of course, is assuming that the difference between the spectra of the variable components and a $\nu^{1/3}$ spectrum is due to extinction. As an independent check of the values we get from the flux variation gradient method, we also use the Balmer decrement
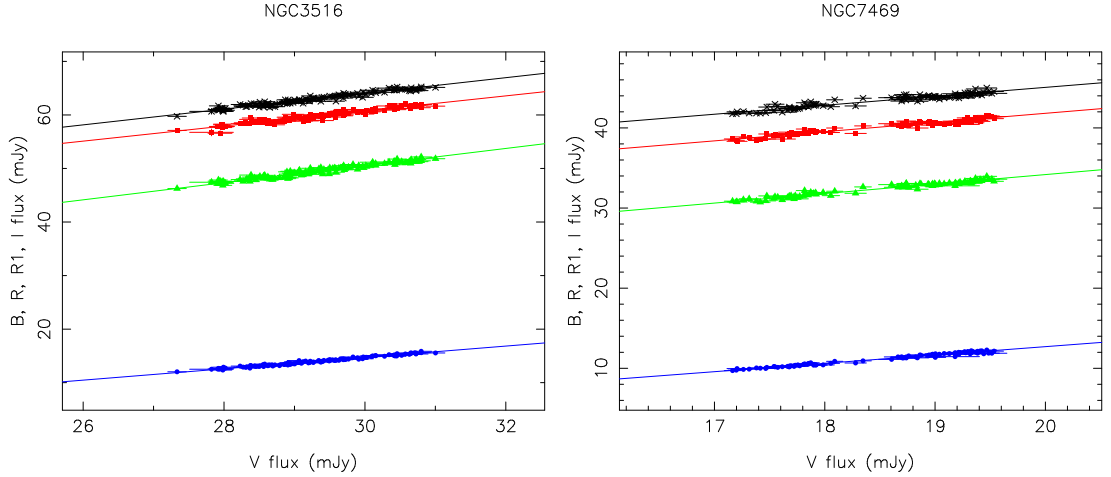
Figure 3.6: Flux-flux diagrams for NGC 3516 (left) and NGC 7469 (right). B (blue, circles), R (green, triangles), R1 (red, squares) and I (black, crosses) flux is plotted against V flux at corresponding times. The best straight line fits are also shown.

method (e.g. Reynolds et al., 1997). As extinction by cosmic dust is highly wavelength dependent it can change observed line flux ratios significantly away from intrinsic values. In this method, the observed Hα to Hβ broad line ratio is compared with an assumed intrinsic ratio, which we take to be 3.1 (Gaskell & Ferland, 1984) with the difference between the two determining the extinction required.

Using these two methods the nuclear extinction has been calculated for these objects by Hartmut Winkler (private communication), and the results are presented in Table 3.4. A comparison of the reddening determined using these two methods is shown in Fig. 3.7. Whilst the nuclear extinctions determined by these two methods do not agree exactly (this could be due to difficulties isolating just the broad component of the Hα and Hβ lines), they both show that generally there is significantly more nuclear extinction than galactic extinction. Additionally, those AGN with higher nuclear extinction from one method also have high nuclear extinction from the other, and similarly for low values (see Fig. 3.7). This confirms that there is significant extinction in the central regions of these AGN that needs to be accounted for in our models.

Table 3.4: Nuclear extinction, $E(B - V)_n$, determined by the flux-flux and Balmer decrement methods, as well as the extinction due to our own Galaxy, $E(B - V)_g$. The total extinction is just the sum of both components.

Object	$E(B - V)_g$	$E(B - V)_n$ (flux-flux)	$E(B - V)_n$ (Balmer decrement)
1E 0754.6+3928	0.066	0.00	0.04
Akn 120	0.128	0.00	0.04
MCG+8-11-11	0.217	0.13	0.34
Mrk 335	0.035	0.07	0.00
Mrk 509	0.057	0.00	0.11
Mrk 6	0.136	0.28	0.48
Mrk 79	0.071	0.09	0.20
NGC 3227	0.023	0.26	0.31
NGC 3516	0.042	0.16	0.15
NGC 4051	0.013	0.17	0.21
NGC 4151	0.028	0.15	0.04
NGC 5548	0.020	0.16	0.28
NGC 7469	0.069	0.04	0.09
3C 390.3	0.071	0.14	0.26
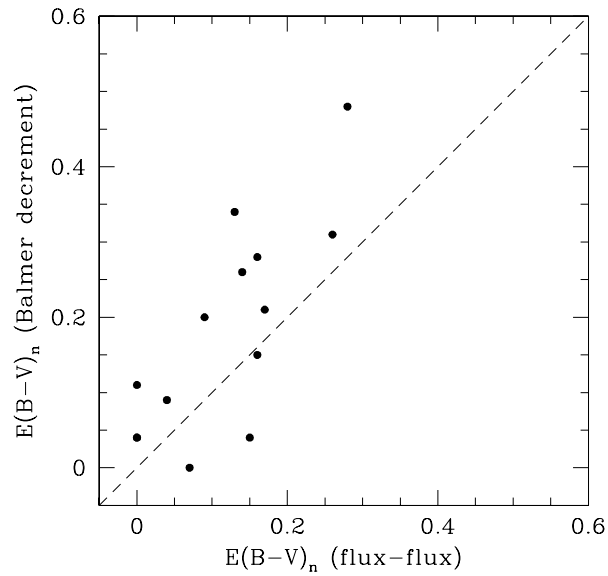
Figure 3.7: Comparison of $E(B - V)_n$ determined by the flux-flux and Balmer decrement methods. The dashed line indicates a one-to-one relationship.
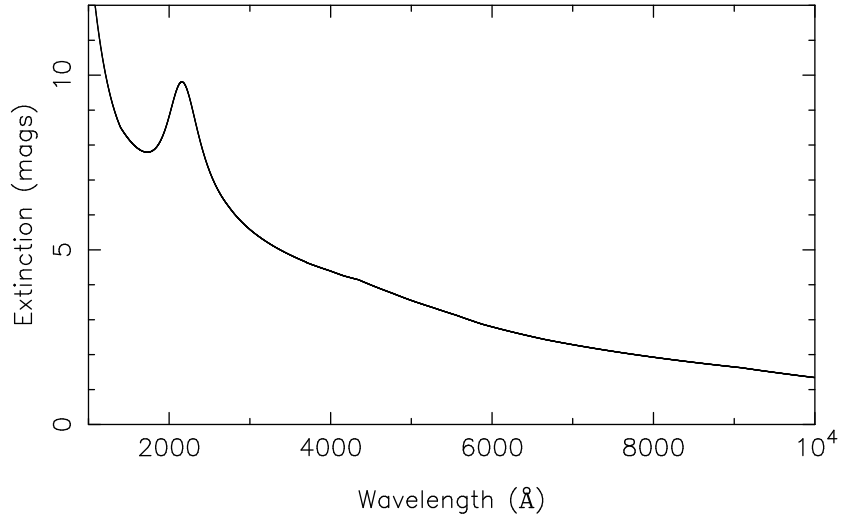
Figure 3.8: The adopted extinction law of Nandy et al. (1975) and Seaton (1979) evaluated at $E(B - V) = 1.0$.

3.4 Results

We use the model described in the previous section to fit the data from all 14 AGN from the Sergeev et al. sample. Specifically, we fit the model to the time-delays, and the maximum and minimum SED by minimising χ^2 using a downhill simplex (the 'amoeba' from Numerical Recipes in Fortran, Press et al., 1992) to determine the best-fitting non-linear parameters, whilst optimising the linear parameters using optimal scaling. For the time-delays we adopt the peak of the CCF rather than the centroid. The peak time-delays are generally smaller than the centroid delays (see Fig. 3.4 for a comparison) and therefore gives a lower measurement of the distance. We adopt the combined extinction law of Nandy et al. (1975) and Seaton (1979), shown in Fig. 3.8. Whilst the nuclear reddening curve for AGN is seen to be different to this in the UV (where we are not concerned about here), the optical is very similar (Gaskell et al., 2004).

To determine the uncertainties in each of the fit parameters, we hold the parameter of interest fixed at a range of values either side of the best-fit value. At each fixed value, the other parameters are optimised and the χ^2 value determined. The range of values is chosen so that it covers $\Delta\chi^2 = 1.0$. A parabola is then fit to the points, and forced to be a minimum (and hence have zero gradient) at the best-fit value. From the parabola 1-σ errors are determined from where $\Delta\chi^2 = 1.0$. An example of this is shown in Fig. 3.9.
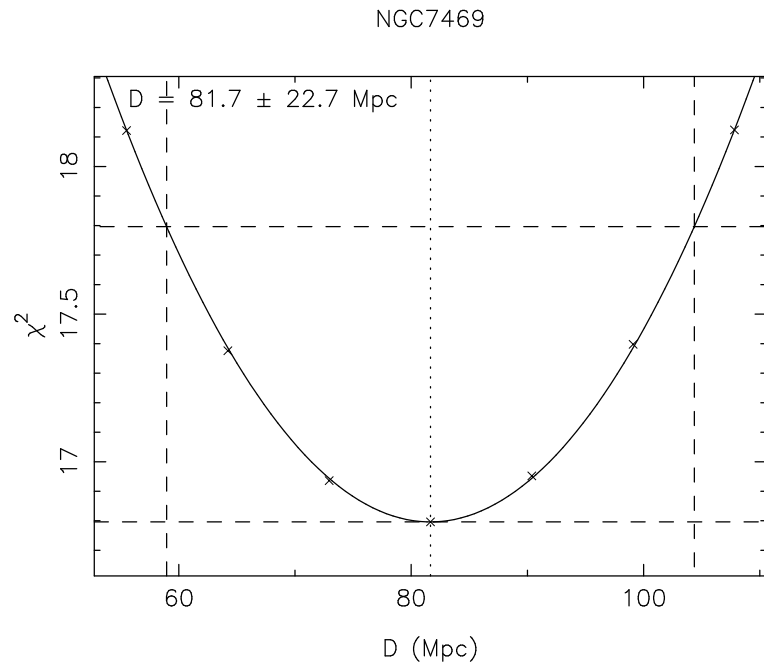
NGC7469

Figure 3.9: χ^2 error parabola for the distance to NGC 7469. Solid line is the best-fit parabola to the χ^2 values determined at a range of distances either side of the best-fit distance. The dotted line indicates the location of the best-fit distance. Dashed horizontal lines indicate χ^2_{min} and $\chi^2_{min} + 1$. Dashed vertical lines indicate 1-σ errors in the distance, i.e., the distances that correspond to $\chi^2_{min} + 1$.

We present the best-fitting models for each of the AGN in Fig. 3.10, and the best-fitting parameters in Table 3.5. Note that the extinction values are close to those determined by the two other methods (see Fig. 3.11 for a comparison). In several cases there are deviations of the difference spectrum from the best-fit model resulting in high values of reduced χ^2. This could likely be due to contributions from broad emission lines. For instance, Hα lies in the R-band, and various Balmer lines and Fe II features lie in the B-band (see Fig. 3.12). The R-band does sometimes appear higher than the model fit, particularly in cases where the χ^2 is high, as would be expected from contributions by Hα.

To check whether the determined galaxy spectra are realistic, we plot the galaxy spectra dereddened for galactic interstellar extinction, all normalised to the I band flux in Fig. 3.13. We do not deredden for the nuclear extinction that we have determined, as this reddening is expected to be due to dust in the nuclear region and not the galaxy as a whole. Additionally, we plot the galaxy spectrum for a Sab galaxy (as expected for a Seyfert) using the intrinsic galaxy colours of Fukugita et al. (1995). Whilst the majority of galaxy fluxes match the model galaxy in the V and R1 bands, all of the galaxies have a higher flux than the model in the R band. We suggest that this is likely due to strong narrow Hα from the narrow line region of the AGN that falls within this band (see Fig. 3.12), making the R band galaxy flux higher than for a typical Sab galaxy. To check this we load the spectrum of 3C 390.3 shown in Fig. 3.12 into the synthetic photometry package XCAL, and calculate the predicted flux in the R band. We then subtract the Hα line from this spectrum and calculate the predicted flux in the R band once again. We find a factor of 1.3 difference between the 2 spectra. Comparing the 3C 390.3 R band galaxy flux that we determine with that expected for an Sab galaxy we find a factor of 1.5 different. Given that the Sab galaxy model is not going to perfectly match the actual galaxy spectrum of 3C 390.3, it seems reasonable that the observed difference could be due to Hα.

There is one galaxy spectrum, 1E 0754.6+3928, that is significantly different from all the others. In particular, the R1 flux is much higher than the other galaxies. This object has the highest redshift of the sample, with $z = 0.096$. The Hα line will have therefore shifted from an emitted wavelength of 6563 Å to 7193 Å, and into the R1 filter. Note that the next highest redshift object in the sample is 3C 390.3, at $z = 0.056$, not high enough to shift the line significantly into the R1 band (see Fig. 3.12).
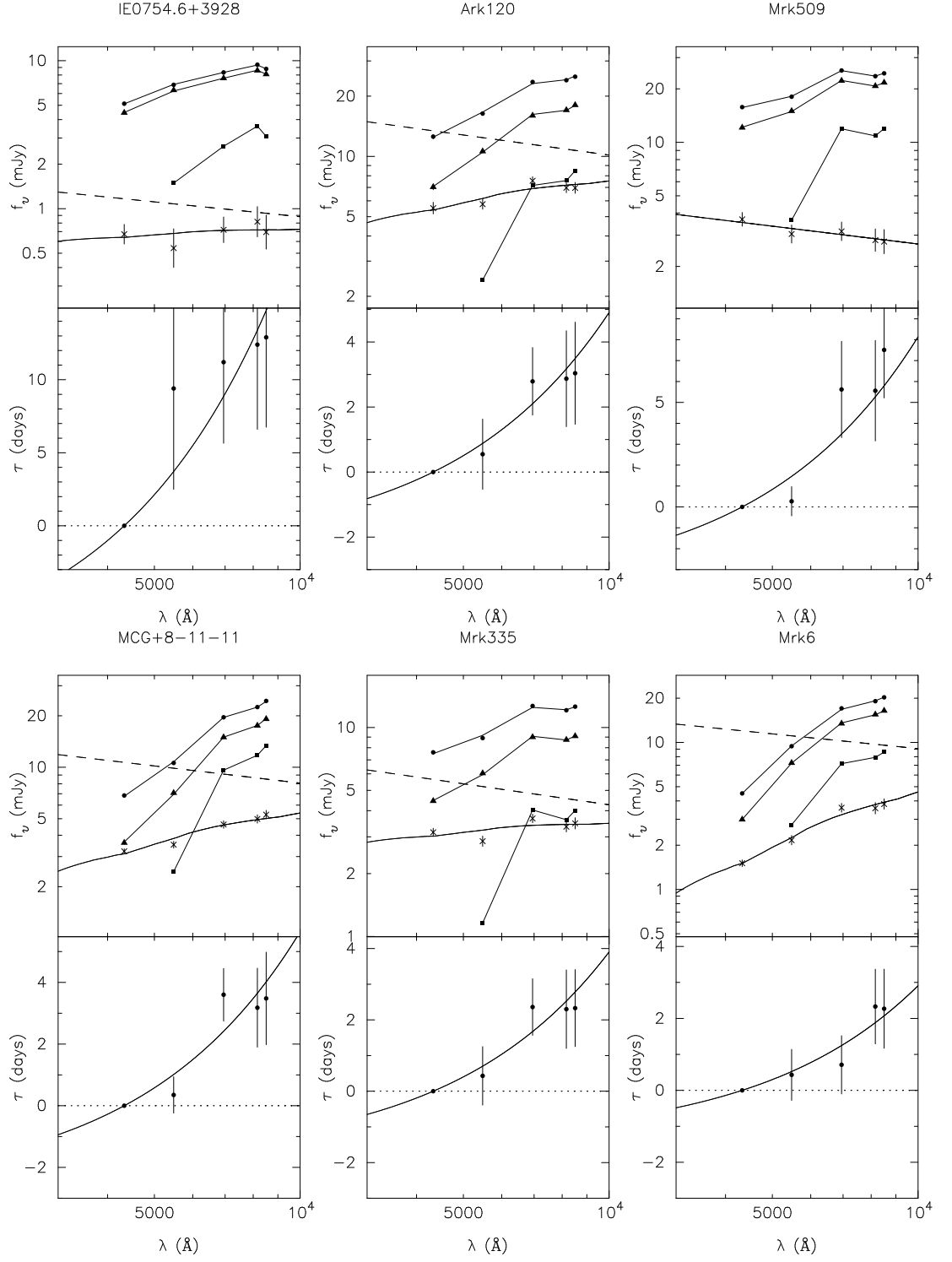
Figure 3.10: Reprocessing model fits for all 14 AGN. Each double panel (described next) shows the fit for one AGN. *Top:* Maximum (circles) and minimum (triangles) spectra, with best-fitting model. Difference spectrum (crosses), with reddened accretion disc model. De-reddened disk model is given by the dashed line. Squares indicate best-fit galaxy fluxes. *Bottom:* Time-delay distribution with best fit model. Time-delays relative to B-band, and determined from the peak of the CCF. Figures continued on the next page.

Figure 3.10 (continued)

92

NGC7469

3C390.3
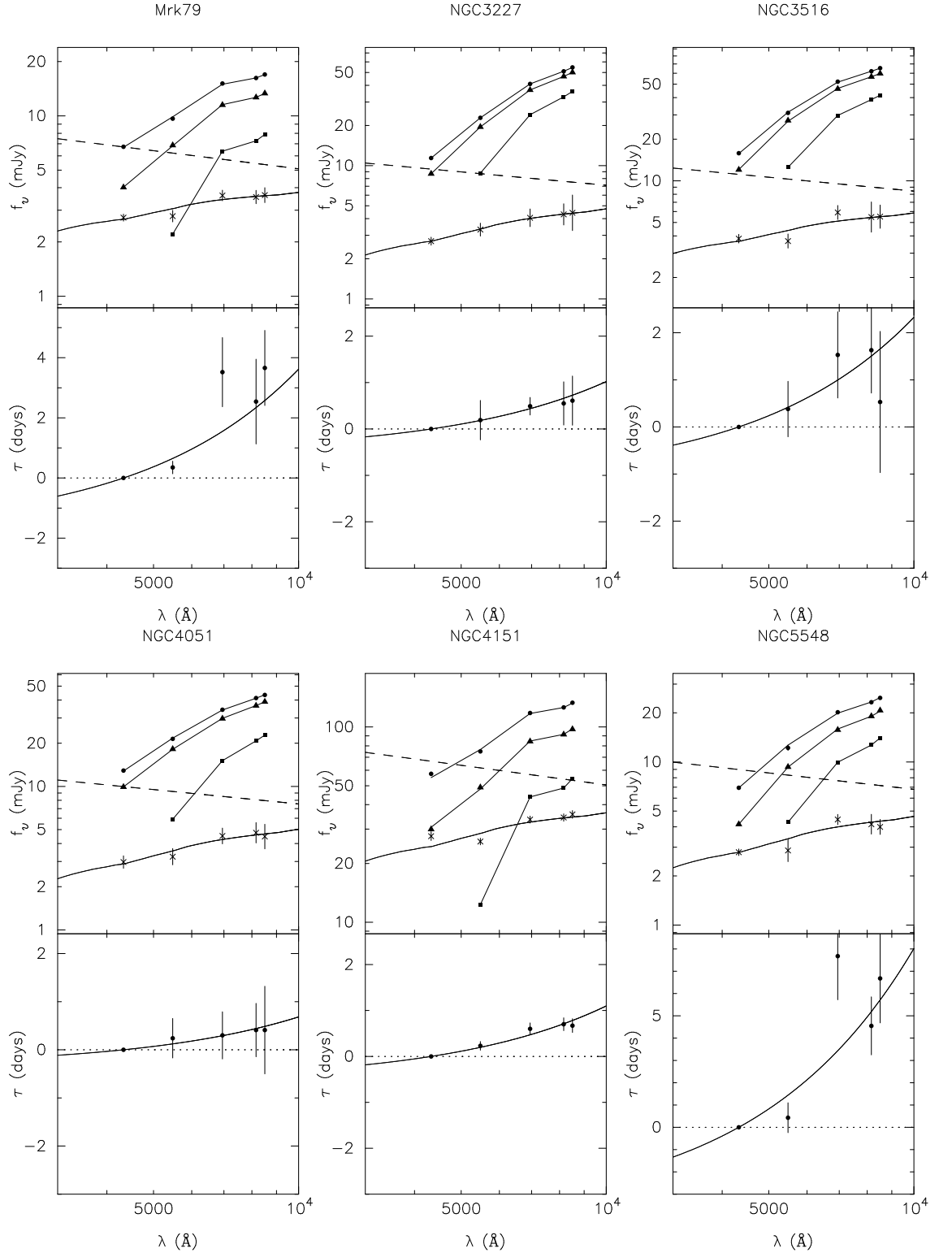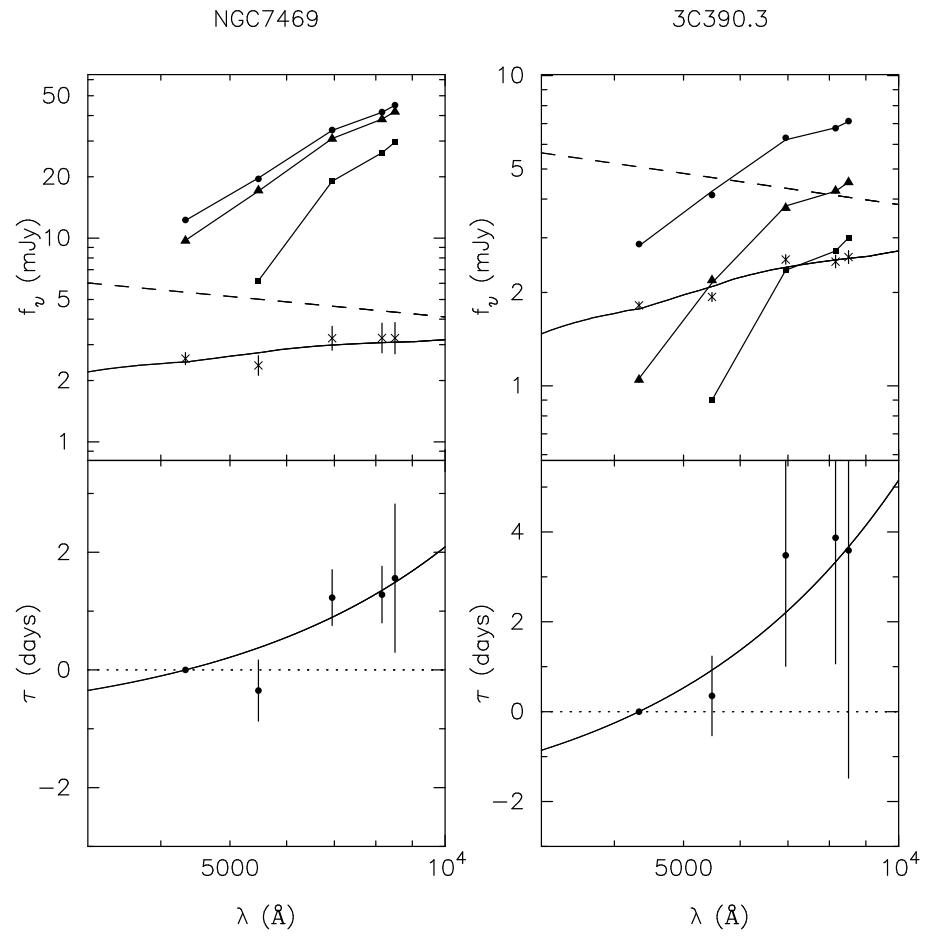
Figure 3.10 (continued)

Table 3.5: Best-fitting parameters from reprocessing model. $M\dot{M}$ is calculated using the faint state temperature. This gives a maximum value for this product, as the temperature in the faint state will not entirely be due to viscous heating and there will be some contribution from irradiation.

Object	D (Mpc)	cz/D (km s^{-1} Mpc^{-1})	$E(B-V)$	T_F (K)	T_B (K)	$M\dot{M}$ (10^7 M$_\odot^2$ yr^{-1})	χ^2_ν
1E 0754.6+3928	1345. ± 372.	21.4 ± 5.9	0.16 ± 0.04	54449. ± 10951.	57253. ± 10920.	870	1.1
Akn 120	192. ± 51.	50.5 ± 13.4	0.24 ± 0.01	16857. ± 3345.	20848. ± 4136.	8.0	5.0
MCG+8-11-11	257. ± 50.	23.9 ± 4.6	0.32 ± 0.01	18499. ± 2711.	23309. ± 3416.	12.	5.3
Mrk 335	225. ± 55.	34.4 ± 8.4	0.16 ± 0.01	14372. ± 2612.	17438. ± 3167.	4.2	7.8
Mrk 509	419. ± 99.	24.6 ± 5.8	0.00 + 0.01	26386. ± 4691.	29035. ± 5162.	48.	1.4
Mrk 6	102. ± 33.	55.3 ± 17.9	0.54 ± 0.01	11809. ± 2844.	13758. ± 3313.	1.9	2.9
Mrk 79	190. ± 45.	35.1 ± 8.3	0.24 ± 0.01	13600. ± 2375.	16458. ± 2875.	3.3	3.3
NGC 3227	33. ± 11.	35.5 ± 11.8	0.33 ± 0.03	5543. ± 1359.	6137. ± 1505.	0.09	0.1
NGC 3516	69. ± 29.	38.3 ± 16.1	0.29 ± 0.03	10298. ± 3255.	11371. ± 3593.	11.	4.0
NGC 4051	21. ± 18.	32.9 ± 28.2	0.32 ± 0.03	4114. ± 2718.	4526. ± 2926.	0.03	0.8
NGC 4151	20. ± 2.	49.5 ± 5.0	0.26 ± 0.01	5464. ± 489.	6806. ± 609.	0.09	11.5
NGC 5548	365. ± 66.	14.1 ± 2.5	0.31 ± 0.02	24674. ± 3281.	29916. ± 3978.	36.	4.6
NGC 7469	82. ± 23.	59.6 ± 16.7	0.21 ± 0.03	9579. ± 1963.	10424. ± 2136.	0.8	2.8
3C 390.3	423. ± 216.	39.8 ± 20.3	0.27 ± 0.01	15778. ± 6064.	22825. ± 8766.	6.1	8.5

3.4.1 The Hubble Constant

Having measured distances to the 14 AGN using the continuum reverberation method detailed above, we are now in a position to measure Hubble's constant, H_0. Assuming a cosmological constant form for Ω_Λ, in the Friedmann-Robertson-Walker metric, the luminosity distance is determined by:

$$D_L = \frac{c}{H_0}(1+z)|\Omega_k|^{-1/2}S_k \left\{ |\Omega_k|^{1/2} \int_0^z dz' \left[(1+z')^2(1-\Omega_M z') - z'(2+z')\Omega_\Lambda \right]^{-1/2} \right\} , \tag{3.15}$$

where $\Omega_k = 1 - \Omega_M - \Omega_\Lambda$ and S_k is sinh for $\Omega_k > 0$ and sin for $\Omega_k < 0$, for $\Omega_k = 0$, Eq. 3.15 reverts to $cH_0^{-1}(1+z)$ times the integral (Carroll et al., 1992). We assume the current standard cosmology with $\Omega_M = 0.3$ and $\Omega_\Lambda = 0.7$ when fitting this model. As there is quite a large scatter in the distances (see Fig. 3.14), we also include a fractional systematic error, f_0, as a parameter in the fit to account for this intrinsic scatter. The uncertainty on a single distance measurement, D, is then given by $\sigma_i^2(D) = \sigma_D^2 + f_0^2 D^2$, where σ_D^2 is the measurement uncertainty on the distance from the fit. One cannot minimise χ^2 when including such a term in the fit as continuing to increase f_0 will continue to decrease χ^2 with no end. Instead we maximise the likelihood, which is equivalent to minimising $-2\ln L$, which includes a penalty for expanding the error bars:

$$-2\ln L = \chi^2 + 2\sum_{i=1}^{N} \ln(\sigma_i) + \text{const} , \tag{3.16}$$

where there are N data points, and $L \sim \exp(-\chi^2/2)/(\prod_i \sqrt{2\pi}\sigma_i)$. The resulting fit is shown in Fig. 3.14. We find, $H_0 = 42.3 \pm 5.0$ km s^{-1} Mpc^{-1} and $f_0 = 0.29$, with a reduced $\chi^2 = 0.93$. The implications of this result are discussed in the next section.

3.5 Discussion

Whilst the time-delay distributions are consistent with reprocessing in a disc, and fluxes and difference spectra can be fit by such a model (provided an estimate for the nuclear dust extinction is used), the distances determined using this method lead to a significantly smaller value of H_0 (by a factor of ~ 1.7) than determined by other methods - those that rely on the distance ladder e.g., the *HST* Key Project $H_0 = 72 \pm 8$ km s^{-1} Mpc^{-1} (Freedman et al., 2001), and other direct methods such as gravitational lensing time delays and the Sunyaev-Zeldovich effect (see Chp. 1 for more details of these methods).
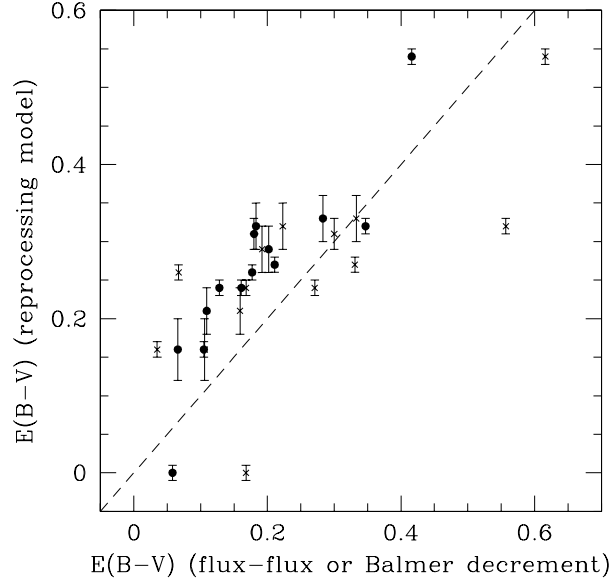
Figure 3.11: A comparison of the total E(B-V) values determined via the reprocessing model and the flux-flux and Balmer decrement methods. Circles indicate points determined by the flux-flux method, and crosses indicate those determined by the Balmer decrement method. Dashed line indicates a one-to-one relationship.
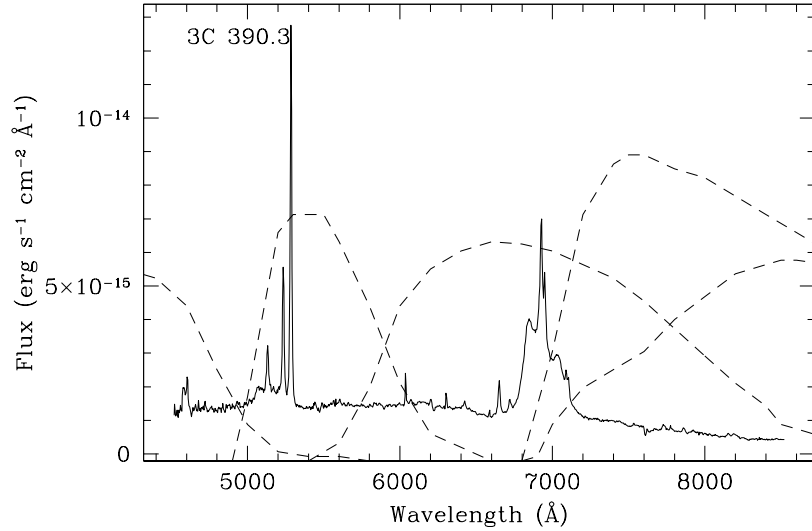
Figure 3.12: Optical spectrum of 3C 390.3, with the filter passbands shown (dashed line). The filters (from left to right) are the Crimean B, V, R, R1 and I. Note that Hα sits in the R-band. 3C 390.3 is the object with the second highest redshift in our sample ($z = 0.056$). Hence, in all other objects (expect 1E 0754.6+3928, which has $z = 0.096$), the Hα line will be closer to its emitted wavelength of 6563 Å.
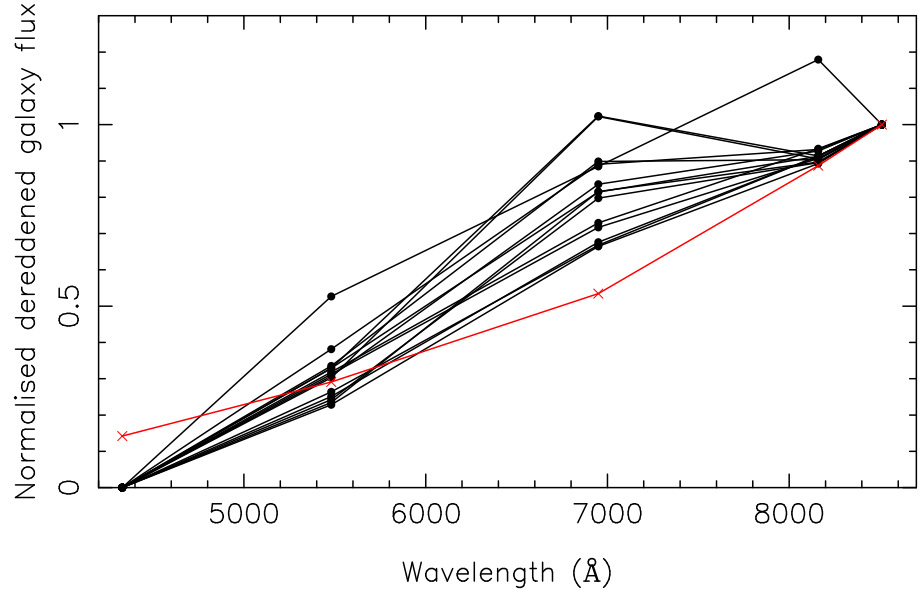
Figure 3.13: Dereddened galaxy spectra normalised to the I band (circles). Note the B-band galaxy flux is forced to be zero in the fit. The red crosses show the galaxy spectrum for an Sab galaxy using the intrinsic galaxy colours of Fukugita et al. (1995).
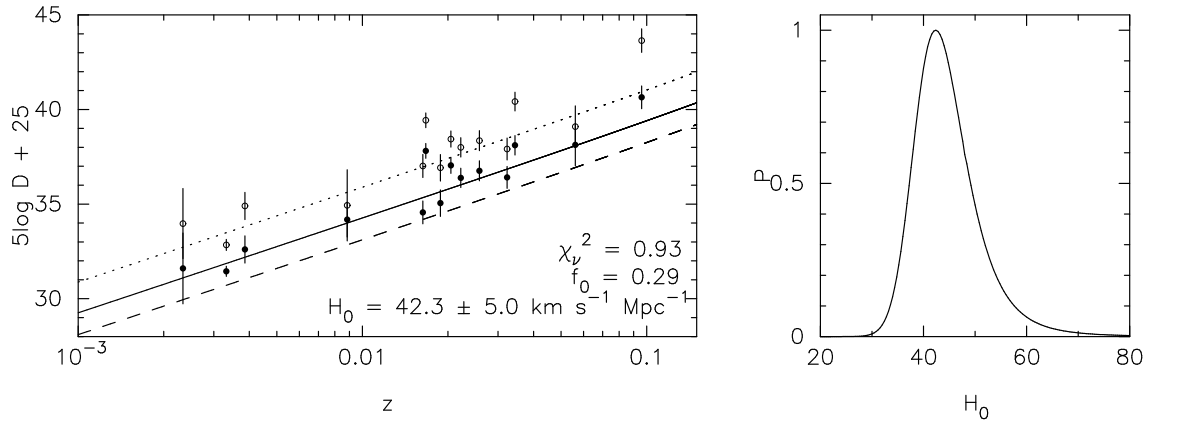
Figure 3.14: *Left:* Hubble diagram for 14 AGN from the Sergeev et al. sample. Distance modulus is plotted vs redshift. The solid line is the best-fitting model (fit to the filled circles), where as the dashed line indicates $H_0 = 72$ km s^{-1} Mpc^{-1}. The filled circles are for the distances determined when the B-band galaxy flux is $= 0$, and the open circles are for when the B-band galaxy is set to the maximum possible. The dotted line is the best-fit to the open circles. *Right:* Probability distribution for H_0.

All the observational evidence currently points towards a value of H_0 that is around 70 km s^{-1} Mpc^{-1}. As both direct methods and distance ladder methods both point to values of H_0 much greater than what we find, we interpret our result in terms of what this large difference in H_0 implies for the simple disc reprocessing model we have assumed. We note that it is not possible to fit the data assuming that $H_0 = 72$ km s^{-1} Mpc^{-1} as whilst the difference spectrum could still be matched, the disc fluxes would have to be greater than the observed flux from the entire nucleus.

One suggestion for the difference is that the lags measured via cross-correlation are biased to high values, hence giving low distances. As the cross-correlation function (CCF) is the convolution of the delay map with the auto-correlation function (ACF), changes in the driving lightcurve properties (i.e. in the ACF), can lead to a different CCF, and hence a different lag, without changing the delay map. If this is the case, one might expect to see a correlation between the residuals of the Hubble-diagram fit and the full-width half maximum of the ACF, however, none were found (see Fig. 3.15).

Another possible suggestion for the difference is that this systematic shift is because the irradiating source does not illuminate the entire disc. If this is the case, then the solid angle over which the reprocessed optical emission is coming from at each annulus in the disc, will be less than $2\pi R \, \mathrm{d}R \, \cos i$ and hence the distances will be closer than determined and H_0 would be greater. We briefly consider several possible causes of this. Firstly, the irradiating source may be anisotropic, only illuminating specific parts of the disc. Secondly, the surface of the disc may not be flat enough. For instance, if the surface was bumpy, one can imagine that only the front side of the bump would be illuminated and that large bumps would actually place some of the disc in shadow. For there to be a factor of ~ 2 increase in H_0, there would need to be a factor of 4 increase in the actual disc flux (as $f_\nu \propto D^{-2}$ and $H_0 \propto 1/D$). Therefore one quarter of the disc would need to be illuminated, and the remaining three quarters not for the true disc flux to be four times larger than that observed. In the lamppost model for disc illumination (e.g., Collin et al., 2003) this would be hard to achieve as in this model the irradiating source is high above the central black hole and illuminates it in all directions. Any bumps in the surface of the disc are not expected to be a significant proportion of the thickness of the disc (Mayer, M., private communication) and so could not cause the required level of shadowing. However, if the illumination of the disc was more localised, for instance due to magnetic flares in the disc corona just above the disc surface (e.g., Collin et al., 2003) then, it is easier to picture

that only a small amount of the disc is irradiated.

It is important to consider whether the determined dust attenuation is reasonable and whether additional extinction can be used to explain an increased true flux. As extinction is wavelength-dependent, increasing its magnitude would also cause a change in shape of the spectral energy distribution, therefore only if the true extinction curve differed from the one used could more extinction be allowed. However, as we note below, if the dust extinction curve is significantly different from the one that was used, correlations between the residuals of the model fit and the $E(B-V)$ value determined would likely be seen, and they are not. Additionally, a recent study of the nuclear reddening curve for AGN (Gaskell et al., 2004) find a curve that is similar to previously used models in the optical (such as the one we adopt), although it differs significantly in UV (which would not affect our analysis). The typical $E(B-V)$ values that they find for AGN are in the same range as our values.

Alternatively, it could be that the geometry and emission from AGN accretion discs could turn out to be significantly more complicated than the simple reprocessing model we have assumed. One possibility is that in some objects reprocessing is not the cause of the observed variability. For instance, Uttley et al. (2003) find that the amplitude of the long-term variability in NGC 5548 is larger than that of the X-ray variability, implying that X-ray reprocessing is not the dominant source of the continuum variability. These authors note that as NGC 5548 is a relatively high mass, low accretion rate Seyfert 1 it will have an optical emitting region that is closer to the black hole (in terms of Schwarzschild radii, R_S) than in more typical Seyferts with lower masses and higher accretion rates. They find that 50% of the 5100Å emission is contained within 42 R_S of the black hole and that the thermal timescale at this radius is ∼280 days which is consistent with the timescales of variability in this object. Therefore it is conceivable that something like sound wave propagations in the upper layer of the accretion disc could account for the long-term variability, at least in the high-mass, low accretion rate objects like NGC 5548. However, it is not obvious how such a model could explain the origin of the observed time delays, as with inward propagating sound waves one would see the cooler outer part of the disc vary before the hotter inner parts, the opposite direction than needed.

Observationally, what can be done to understand AGN accretion discs more is to have high-cadence (at least once a night), long-term (several months) monitoring to deter-

mine the wavelength-dependent time delays with significantly higher accuracy. The errors in the distances we have determined here are dominated by the errors in the time-delay measurements. Additionally, a high-fidelity velocity delay map of an AGN broad-line region would make a significant step towards understanding the innermost regions of AGN, and with possible implications for AGN accretion discs.

The large scatter in the distances around the best-fitting cosmological model is also a concern. An extreme example of this are the two objects, NGC 7469 and NGC 5548, that have almost identical redshifts - in the Hubble diagram they are separated by approximately 3 magnitudes in the distance modulus. Whilst some of the scatter seen is likely due to the fact that we have adopted an inclination angle of $i = 45°$ for all objects (as might be expected for a type I AGN), this affect is only small - the distance goes like $(\cos i)^{1/2}$. According to unified AGN schemes (e.g. Antonucci, 1993), for type I objects where we see the broad-emission line region, $i < 60°$ and so $0.707 \leq (\cos i)^{1/2} \leq 1$. Thus, whilst the inclination does cause scatter, it cannot account for the large difference between NGC 7469 and NGC 5548. Comparing the lightcurves, ACF and CCFs for these two objects (Figs. 3.2 and 3.3), it is seen that NGC 5548 is more slowly varying, and hence has a broader ACF, suggesting that maybe a difference between the two objects could be due to biased time delay measurements. However, as noted above, no correlations are seen between the residuals and the ACF FWHM over the 14 objects as a whole (see Fig. 3.15).

To investigate further possible causes of this scatter, correlations between the residuals of the fit and various AGN properties and parameters of the fit were looked for. For instance, if the nuclear dust is significantly different to the extinction law that we have adopted, correlations of the residuals with $E(B - V)$ might be expected. Correlations with the mass, luminosity, fraction of Eddington luminosity, $E(B - V)$, ACF width, and fractional contribution of the galaxy to the minimum flux in the V were looked for, but none were found (see Fig. 3.15). Here we use the reverberation mapping masses for these objects determined by Peterson (2004). One possible explanation for the residuals could be due to the fact that we fix the galaxy in the B-band to be zero, in our method we have no way of determining this. This is clearly an incorrect assumption, and better constraints on the galaxy contribution may significantly improve matters.

To check the possible range in distance if the B-band galaxy flux is allowed to be non-zero (which it clearly will be), we also fit the disc reprocessing model when allowing
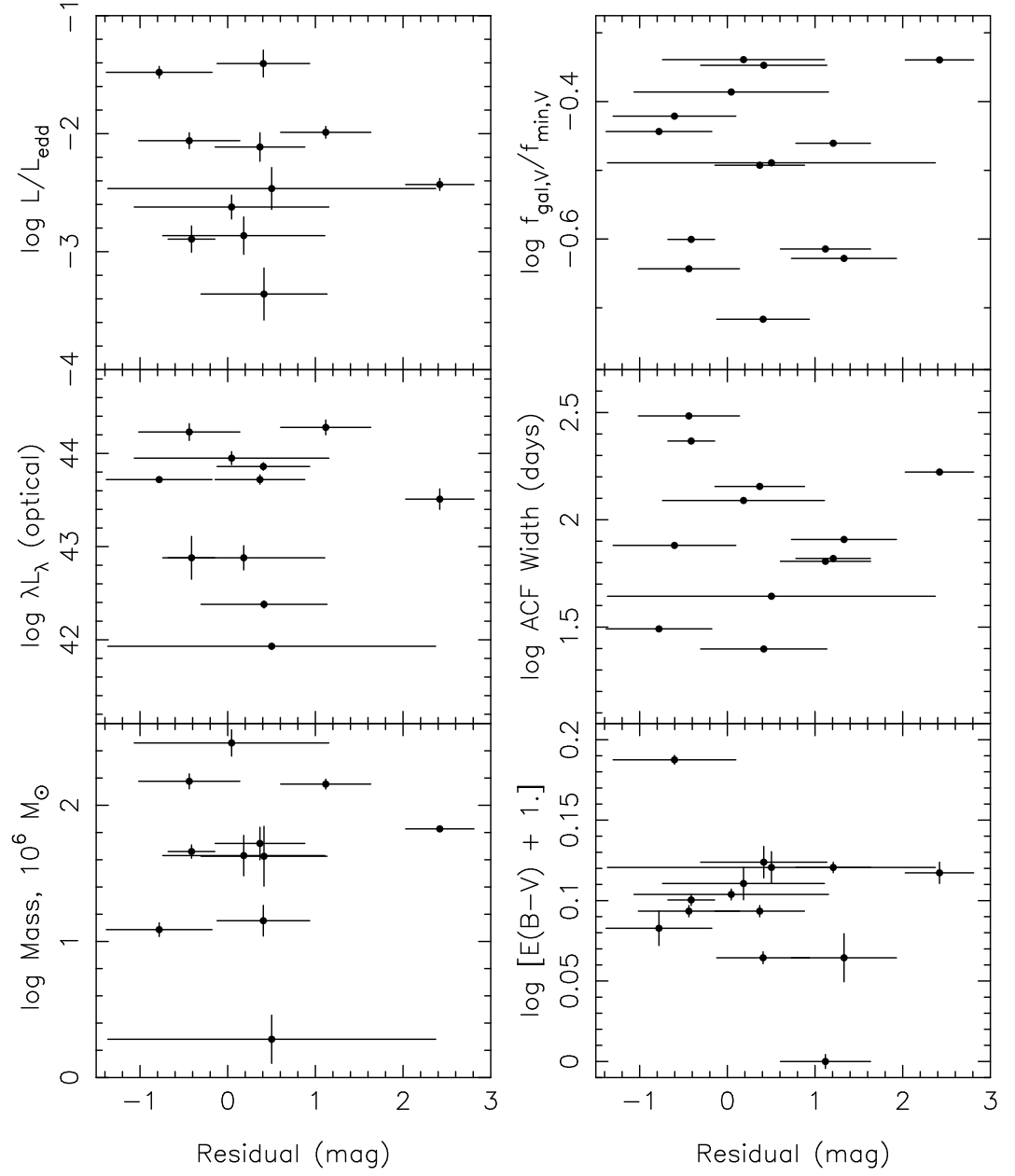
Figure 3.15: The residuals of the Hubble diagram fit are compared with various AGN properties and parameters of the fit.

the B-band galaxy flux to be the maximum possible value, i.e., equal to the minimum flux from the lightcurve. Such a fit gives the maximum distance (and hence the minimum H_0) possible. Fitting to these distances gives $H_0 = 20.0 \pm 2.0$ km s^{-1} Mpc^{-1}. The distances and best-fitting model are shown in Fig. 3.14, as open circles and the dotted line, respectively. This indicates that the possible range in H_0 if a reasonable B-band galaxy flux is determined for each galaxy will be between 20.0 and 42.0 km s^{-1} Mpc^{-1}. In any case, our conclusions still stand that too small a value of H_0 is determined by this model.

3.5.1   Possible cosmological probe?

A systematic shift in the distance determination that is apparent in this analysis is not necessarily a problem when wanting to determine cosmological parameters other than H_0. For Ω_M and Ω_Λ, it is the *shape* of the redshift-distance relationship that matters. It is therefore possible that even without understanding this offset, this method can be used as a cosmological probe provided that the systematic shift is redshift, and luminosity, independent. As mentioned earlier, AGN are numerous throughout the Universe, out to extremely high redshift. As they are intrinsically extremely luminous objects, accurate photometry can be obtained out to redshifts far greater than supernovae type Ia can be observed. It is this that could allow similar accuracy in Ω_M and Ω_Λ from significantly less objects. More luminous AGN will need to be observed at greater redshifts, however, and although more luminous quasars are known to be less variable, quasar variability increases toward the blue part of the spectrum (Vanden Berk et al., 2004). From studies of 25,000 quasars in the Sloan Digital Sky Survey, Vanden Berk et al. (2004) also find a positive correlation of variability amplitude with redshift. The redshift will move the observable region of the spectrum into the UV (in the emitted-frame), which is more variable, and likely has less galaxy contamination, however the time-delays there will be shorter. Counteracting this is time-dilation effects, which mean the observed time-delay will be longer than the emitted time-delay.

To explore possible constraints on Ω_M and Ω_Λ through monitoring programs, we simulate the distances to a sample of AGN. With the current dataset we have around 25% errors in the distance, but the monitoring was only once every 2-3 days, improved temporal sampling should significantly improve the accuracy of the time-delay measured, and hence

the distance determined. We therefore assume that the distances can be measured to 15% accuracy, which is by no means impossible given high-cadence monitoring with a suite of robotic telescopes across the globe. As a sample we choose the 14 AGN in this work, as well as the 30 variability discovered AGN from the QUEST1 survey (Quasar Equatorial Survey Team, Phase 1, Rengstorf et al., 2004). This provides known variable AGN over a range of redshifts. In the simulation, we determine the distances from the redshift, assuming $\Omega_M = 0.3$, $\Omega_\Lambda = 0.7$ and $H_0 = 72$ km s^{-1} Mpc^{-1}. We add a random Gaussian-distributed error to each of the points, with a mean of 0.0, and 1-$\sigma = 15\%$. We then fit Eq 3.15 by minimizing χ^2.

The results of this simulation are shown in Fig. 3.16, and the supernovae 1a results, using data from Riess et al. (2004) are shown in Fig. 3.17 for comparison. For each value of Ω_M and Ω_Λ optimal scaling is used to determine the best value of H_0. The best-fitting model for a flat Universe ($\Omega_{tot} = \Omega_M + \Omega_\Lambda = 1.0$) is indicated in each figure. The probability distribution for H_0 in these figures is determined for a flat Universe and also when there is no constraint on Ω_{tot}. In the case of assuming a flat Universe, for each value of H_0 the best-fitting model and the probability are determined - the only free parameter is Ω_M, as the condition that $\Omega_{tot} = 1.0$ determines Ω_Λ. Clearly, the input model is retrieved from the simulations, showing that this method has potential as a cosmological probe, if the systematics can be understood, or are redshift independent.

3.6   Conclusions

We have fitted the wavelength-dependent time-delays and optical SEDs of 14 AGN using a disc reprocessing model, which has allowed a measure of the nuclear reddening in these AGN, as well as a measurement of the distances to the AGN. However, the distances calculated using this method imply $H_0 = 42.3 \pm 5.0$ km s^{-1} Mpc^{-1}, a factor of 1.7 less than the value that all other methods seem to be pointing to. One possible suggestion for the difference is that this systematic shift is because the irradiating source does not illuminate the entire disc. If this is the case, then the solid angle over which the reprocessed optical emission is coming from at each annulus in the disc, will be less than $2\pi R \, \mathrm{d}R \, \cos i$ and hence the distances will be closer than determined and H_0 would be greater. Even with a systematic shift, it may be possible to use this method to probe Ω_M and Ω_Λ, as
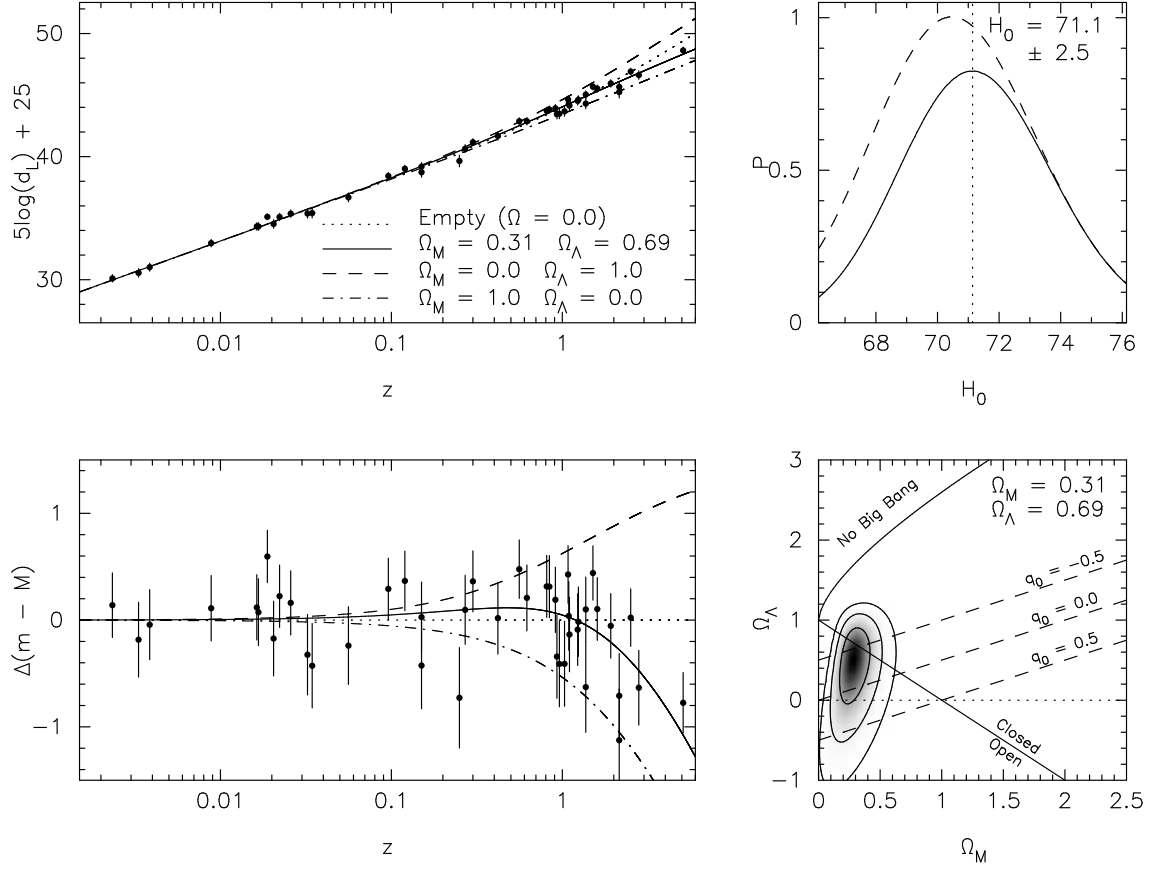
Figure 3.16: Simulation of constraints on H_0, Ω_M and Ω_Λ from 44 AGN. *Top left:* Distance modulus vs. redshift for the 44 AGN. Various cosmological models are shown, with the solid line indicating the best-fitting flat cosmology. *Bottom left:* Magnitude difference between the distance modulus and an empty Universe. *Top right:* Probability distribution for H_0. The solid line indicates the probability distribution when a flat cosmology is assumed, and the dashed line shows the distribution with no constraint on Ω_{tot}.*Bottom right:* Probability distribution for Ω_M and Ω_Λ. Contours indicate 1, 2 and 3-σ confidence limits.
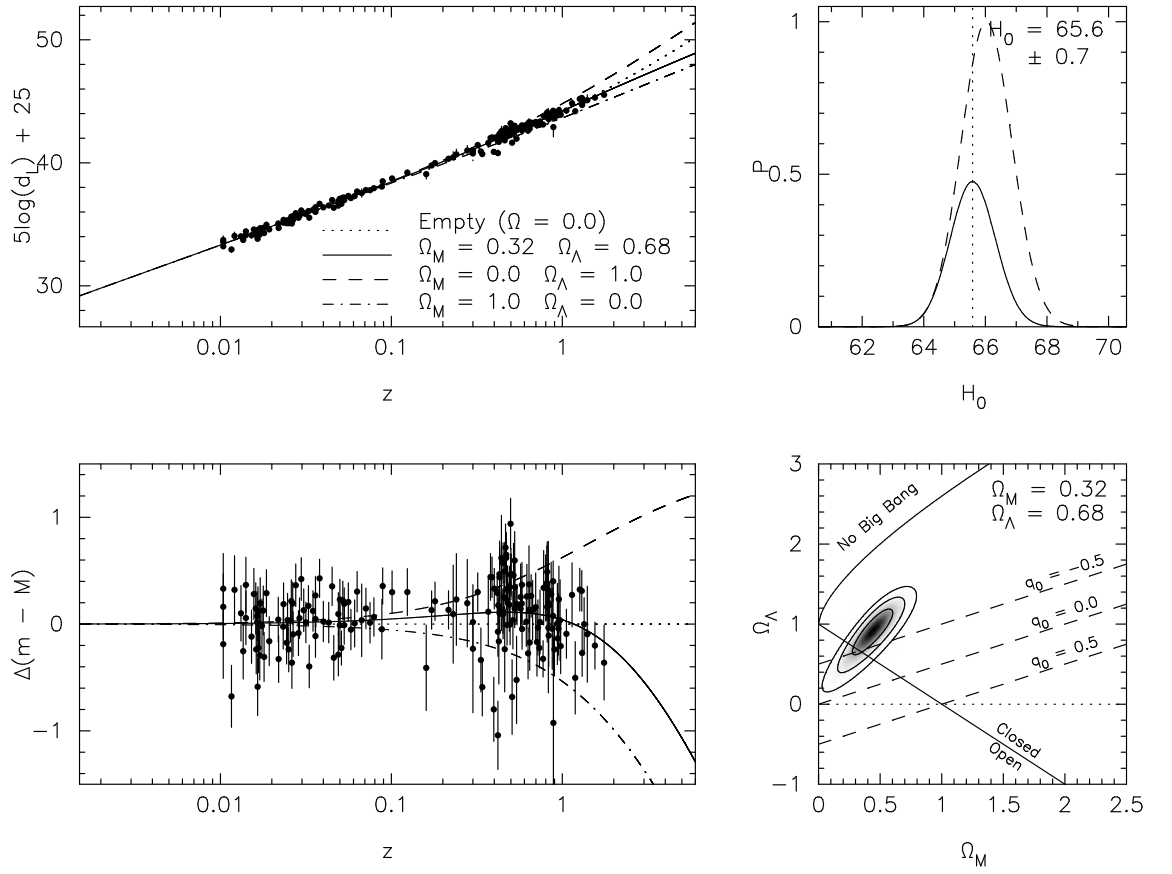
Figure 3.17: Constraints on H_0, Ω_M and Ω_Λ from 185 supernovae type 1a. Data from Riess et al. (2004). Plots same as in Fig.3.16.

it is the *shape* of the redshift-distance relationship that matters. We have presented a simulation showing possible constraints from long-term monitoring of 44 AGN.

CHAPTER 4

X-ray variability during the quiescent state of the neutron-star X-ray transient in the globular cluster NGC 6440

This thesis now changes direction, with the focus changing from AGN to quiescent emission from neutron star X-ray transients within our own Galaxy. Firstly, *Chandra* observations of a transient in the globular cluster NGC 6440 are presented.

4.1 Introduction

Globular clusters are ideal for studying X-ray transients in quiescence as the distance to the host clusters can usually be determined more accurately than for the Galactic quiescent X-ray binaries. Here we report on *Chandra* observations of the globular cluster NGC 6440 which is known to harbour a bright neutron-star X-ray transient. NGC 6440 is a globular cluster at a distance of 8.5 ± 0.4 kpc and reddened by *E(B-V)* = 1.0 (Ortolani et al., 1994). A transient in NGC 6440 was first seen during an outburst in December 1971 to January 1972 (Markert et al., 1975; Forman et al., 1976). In August 1998, a second outburst was detected by the Wide Field Camera (WFC) on-board *BeppoSAX* (in 't Zand et al., 1998) and the All-Sky Monitor (ASM) on-board the *Rossi X-ray Timing Explorer (RXTE)*. During this outburst four type I X-ray bursts were detected (in 't Zand et al., 1999b), demonstrating the neutron star nature of the compact object. An optical follow-up of this outburst found two possible candidates, V1 and V2, for the optical counterpart of the transient (Verbunt et al., 2000).

in 't Zand et al. (2001) and Pooley et al. (2002b) reported on a *Chandra* observation of NGC 6440 nearly 2 years after the end of the 1998 outburst. The neutron-star X-ray transient was in quiescence and Pooley et al. (2002b) detected 24 low-luminosity X-ray sources in this globular cluster. They also reported that 4-5 quiescent neutron stars might be present in this cluster, based on their X-ray luminosities and soft, thermal X-ray spectra. Their source CX1 was the brightest low-luminosity source in the cluster and its position was consistent with that of V1 in Verbunt et al. (2000) and possibly the quiescent counterpart of the bright transient source. This issue was resolved in August 2001, when the *RXTE*/ASM and the *BeppoSAX*/WFC detected another outburst from the transient in NGC 6440. in 't Zand et al. (2001) obtained a brief *Chandra* observation during this outburst which resulted in a sub-arcsecond position of the source. They found that the 1998 and 2001 transient is associated with CX1 from Pooley et al. (2002b) and V1 from Verbunt et al. (2000). From here on, we refer to the quiescent counterpart of the neutron-star transient in NGC 6440 as CX1 after Pooley et al. (2002b).

To study the quiescent counterpart CX1 of the neutron-star transient and the additional low-luminosity X-ray sources in NGC 6440 in more detail, we observed NGC 6440 for a third time using *Chandra*. Our observation was taken whilst this transient was in a quiescent state and we compare this new *Chandra* observation with the previous *Chandra*

observation of the transient in a quiescent state by in 't Zand et al. (2001) and Pooley et al. (2002b), to study potential variability of the quiescent X-ray emission of the source. The additional low-luminosity sources in NGC 6440 will be studied in future work.

4.2 Observations and Analysis

On 2003 June 26 we observed NGC 6440 with *Chandra* for 24 ks using only the S3 chip of the ACIS-S detector. In Figure 4.1 we show the *RXTE* ASM light curve of the transient since January 1996. In this figure we indicate when the *Chandra* observations were performed. It can be seen that CX1 was not in a bright outburst phase during the 2000 July 4 observation and our 2003 June 26 observation (as we shall show below, CX1 was in a quiescent state during both observations). The location of the August 1998 outburst is also marked on. This outburst is barely detected with the *RXTE* ASM, and in this figure the data are binned over 7 days and so only one bin is slightly above the noise (see also in 't Zand et al., 1999b). Since February 1999, the Proportional Counter Array (PCA) on-board *RXTE* has been monitoring the Galactic centre region, which includes NGC 6440, about twice a week (Swank & Markwardt, 2001). Since the start of this monitoring campaign, only the 2001 outburst has been detected (C. B. Markwardt 2004, private communication). The PCA is an order of magnitude more sensitive than the ASM and so weak outbursts which might have been missed by the ASM should have been detected by the PCA. However, we cannot exclude that before February 1999, weak outbursts with X-ray fluxes below the ASM detection threshold, may have gone undetected.

Data reduction and analysis of the 2003 June 26 and 2000 July 4 observations was performed using the CIAO 3.0.2 software package provided by the *Chandra* X-ray Center and following the threads listed on the CIAO web pages[1]. Background flares were searched for but none were found, thus we used all available data in our analysis.

4.2.1 Image Analysis

A false colour image of the cluster was produced from the 2003 June 26 observation (hereafter observation 2; see Fig.4.2, right panel) and a similar image was produced from

---

[1] Available at http://cxc.harvard.edu/ciao/
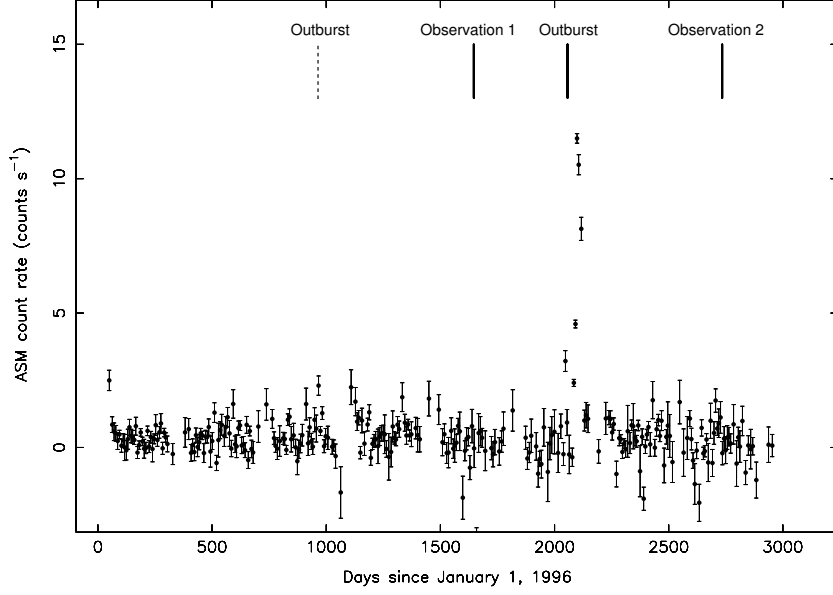
Figure 4.1: *RXTE* ASM light curve of the transient in NGC 6440. Each point is averaged over seven days. The dates of the three *Chandra* observations are marked with solid lines. It can be seen that both observation 1 and observation 2 were taken whilst the neutron star X-ray transient in NGC 6440 was in a quiescent state. The dashed line indicates the 1998 August outburst.

the 2000 July 4 observation for comparison (observation 1; see Fig. 4.2, left panel). It can be seen that during both of these observations, the source was in a quiescent state (see in 't Zand et al., 2001, for a comparison of observation 1 with the August 2001 *Chandra* observation of the source in outburst). In this figure, the red colour is for the 0.3-1.5 keV energy range, green for 1.5-2.5 keV, and blue for 2.5-8.0 keV. When creating these images we removed the pixel randomization that is added in the standard data processing, this slightly enhances the spatial resolution of the images. We used `wavdetect` (Freeman et al., 2002) to detect the point sources in the cluster and determine their positions. `wavdetect` is a wavelet-based source detection algorithm. To determine that we had correctly identified CX1 in the new observation we calculated the coordinate offset between the two observations of the five brightest sources detected (CX2 - CX6, as named in Pooley et al., 2002b). The mean offset in RA $= 0.39''$ and in Dec $= -0.07''$ with standard deviations of these offsets being $0.11''$ in RA and $0.13''$ in Dec. The offset of CX1 between the two observations was $0.41''$ in RA and $-0.04''$ in Dec. These offsets are well within one standard deviation of the averaged offsets measured for the other sources, hence we conclude that we have detected the same source in both observations.
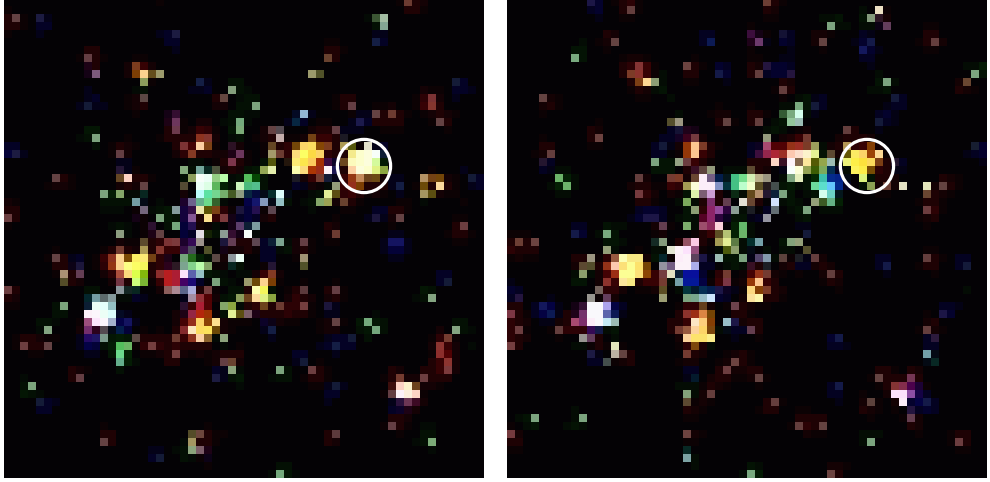
Figure 4.2: *Chandra* X-ray images of the globular cluster NGC 6440. The left panel shows the data obtained in the 2000 July 4 *Chandra* observation, where as the right panel shows the new *Chandra* observation from 2003 June 26. The location of CX1 is marked with a circle. Both images show the neutron star X-ray transient CX1 in a quiescent state. They are both plotted on the same scale ($29.5'' \times 29.5''$) for direct comparison. East is left and north is upward. The red colour is for the 0.3-1.5 keV energy range, green for 1.5-2.5 keV, and blue for 2.5-8.0 keV.

4.2.2 Spectral Analysis

Figure 4.2 shows a change in colour of the source between the two observations. The more yellowish X-ray colours of the second observation suggest that the spectrum is softer in the second observation. Since the launch of *Chandra* there has been continuous degradation of the ACIS quantum efficiency[2] which is most severe at lower energies. The effect of this degradation would be to make the second observation harder, and hence this actually strengthens our impression based on a comparison of the two images that the spectrum of the second observation is softer.

We extracted the count rates using a circle of radius $1.5''$ centred on the source position as the source extraction region and an annulus from $17''$ to $28''$ centred on the cluster centre as the background region. No sources were detected in this annulus. For the source CX1 we detected 247 photons for observation 1 (for the photon energy range 0.3 - 10 keV)[3] with 0.7 background photons giving a net count rate of 0.0106 ± 0.0007

---

[2]See http://cxc.harvard.edu/cal/Acis/Cal_prods/qeDeg/

[3]A total number of 251 photons are detected for observation 1 in the full energy range of Chandra, as

counts s^{-1} compared to 108 photons for observation 2 (also for the photon energy range 0.3 - 10 keV), 0.6 background photons, and a net count rate of 0.0045 ± 0.0004 counts s^{-1}. Clearly, we see a difference in the net count rates between the two observations strongly suggesting that the source was variable between the two quiescent observations. To further investigate the spectral and count rate variations we observed, we extracted the source spectra using the randomized data and the same extraction regions as above by using the CIAO tool `psextract`. This also creates the response matrices and ancillary response files, and automatically corrects the latter for the degradation of the low-energy quantum efficiency of the CCD as mentioned above. The spectrum was grouped into bins of 10 counts. Greater than 15 - 20 counts per bin are formally required to use the χ^2 statistic, but we decided on this number because the 2nd observation had few net counts. We checked our results by using the Cash statistics (Cash, 1979) and found the results to be consistent with the χ^2 method (within the 90 per cent confidence levels); we only present results obtained using χ^2 statistics. In our spectral analysis we use the neutron star hydrogen atmosphere (NSA) model for weakly magnetised neutron stars (Zavlin, Pavlov & Shibanov, 1996). Various other models, including blackbody and disk blackbody models, fit the data satisfactorily but the NSA model is the most commonly used and currently accepted to be a better physical description of the emission originating from neutron star surfaces than other models (see e.g. Rutledge et al., 1999, 2000, and Chp. 1, for an in depth discussion).

Individual Spectral Fits

Initially we fitted the two spectra separately using `XSPEC` version 11.2.0 (Arnaud, 1996). For observation 1 the model used consists of an absorbed neutron star atmosphere (NSA) model plus a power-law. The inclusion of a power-law to account for the hardest photons significantly improves the fit. For observation 2, however, the inclusion of a power-law does not improve the fit and, in fact, when a power-law is included, `XSPEC` forces the value of the power-law index to a high, unphysical value. For example, when assuming a distance to the source of $d = 8.1$, 8.5 or 8.9 kpc, the best fitting power-law index is 9.5 in each case. An absorbed NSA model excluding a power-law is therefore used when fitting the spectrum of observation 2.

---

previously found in in 't Zand et al. (2001).

The normalization in the NSA model (Zavlin et al., 1996) is given as $1/d^2$ where d is the distance in parsecs. When leaving the normalization of the NSA model free this parameter could not be constrained well, with values between 9.2×10^{-7} and 1.2×10^{-10} and a best fit value of 5.0×10^{-9}. This corresponds to a distance range of 1 - 93 kpc with a best fit value of 14 kpc. Leaving the NSA normalization free leads to large uncertainties in the other parameters too. The best known distance to NGC 6440 from optical observations is well defined as being 8.5 ± 0.4 kpc (Ortolani et al., 1994) which is consistent with our range of distances. By fixing the NSA normalization, the uncertainties in the other parameters are significantly reduced. We set the NSA normalization using $d = 8.1$, 8.5 and 8.9 kpc, fully covering the allowed distance range from the optical observations. A 'canonical' neutron star with a mass of 1.4 M$_\odot$ and a radius of 10 km was also assumed. Therefore, the only allowed free parameter in the NSA model was the temperature. When fitting to the individual observations the column density and the power-law spectral index and normalization were free parameters. The results of the spectral fits to the individual observations are shown in Tables 4.1 and 4.2. From these results it can be seen that the different NSA normalization values do not greatly affect the fit parameters. The flux of the source is seen to change between the two observations. The model was extrapolated to the energy range 0.01-100 keV to give an estimate of the bolometric flux. Between the two observations the 0.5-10 keV flux decreases by a factor of $\sim$2. To determine the errors in the fluxes, each free fit parameter was fixed to its minimum or maximum value in turn, and only one at a time with the exception of the power law component. This component was fixed to its best fitting value as it is highly unconstrained and if left free gives unreasonably large errors (e.g. a factor of approximately 10^2). The model was then refitted to the data and new flux values calculated. Once this was done for every free parameter, the total flux range was used to give the flux errors.

Combined Spectral Fits

To further investigate the cause behind the variation in flux we fit the two observations simultaneously (Table 4.3). The spectra and fitted models can be seen in Fig. 4.3. As we expect the column density to be very similar for each observation, it was decided to tie this parameter between observations. Again a canonical neutron star was used and only the temperature in the NSA model was left as a free parameter. The power-law spectral

Table 4.1: Spectral results for observation 1. The error bars represent 90% confidence levels. For the NSA model, we used a neutron star mass of 1.4 $M_\odot$, a radius of 10 km and the neutron star hydrogen atmosphere model for weakly magnetized neutron stars of Zavlin et al. (1996).

	Assumed Distance to NGC 6440		
Model Parameter	8.1 kpc	8.5 kpc	8.9 kpc
$N_H \left(10^{22}\,\text{cm}^{-2}\right)$	0.7 ± 0.1	0.7 ± 0.1	0.7 ± 0.1
kT_{eff}^{∞} (eV)	88 ± 5	91 ± 5	92 ± 5
Power-law index	2.5 ± 1.0	2.4 ± 1.0	2.4 ± 1.0
Power-law normalization (10^{-5})	$2.2^{+3.5}_{-1.4}$	$2.0^{+3.4}_{-1.3}$	$1.9^{+3.3}_{-1.3}$
Flux (0.5 - 10 keV) (10^{-13} ergs cm^{-2} s^{-1})	1.9 ± 0.4	1.8 ± 0.4	1.8 ± 0.4
Fraction of 0.5 - 10 keV flux in power-law	0.41 ± 0.2	0.40 ± 0.2	0.40 ± 0.2
NSA contribution to the bolometric flux (10^{-13} ergs cm^{-2} s^{-1})	1.7 ± 0.4	1.7 ± 0.4	1.6 ± 0.4
χ_ν^2	0.74	0.73	0.73

Table 4.2: Spectral results for observation 2. The error bars represent 90% confidence levels. For the NSA model, we used a neutron star mass of 1.4 $M_\odot$, a radius of 10 km and the neutron star hydrogen atmosphere model for weakly magnetized neutron stars of Zavlin et al. (1996).

Model Parameter	Assumed Distance to NGC 6440		
	8.1 kpc	8.5 kpc	8.9 kpc
$N_H \left(10^{22}\,\text{cm}^{-2}\right)$	0.7 ± 0.2	0.7 ± 0.2	0.7 ± 0.2
kT_{eff}^{∞} (eV)	85 ± 5	87 ± 5	88 ± 5
Flux (0.5 - 10 keV) (10^{-13} ergs cm^{-2} s^{-1})	0.9 ± 0.3	0.9 ± 0.2	0.9 ± 0.2
Bolometric flux (10^{-13} ergs cm^{-2} s^{-1})	1.5 ± 0.3	1.4 ± 0.3	1.4 ± 0.3
χ_ν^2	0.66	0.66	0.65

index and normalization for the first observation were allowed to be free, where as the normalization was initially fixed to zero for the second observation. After the model had been fit to the data, the power-law spectral index of the second observation was fixed to the value obtained for the first observation and the 90 per cent confidence limit on the normalization was determined. This gives us an indication of the upper limit of the power-law normalization for the second observation, assuming that the power-law spectral index was the same for both observations. In this case, taking the distance to the source to be 8.5 kpc, we get an upper limit on the power-law normalization of 1.7×10^{-5}, with the power-law index being 2.5. This gives a corresponding upper limit on the unabsorbed 0.5-10 keV flux of 1.0×10^{-13} erg cm^{-2} s^{-1} and hence the maximum contribution of the power law component to the 0.5-10 keV flux of 10 per cent. Similar upper limits were determined when taking $d = 8.1$ and 8.9 kpc (see Tab. 4.3). Power-law indices that are lower than our observed value for the first observation have been measured in other systems (e.g. Rutledge et al., 1999), and it is possible that the power-law index could have changed between the observations. Therefore, to investigate whether the power-law index or normalization is variable between the two observations the upper limits were also determined when setting the power-law spectral index of the second observation to 0.5 and 1.0. The corresponding upper limits in the power law normalization were 2.9×10^{-6} and 4.3×10^{-6} respectively when taking the distance of the source to be 8.5 kpc. This gives unabsorbed 0.5-10 keV fluxes of 1.6×10^{-13} and 1.3×10^{-13} erg cm^{-2} s^{-1} and the maximum contributions of the power-law component to the 0.5-10 keV flux of 44 and 31 per cent, respectively. As the upper-limit to the power-law normalization for observation 2 is strongest when the power-law has a spectral index equal to that of the first observation, it is possible that the power-law index remains unchanged between the observations and it is the normalization that has changed, though we cannot be conclusive.

Assuming that the distance to the source is 8.5 kpc, we found an unabsorbed 0.5-10 keV flux of $1.9 \pm 0.3 \times 10^{-13}$ erg cm^{-2} s^{-1} in observation 1 and $0.9 \pm 0.2 \times 10^{-13}$ erg cm^{-2} s^{-1} in observation 2. Our results show that the unabsorbed 0.5-10 keV flux reduces by a factor of 2.1 ± 0.6 between the first and second observation. This confirms our conclusion (section 4.2.2) that the neutron star X-ray transient in NGC 6440 exhibits variability in quiescence. The contribution to the bolometric flux from the NSA component was found to be $1.6 \pm 0.4 \times 10^{-13}$ erg cm^{-2} s^{-1} in observation 1 whereas all the bolometric flux comes from the NSA component in observation 2 and is found to be $1.4 \pm 0.2 \times 10^{-13}$ erg cm^{-2}
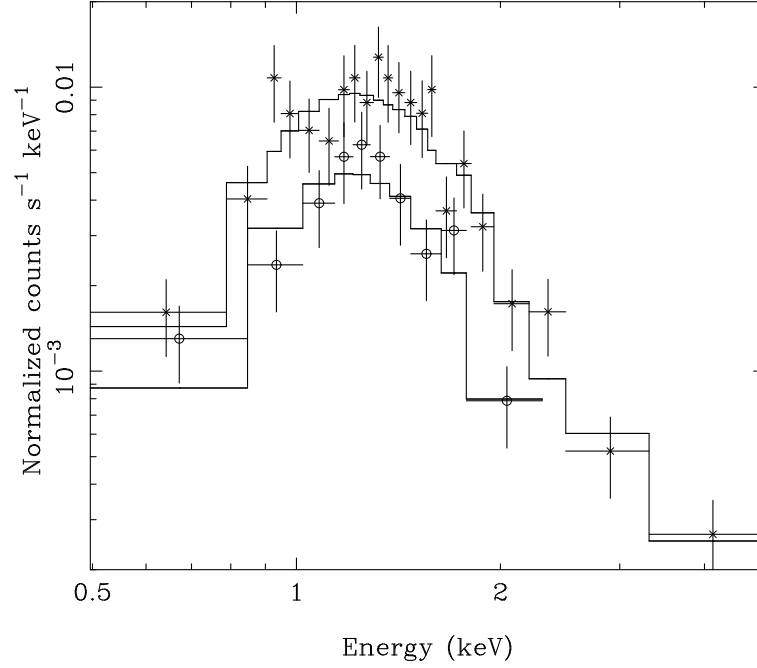
Figure 4.3: X-ray spectra of the X-ray transient neutron star in NGC 6440 during observation 1 (crosses) and observation 2 (circles). The solid lines through the data points are the best fitting models to the data.

Table 4.3: Spectral results when simultaneously fitting to observations 1 and 2. The error bars represent 90% confidence levels. For the NSA model, we used a neutron star mass of 1.4 $M_\odot$, a radius of 10 km and the neutron star hydrogen atmosphere model for weakly magnetized neutron stars of Zavlin et al. (1996).

| | Assumed Distance to NGC 6440 | | |
Model Parameter	8.1 kpc	8.5 kpc	8.9 kpc
Parameters for obs. 1			
$N_H \left(10^{22}\,\mathrm{cm}^{-2}\right)$	0.7 ± 0.1	0.7 ± 0.1	0.7 ± 0.1
$kT_{\mathrm{eff}}^{\infty}$ (eV)	87 ± 5	89 ± 4	92 ± 5
Power-law index	2.6 ± 0.8	2.5 ± 0.8	2.4 ± 0.9
Power-law normalization (10^{-5})	$2.7^{+2.7}_{-1.5}$	$2.3^{+2.5}_{-1.3}$	$2.0^{+2.3}_{-1.2}$
Flux (0.5 - 10 keV) (10^{-13} ergs cm^{-2} s^{-1})	1.9 ± 0.3	1.9 ± 0.3	1.8 ± 0.3
Fraction of 0.5 - 10 keV flux in power-law	0.46 ± 0.2	0.43 ± 0.2	0.40 ± 0.2
NSA contribution to the bolometric flux (10^{-13} ergs cm^{-2} s^{-1})	1.6 ± 0.4	1.6 ± 0.4	1.6 ± 0.3
Parameters for obs. 2			
$kT_{\mathrm{eff}}^{\infty}$ (eV)	85 ± 4	86 ± 4	88 ± 4
Power-law normalization (10^{-5})	< 2.0	< 1.7	< 1.5
Flux (0.5 - 10 keV) (10^{-13} ergs cm^{-2} s^{-1})	0.9 ± 0.2	0.9 ± 0.2	0.9 ± 0.2
Bolometric flux (10^{-13} ergs cm^{-2} s^{-1})	1.5 ± 0.2	1.4 ± 0.2	1.4 ± 0.2
χ^2_ν	0.69	0.68	0.68
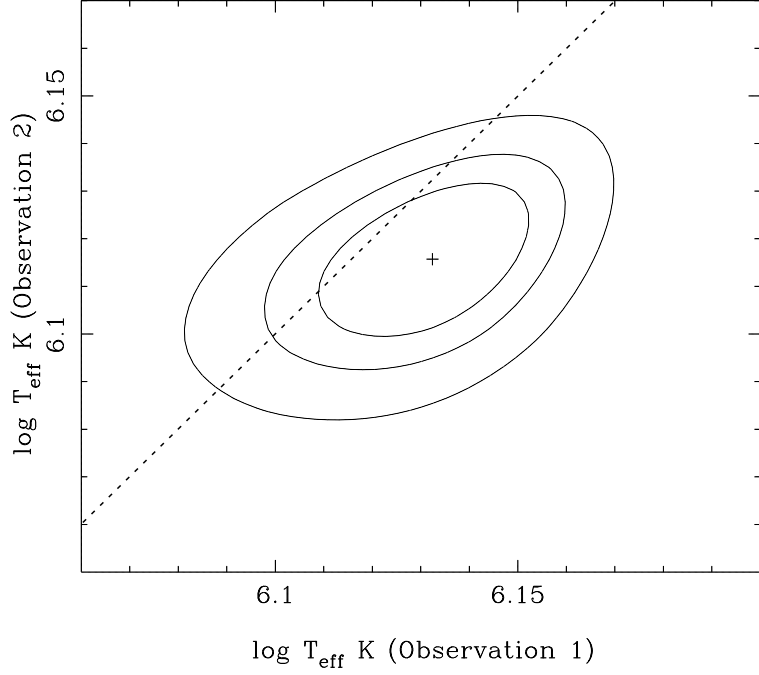
Figure 4.4: Comparison of the effective temperature (for an observer on the surface of the neutron star) between observations 1 and 2 when taking the distance to the source to be 8.5 kpc. The contours mark the 68.3%, 90%, and 99% confidence levels. The dashed line indicates where the temperature of observation 1 equals the temperature of observation 2. The contours were determined with the power-law fixed to the best fitting value.

s^{-1}. So, the NSA component of the bolometric flux is seen to be consistent between the two observations. The corresponding effective temperatures of the thermal component for the two observations are seen to remain constant to within the 68.3% (1-σ) confidence level. This is illustrated in Fig. 4.4 where the line of equal temperature between the observations goes within this 68.3% confidence contour.

4.3 Discussion

We have presented a new *Chandra* observation of the globular cluster NGC 6440 during a time when the neutron-star X-ray transient CX1 was in a quiescent state and compared this observation with a previous *Chandra* observation also taken whilst CX1 was in a quiescent state. Both spectra have been acceptably fitted with NSA models using a 'canonical' neutron star at the distance of NGC 6440 combined with galactic absorption. In observation 1 the addition of a power-law component improves the fit at higher energies,

117

as has previously been found for other quiescent neutron stars (e.g. Aql X-1 (Rutledge et al., 2001a, 2002a; Campana et al., 1998b), Cen X-4 (Rutledge et al., 2001b; Campana et al., 2004)), but the addition of such a term to the second observation does not improve the fit. We have shown that the 0.5-10 keV flux is seen to decrease by a factor of ~ 2 between these two observations and that the neutron star atmosphere component to the bolometric flux is seen to be consistent. Our results for observation 1 are found to be consistent with the previous analysis by in 't Zand et al. (2001).

Other quiescent neutron stars which have been observed to be variable during quiescence include Aql X$-$1, Cen X$-$4, MXB 1659$-$29 and KS 1731$-$260. Rutledge et al. (2001a, 2002a) account the variability in Aql X-1 to a change in the neutron star effective temperature caused by variable residual accretion onto the neutron star, whereas Campana & Stella (2003) prefer to explain the variability due to correlated variations of the power-law component and the local column density, supporting the idea of shock emission. The variability in Cen X-4 has been attributed to a changing power-law component (Rutledge et al., 2001b) or a variable local column density combined with variation in either the soft or hard spectral component, or both (Campana et al., 2004). Long accretion events in MXB 1659$-$29 and KS 1731$-$260 heated the crust of the neutron stars in these systems considerably out of thermal equilibrium with the cores and the quiescent variability can be explained by the cooling of the crusts toward renewed equilibrium with the cores (Wijnands et al., 2004, recent observations of these sources are presented in Chapter 6). However, the outbursts of the transient in NGC 6440 are short (compared to the outbursts of MXB 1659$-$29 and KS 1731$-$260) during which the neutron star crust is only slightly heated and soon (within weeks; e.g. Brown et al., 1998) after the end of the outbursts, the crust will be in thermal equilibrium with the core. Since our quiescent observations were both taken ~ 2 years after the end of the outbursts, we expect that the crust has already reached equilibrium with the core and therefore a cooling crust can probably not explain the observed variability.

From our spectral analysis of CX1, the significant difference between the observations to note is the undetectability of a power-law component in the second observation. Although a hard power-law component is seen in observation 1, it is not detected in observation 2. Both observations were of the same exposure and so will be equally sensitive to the hard tail. For the photon energy range 3-10 keV, 15.7 net counts were detected from the source in the first observation (0.3 background counts), whereas no counts were

detected in this energy range in second observation. Clearly, there is a definite change in the power-law component between these observations. But, it is unclear from these results whether this is due to a variable spectral index or normalization, or both. This change in property, or properties, of the power-law component likely accounts for almost all of the change in luminosity. The unchanging neutron star effective temperature between the observations supports the idea that the thermal quiescent luminosity is set by deep crustal heating (Brown et al., 1998).

We have clearly shown that the neutron star X-ray transient in NGC 6440 was variable between two quiescent observations. This variability is attributable to a change in the power-law component whilst the thermal component is consistent with remaining constant. This is similar to the results found for Aql X-1 (Campana & Stella, 2003) and Cen X-4 (Campana et al., 2004) where the thermal component from the neutron star is consistent with remaining constant and the power-law is seen to be variable. These observations all indicate that there is a stable thermal flux coming from the neutron star surface, likely set by deep crustal heating, and a variable flux at higher energies. Although the nature of the power-law component is uncertain, one proposal is that it could be due to matter interacting with the magnetic field of the neutron star in some way (e.g., Campana et al., 1998a; Campana & Stella, 2000). In particular, Campana & Stella (2003) and Campana et al. (2004) explain variable power-law flux they observed as emission at the shock between a pulsar wind and a variable amount of inflowing matter from the companion star. They base this on the fact that they found evidence that the spectral variability in Aql X-1 and Cen X-4 could be interpreted as correlated variations of the power-law component and the local column density. Unfortunately, we were unable to determine if a similar correlation in CX1 was underlying the spectral variability we found in this source, as we cannot fit a power-law to both observations. However, some variation in accretion rate onto the magnetosphere or variation in the interaction of the pulsar wind with the matter still outflowing from the companion star could, in principle, explain the variability observed in CX1, with less matter interacting with the neutron star magnetic field during observation 2 compared to observation 1. If there is residual accretion occurring it is unlikely to accrete down to the surface since that would produce thermal-like emission (Zampieri et al., 1995), due to the heating of the surface, over the thermal flux expected from a cooling neutron star.

The transient in NGC 6440 was seen to be in a quiescent state since the outburst in

1971 until the 1998 outburst, and then until the 2001 outburst. We can use this information to predict the thermal flux during quiescence. From the time averaged accretion flux, $\langle F_{acc} \rangle$, the expected thermal flux in quiescence, F_q, can be predicted using the Brown et al. (1998) model and assuming standard core cooling: $F_q = \langle F_{acc} \rangle / 135$ (Brown et al., 1998; Wijnands et al., 2001a; Rutledge et al., 2002a). From this, it can be derived (Wijnands et al., 2001a) that $F_q \sim t_o / (t_o + t_q) \times \langle F_o \rangle / 135$, where $\langle F_o \rangle$ is the time-averaged flux during outburst, t_o is the time the source was in outburst, and t_q the averaged time the source is in quiescence. The time-averaged flux during outburst for CX1 can be estimated from the $RXTE$/ASM lightcurve (see Fig. 4.1). To convert the ASM count rate to a flux, we use PIMMS (the Portable, Interactive Multi-Mission Simulator), modelling the outburst spectrum as a power-law with index 1.7 and $N_H = 1.2 \times 10^{22}$ cm^{-2} (valid for the energy range 1-40 keV; in 't Zand et al., 1999b). This gives the time-averaged flux during outburst as $\langle F_o \rangle = 5.79 \times 10^{-9}$ erg cm^{-2} s^{-1} in the energy range 1-40 keV. However, the bolometric flux could be a factor of a few higher than this depending on the correct spectral model and energy range. Assuming that no other outbursts were detected since the 1971 outburst, we get the total time in quiescence up until the 2001 outburst as $t_q = 10973$ days, estimating the total outburst time, $t_o \sim 43$ days (from the ASM lightcurve). The predicted quiescent flux is therefore, $F_q = 1.7 \times 10^{-13}$ erg cm^{-2} s^{-1}. Although the bolometric correction could make this predicted flux a factor of a few higher, the uncertainties in our assumptions are likely to be large, making this predicted flux in good agreement with the observed quiescent flux of the NSA component that we found from the Chandra observations (Tables 4.1, 4.2, and 4.3). This shows that the standard cooling model can account for the observed behaviour of CX1. Other quiescent neutron stars cannot easily be explained by the standard cooling model and require enhanced core cooling, for example, KS1731-260 and MXB 1659-29 (Chp. 6) and Cen X-4 (Rutledge et al., 2001b), in which case the neutron stars in these systems could be more massive (> 1.7 M$_\odot$) than those in prototypical neutron star transients (e.g. Colpi et al., 2001). Further monitoring of this, and other, neutron star transients in a quiescent state will better constrain the quiescent properties and help determine the cause of the observed variability.

A *Chandra* X-ray observation of the globular cluster Terzan 1

Continuing the study of neutron star X-ray transients in globular clusters, a *Chandra* observation of the globular cluster Terzan 1 is presented in this chapter. As well as studying the known NS transient in quiescence, the X-ray source population of the globular cluster is looked at on the whole.

This chapter is based on a paper published in the Monthly Notices of the Royal Astronomical Society, by Cackett, E. M., Wijnands, R., Heinke, C. O., Pooley, D., Lewin, W. H. G., Grindlay, J. E., Edmonds, P. D., Jonker, P. G., and Miller, J. M. (2006, MNRAS, 369, 407).

5.1   Introduction

Many quiescent neutron stars and other quiescent low-mass X-ray binaries have been found in several globular clusters using the *Chandra* and *XMM-Newton* X-ray observations (see Heinke et al., 2003b; Pooley et al., 2003, and references therein). Galactic globular clusters provide an ideal location to study these types of sources - the distance to host clusters can usually be determined more accurately than for the Galactic quiescent X-ray binaries. The known distance and reddening allows accurate luminosities to be derived and removes the distance uncertainty from the quiescent properties. The high incidence of compact binaries in globular clusters is likely explained by the formation of such binaries via exchange encounters in the very dense environments present (e.g. Verbunt & Hut, 1987; Hut, Murphy & Verbunt, 1991), though the ultracompact systems may be formed via direct collisions followed by orbital decay (Ivanova et al., 2005). See Chp 1. for more discussion.

Terzan 1 (Terzan, 1966) is a globular cluster at a distance of 5.2 ± 0.5 kpc and a reddening of $E(B-V) = 2.48 \pm 0.1$ (Ortolani et al., 1999). In 1980, the *Hakucho* satellite detected X-ray bursts from a source located in Terzan 1 (Makishima et al., 1981; Inoue et al., 1981). Several years later, the persistent source X1732−304 was detected within Terzan 1 with SL2-XRT onboard Spacelab 2 (Skinner et al., 1987) and *EXOSAT* (Warwick et al., 1988; Parmar et al., 1989). This is likely to be the same source as the bursting source detected previously by *Hakucho*. Subsequent X-ray observations with *ROSAT* (Johnston et al., 1995; Verbunt et al., 1995) detected the source with a similar luminosity, between 2.0×10^{35} ergs s^{-1} and 1.3×10^{36} ergs s^{-1} (see Fig. 3 of Guainazzi et al., 1999). It is also assumed that X1732−304 is the source of hard X-rays detected with the SIGMA and ART-P telescopes (Borrel et al., 1996a,b; Pavlinsky et al., 1995). A possible radio counterpart of X1732−304 was observed with the VLA within the *ROSAT* error circles (Marti et al., 1998).

A *BeppoSAX* observation of X1732−304 in April 1999 discovered the source in a particularly low state with the X-ray intensity more than a factor of 300 lower than previous measurements (Guainazzi et al., 1999). A more recent short (~ 3.6 ks) *Chandra* HRC-I observation of Terzan 1 did not conclusively detect X1732−304 with a 0.5-10 keV luminosity upper limit of $(0.5 - 1) \times 10^{33}$ ergs s^{-1} depending on the assumed spectral model (Wijnands, Heinke & Grindlay, 2002b). However, an additional X-ray source, CXOGLB J173545.6-302900, was detected by this observation.

In this chapter we study the X-ray sources detected in a recent $\sim$19 ks *Chandra* ACIS-S observation of Terzan 1 and discuss possible quiescent counterparts of the neutron-star X-ray transient X1732−304.

5.2 Observations and Analysis

Terzan 1 was observed with the *Chandra X-ray Observatory* for $\sim$19 ks on 2005 May 10. The observation was made with the Advanced CCD Imaging Spectrometer (ACIS) with the telescope aim point on the back-illuminated S3 chip, this increases the sensitivity to low energy X-rays compared to the front-illuminated chips. Data reduction was performed using the CIAO v3.2.2 software with the calibration database CALDB v3.1.0, provided by
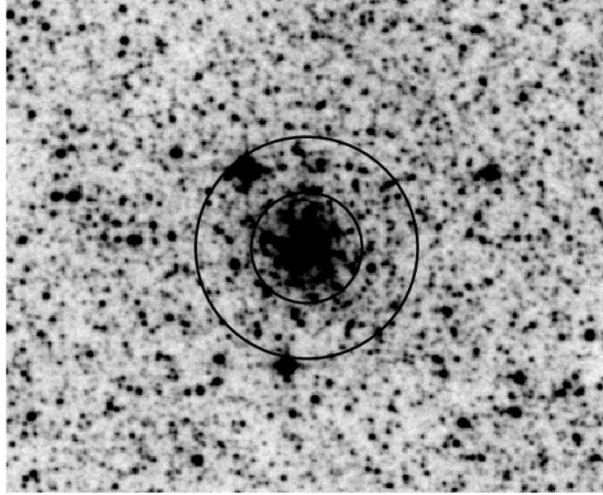
Figure 5.1: Digitized Sky Survey (DSS) image of Terzan 1. This IR plate was originally taken with the UK Schmidt Telescope. The inner circle indicates a radius of $0.'7$ and the outer circle indicates a radius of $1.'4$.

the *Chandra* X-ray Center and following the science threads listed on the CIAO website[1]. No background flares were found, so all available data was used in our analysis. We removed the pixel randomisation added in the standard data processing as this slightly increases the spatial resolution of the images.

5.2.1 Source Detection

The CIAO tool `wavdetect` (Freeman et al., 2002) was used to detect the sources. We detected the sources in the 0.5-8.0 keV energy band. A detection threshold was chosen to give ∼1 false source over the S3 chip. We detect 39 sources over the entire S3 chip with 4 detected counts or greater, after the addition of one extra source close to the cluster centre that was missed by `wavdetect` yet clearly a source. Analysing the sources that are within the globular cluster half-mass radius allows a good balance between including most of the cluster sources and minimising the number of nearby objects or background AGN (see Fig. 1 from Pooley et al., 2002b, for example). Trager et al. (1995) define the half-mass radius for this cluster to be 3.82 arcmin, however, they note that their measurement of this value is 'particularly unreliable'. As this value for the half-mass radius is particularly large, and given that the majority of X-ray binaries in the cluster will be concentrated at

---

[1]Available at http://cxc.harvard.edu/ciao/.

the centre we chose a smaller region of size $1\!\!.\!4$ within which to analyse the X-ray sources (Fig. 5.1 shows a DSS image of Terzan 1). Within this $1\!\!.\!4$ region we find 14 sources. The *Chandra* image of the cluster is shown in Fig. 5.2 where all sources within the $1\!\!.\!4$ region are highlighted. These sources are listed in descending number of detected counts in Table 5.1, also included in this table is a list of sources on the S3 chip that are not within $1\!\!.\!4$ of the cluster center, listed in decreasing 0.5-8 keV counts. The position of the brightest source we detect, CX1, is consistent with the position of the source CXOGLB J173545.6-302900 from the previous *Chandra* HRC-I observation of Terzan 1 (Wijnands et al., 2002b). From the density of sources on the S3 chip outside of the $1\!\!.\!4$ region, we expect to find 2.2 sources not associated with the cluster (background or foreground objects) within the $1\!\!.\!4$ region (assuming the sources outside this region are not associated with the cluster). This is in approximate agreement with the $\log N - \log S$ relationships of Giacconi et al. (2001), which characterizes the number of sources, N, above a particular source flux, S. Thus we expect that 2 of the 14 sources we detect within $1\!\!.\!4$ are background or foreground sources.
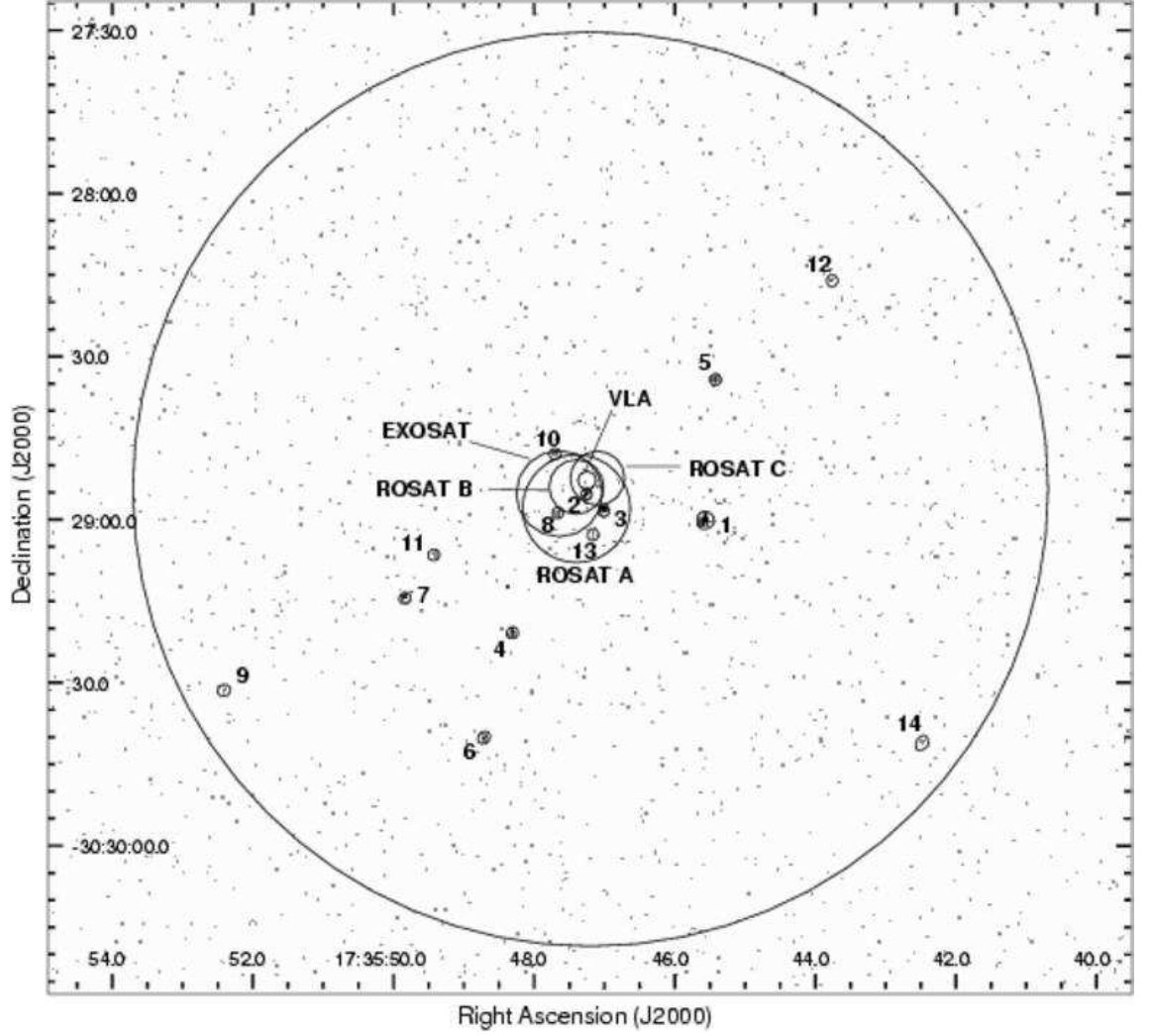
Figure 5.2: *Chandra* ACIS-S image of the globular cluster Terzan 1 in the 0.5-8.0 keV energy band. The large outer circle represents the $1'.4$ region within which we analyse the sources. The 14 sources within this region are labelled (in order of decreasing counts in the 0.5-8.0 keV band) and the extraction regions overlaid. Also shown are the 1σ error circles for three *ROSAT* pointings (using positions for pointings A and B from Johnston et al. (1995) and the updated position for pointing C from Verbunt (2005)), the 90% confidence level radius for the *EXOSAT* observation (Parmar et al., 1989), and the 90% confidence level radius of the radio source detected with the VLA (Marti et al., 1998). We predict that 2 of the detected sources are not associated with the cluster.

Table 5.1: Names, positions (J2000), and background-subtracted counts in four X-ray energy bands are given for the 14 sources detected within $1'\!.4$ of the center of Terzan 1 and the sources detected on the rest of the S3 chip. The statistical error (from `wavdetect`) in the positions of all the sources is $\leq 0''\!.1$, and thus the total positional error is dominated by the uncertainty in the absolute astrometry ($0''\!.6$, Aldcroft et al., 2000). We therefore estimate the 1σ positional error for all sources to be $\sim 0''\!.6$. The count extraction region for each source within the $1'\!.4$ region is shown in Fig. 5.2. The source CX1 was first detected (and named) by Wijnands et al. (2002b).

Source Name (Label)	R.A. (h m s)	Dec. ($^\circ$ $'$ $''$)	Net Counts 0.5 - 8.0 keV	0.5 - 1.5 keV	0.5 - 4.5 keV	1.5 - 6.0 keV
(1)	(2)	(3)	(4)	(5)	(6)	(7)
CXOGLB J173545.6-302900 (CX1)	17 35 45.57	-30 29 00.1	225^{+16}_{-15}	10^{+4}_{-3}	157^{+14}_{-13}	189^{+15}_{-14}
CXOGLB J173547.2-302855 (CX2)	17 35 47.26	-30 28 55.3	43^{+8}_{-7}	13^{+5}_{-4}	38^{+7}_{-6}	29^{+7}_{-5}
CXOGLB J173547.0-302858 (CX3)	17 35 47.02	-30 28 58.4	31^{+7}_{-6}	15^{+5}_{-4}	31^{+7}_{-6}	16^{+5}_{-4}
CXOGLB J173548.3-302920 (CX4)	17 35 48.31	-30 29 20.8	29^{+6}_{-5}	27^{+6}_{-5}	28^{+6}_{-5}	1^{+2}_{-1}
CXOGLB J173545.4-302834 (CX5)	17 35 45.42	-30 28 34.2	19^{+5}_{-4}	3^{+3}_{-2}	17^{+5}_{-4}	15^{+5}_{-4}
CXOGLB J173548.7-302940 (CX6)	17 35 48.71	-30 29 40.0	17^{+5}_{-4}	0^{+2}	11^{+4}_{-3}	15^{+5}_{-4}
CXOGLB J173549.8-302914 (CX7)	17 35 49.84	-30 29 14.4	16^{+5}_{-4}	1^{+2}_{-1}	13^{+5}_{-4}	15^{+5}_{-4}
CXOGLB J173547.6-302858 (CX8)	17 35 47.67	-30 28 58.7	15^{+5}_{-4}	1^{+2}_{-1}	13^{+5}_{-4}	14^{+5}_{-4}
CXOGLB J173552.4-302931 (CX9)	17 35 52.41	-30 29 31.3	7^{+4}_{-3}	0^{+2}	7^{+4}_{-3}	7^{+4}_{-3}
CXOGLB J173547.7-302847 (CX10)	17 35 47.71	-30 28 47.9	6^{+4}_{-2}	1^{+2}_{-1}	5^{+3}_{-2}	4^{+3}_{-2}
CXOGLB J173549.4-302906 (CX11)	17 35 49.42	-30 29 06.4	5^{+3}_{-2}	1^{+2}_{-1}	4^{+3}_{-2}	3^{+3}_{-2}

Table 5.1 – continued from previous page

	R.A.	Dec.	Net Counts			
Source Name (Label)	(h m s)	(° ′ ″)	0.5 - 8.0 keV	0.5 - 1.5 keV	0.5 - 4.5 keV	1.5 - 6.0 keV
(1)	(2)	(3)	(4)	(5)	(6)	(7)
CXOGLB J173543.7-302816 (CX12)	17 35 43.77	-30 28 16.0	5^{+3}_{-2}	1^{+2}_{-1}	5^{+3}_{-2}	4^{+3}_{-2}
CXOGLB J173547.1-302902 (CX13)	17 35 47.17	-30 29 02.7	4^{+3}_{-2}	0^{+2}	4^{+3}_{-2}	4^{+3}_{-2}
CXOGLB J173542.4-302941 (CX14)	17 35 42.49	-30 29 41.0	4^{+3}_{-2}	1^{+2}_{-1}	4^{+3}_{-2}	3^{+3}_{-2}
Sources likely not associated with Terzan 1:						
CXOU J173538.1-303032	17 35 38.13	-30 30 32.1	128^{+12}_{-11}	2^{+3}_{-1}	100^{+11}_{-10}	121^{+12}_{-11}
CXOU J173548.1-303420	17 35 48.13	-30 34 20.2	74^{+10}_{-9}	66^{+9}_{-8}	73^{+10}_{-9}	8^{+4}_{-3}
CXOU J173553.1-303433	17 35 53.12	-30 34 33.2	56^{+9}_{-8}	46^{+8}_{-7}	57^{+9}_{-8}	10^{+5}_{-3}
CXOU J173545.6-303204	17 35 45.61	-30 32 04.9	45^{+8}_{-7}	37^{+7}_{-6}	44^{+8}_{-7}	8^{+4}_{-3}
CXOU J173536.4-302917	17 35 36.49	-30 29 17.9	31^{+7}_{-6}	5^{+3}_{-2}	30^{+7}_{-5}	26^{+6}_{-5}
CXOU J173535.9-303143	17 35 35.94	-30 31 43.4	30^{+7}_{-6}	2^{+3}_{-1}	21^{+6}_{-5}	25^{+6}_{-5}
CXOU J173547.1-303426	17 35 47.16	-30 34 26.1	27^{+7}_{-5}	7^{+4}_{-3}	24^{+6}_{-5}	21^{+6}_{-5}
CXOU J173557.2-302839	17 35 57.27	-30 28 39.2	19^{+5}_{-4}	3^{+3}_{-2}	15^{+5}_{-4}	15^{+5}_{-4}
CXOU J173559.8-303016	17 35 59.88	-30 30 16.8	17^{+5}_{-4}	5^{+3}_{-2}	17^{+5}_{-4}	12^{+5}_{-3}
CXOU J173547.7-303332	17 35 45.78	-30 33 32.5	17^{+5}_{-4}	1^{+2}_{-1}	12^{+5}_{-4}	14^{+5}_{-4}
CXOU J173534.2-302715	17 35 34.28	-30 27 15.3	13^{+5}_{-4}	1^{+2}_{-1}	10^{+4}_{-3}	11^{+4}_{-3}
CXOU J173533.7-303002	17 35 33.79	-30 30 02.5	13^{+5}_{-4}	1^{+2}_{-1}	7^{+4}_{-3}	8^{+4}_{-3}

Table 5.1 – continued from previous page

Source Name (Label)	R.A. (h m s)	Dec. (° ′ ″)	Net Counts 0.5 - 8.0 keV	0.5 - 1.5 keV	0.5 - 4.5 keV	1.5 - 6.0 keV
(1)	(2)	(3)	(4)	(5)	(6)	(7)
CXOU J173556.0-302717	17 35 56.00	-30 27 17.3	12^{+5}_{-4}	1^{+2}_{-1}	7^{+4}_{-3}	10^{+4}_{-3}
CXOU J173550.1-303155	17 35 50.10	-30 31 55.0	9^{+4}_{-3}	3^{+3}_{-2}	10^{+4}_{-3}	7^{+4}_{-3}
CXOU J173554.2-302728	17 35 54.28	-30 27 28.8	8^{+4}_{-3}	0^{+2}	8^{+4}_{-3}	8^{+4}_{-3}
CXOU J173544.2-302736	17 35 44.22	-30 27 36.2	8^{+4}_{-3}	6^{+4}_{-2}	8^{+4}_{-3}	2^{+3}_{-1}
CXOU J173603.7-302849	17 36 03.72	-30 28 49.9	8^{+4}_{-3}	3^{+3}_{-2}	8^{+4}_{-3}	4^{+3}_{-2}
CXOU J173544.0-303134	17 35 44.07	-30 31 34.8	8^{+4}_{-3}	2^{+3}_{-1}	5^{+3}_{-2}	5^{+3}_{-2}
CXOU J173602.1-303225	17 36 02.11	-30 32 25.0	7^{+4}_{-3}	0^{+2}	7^{+4}_{-3}	8^{+4}_{-3}
CXOU J173535.9-302650	17 35 35.91	-30 26 50.9	7^{+4}_{-3}	1^{+2}_{-1}	6^{+3}_{-2}	6^{+4}_{-2}
CXOU J173539.7-303007	17 35 39.77	-30 30 07.0	6^{+4}_{-2}	0^{+2}	4^{+3}_{-2}	5^{+3}_{-2}
CXOU J173555.0-302721	17 35 55.05	-30 27 21.9	5^{+3}_{-2}	1^{+2}_{-1}	5^{+3}_{-2}	4^{+3}_{-2}
CXOU J173540.7-302734	17 35 40.72	-30 27 34.0	5^{+3}_{-2}	0^{+2}	5^{+3}_{-2}	5^{+3}_{-2}
CXOU J173547.8-303039	17 35 47.85	-30 30 39.0	4^{+3}_{-2}	4^{+3}_{-2}	4^{+3}_{-2}	0^{+2}
CXOU J173544.7-303125	17 35 44.76	-30 31 25.6	4^{+3}_{-2}	1^{+2}_{-1}	4^{+3}_{-2}	3^{+3}_{-2}

5.2.2 Source Extraction

The IDL tool ACIS Extract (Broos et al., 2002) was used for source photometry and extraction of spectra. ACIS Extract makes use of CIAO, FTOOLS, ds9 display capability, and the TARA IDL software. ACIS Extract constructs polygon source extraction regions which are approximate contours of the ACIS point-spread function (PSF). The user specifies the fraction of the PSF to be enclosed by the contour. The shape of the PSF at the location of each source is calculated using the CIAO tool *mkpsf*. For all our sources, except one, the PSF fraction contour level was set to 90%, evaluated at 1.5 keV. For the brightest source the PSF fraction was increased to 95%. With the chosen contour levels there is no overlapping of source extraction regions.

For each source a spectrum, lightcurve and event list was extracted. The response matrix (RMF) and auxiliary response (ARF) files for each source are constructed using the CIAO tools *mkacisrmf* and *mkarf*. Background subtracted photometry was computed for each source in several different energy bands: 0.5-1.5 keV (X_{soft}), 0.5-4.5 keV (X_{med}), and 1.5-6.0 keV (X_{hard}). These energy bands were chosen to be consistent with previous globular cluster studies in the literature (e.g. Grindlay et al., 2001a,b; Pooley et al., 2002a,b; Heinke et al., 2003a,?,b, 2005; Bassa et al., 2004). Table 5.1 lists the counts in each of these bands for all the sources. From the counts in the X_{soft}, X_{med} and X_{hard} bands we create an X-ray color magnitude diagram, plotting the logarithm of the number of counts in the X_{med} band against the X-ray color, defined as $Xcolor = 2.5 \log X_{soft}/X_{hard}$ (Grindlay et al., 2001a,b; Pooley et al., 2002a,b; Heinke et al., 2003a,?,b, 2005, though we note that Pooley et al. do not use the factor of 2.5) (see Fig. 5.3). Photoelectric absorption reduces the number of counts detected and hence affects the X-ray colors and magnitudes. To allow comparison with sources in other globular clusters this needs to be corrected for. However, it is important to note that absorption affects each source differently. We determine an approximate correction for the effects of absorption by investigating the drop in count rate due to absorption for 3 typical spectra: a 3 keV thermal bremsstrahlung, a 0.3 keV blackbody, and a power-law with photon index, $\Gamma = 2$. (e.g. Pooley et al., 2002a,b). Using PIMMS (the Portable, Interactive Multi-Mission Simulator), we determine the factor by which the count rate lowers with the inclusion of photoelectric absorption at the column density seen for Terzan 1. The optical reddening, $E(B-V) = 2.48 \pm 0.1$ (Ortolani et al., 1999), is converted to a column density $N_H = 1.36 \times 10^{22}$ cm^{-2} ($N_H/E(B-V) = 5.5 \times 10^{21}$
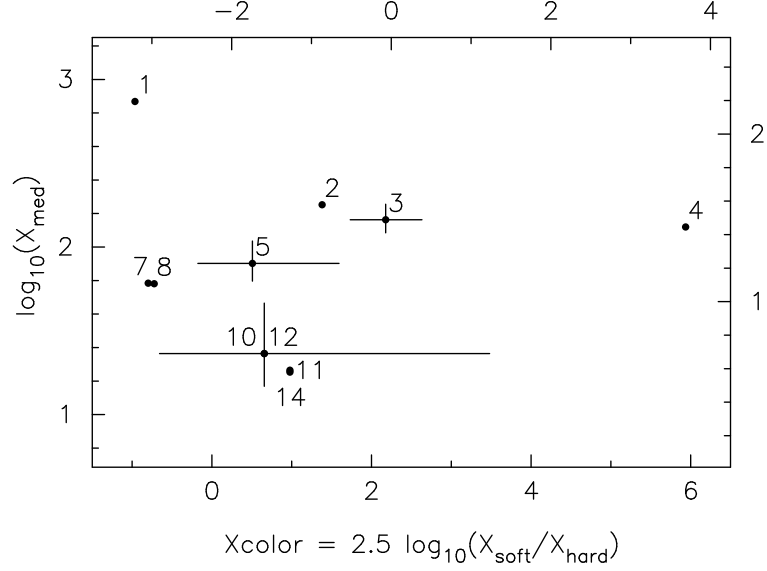
Figure 5.3: X-ray color magnitude diagram for Terzan 1. The lower and left axes show the colors and magnitudes from the absorption-corrected counts, whilst the upper and right axes show the colors and magnitudes determined from the observed counts. We approximately correct for photoelectric absorption by shifting the data +0.69 units on the left axis and +2.25 units on the lower axis. Absorption affects each source differently, and our correction is only an approximation based on typical spectra of globular cluster sources. For the purposes of clarity, only a few error bars are shown. CX6, CX9 and CX13 are not shown as they have no counts in the X_{soft} band.

cm^{-2}, from Predehl & Schmitt, 1995, using $R = 3.1$). Absorption affects the X_{soft} band the most, with the absorbed count rate a factor of 13.92 lower on average for the three models. The other average correction factors are 4.85 for X_{med} and 1.76 for the X_{hard}. There is not a significant difference in the correction factors for the different models. This leads to a shift in Xcolor of +2.25 and a shift in $logX_{med}$ of +0.69. The lower and left axes of Fig. 5.3 show the absorption corrected colors and magnitudes, where as the upper and right axes show the observed values.

5.2.3 Spectral Analysis

Using XSPEC (v. 11.3.2) (Arnaud, 1996) we fit the four brightest sources (CX1 - CX4) within the 1.'4 region. We attempt to fit each of the sources with 3 different models:

the neutron star atmosphere model of Zavlin et al. (1996), a thermal bremsstrahlung model and a simple power-law. We both fix the column density at the cluster value ($N_H = 1.36 \times 10^{22}$ cm^{-2}) and allow it to be free, using the photoelectric absorption model `phabs`. Errors in the fluxes were calculated by fixing the free-parameters to their maximum and minimum value in turn, and only one at a time. The model was then re-fitted to the data and flux values calculated. Once this was done for every free parameter, the flux range was used to give the flux errors.

We discuss each of these sources below. Table 5.2 gives the luminosities of the Terzan 1 sources as determined by spectral fits for CX1-3 assuming a distance to the cluster of 5.2 kpc. The luminosities for the other sources are determined by estimating the fluxes from the detected source counts using PIMMS, and assuming the cluster N_H and a power-law with $\Gamma = 2.0$. A power-law with $\Gamma = 2.0$ corresponds to an absorption-corrected Xcolor~ 0.6, which is consistent with the majority of these sources (see Fig. 5.3).

CXOGLB J173545.6-302900 (CX1)

The background-subtracted spectrum was grouped to have a minimum of at least 15 counts per bin. Both the neutron star atmosphere model and thermal bremsstrahlung model do not fit the spectrum satisfactorily with either the cluster N_H or allowing it to be a free parameter. A power-law model, with absorption at the cluster value, fits with a photon index, $\Gamma = 0.2 \pm 0.2$ and a reduced $\chi_\nu^2 = 0.92$ for 13 degrees of freedom (dof). Allowing the photoelectric absorption to be a free parameter leads to a fit with $N_H = 2.4^{+1.8}_{-1.1} \times 10^{22}$ cm^{-2}, $\Gamma = 0.7^{+0.7}_{-0.6}$, and $\chi_\nu^2 = 0.82$ for 12 dof. The photon index of the source from these power-law fits is unusually hard for globular cluster sources, and from the X-ray color-magnitude diagram it can be seen that this is the hardest source in the cluster. Only a few known globular cluster sources have $\Gamma < 1.0$ and most tend to have $\Gamma > 1.5$. An example of a globular cluster source that under some observing conditions could look like CX1 is the CV X9 in 47 Tuc (Heinke et al., 2005). This source has very strong soft X-ray emission (see Fig. 18 in Heinke et al., 2005), due to oxygen lines. Above ~ 5 keV it shows more flux than can be accounted for with simple bremsstrahlung or power-law models; possibly this is due to partial covering absorption. Observing this object only above 2 or 3 keV (for instance, if it was in Terzan 1 and heavily obscured) would give an effective photon index of ~ 0.3. Recently, Muno et al. (2004) detected many X-ray sources in the

Table 5.2: Luminosities for X-ray sources in Terzan 1. For CX1-CX3 the luminosities have been calculated from the spectral fits (see text). For the other sources, PIMMS was used to estimate the fluxes from the detected source counts, assuming the cluster N_H and a power-law with $\Gamma = 2.0$. No luminosity is given for CX4 as it is possibly a foreground object.

Source	X-ray Luminosity (ergs s^{-1})	
	0.5-2.5 keV	0.5-10 keV
CX1	$0.5^{+1.7}_{-0.3} \times 10^{33}$	$2.0^{+1.8}_{-0.3} \times 10^{33}$
CX2	$1.9^{+1.3}_{-0.7} \times 10^{32}$	$2.6^{+1.1}_{-0.5} \times 10^{32}$
CX3	$4.3^{+5.8}_{-2.4} \times 10^{32}$	$4.5^{+5.7}_{-2.1} \times 10^{32}$
CX5	$4.9 \pm 1.6 \times 10^{31}$	$8.5^{+2.4}_{-2.0} \times 10^{31}$
CX6	$8.1^{+11.7}_{-5.5} \times 10^{30}$	$7.6^{+2.4}_{-1.9} \times 10^{31}$
CX7	$2.1^{+1.5}_{-0.9} \times 10^{31}$	$7.2^{+2.3}_{-1.8} \times 10^{31}$
CX8	$1.3^{+1.2}_{-0.7} \times 10^{31}$	$6.7^{+2.3}_{-1.7} \times 10^{31}$
CX9	$1.7^{+1.4}_{-0.8} \times 10^{31}$	$3.1^{+1.7}_{-1.2} \times 10^{31}$
CX10	$3.9^{+10.0}_{-3.6} \times 10^{30}$	$2.6^{+1.6}_{-1.1} \times 10^{31}$
CX11	$8.1^{+11.7}_{-5.5} \times 10^{30}$	$2.2^{+1.6}_{-1.2} \times 10^{31}$
CX12	$1.3^{+1.2}_{-0.7} \times 10^{31}$	$2.2^{+1.6}_{-1.2} \times 10^{31}$
CX13	$3.9^{+10.0}_{-3.6} \times 10^{30}$	$1.7^{+1.5}_{-0.9} \times 10^{31}$
CX14	$1.7^{+1.4}_{-0.8} \times 10^{31}$	$1.7^{+1.5}_{-0.9} \times 10^{31}$

Galactic Center that have hard spectra, with a median photon index $\Gamma = 0.7$, though many have $\Gamma \leq 0$. These authors suggest that most of the sources are intermediate polars. Intermediate polars are more luminous and harder than other CVs. The hardness of these sources is thought to be due to local absorption (in addition to Galactic absorption) that is partially covering the X-ray emitting region, for example by material in the accretion flow. We therefore model CX1 absorbed by the average cluster absorption (using the `phabs` model, and fixing $N_H = 1.36 \times 10^{22}$ cm^{-2}), plus an additional partially-covering absorption component that affects a fraction of the emitting region (using the `pcfabs` model). This leads to a fit with $\chi^2_\nu = 0.78$ for 11 dof. This spectral fit is shown in Fig. 5.4. We get a higher photon index, with $\Gamma = 1.1^{+1.0}_{-0.9}$, with the partial absorption component having $N_H = 3.4^{+3.8}_{-3.2} \times 10^{22}$ cm^{-2} and a covering fraction of $0.8^{+0.2}_{-0.6}$. Thus, the partial covering absorption can explain the extreme hardness as the photon index has increased, and the source could be a intermediate polar. However, it is not possible to distinguish between the quality of these fits given the values of reduced χ^2_ν.

From this model we calculate the unabsorbed 0.5-2.5 keV luminosity $= 0.5^{+1.7}_{-0.3} \times 10^{33}$ ergs s^{-1} and the unabsorbed 0.5-10 keV luminosity $= 2.0^{+1.8}_{-0.3} \times 10^{33}$ ergs s^{-1} (assuming a distance of 5.2 kpc).

CXOGLB J173547.2-302855 (CX2)

As this source only has a total of 42.8 net counts in the 0.5-8 keV band, we did not group this spectrum into bins and cannot use χ^2 statistics. We therefore fit the spectrum in `XSPEC` using Cash statistics (Cash, 1979) without subtracting a background spectrum (as Cash statistics cannot be used on background subtracted spectra). This should introduce a minimal error as there are only 0.2 background photons in the extraction region. To investigate the quality of fits, the 'goodness' command is used. This generates 10,000 Monte Carlo simulated spectra based on the model. If the model provides a good description of the data then approximately 50% of the simulations should have values of the Cash fit statistic that are lower than that of the best-fitting model. We define the fit quality as the fraction of the simulated spectra with values of the Cash statistic lower than that of the data. Both very low and very high values of the fit quality indicate that the model is not a good representation of the data.

Fitting a neutron star atmosphere model to this spectrum (with the radius $= 10$ km,
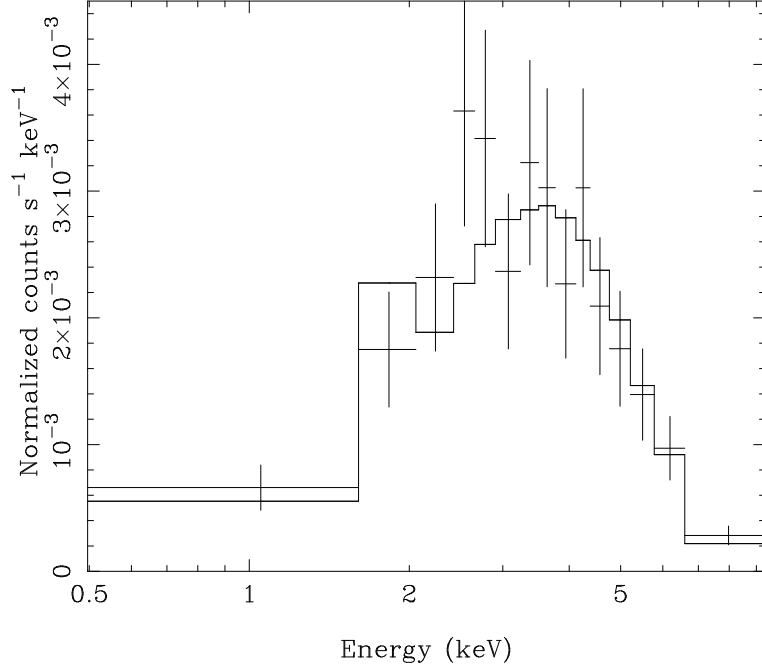
Figure 5.4: The spectrum of the brightest source in Terzan 1, CXOGLB J173545.6-302900 (CX1).

the mass = 1.4 $M_\odot$ and the normalisation = $1/d(pc)^2 = 3.7 \times 10^{-8}$) does not give a good fit, with a fit quality of 1.0. Fitting a thermal bremsstrahlung model also gives a reasonably poor fit, with a fit quality of 0.85. An improved fit is obtained when this spectrum is fitted with a simple power-law model at the cluster N_H, giving a photon index, $\Gamma = 2.5 \pm 0.6$ and a fit quality of 0.65. Allowing the N_H to be a free parameter, gives $N_H = 1.2^{+0.8}_{-0.6} \times 10^{22}$ cm^{-2}, $\Gamma = 2.3 \pm 1.0$ and a fit quality of 0.7. Such a value of the photon index suggests that this could be a hybrid thermal plus power-law spectrum, but there are not enough counts to be conclusive. From the X-ray color-magnitude diagram we see that this source is relatively soft and so it is possible that it could be a quiescent neutron star X-ray binary. We determine a 0.5-2.5 keV luminosity of $1.9^{+1.3}_{-0.7} \times 10^{32}$ ergs s^{-1} and a 0.5-10 keV luminosity of $2.6^{+1.1}_{-0.5} \times 10^{32}$ ergs s^{-1} from the power-law fit with the cluster column density.

CXOGLB J173547.0-302858 (CX3)

This source also has too few counts to use χ^2 statistics and so we again use Cash statistics. A simple power-law fit at the cluster column density gives a photon index, $\Gamma = 3.9 \pm 1.2$ and a fit quality of 0.51. Such a high photon index strongly suggests a soft thermal spectrum, which is also indicated by the X-ray color. A neutron star atmosphere fit (with the radius = 10 km, the mass = 1.4 $M_\odot$ and the normalisation = $1/d(pc)^2 = 3.7 \times 10^{-8}$) at the cluster column density gives $T_{eff}^\infty = 73.7^{+3.3}_{-3.7}$ eV with a fit quality of 0.65. Allowing the column density to be a free parameter does not greatly improve the fit, with $N_H = 1.8^{+0.5}_{-0.4} \times 10^{22}$ cm^{-2}, $T_{eff}^\infty = 78.9 \pm 6.7$ eV and a fit quality of 0.62. A thermal bremsstrahlung fit with the cluster column density gives $kT = 0.6^{+0.6}_{-0.2}$ keV with a fit quality of 0.68, where as with the column density left free we get $N_H = 1.8^{+1.3}_{-0.9}$ cm^{-2} and $kT = 0.4^{+1.0}_{-0.2}$ keV with a fit quality of 0.77. We determine a 0.5-2.5 keV luminosity of $4.3^{+5.8}_{-2.4} \times 10^{32}$ ergs s^{-1} and a 0.5-10 keV luminosity of $4.5^{+5.7}_{-2.1} \times 10^{32}$ ergs s^{-1} from the power-law fit with the cluster column density. From its spectrum, this source could be a quiescent neutron star.

CXOGLB J173548.3-302920 (CX4)

Cash statistics have also been used to analyse this source. This source is the softest source within the cluster, with an extremely high X-ray color. There is no valid power-law fit when fixing the column density to the cluster value. However, leaving this free we get a fit with $N_H = 0.7^{+0.5}_{-0.6} \times 10^{22}$ cm^{-2}, $\Gamma = 7.1^{+2.9}_{-4.3}$ and a fit quality of 0.74. There is no good fit for either a neutron star atmosphere model or a bremsstrahlung model. Such a soft X-ray color and spectrum, and the measured N_H being much lower than the cluster value suggest that this source may not be associated with the cluster and maybe a foreground object with a lower column density. However, there is no counterpart seen in the DSS or 2MASS images. As this could possibly be a foreground object and the model is highly uncertain, we have not determined a luminosity for this source.

5.3 Discussion

5.3.1 The neutron-star X-ray transient X1732−304 in quiescence

The most likely candidate for the quiescent counterpart of the neutron-star X-ray transient X1732−304 is CX2. Of the 4 sources that are within the *ROSAT* error circles, it is the only one contained in all three and contained within the *EXOSAT* error circle (see Fig. 5.2, note that the 3 separate error circles are from the 3 separate *ROSAT* observations of the source). From the X-ray color-magnitude diagram we see that this source is relatively soft and its spectrum suggests that it could be a hybrid thermal plus power-law source. Thus, it is possible that it could be a quiescent neutron star X-ray binary. The fact that it cannot be fit with a power-law spectrum alone is consistent with what was found by Jonker et al. (2004b); that the power-law fractional contribution increases for sources with luminosities decreasing from 10^{33} erg s^{-1} to 10^{32} erg s^{-1}. The position of CX2 is consistent with the position of 3 photons detected by Wijnands et al. (2002b) and has a flux slightly lower than their predicted upper-limit. CX3 also has a suitably soft X-ray color and spectrum to be a possible candidate, however, its position is only fully consistent with the *ROSAT* A pointing and it is on the edge of the error circles for the *EXOSAT* and *ROSAT* B and C observations. Although CX3 cannot be ruled out as the possible quiescent counterpart, CX2 is the most likely candidate.

The source CX2 is also closest to, though not fully consistent with, the position of the radio source detected with the VLA which might be the radio counterpart of the transient. The position of this VLA source (RA: $17^{h}35^{m}47.^{s}27$, Dec: $-30°28'52''.8$) is accurate to $1.7''$ (90% confidence level radius, Marti et al., 1998), however, the phase calibrator for these VLA observations had calibrator code C, which could mean a maximum systematic error of $0''.15$ (J. Marti, private communication). The offset between the radio and X-ray position is $2.5''$. The *Chandra* pointing accuracy is within the typical $0''.6$ absolute astrometry (90% confidence level radius) (Aldcroft et al., 2000) as we find that the position of the X-ray source CXOGLB J173545.6-302900 (CX1) is consistent with the position of the same source in a previous *Chandra* observation of the cluster, with an offset of only $0''.3$. Given the uncertainties in the X-ray and particularly the radio position only a small systematic offset is required for the sources to be fully consistent.

For an additional check of the accuracy of the *Chandra* pointing, possible optical and

infra-red counterparts were searched for. We searched for USNO-B1.0 (Monet et al., 2003) point sources that are close to ACIS Extract positions for the X-ray sources on the S3 chip. From this we get 3 optical sources that match the X-ray positions to within the $0''\!.6$ absolute astrometry (90% confidence level radius) for *Chandra* (Aldcroft et al., 2000). These sources are CXOU J173544.2-302736, CXOU J173545.6-303204 and CXOU J173536.4-302917 and have offsets of $0''\!.07$, $0''\!.39$, and $0''\!.54$ respectively. The corresponding USNO-B1.0 sources are 0594-0571302, 0595-0586465, and 0594-0571303 which have positional accuracies of $0''\!.2$, $0''\!.1$, $0''\!.4$ respectively (averaging the error in R.A. and Dec.). Matches with the 2MASS All-Sky Catalog of Point Sources (Cutri et al., 2003) were also searched for. Of the USNO-B1.0 matched sources, CXOU J173545.6-303204 is the only one to match a 2MASS source, with an offset of $0''\!.58$. CXOU J173550.1-303155 also has a possible 2MASS counterpart, with an offset of $0''\!.57$. The possible optical (USNO-B1.0) counterpart for this source has an offset of $0''\!.78$. To check how many accidental matches we get, we apply a random offset of up to $20''$ and count the number of matches (sources found to be within $0''\!.6$ of each other). This was repeated 1000 times and the number of mean accidental matches of X-ray sources with the USNO-B1.0 catalogue was found to be 0.2 ± 0.5. The 3 sources we find is significantly above this mean.

As the radio source is not seen to be fully consistent with any X-ray source there is the possibility that it is an unrelated source, for example a background AGN or quasar, in which case the radio source would likely still be present and any future radio observation might prove this. It is also possible that we may not have detected X1732−304 in quiescence. Only one photon is detected in the 0.5-8 keV band within the VLA error circle, which could very likely be a background photon. Assuming fewer than 5 counts were detected in the VLA error circle, this gives an upper limit on the count rate of 2.7×10^{-4} counts s^{-1}. We use XSPEC to estimate an upper limit on the flux from this count rate. Initially we fix the parameters of an absorbed neutron star atmosphere model to the appropriate cluster values expected for the effective temperature. The effective temperature is then adjusted to match the required count rate of 2.7×10^{-4} counts s^{-1}. The unabsorbed 0.5-10 keV luminosity upper limit is then determined to be 8×10^{31} ergs s^{-1}. Such a luminosity is slightly lower than typically seen for quiescent neutron stars (e.g. Heinke et al., 2003b; Pooley et al., 2003) although this scenario cannot be ruled out.

Assuming that CX2 is the quiescent counterpart to X1732−304, it is possible to put limits on the length of time that the source will stay in quiescence. In the deep

crustal heating model of quiescent neutron star emission (Brown et al., 1998) the quiescent luminosity depends on the time-averaged accretion rate of the source. Assuming standard core cooling, it is then possible to relate the quiescent flux, F_q, and the average flux during outburst, $\langle F_0 \rangle$, with the average time the source is in outburst, t_0, and quiescence, t_q, via $F_q \approx t_o/(t_o + t_q) \times \langle F_o \rangle/135$ (e.g., Wijnands et al., 2001a, 2002b). We use the bolometric flux during outburst as estimated by Wijnands et al. (2002b) to be 1.5×10^{-9} ergs cm^{-2} s^{-1}. To place upper limits on the thermal quiescent flux we use the neutron star atmosphere fit to the spectrum of CX2 with the column density at the cluster value. We fix the temperature to the upper limit from the fit and determine the bolometric flux (generating a dummy response from 0.001 - 100 keV and extrapolating the model). This gives $F_q < 3.3 \times 10^{-13}$ ergs cm^{-2} s^{-1}. The outburst from X1732$-$304 was seen to last at least 12 yr, so, assuming that $t_0 = 12$ yr, we get $t_q > 395$ yr. However, it is not clear how long the source was in outburst when it was first detected. If we assume that $t_0 = 17$ yr, then the lower limit for the quiescent time increases to $t_q > 560$ yr. We note that the long outburst episode of this transient will have heated the crust significantly out of thermal equilibrium with the core and therefore the crust might still be cooling down toward equilibrium again. If that is the case, then the thermal flux related to the state of the core is even lower than the measured value (hence the core is cooler) and the quiescent episode should be even longer to allow the core to cool down. We note that if CX2 is not the counterpart of the transient quiescent flux would be lower and therefore the predicted quiescent episodes would be even longer.

Disc-instability models suggest that such a long quiescent should not occur. During quiescence the disk will slowly fill up again and at some point, even a small change in mass transfer rate should trigger an outburst (e.g., Lasota, 2001). Another neutron star X-ray transient observed to have been in outburst for >10 yr is KS 1731-260 (see Chp. 6). The quiescent flux of this neutron star also leads to the length of predicted quiescent episodes of several hundred years (Wijnands et al., 2001a). However, the neutron star X-ray transient in the globular cluster NGC 6440 has much shorter outbursts and quiescent periods that are consistent with the observed quiescent flux (Chp. 4). Thus, it appears that for the quasi-persistent neutron stars X1732$-$304 and KS 1731-260 to be as cool as observed in quiescence either the quiescent periods are several hundreds of years long, or the quiescent periods are much shorter and enhanced neutrino cooling is required for the neutron star to cool more quickly. In the latter case it is possible that in these systems

the neutron stars are relatively heavy as suggested by Colpi et al. (2001).

5.3.2 Comparison with other globular clusters

Pooley et al. (2003) found a relationship between the number of X-ray sources (with 0.5-6 keV luminosity $L_X > 4 \times 10^{30}$ ergs s^{-1}) in a globular cluster and the stellar encounter rate of the cluster (see Fig. 1.11). These authors calculate the stellar encounter rate by performing a volume integral of the encounter rate per unit volume, $R \propto \rho^2/v$ (where ρ is the density and v is the velocity dispersion), out to the half-mass radius. This requires knowing the core density and velocity dispersion. Unfortunately, for Terzan 1 there are no measurements of the velocity dispersion available. However, we can relate the velocity dispersion to the core density, ρ_0, and core radius, r_c, via the virial theorem, and thus can estimate the encounter rate by $\rho_0^{1.5} r_c^2$ (Verbunt, 2003). As Terzan 1 is a 'core-collapse' cluster and the core is not well-defined, any estimate for the encounter rate based on core values will be unreliable. However, using the values for the core density, ρ_0, and core radius, r_c, from the Harris catalog (Harris, 1996, February 2003 version) we find that the core is a factor of 3.4 less dense than that of 47 Tuc and the core radius is a factor of 8 times smaller. We therefore estimate that the encounter rate of Terzan 1 will be a factor of $3.4^{1.5} \times 8^2 \sim 400$ smaller than in 47 Tuc. Thus, based on the core density and core radius, the encounter rate for Terzan 1 is many tens to hundreds of times smaller than the value of 47 Tuc. As 47 Tuc has a encounter rate of 396 (in the Pooley et al., 2003, normalisation), we estimate that Terzan 1 has an encounter rate of ~ 1, which from the Pooley et al. (2003) relationship would imply that there should only be ~ 1 X-ray source in Terzan 1. This is clearly not the case, as we detect 14 sources (though 2 are predicted to be not associated with the cluster).

As noted above, Terzan 1 is a core-collapse cluster, therefore any estimate based on the core radius and density will be unreliable. Thus, it is important to determine whether any change in these parameters could make this cluster consistent with the relationship. If the core radius is larger than assumed, this will have the corresponding effect of decreasing the computed density of the core, therefore it is difficult to increase the estimated encouter rate of Terzan 1 by the required factor of $\sim$50 to make it consistent with the Pooley et al. (2003) relationship. For instance, increasing the assumed core radius by a factor of 3 (to 7″2) decreases the computed core density by a factor of 3.09 (following Djorgovski, 1993),

and thus will increase the computed encounter rate by only a factor of 1.66. Uncertainty in the distance has a similarly small effect on the cluster parameters. Uncertainty in the reddening towards Terzan 1 can also have an effect on the estimated core density as the core density is calculated from the extinction corrected central surface brightness. In fact, using E(B-V)=2.48 (Ortolani et al., 1999), rather than the value from the Harris catalog, will increase ρ_0 by 77%, although still not enough to eliminate the discrepancy with the Pooley et al. (2003) relation.

To account for the number of detected X-ray sources it may be that the cluster was previously much larger and that most of the stars have been lost, perhaps due to passages through the Galactic disk as was suggested for NGC 6397 by Pooley et al. (2003). This idea is supported by the fact that Terzan 1 is in the bulge of the Galaxy and has the closest projection to the Galactic centre among known globular clusters. Further evidence for a previously more massive cluster comes from the spectroscopic study of Terzan 1 by Idiart et al. (2002). These authors identify apparent members of Terzan 1 with substantially higher metallicity and suggest that Terzan 1 may have captured these stars from the bulge during a previous epoch when the cluster was significantly more massive.

5.4 Conclusions

We have presented a ∼19 ks *Chandra* ACIS-S observation of the globular cluster Terzan 1. Within 1.4 arcmin of the cluster centre we detect 14 X-ray sources and predict that 2 of these are not associated with the cluster (background AGN or foreground objects). The brightest of these sources, CX1, is consistent with the position of CXOGLB J173545.6-302900 first observed during a short *Chandra* HRC-I observation of Terzan 1 (Wijnands et al., 2002b). This source has a particulary hard spectrum for a globular cluster source, with a simple power-law fit giving a photon index of 0.2 ± 0.2. Such a hard spectrum suggests that this could be an intermediate polar (Muno et al., 2004). The position of the second brightest source, CXOGLB J173547.2-302855 (CX2), is the only source to have a position that is consistent with all 3 of the previous *ROSAT* pointings that observed the neutron star transient X1732−304 (Johnston et al., 1995) as well as the *EXOSAT* observation. This source's X-ray color and spectrum suggest that it could be a quiescent neutron star and therefore we find that this source is the most likely candidate for the

quiescent counterpart of X1732−304. CX2 has a position closest to the position of the radio source detected in Terzan 1 by the VLA (Marti et al., 1998), though the positions are not fully consistent. Assuming standard core cooling, from the quiescent flux of CX2 we predict extremely long (>400 yr) quiescent episodes of X1732−304, or enhanced core cooling, to allow the neutron star to cool. Having estimated the stellar encounter rate of this cluster we find significantly more sources than expected by the relationship of Pooley et al. (2003) perhaps because the cluster was previously much larger and that most of the stars have been lost due to passages through the Galactic disk.

Cooling of the quasi-persistent neutron star X-ray transients KS 1731−260 and MXB 1659−29

In this chapter I present monitoring *Chandra* and *XMM-Newton* observations of two quiescent neutron star transients. These transients are both now in quiescence, after unusually long outbursts. These outbursts caused the neutron star crust to be heated out of thermal equilibrium with the core, and with these observations we track the cooling of the crust back into thermal equilibrium over a period of 4 years.

This chapter is based on a paper that has been accepted for publication in the Monthly Notices of the Royal Astronomical Society, by Cackett, E. M., Wijnands, R., Linares, M., Miller, J. M, Homan, J. and Lewin, W. H. G.

6.1 Introduction

Some X-ray transients (the quasi-persistent transients) spend an unusually long time in outburst, with outbursts lasting years to decades rather than the more common weeks to months. For the neutron-star quasi-persistent transients, during outbursts, the crust of the neutron star is heated to a point beyond thermal equilibrium with the stellar interior. Once accretion falls to quiescent levels, the crust cools thermally, emitting X-rays, until it reaches equilibrium again with the core (e.g., Rutledge et al., 2002b). Crust cooling curves allow us to probe the properties of neutron stars, such as, the kind of core cooling processes at work (which depends on the equation of state of ultra dense matter) and the heat conductivity of the crust (which likely depends on the properties of the iron lattice of the crust, such as its purity). While it is expected that the crust can cool significantly

between outbursts, the neutron star core should only cool significantly on much longer timescales. X-ray observations of the two quasi-persistent neutron star X-ray transients KS 1731−260 (Wijnands et al., 2001a; Wijnands, 2002; Wijnands et al., 2002a; Rutledge et al., 2002b; Wijnands, 2005) and MXB 1659−29 (Wijnands et al., 2003, 2004; Wijnands, 2004, 2005) have tracked the initial cooling of these neutron stars once they went into a quiescent state. In this chapter, we present additional *Chandra* and *XMM-Newton* observations that further track the cooling of these two neutron stars as they return to thermal equilibrium with the core.

6.1.1   KS 1731−260

KS 1731−260 was first detected in outburst in August 1989 by the *Mir-Kvant* instrument and further analysis revealed that the source was also found to be active in October 1988 (Sunyaev, 1989; Sunyaev et al., 1990a). As no previous telescopes had detected this source, it was classified as a soft X-ray transient and the detection of type I X-ray bursts identified the compact object as a neutron star. Since then, until early 2001, the source remained bright and was observed by many X-ray telescopes including the ART-P and SIGMA telescopes aboard *GRANAT*, *Ginga, ROSAT, RXTE, ASCA*, and *BeppoSAX* (Sunyaev, 1990b; Barret et al., 1992; Yamauchi & Koyama, 1990; Barret et al., 1998; Smith et al., 1997; Wijnands & van der Klis, 1997; Muno et al., 2000; Narita et al., 2001; Kuulkers et al., 2002). In early 2001, KS 1731−260 was undetected by monitoring observations by the All-Sky Monitor (ASM) on-board the *Rossi X-ray Timing Explorer* (*RXTE*) as can be seen by the ASM lightcurve of this source in Fig. 6.1 (top). Further pointed *RXTE* observations with the Proportional Counter Array (PCA) and the bulge scan observations of the Galactic centre region did not detect the source, with the first non-detection by the PCA observations on 2001 February 7 (Wijnands et al., 2001a). Using archival *RXTE*/PCA data, we find that the final detection of the source with *RXTE* was on 2001 January 21, thus it was still in outburst and actively accreting on this date. We extracted the *RXTE* X-ray spectrum of the source on that day and find that a 2-10 keV unabsorbed flux of $\sim 2.3 \times 10^{-10}$ ergs cm^{-2} s^{-1} which corresponds to a luminosity of $\sim 1 \times 10^{36}$ erg s^{-1} for a distance of 7 kpc (we assume a distance to KS 1731−260 of 7 kpc throughout the chapter, Muno et al., 2000). Thus, KS 1731−260 went into a quiescent state sometime after 2001 January 21 and it was actively accreting for around 12.5 years.
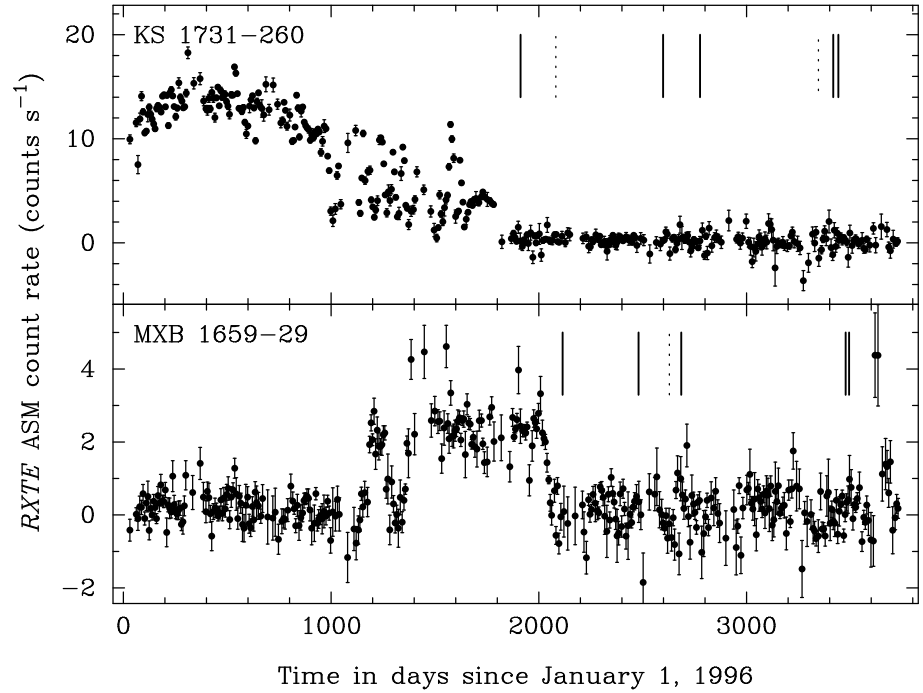
Figure 6.1: *RXTE* All-Sky Monitor 7-day averaged lightcurve for KS 1731−260 (top) and MXB 1659−29 (bottom). The times of the *Chandra* and *XMM-Newton* observations of these sources during quiescence are marked by solid and dotted vertical lines respectively. The last detection of KS 1731−260 in outburst was 1847 days after 1996 January 1, and the last detection of MXB 1659−29 was 2076 days after 1996 January 1.

This last detection in outburst gives a much better constraint than had previously been found for when this source turned off. Unfortunately, there are no other known outbursts of this source, thus we are unable to tell whether this is a typical outburst for this source, or whether previous outbursts have been significantly longer or shorter.

Within two months of KS 1731–260 going into a quiescent phase there was a ∼20 ks *Chandra* Advanced CCD Imaging Spectrometer (using ACIS-S mode) observation of this source on 2001 March 27 (Wijnands et al., 2001a). These authors detected the source at an unabsorbed flux of $\sim 2 \times 10^{-13}$ ergs cm^{-2} s^{-1} (0.5-10 keV), which corresponds to a 0.5-10 keV luminosity of $\sim 1 \times 10^{33}$ ergs s^{-1}, a factor of 10^3 lower than at the last *RXTE*/PCA detection. Observations by *BeppoSAX* confirmed the low flux of the source (Burderi et al., 2002) reported by Wijnands et al. (2001a). Wijnands et al. (2001a) note that this luminosity is much lower than expected if this is due to the cooling of the neutron star unless the source spends an unusually long amount of time in a quiescent state (at least several hundred years) and even longer if the crust is dominating emission from the

neutron star, or that alternatively, enhanced cooling of the core occurs due to higher levels of neutrino emission. Rutledge et al. (2002b) note that given the long outburst, the crust would be dominating the thermal emission from the neutron star as it would have been heated significantly out of equilibrium with the core. Given the accretion history of this source Rutledge et al. (2002b) simulate the quiescent lightcurve for the source, finding that depending on the crust and core microphysics, the cooling timescale for the crust to return to equilibrium with the core ranges from 1 to 30 years.

Additional X-ray observations of this source in quiescence with *XMM-Newton* in 2001 September 13-14 revealed that the source had dimmed further to a 0.5-10 keV luminosity of approximately $(2-5) \times 10^{32}$ ergs s^{-1} (Wijnands et al., 2002a). Under the neutron star cooling model, this decrease in luminosity is interpreted as rapid cooling of the the neutron star crust (a factor a $\sim$2-3 in just half a year) suggesting that the crust has a high thermal conductivity and that enhanced core cooling processes are required for the core to be so cool. Preliminary analysis of two extra *Chandra* observations of this source on 2003 February 11 and 2003 August 8 yet again showed a further decrease in the luminosity of the source with a possible flattening of the luminosity cooling curve suggesting that the crust may have returned to equilibrium with the core (Wijnands, 2005). In this chapter we present the final analysis of these *Chandra* data, re-analyse all the previous *Chandra* and *XMM-Newton* observations of this source in quiescence and also present 2 additional *Chandra* observations and 1 additional *XMM-Newton* observation of this source.

6.1.2   MXB 1659−29

MXB 1659−29 is an X-ray transient discovered by Lewin et al. (1976) with *SAS-3* in 1976 October. Type-I X-ray bursts detected by these initial observations established that the compact object was a neutron star. Between 1976 October and 1978 September, this source was detected several times by both *SAS-3* and *HEAO 1* (Lewin et al., 1978; Share et al., 1978; Griffiths et al., 1978; Doxsey et al., 1979; Cominsky et al., 1983; Cominsky & Wood, 1984, 1989). The source exhibits X-ray eclipses and dips with a period of $\sim$ 7.1 hr, due to the orbital period (Cominsky & Wood, 1984, 1989). In 1979 July, the *Hakucho* satellite failed to detect the source (Cominsky et al., 1983), and later observations by *EXOSAT* and *ROSAT* (Oosterbroek et al., 2001; Verbunt, 2001) failed to detect the source also. The 0.5-10 keV upper limit on the unabsorbed flux from the *ROSAT* observations in 1991

and 1992 is $(1-2) \times 10^{-14}$ ergs cm^{-2} s^{-1} (Verbunt, 2001; Wijnands, 2002; Oosterbroek et al., 2001).

The source remained in a quiescent state for a period of 21 years, until on 1999 April 2 *BeppoSAX* detected the source in outburst again (in 't Zand et al., 1999a). This outburst was also detected by the *RXTE* ASM (see the ASM lightcurve in Fig. 6.1) and studied in detail by pointed observations with the *RXTE* PCA, *BeppoSAX* and *XMM-Newton* (Wachter et al., 2000; Oosterbroek et al., 2001; Sidoli et al., 2001; Wijnands et al., 2001b, 2002c).

After an outburst of approximately 2.5 years in length, MXB 1659−29 went back into a quiescent state in 2001 September. The last detection of the source was on 2001 September 7 with the *RXTE* PCA, and the source was not detected on 2001 September 14, 24, 30 (Wijnands et al., 2002c). Just over a month after the source returned to a quiescent state, *Chandra* observations, on 2001 October 15, detected it with an unabsorbed 0.5-10 keV flux of $(2.7-3.6) \times 10^{-13}$ ergs cm^{-2} s^{-1} which corresponds to a 0.5-10 keV luminosity of $(3.2-4.3) \times 10^{33}$ ergs s^{-1} for a distance of 10 kpc (Wijnands et al., 2003). This flux is a factor greater than 10 higher than the *ROSAT* non-detection upper limit during quiescence in the early 1990s, suggesting that the emission is dominated by thermal emission from the neutron star crust that has been heated significantly out of thermal equilibrium with the core. However, as in the case of KS 1731−260, the flux was lower than expected given the accretion history, suggesting that enhanced cooling processes are occurring in the core. Further *Chandra* observations of MXB 1659−29 in quiescence on 2002 October 15 and 2003 May 9 showed that the flux was decaying exponentially, with the source flux decreasing by a factor of 7-9 over the 1.5 years between the 2001 and 2003 *Chandra* observations (Wijnands et al., 2004; Wijnands, 2004, 2005). This is consistent with the accretion-heated crust cooling down in quiescence. The rapid timescale of the cooling implies that the crust may have a large thermal conductivity (Wijnands et al., 2004; Wijnands, 2004, 2005). In this chapter we re-analyse all the previous observations of this source in quiescence with *Chandra* and also present 2 additional *Chandra* observations and 1 additional *XMM-Newton* observation of this source.

Table 6.1: Details of the *Chandra* (CXO) and *XMM-Newton* (XMM) observations of KS 1731−260. The *XMM-Newton* observations 0137950201 and 0137950301 were so close in time that they were merged together. Here we give the details for the merged data. The background-subtracted net count rate is for the 0.5-10 keV band.

ObsID (Telescope)	Date	Good Time (ks)	Net Count Rate (counts s^{-1})
2428 (CXO)	2001 March 27	19.4	$(9.0 \pm 0.7) \times 10^{-3}$
0137950201/301 (XMM)	2001 September 13/14	46.0 (MOS1)	$(1.7 \pm 0.2) \times 10^{-3}$ (MOS1)
		46.1 (MOS2)	$(2.0 \pm 0.2) \times 10^{-3}$ (MOS2)
		33.8 (pn)	$(3.7 \pm 0.4) \times 10^{-3}$ (pn)
3796 (CXO)	2003 February 11	29.7	$(1.4 \pm 0.2) \times 10^{-3}$
3797 (CXO)	2003 August 8	29.7	$(1.1 \pm 0.2) \times 10^{-3}$
0202680101 (XMM)	2005 February 28/March 1	70.0 (MOS1)	$(2.4 \pm 1.6) \times 10^{-4}$ (MOS1)
		70.0 (MOS2)	$(6.4 \pm 1.7) \times 10^{-4}$ (MOS2)
		46.0 (pn)	$(1.1 \pm 0.4) \times 10^{-3}$ (pn)
6279 (CXO)	2005 May 10	10.4	$(0.5 \pm 0.3) \times 10^{-3}$
5468 (CXO)	2005 June 4	38.5	$(0.8 \pm 0.2) \times 10^{-3}$

6.2 Observations and Analysis

6.2.1 KS 1731−260

Here we analyse 5 *Chandra* and 3 *XMM-Newton* observations of KS 1731−260 in a quiescent state spread over ∼4 years since the end of the outburst in 2001 February. Details of all the observations are given in Table 6.1. We will first describe the analysis of the *Chandra* and then the *XMM-Newton* data.

Chandra analysis

All the *Chandra* observations were taken in ACIS-S configuration. The *Chandra* data were reprocessed and analysed using CIAO (v3.3) and CALDB (v3.2.1) following the standard analysis threads. For all of the *Chandra* observations, the source lightcurve and spectrum was extracted from a circle of radius 3″ around the source position, and the background lightcurve and spectrum was extracted from a source-free annulus with inner radius 7″ and outer radius 25″. We checked the background lightcurve for significant background flares, and none were found. The background-subtracted net count rates in the 0.5-10 keV band

are given in Table 6.1.

XMM-Newton analysis

The first two *XMM-Newton* observations were separated by only a matter of hours, therefore we combine both of these together to increase sensitivity (as did Wijnands et al., 2002a). Here we analyse data from the three EPIC instruments on-board *XMM-Newton* - the two metal oxide semiconductor (MOS) cameras and the pn camera which were operated in full-frame mode with the thin filter in all the observations. To analyse the *XMM-Newton* data we use the Science Analysis Software (SAS, version 6.5.0). We extract source lightcurves and spectra from a circle of radius $10''$. The background extraction region was chosen to be a source-free circle of radius $1'$ close to the source position. An annulus was not used because of the location of a nearby source, 2MASSI J173412.7-260548, approximately $30''$away. Although this source is also present in the *Chandra* data the significantly better angular resolution of *Chandra* allows the use of an annulus for background extraction.

In the merged observations (ObsID 0137950201/301) background flares were present. We kept all data where the count rate for PI > 10 keV was less than 10 counts s^{-1} for both the MOS and pn. In the last *XMM-Newton* observation (ObsID 0202680101) background flares were also present. In this case we kept all data where the count rate for PI > 10 keV was less than 10 counts s^{-1} for the MOS and less than 15 counts s^{-1} for the pn. We note that in this last observation the source is not obviously present when viewing an image in the full energy range. It only becomes apparent when restricting the energy range to between 1 and 2 keV where the vast majority of the photons from the source are emitted during this observation. The net count rates for these observations are given in Table 6.1.

Spectral analysis

For spectral analysis of the data we use `XSPEC` (Arnaud, 1996). The data was fit with an absorbed neutron star hydrogen atmosphere model (nonmagnetic case, Zavlin, Pavlov & Shibanov, 1996; Pavlov, Shibanov & Zavlin, 1991) with the mass and radius fixed at the canonical values (1.4 M$_\odot$ and 10 km respectively). Both the *Chandra* and *XMM-Newton* data were fit simultaneously with the column density tied between the observations

and the temperature left as a free parameter. The column density was tied between the observations as there were too few counts in the last observations to constrain this parameter. The parameters for the EPIC MOS1, MOS2 and pn spectra for each *XMM-Newton* observation were all tied. The normalisation of the neutron star atmosphere model was fixed for a distance of 7 kpc (distance determined by Muno et al., 2000). Although this distance is uncertain, if this parameter is left free it goes to an unrealistic value that would put the distance to the source at ~ 20 kpc (although the error on the distance is very large and includes the assumed 7 kpc distance). Hence, we chose to fix the distance at 7 kpc.

The data were unbinned, due to the low number of counts in the last few observations, and the W statistic (Wachter et al., 1979) was used in the spectral fitting process with background subtraction. The W statistic is adapted from the Cash statistic (Cash, 1979), but allows background subtraction. We note that spectral fitting to the first *Chandra* observation using both χ^2 and W-statistics resulted in the same parameters to within the uncertainties. To determine the bolometric flux we extrapolated the model to the energy range 0.01 - 100 keV, which gives approximate bolometric fluxes. The results of the spectral fits are detailed in Table 6.2. The spectral parameters for the first *Chandra* and *XMM-Newton* observations are consistent with those determined by Wijnands et al. (2002a). We also note that we get results consistent with the previously published data for KS 1731−260 Wijnands et al. (2002a) when using alternative models to the NSA model (i.e., a blackbody model).

Cooling curves

It is clear from Table 6.2 that both the effective temperature for an observer at infinity ($T_{\rm eff}^\infty$) and the bolometric flux $F_{\rm bol}$ decrease significantly with time. This cooling cannot be fit by a simple exponential decay, giving reduced χ^2 values of 4.3 and 4.8 for fits to the temperature and flux curves (see the dotted curves in Fig. 6.2. However, it is fit well by an exponential decay that levels off to a constant offset of the form $y(t) = a \exp\left[-(t - t_0)/b\right] + c$, with a a normalisation constant, b the e-folding time, c a constant offset, and t_0 the start time. When fitting to the data, t_0 was fixed to midday on the last day that the source was observed to be active, MJD 51930.5, though we find that the other parameters are not very sensitive to the exact value of t_0. The best-fitting cooling

149

Table 6.2: Neutron star atmosphere model fits to the X-ray spectrum of KS 1731−260 for 5 *Chandra* (CXO) and 3 *XMM-Newton* (XMM) observations. Luminosity is calculated assuming a distance to the source of 7 kpc. 1-σ errors on the parameters are given. The Modified Julian Date (MJD) given correspond to the mid-point of the observation. Note the column density parameter is tied between the observations when simultaneously fitting the data, and we determine $N_H = (1.3 \pm 0.1) \times 10^{22}$ cm^{-2}.

ObsID (Telescope)	MJD	kT$^\infty_{\text{eff}}$ (eV)	Bolometric flux $(10^{-13}$ ergs cm^{-2} s$^{-1})$	Luminosity $(10^{32}$ ergs s$^{-1})$
2428 (CXO)	51995.1	103^{+2}_{-3}	$4.2^{+0.3}_{-0.5}$	24^{+2}_{-3}
0137950201/301 (XMM)	52165.7	88 ± 2	2.2 ± 0.2	13 ± 1
3796 (CXO)	52681.6	76 ± 3	1.2 ± 0.2	7 ± 1
3797 (CXO)	52859.5	72 ± 4	1.0 ± 0.2	6 ± 1
0202680101 (XMM)	53430.5	70 ± 3	$0.9^{+0.2}_{-0.1}$	5 ± 1
6279 (CXO)	53500.4	67^{+6}_{-9}	0.8 ± 0.3	4 ± 2
5468 (CXO)	53525.4	70 ± 3	0.9 ± 0.2	5 ± 1

curves are shown in Fig. 6.2. For the T^∞_{eff} curve $a = 39.5 \pm 3.6$ eV, $b = 325 \pm 101$ days, and $c = 70.0 \pm 1.6$ eV, with $\chi^2_\nu = 0.2$. For the F_{bol} curve $a = (4.3 \pm 0.5) \times 10^{-13}$ ergs cm^{-2} s^{-1}, $b = 212 \pm 60$ days, and $c = (9.2 \pm 0.9) \times 10^{-14}$ ergs cm^{-2} s^{-1}, with $\chi^2_\nu = 0.4$. The reason for the difference between the e-folding times of the flux and effective temperature curves is explained below.

Relationship between flux and temperature cooling timescales

Assuming that the X-rays are due to some blackbody-type emission, then the flux, F, and temperature, T, and just simply related via

$$F = AT^4 \,, \tag{6.1}$$

where $A = \frac{R^2}{D^2}\sigma$ and R is the emitting radius, D the distance, and σ the Stefan-Boltzmann constant. We are modelling the cooling of the neutron star surface as an exponential decay to a constant level, i.e.,

$$T(t) = T_\infty + T'(t) \tag{6.2}$$
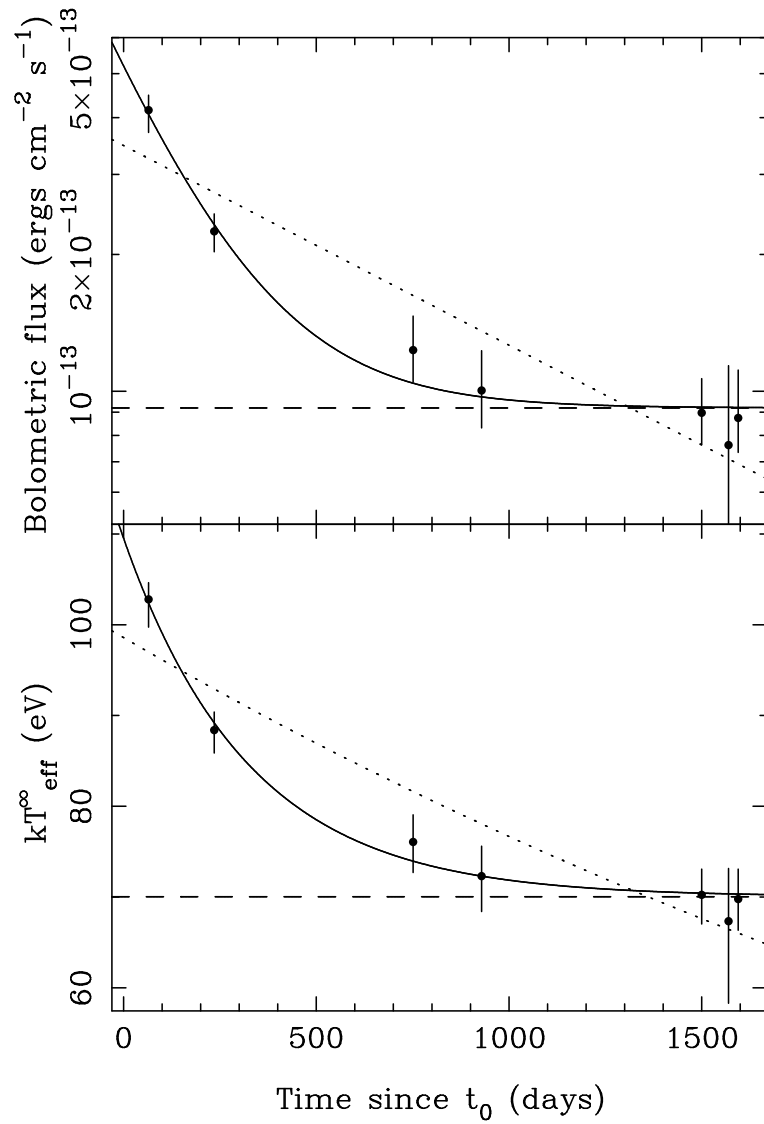
Figure 6.2: Cooling curves for KS1731−260. *Top*: Bolometric flux versus time since t_0, the last detection of the source accreting. The solid line shows the best fitting exponential decay to a constant. The constant is indicated as a dashed line. The dotted line shows the best fitting simple exponential decay, which does not fit the data well. *Bottom*: Effective temperature for an observer at infinity versus time since the end of the outburst. The lines are as above.

where T_∞ is the temperature at $t = \infty$ which we assume here to be constant, and $T'(t)$ describes the evolution of the temperature of the neutron star crust with time, which we model as:

$$T'(t) = a \exp\left[-(t - t_0)/b\right],\qquad(6.3)$$

with a a normalisation constant, b the e-folding time, and t_0 the start time. Combining Eq. 6.1 and 6.2, leads to

$$F(t) = AT(t)^4 = A[T_\infty + T'(t)]^4 .\qquad(6.4)$$

At the start of the cooling, when $T_\infty \ll T'(t)$, then the $T'(t)^4$ term dominates, and Eq. 6.4 becomes

$$F(t) \approx AT'(t)^4 = Aae^{-4(t-t_0)/b} .\qquad(6.5)$$

and there should be a factor of 4 difference between the e-folding times of F and T. This was found to be the case for the initial cooling of MXB 1659$-$29 (Wijnands et al., 2004). However, further on in the cooling, once $T'(t) \sim T_\infty$, then the e-folding time of F becomes a complicated function of the e-folding time of T due to the constant term. Finally, once the cooling is negligible and $T'(t) \ll T_\infty$, then obviously, $F(t) = AT_\infty^4$.

6.2.2   MXB 1659$-$29

We analyse 5 *Chandra* observations and 1 *XMM-Newton* observation of MXB 1659$-$29 whilst the source was in a quiescent state spanning a period of $\sim$4 years after the end of the outburst in September 2001. Details of the observations are given in Table 6.3. We will first describe the *Chandra* and then the *XMM-Newton* data reduction and analysis.

Chandra analysis

All the *Chandra* observations of this source were taken in the ACIS-S configuration. As in the analysis of the *Chandra* data for KS 1731$-$260, we reprocess and analyse the data using Ciao (v3.3), Caldb (v3.2.1) and the standard analysis threads. For all of the *Chandra* observations, the source lightcurve and spectrum was extracted from a circle of radius $3''$ around the source position, and the background lightcurve and spectrum was extracted from a source-free annulus with inner radius $7''$ and outer radius $22''$. We checked the background lightcurve for significant background flares, and none were found.

Table 6.3: Details of the *Chandra* (CXO) and *XMM-Newton* (XMM) observations of MXB 1659−29. The background-subtracted net count rate is for the 0.5-10 keV band.

ObsID (Telescope)	Date	Good Time (ks)	Net Count Rate (counts s^{-1})
2688 (CXO)	2001 October 15	17.9	$(5.2 \pm 0.2) \times 10^{-2}$
3794 (CXO)	2002 October 15	26.1	$(9.8 \pm 0.6) \times 10^{-3}$
0153190101 (XMM)	2003 March 13	65.3 (MOS1)	$(3.2 \pm 0.3) \times 10^{-3}$ (MOS1)
		65.4 (MOS2)	$(2.9 \pm 0.3) \times 10^{-3}$ (MOS2)
		47.1 (pn)	$(1.1 \pm 0.1) \times 10^{-2}$ (pn)
3795 (CXO)	2003 May 9	26.2	$(3.9 \pm 0.4) \times 10^{-3}$
5469 (CXO)	2005 July 8	27.7	$(1.1 \pm 0.2) \times 10^{-3}$
6337 (CXO)	2005 July 25	17.8	$(0.7 \pm 0.2) \times 10^{-3}$

The analysis of the data for MXB 1659−29 is complicated by the fact that this source is eclipsing with an eclipse duration of ∼900 s and period of 7.1 hr (Cominsky & Wood, 1984, 1989; Wachter et al., 2000; Oosterbroek et al., 2001), and so we receive no (or minimal at most) counts from the source during the eclipse in quiescence (Wijnands et al., 2003). While there are enough counts in the first *Chandra* observation to detect the eclipse in the lightcurve (Wijnands et al., 2003), this is impossible with later observations and so we manually reduce the exposure time by 900 s to compensate for the source being in eclipse, having checked that only one eclipse occurs during each observation using the ephemeris of Oosterbroek et al. (2001). The background-subtracted net count rates in the 0.5-10 keV band are given in Table 6.3.

XMM-Newton analysis

To analyse the *XMM-Newton* observation of MXB 1659−29 we use Sas (version 6.5.0). We analyse data from the EPIC MOS1, MOS2 and pn cameras which were operated in full-frame mode with the medium filter (the source is too faint to be detected on the RGS). The source lightcurve and spectrum was extracted from a circle with a 15″radius. The background lightcurve and spectrum was extracted from a source-free annulus with inner radius of 40″and outer radius of 100″. Several background flares were present during the

observation. We chose to keep all data where the count rate for PI > 10 keV was less than 7 counts s^{-1} for the MOS and less than 10 counts s^{-1} for the pn detector. Using the ephemeris of Oosterbroek et al. (2001) we determined that 3 eclipses occurred during the good time of the MOS observations, and so we manually reduce the exposure times for the MOS observations by 2.7 ks. In the pn observations several flaring events occurred during the eclipse times. We determine the total amount of good time for the pn during the eclipses to be 1.675 ks, and thus we reduce the exposure time by this amount. The net count rates for this *XMM-Newton* observation are given in Table 6.3.

Spectral analysis

We perform a similar spectral analysis for the MXB 1659−29 data as for the KS 1731−260. The *Chandra* and *XMM-Newton* spectra are left unbinned and fit simultaneously with an absorbed non-magnetic neutron star hydrogen atmosphere model using the W statistic with background subtraction. The column density is tied between the separate observations, the mass and radius fixed at their canonical values, and the temperature was the only parameter left free between the observations. The parameters are tied between the MOS1, MOS2 and pn spectra of the *XMM-Newton* observation. The distance to this source is in the range 10-13 kpc (Muno et al., 2001; Oosterbroek et al., 2001). When leaving the normalisation as a free parameter in the *Chandra* fits this leads to a distance to the source of 7.8 kpc with no constraint on the upper limit of the distance and a lower limit of 6.2 kpc. So that the uncertainty in the distance does not dominate the uncertainties in the other parameters, we fix the normalisation of the neutron star atmosphere for a distance of 10 kpc. Spectral parameters determined by these fits are detailed in Table 6.4. The parameters we find for the first three *Chandra* observations which were previously analysed by Wijnands et al. (2004) are consistent with the values these authors determined when assuming the same distance.

Cooling curves

From the spectral fitting we find that both $T_{\mathrm{eff}}^{\infty}$ and F_{bol} decrease significantly with time after the end of the outburst. We measure an unabsorbed 0.5 - 10 keV flux of $6.3^{+2.7}_{-2.5} \times 10^{-15}$ ergs cm^{-2} s^{-1} during the last *Chandra* observation which is now lower than the upper

Table 6.4: Neutron star atmosphere model fits to the X-ray spectrum of MXB 1659−29 for 5 *Chandra* (CXO) and 1 *XMM-Newton* (XMM) observations. Luminosity is calculated assuming a distance to the source of 10 kpc. 1-σ errors on the parameters are given. The MJD given correspond to the mid-point of the observation. Note the column density parameter is tied between the observations when simultaneously fitting the data, and we determine $N_H = (0.20 \pm 0.02) \times 10^{22}$ cm^{-2}.

ObsID (Telescope)	MJD	kT$^{\infty}_{\text{eff}}$ (eV)	Bolometric flux (10^{-14} ergs cm^{-2} s^{-1})	Luminosity (10^{32} ergs s^{-1})
2688 (CXO)	52197.8	121 ± 2	41 ± 3	49 ± 3
3794 (CXO)	52563.2	85 ± 2	10 ± 1	12 ± 1
0153190101 (XMM)	52712.2	77 ± 1	$6.6^{+0.4}_{-0.5}$	$7.9^{+0.5}_{-0.6}$
3795 (CXO)	52768.9	73^{+2}_{-1}	$5.1^{+0.6}_{-0.4}$	$6.1^{+0.7}_{-0.4}$
5469 (CXO)	53560.0	58^{+3}_{-4}	$2.0^{+0.4}_{-0.5}$	$2.4^{+0.5}_{-0.6}$
6337 (CXO)	53576.7	54^{+4}_{-5}	1.5 ± 0.5	1.8 ± 0.6

limit from the previous non-detection with *ROSAT* in the early 1990s when the source had been in quiescence for over 10 years. As with KS 1731−260 this cooling cannot be fit by a simple exponential decay curve, giving reduced χ^2 values of 17.5 and 13.6 for fits to the temperature and flux curves (see dotted line in Fig.6.3) . The cooling curves require an exponential decay which levels off to a constant of the form $y(t) = a \exp\left[-(t - t_0)/b\right] + c$. When fitting to the data, t_0 was fixed to midday on the last day that the source was observed to be active, MJD 52159.5. The best-fitting cooling curves are shown in Fig. 6.3. For the T^{∞}_{eff} curve $a = 75.0 \pm 2.8$ eV, $b = 505 \pm 59$ days, and $c = 51.6 \pm 1.4$ eV, with $\chi^2_{\nu} = 0.5$. For the F_{bol} curve $a = (4.5 \pm 0.2) \times 10^{-13}$ ergs cm^{-2} s^{-1}, $b = 242 \pm 13$ days, and $c = (1.7 \pm 0.3) \times 10^{-14}$ ergs cm^{-2} s^{-1}, with $\chi^2_{\nu} = 0.5$.

6.3   Discussion

We have presented *Chandra* and *XMM-Newton* observations monitoring two quasi-persistent neutron star X-ray transients (KS 1731−260 and MXB 1659−29) in a quiescent state. The long accretion episodes onto both of these neutron stars before they went into quiescence significantly heated the neutron star crust out of equilibrium with the core. The moni-
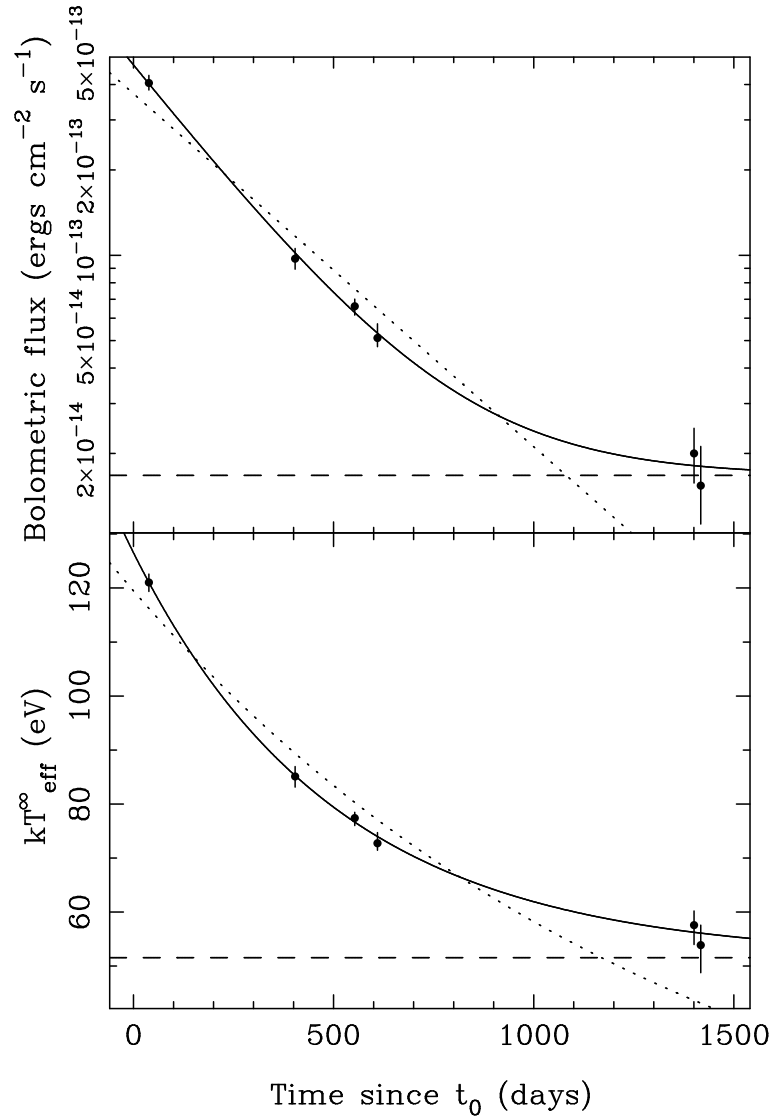
Figure 6.3: Cooling curves for MXB1659−29. *Top*: Bolometric flux versus time since t_0, the last detection of the source accreting. The solid line shows the best fitting exponential decay to a constant. The constant is indicated as a dashed line. The dotted line shows the best fitting simple exponential decay, which does not fit the data well. *Bottom*: Effective temperature for an observer at infinity versus time since the end of the outburst. The lines are as above.

toring observations cover a period of ~4 years since the sources returned to quiescence. Spectral fitting with an absorbed neutron star hydrogen atmosphere model to the data has clearly shown both of them cooling exponentially over time. From the initial results of this monitoring (Wijnands et al., 2002a, 2004) and the preliminary results of Wijnands (2005) it was not clear whether either of the neutron star crusts had reached thermal equilibrium with the cores. However, the results of this latest monitoring indicates that KS 1731−260 and MXB 1659−29 have now reached equilibrium again and we have been able to measure the base level of the flux and effective temperature of these sources resulting from the state of the hot core. The additional data in this current work provides a significant improvement on the previous work with respect to constraints on the cooling curve.

KS 1731−260 initially decreased by a factor of 2 in bolometric flux over the first half a year. Over the ~4 years since the source went into quiescence it has decreased in flux by a factor of ~5. It reached this level ~2.5 years after the end of the outburst and has remained at it since then, indicating that the crust returned to equilibrium with the core in this amount of time. This base level is set by the temperature of the core, which depends on the time-averaged mass accretion rate onto the source over thousands of years. Fitting an exponential decay with a constant offset to the data we get the equilibrium temperature to be 70.0 ± 1.6 eV, and the base bolometric flux level due to thermal emission from the core as $(9.2 \pm 0.9) \times 10^{-14}$ ergs cm^{-2} s^{-1}, which corresponds to a luminosity of $(5.4 \pm 0.5) \times 10^{32}$ ergs s^{-1}. The e-folding times of the exponential decay were determined to be 325 ± 101 days for the temperature cooling curve and 212 ± 60 days for the flux cooling curve.

MXB 1659−29 decreased by a factor of 4 in bolometric flux over the first year after going into quiescence, and by a factor of 24 over the ~4 years of monitoring. Wijnands et al. (2004) found no evidence after the first 3 *Chandra* observations of this source that the temperature or flux was reaching a equilibrium level set by the temperature of the core. The additional last 2 *Chandra* observations presented here indicate that the rate of cooling has decreased. Fitting an exponential decay with a constant offset to the data reveals that it has reached the base level which we determine to be 51.6 ± 1.4 eV for the temperature and $(1.7 \pm 0.3) \times 10^{-14}$ ergs cm^{-2} s^{-1} for the bolometric flux, which corresponds to a luminosity of $(2.0 \pm 0.4) \times 10^{32}$ ergs s^{-1} (assuming d=10 kpc). The e-folding times of the exponential decay were determined to be 505 ± 59 days for the temperature cooling curve

and 242 ± 13 days for the flux cooling curve.

Rutledge et al. (2002b) calculated detailed cooling curves for KS 1731$-$260 predicting the behaviour of the quiescent thermal emission from the neutron star given the source's accretion history (see their fig. 3). Their models compare how the emission could evolve for standard versus enhanced core cooling and low versus high crust thermal conductivity. These authors find that regardless of the core cooling, if the crust has a low thermal conductivity, then the crust should dominate emission over the core for $\sim$30 years, after which time there is a large drop in the source luminosity. For high-conductivity crusts the timescale for this transition is much shorter, $\sim$1 year. Comparing these timescales to the observed cooling of KS 1731$-$260, then, in the context of these models, the crust in this source must have a high thermal conductivity (Wijnands et al., 2002a; Wijnands, 2005), suggesting that it may be made of a pure iron lattice as increasing levels of impurity lower the conductivity. Unfortunately no detailed cooling curves have been calculated for MXB 1659$-$29. As the cooling is dependent on the accretion history of the source, we cannot directly compare the cooling of MXB 1659$-$29 with the model curves calculated for KS1731$-$260 by Rutledge et al. (2002b). However, in these models to see a rapid drop in flux within a few years of the source going into quiescence the crust must have a high conductivity, though there may be other physical processes in the crust that allow it to cool rapidly. In particular, we note that the Rutledge et al. (2002b) models do not include Cooper-pair neutrino emission in the crust which will change the behaviour significantly (e.g., Yakovlev, Kaminker & Levenfish, 1999). See the discussion in Jonker et al. (2006) for further comment on this difference.

Once the crust has cooled, the quiescent luminosity is set by the emission from the hot core (Rutledge et al., 2002b). In the standard core cooling mechanisms the heat lost by neutrino emission is negligible and thus the heat deposited in the star is radiated as thermal emission. In the case where enhanced core cooling is allowed, the enhanced level of neutrino emission, via the direct Urca process or Cooper-pairing, means that the vast majority of heat deposited escapes as neutrinos (Colpi et al., 2001; Ushomirsky & Rutledge, 2001; Rutledge et al., 2002b; Gusakov et al., 2004). If enhanced core cooling occurs, then the quiescent luminosity set by the core temperature is significantly lower than if only standard core cooling occurs. We note that continued cooling is predicted in the Rutledge et al. (2002b) models after the crust and core are in equilibrium. However, this cooling is at a significantly slower rate.

Importantly, in both sources we have now measured the thermal equilibrium temperature, which is set by the core temperature, for the first time. The quiescent luminosity at the equilibrium level of both these sources is quite typical of the quiescent emission from other 'normal' X-ray transients (e.g. see fig. 5 in Jonker et al., 2004b) whose outbursts are not as long as those of either source and last usually for only weeks to months. For the core of KS 1731−260 and MXB 1659−29 to have a similar temperature, and hence quiescent luminosity, to the other X-ray transients then either the time-averaged mass accretion rate has to be similar to the other X-ray transients, or enhanced levels of core cooling are required. For the time-averaged mass accretion rates to be similar to other X-ray transients this would require extremely long periods of quiescence of the order of hundreds to thousands of years if the observed outbursts are typical. For MXB 1659−29 there was only a period of 21 years between outbursts and both known outbursts lasted for several years. The long-timescale accretion history for KS 1731−260 is less clear with only one outburst having been observed, however, extremely long quiescent periods are hard to explain with disk instability models (e.g. Lasota, 2001). The measurement of the equilibrium level for both these sources confirms the previous findings by (Wijnands et al., 2002a, 2004; Wijnands, 2005) from initial monitoring that enhanced core cooling processes are required for these sources.

Comparing the *e*-folding timescales of the two sources, we find that KS 1731−260 cools at a faster rate than MXB 1659−29 (by a factor of ∼1.5), suggesting that the heat conductivity of the crust in KS 1731−260 is greater than that in MXB 1659−29. This interesting difference is likely due to differences in the properties of the crust between the two sources. In the (Rutledge et al., 2002b) models this would mean that KS 1731−260 has less impurities in the crust compared to MXB 1659−29 as a pure iron crust has a higher conductivity than one containing heavier metals also. However, one might expect the opposite to be the case, given that KS 1731−260 was actively accreting for 5 times longer than MXB 1659−29.

Given that we now have accurate cooling curves for these sources, and know the equilibrium level temperature, which places limits on the long-term time-averaged mass accretion rate, theoretical models need to be fit to this data to determine how high the thermal conductivity needs to be and what levels of neutrino emissions are really needed, or any alternative properties that can account for the rapid cooling of the crust. As more than one outburst has been observed for MXB 1659−29, and because the cooling curve

is much better constrained, we suggest that this source is possibly a better object to determine accurate theoretical cooling curves for than KS 1731−260.

Although some neutron-star transients do not require enhanced core cooling to explain their quiescent luminosity e.g. Aql X−1, 4U 1608−522 (Colpi et al., 2001), XTE J2123−058 (assuming the recurrence timescale is >70 years, Tomsick et al., 2004) and SAX J1748.8−2021 in the globular cluster NGC 6440 (Chp. 4), there are several neutron-star transients in addition to KS 1731−260 and MXB 1659−29 that require either very-low time-averaged mass accretion rates or enhanced core cooling to explain their quiescent luminosity e.g. Cen X-4 (Colpi et al., 2001), X1732−304 in the globular cluster Terzan 1 (Chp. 5, Wijnands et al., 2002b), RX J170930.2−263927 (Jonker et al., 2003), SAX J1810.8−2609 (Jonker et al., 2004a), EXO 1747−214 (Tomsick et al., 2005) and 1H 1905+000 (Jonker et al., 2006). While the quiescent luminosity of KS 1731−260 and MXB 1659−29 is comparable to many quiescent neutron star transients, it is significantly higher than the emerging group of quiescent neutron star transients that are very faint in quiescence, with quiescent luminosities of less than 10^{32} ergs s^{-1}. Although these faint quiescent sources include the millisecond X-ray pulsars SAX J1808.4−3658 (Campana et al., 2002), XTE J0929−314, XTE J1751−305 (Wijnands et al., 2005b) and XTE J1807−294 (Campana et al., 2005) which may have different properties due to higher magnetic fields, there are also a number of 'normal' neutron-star X-ray transients that fall into this category (SAX J1810.8−2609, XTE J2123−058, EXO 1747−214). A notable faint quiescent source is the quasi-persistent neutron-star transient 1H 1905+000 as although it was seen to be in outburst for at least 11 years in the 1970s/80s, a recent *Chandra* observation did not detect the source in quiescence, with an upper limit of 1.8×10^{31} ergs s^{-1} (0.5-10 keV; for a distance of 10 kpc, Jonker et al., 2006). Apart from KS 1731−260, MXB 1659−29 and 1H 1905+000, the only other quasi-persistent source to have gone into quiescence is X1732−304 in the globular cluster Terzan 1. In Chapter 5, using recent *Chandra* observations of Terzan 1 we found that the most likely quiescent counterpart to this source has a 0.5-10 keV luminosity of 2.6×10^{32} ergs s^{-1}, about 6 years after the end of an outburst that lasted at least 12 years. For comparison, the 0.5-10 keV luminosities of the last observations of KS 1731−260 and MXB 1659−29 are $2.8^{+0.8}_{-0.6} \times 10^{32}$ ergs s^{-1} and $7.5^{+3.2}_{-2.9} \times 10^{31}$ ergs s^{-1} respectively. Therefore, KS 1731−260, MXB 1659−29 and X1732−304 all have higher quiescent luminosities than 1H 1905+000. However, 1H 1905+000 was observed much longer after the end of its outburst then any of the other 3 sources. While the difference

in quiescent luminosity may suggest that these sources will continue to cool further over the next several decades, it is more likely due to differing long-term time-averaged mass accretion rates or neutron star properties. The differences in the properties of quiescent neutron star transients need to be explored further by additional observations to determine why some sources require enhanced core cooling and why some sources are much fainter than others. Observations of the next quasi-persistent neutron-star transient sources to return to quiescence (EXO 0748−676 and GS 1826−238 are both quasi-persistent sources that are still active) will help determine whether a decline in flux and temperature to a constant level on the timescale of years, rather than decades, is typical.

We used an absorbed neutron star atmosphere model to fit to the data. If we use simple blackbody model in the spectral fitting instead, we get similar cooling curves, yet with different temperatures due to the differences between the shapes of blackbody and neutron star atmosphere spectra. When performing the spectral fits to both sources the normalisation of the neutron star atmosphere component was fixed to the distance of the sources. Unfortunately, these distances are quite uncertain, thus, if the distances are wildly different from the values that we have assumed, the temperatures and fluxes that we get from the spectral fits will be incorrect. However, if the normalisation is left free when fitting, then the uncertainty in this parameter dominates the errors in the other parameters. Importantly, the timescale of the decrease in the temperature and flux of these sources should be unchanged by a different distance, only the absolute values of the temperature and flux will change. If the sources are much closer than assumed then the temperature measured will be lower and the column density higher, and the opposite if the sources are further away, as demonstrated by Wijnands et al. (2004) who fit the first three *Chandra* observations of MXB 1659−29 assuming 3 different distances to the source ranging from 5 - 13 kpc.

While we have interpreted the observations of KS 1731−260 and MXB 1659−29 in terms of the crust and core cooling model there are alternative models to explain quiescent neutron star emission including residual accretion or pulsar shock emission (e.g., Campana et al., 1998a; Menou et al., 1999; Campana & Stella, 2000; Menou & McClintock, 2001). While these are often used to explain the power-law tail present in the spectra of some neutron star transients, residual accretion can produce soft spectra if accretion occurs onto the neutron star surface (Zampieri et al., 1995). However, while variations in the luminosity of the sources in quiescence can be explained by changes in the accretion rate

or the amount of matter interacting with the magnetic field, our observations show that this would have to decrease exponentially in a smooth manner over a period of several years. Given that at the end of the outbursts of 'normal' short-duration neutron-star transients they reach their quiescent states within weeks (e.g. Campana et al., 1998b; Jonker et al., 2003) and that variations in accretion rate are generally not smooth, these alternative models seem unlikely.

We note that from the initial observations of both sources it was found that a power-law component (which is often attributed to residual accretion) in addition to the neutron star atmosphere component was not required to fit the spectra (Wijnands et al., 2001a, 2002a, 2003, 2004). While it has been observed that the contribution from the power-law component compared to the thermal component increases with decreasing quiescent luminosity below $\sim 10^{33}$ ergs s^{-1} (Jonker et al., 2004a,b), the statistics of the last few observations are unfortunately not good enough to check for this. However, if residual accretion is occurring during quiescence it should be on-top of the 'rock bottom' thermal emission due to deep crustal heating (Brown et al., 1998; Rutledge et al., 2002b) that we have now detected. Several neutron star transients have been observed to vary during quiescence e.g. Aql X$-$1, Cen X$-$4 and SAX J1748.8$-$2021 in the globular cluster NGC 6440 (Rutledge et al., 2001a,b, 2002a; Campana & Stella, 2003; Campana et al., 2004, Chp. 4). This variability can be interpreted as a variable power-law component, possibly due to changes in the residual accretion rate or the amount of matter interacting with the magnetic field. Unfortunately this idea is hard to investigate with this data due to the low number of counts in the latter spectra. However, any variability in the flux from KS 1731$-$260 and MXB 1659$-$29 over the next few years around the base set by the thermal emission from the neutron star may indicate that some residual accretion is occurring.

CHAPTER 7

XMM-Newton Discovery of the X-ray Transient
XMMU J181227.8−181234 in the Galactic Plane

In this chapter I present the discovery of an X-ray transient with *XMM-Newton* whilst doing an archival search for faint accreting X-ray sources from the *ASCA* Galactic Plane Survey. The results of the search are discussed, as well as the nature of the transient.

This chapter is based on a paper published in the Monthly Notices of the Royal Astronomical Society by Cackett, E. M, Wijnands, R. & Remillard, R. (2006, MNRAS, 369, 1965).

7.1   Introduction

X-ray binaries are accreting neutron stars and black holes and can be divided into persistent and transient sources. The transient sources exhibit many orders of magnitude variation in their X-ray luminosity due to similar large fluctuations in the mass accretion rate onto the compact objects. Due to instrument limitations, most of our understanding of these systems is based on the properties and behaviour of the brightest systems ($L_x > 10^{36} - 10^{37}$ erg s^{-1}). Although quite a few lower luminosity systems (with L_x between 10^{34} and 10^{36} erg s^{-1}) are known, they remain enigmatic as they have not be studied in the same systematic way as their brighter counterparts. We have initiated several programs to systematically investigate the lower luminosity accreting neutron stars and black holes. One of these programs is to search and study very faint X-ray transients (with peak luminosities of 10^{34} and 10^{36} erg s^{-1}) near the Galactic centre (see Wijnands et al., 2006).

Another program we are performing is to identify the many X-ray sources which were found during several different previous X-ray surveys of the Galactic centre and the Galactic plane (e.g., Sugizaki et al., 2001; Sidoli et al., 2001; Sakano et al., 2002). In particular, the *ASCA* Galactic Plane Survey (Sugizaki et al., 2001) detected 163 sources in the Galactic Plane, and those that are at a distance of 8 kpc approximately fall into the $L_x = 10^{34}$ to 10^{36} ergs s^{-1} range. The majority of the sources remain unidentified due to the poor spatial resolution of the *ASCA* observations. We have started a detailed investigation of the archival *XMM-Newton* and *Chandra* data for observations of these *ASCA* sources. Such observations will lead to better positional accuracy which will be used to follow up the X-ray sources at optical and IR wavelengths to try to constrain the nature of the sources. We will also study the X-ray spectral and timing properties which will provide additional insight into the nature of these sources. Whilst studying the archival *XMM-Newton* observations, we discovered a rather bright X-ray transient. In this chapter we report on this discovery, as well as discussing 3 sources first detected by the *ASCA* Galactic Plane Survey. In future work we will discuss in detail the results of our archival searches for the *ASCA* and other low-luminosity sources.

7.2 XMM-Newton Observation

XMM-Newton (Jansen et al., 2001) observed a region of the Galactic Plane in the direction of $\alpha = 18h12m6.3s$, $\delta = -18°22'30''$ on March 8, 2003 (see Fig. 7.1, ObsID 0152833701). The observation exposure times are ∼8.7 ks for the EPIC-MOS and ∼7 ks for the EPIC-pn, no background flares are present. The EPIC instrument was operated in full frame mode with the medium filter. The Observation Data Files were processed to produce calibrated event lists using the *XMM-Newton* Science Analysis Software (SAS, version 6.5.0).

In the field of view, we detect a bright source with position $\alpha = 18h12m27.8s$, $\delta = -18°12'34''$ (J2000). The statistical error in this source position is small (0''05) as the source is bright, and so the positional error is dominated by the absolute astrometric accuracy of the telescope, which is estimated to be ∼2'' (Kirsch, 2006). An X-ray source at this position is not identified in catalogues of previous *ROSAT* and *ASCA* surveys of the same region, identifying this source as being transient. However, this source lies close (∼40'') to the 95% confidence error box for the source 1H1812-182 detected during the

NRL Large Area Sky Survey Experiment with the *HEAO 1* satellite (Wood et al., 1984). Although the given position of 1H1812-182 (α = 18h15m27s, δ = $-18°12'55''$, J2000) is $\sim$0.7° from the position of the *XMM-Newton* source, it has a large extended error box with an approximate length of 2.1° and width of 0.03° (= 1.8′). The *HEAO 1* source is therefore a possible X-ray detection of this *XMM-Newton* transient during a previous outburst, though we note that the large error box of 1H1812-182 does not rule out the possibility that it could well be another X-ray source that is unrelated. 1H1812-182 was detected with a flux of 0.1470 ± 0.0025 counts cm^{-2} s^{-1} in the 0.5-25 keV band which corresponds to a 2-10 keV flux of $7.0 \pm 0.1 \times 10^{-10}$ ergs cm^{-2} s^{-1} assuming a Crab-like spectrum (Wood et al., 1984).

As this new *XMM-Newton* source has not been previously detected, we name it XMMU J181227.8$-$181234. Initially, the source was not detected using the All-Sky Monitor (ASM) on-board the *Rossi X-ray Timing Explorer (RXTE)*, however, reprocessing of the ASM data showed that the source was in fact detected (see Section 7.4 for further details).

There is no optical counterpart identified in a Digitized Sky Survey (DSS) image and no counterpart in the 2MASS All-Sky Catalog of Point Sources (Cutri et al., 2003) or USNO-B1.0 (Monet et al., 2003) catalogue within 6″of the source position. The large absorption in this direction makes finding an optical counterpart particularly hard.

7.3 Timing and Spectral Analysis

Extracting a 0.2-10 keV lightcurve from the EPIC-pn and MOS detectors we detect no X-ray bursts (see Fig. 7.2). We use a periodogram analysis (Lomb, 1976; Scargle, 1982) of the combined EPIC-pn and MOS 0.2-10 keV lightcurve, with a time bin of 10s, to search for any pulsations which would help in identifying the nature of the source, but none were found.

This source has a count rate high enough to cause pile-up. Therefore, to perform spectral analysis of this data the pile-up needs to be corrected for. We extract the spectrum using two different methods. Firstly, from an annulus around the source thus excluding the source core which is most significantly effected by pile-up, and secondly from the read-out streak present in the EPIC-pn data. This second method provides a check as to
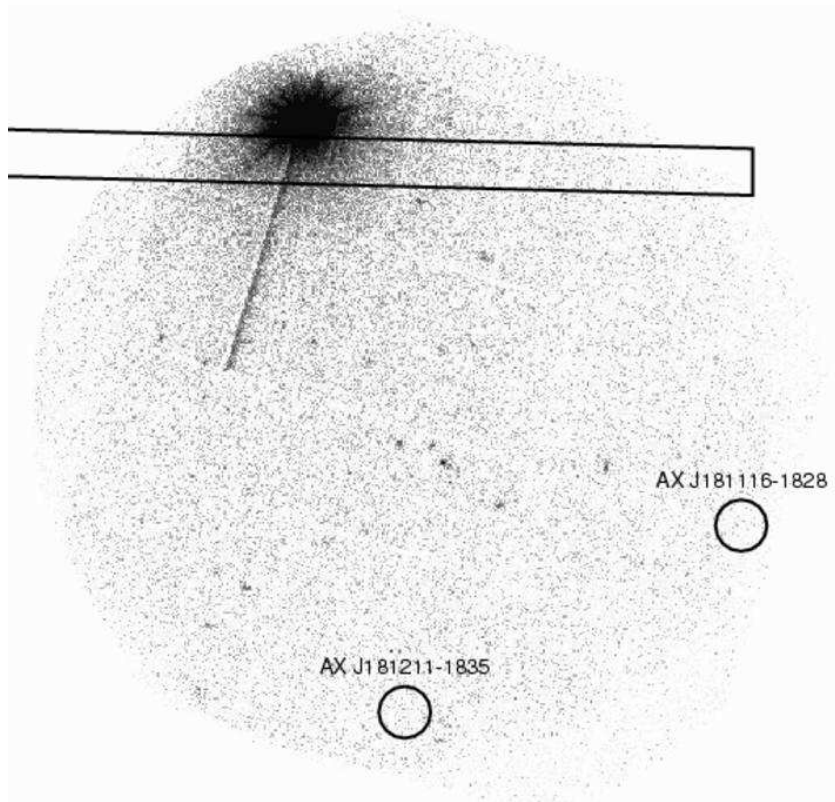
Figure 7.1: Combined EPIC image of the observed region. The transient is clearly seen in the top left of the image. The rectangular error box for source 1H1812-182 observed with the *HEAO 1* satellite is shown (Wood et al., 1984). The error circles for sources AX J1811.2−1828 and AX J1812.1-1835 are shown which were detected during the *ASCA* Galactic Plane Survey (Sugizaki et al., 2001).
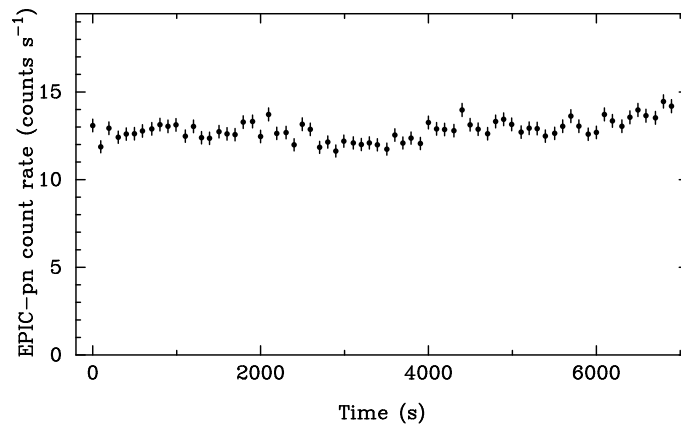

Figure 7.2: EPIC-pn 0.2-10 keV background subtracted lightcurve for XMMU J181227.8−181234. Time binning is 100s.

whether the annulus spectrum is significantly affected by the energy-dependence of the point-spread function.

In the annulus method, we use an annulus of inner radius $15''$ and outer radius $45''$. The background was extracted from a $3'$ circular region close to the transient and containing no detected sources. For the MOS cameras, only single-pixel events (pattern = 0) were selected as recommended for dealing with pile-up by Molendi & Sembay (2003). We use the SAS tool EPATPLOT to make sure that no pile-up was present. Response matrices and ancillary files were created using RMFGEN and ARFGEN.

The data were binned to have a minimum of 25 counts per bin. We use XSPEC (v.11) (Arnaud, 1996) to fit the EPIC-pn, MOS1 and MOS2 data simultaneously. Two different models were fit to the data - an absorbed power-law model and an absorbed multi-colour disk blackbody model (diskbb). Table 7.1 gives the best-fitting parameters for both models and the best-fitting multi-colour disk blackbody model is shown if Fig. 7.3. We find that both models give reasonably good fits. From the spectrum and model fits it is apparent that the source is highly absorbed suggesting that it is not a nearby lower-luminosity source. The power-law fit gives a spectral index, $\Gamma = 2.47 \pm 0.05$, where as the multi-colour disk blackbody fit gives quite a high characteristic temperature of $kT = 2.14 \pm 0.04$ keV. These model fits lead to an unabsorbed 0.5-10 keV flux of $5.3 \pm 0.4 \times 10^{-9}$ ergs cm^{-2} s^{-1} and $1.81 \pm 0.02 \times 10^{-9}$ ergs cm^{-2} s^{-1} for the power-law and multi-colour disk blackbody models respectively. Assuming that this source is at a distance of 8 kpc, this corresponds to a 0.5-10 keV luminosity of $4.1 \pm 0.3 \times 10^{37}$ ergs cm^{-2} s^{-1} for the power-law model and $1.4 \pm 0.02 \times 10^{37}$ ergs cm^{-2} s^{-1} for the multi-colour disk blackbody model, quite typical of other X-ray transients.

The readout streak is only significantly present in the pn image, thus we only extract the readout streak spectrum from the pn data. Binning the data to have a minimum of 25 counts per bin, we again fit in XSPEC using both an absorbed multi-colour disk blackbody model and an absorbed power-law model. The best-fitting parameters are given in Table 7.1, and are seen to be consistent with the parameters from the annulus spectrum. We do not give fluxes for the readout streak spectrum as the photons only hit the CCD in the streak region when the CCD is being read-out, and so the exposure time is incorrect.
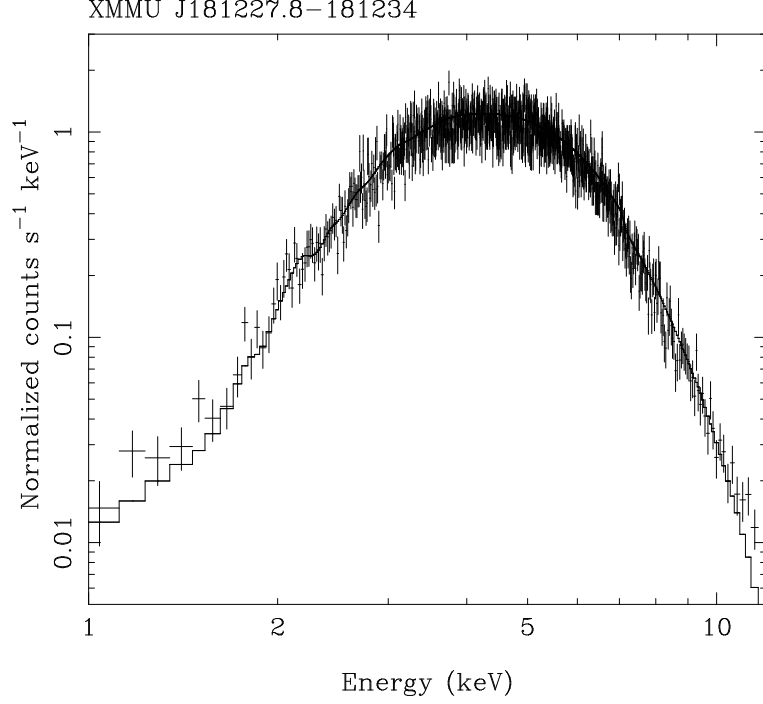
Figure 7.3: EPIC-pn spectrum for XMMU J181227.8−181234 with best-fitting absorbed multi-colour disk blackbody model. The spectrum was extracted from an annulus around source to reduce the effects of pile-up.

Table 7.1: Model fits to the X-ray spectrum of XMMU J181227.8−181234 when fitting the EPIC-pn, MOS1 and MOS2 data simultaneously to a spectrum extracted from the annulus, and when fitting the EPIC-pn spectrum extracted from the readout streak. 1-σ errors on the parameters are given.

Parameter	Annulus		Readout Streak	
	Power-law	diskbb	Power-law	diskbb
N_H ($\times 10^{22}$ cm^{-2})	12.8 ± 0.3	9.7 ± 0.2	$14.3^{+1.6}_{-1.4}$	$10.8^{+1.0}_{-0.9}$
Spectral Index	2.47 ± 0.05		$2.34^{+0.23}_{-0.22}$	
kT (keV)		2.14 ± 0.04		$2.38^{+0.25}_{-0.22}$
0.5-10 keV absorbed flux ($\times 10^{-10}$ ergs cm^{-2} s^{-1})	7.7 ± 0.1	7.6 ± 0.1		
0.5-10 keV unabsorbed flux ($\times 10^{-9}$ ergs cm^{-2} s^{-1})	5.3 ± 0.4	1.81 ± 0.02		
χ^2_ν (d.o.f)	1.4 (1459)	1.3 (1458)	0.99 (124)	0.90 (124)

7.4 *RXTE* All Sky Monitor observations

Initially, the detection of this transient with the *RXTE* ASM was missed, due to the mask that is put around bright sources when looking at deep sky maps. In this case the bright persistent low mass X-ray binary GX 13+1 (4U 1811-17) is ∼1.2° away from the transient. Given the position and time of the outburst, we detect the transient with the *RXTE* ASM. Ron Remillard (private communication) has derived the source position from first principles, given the outburst time interval, that is consistent with the *XMM-Newton* position. Figure 7.4 shows the *RXTE* ASM lightcurve for this source with the outburst clearly visible. The outburst lasts for approximately 50 days, at least, and there is only one outburst detected during the lifetime of *RXTE*. The *XMM-Newton* observation occurs after the peak of the outburst. The ASM count rate at the time of the *XMM-Newton* observation is approximately 3 counts s^{-1}. Using PIMMS (the Portable, Interactive Multi-Mission Simulator), and assuming this count rate and the best-fitting power-law spectral model from Table 7.1, this corresponds to an unabsorbed 0.5-10 keV flux of 6 ×10^{-9} ergs cm^{-2} s^{-1}, similar to that detected with *XMM-Newton*.

The coarse shape of the spectrum in X-ray binary systems may help to reveal the type of the source. To investigate this question, we use the hardness ratios derived from the source count rates in the three standard ASM energy bands: *A* (1.5-3 keV), *B* (3-5 keV) and *C* (5-12 keV). The hardness ratios are then defined as HR1 = B/A and HR2 = C/B. We expect that HR1 is sensitive to both the spectral shape of the X-ray source and the amount of interstellar absorption, while HR2 is more sensitive to just the spectral shape.

The 'dwell-by-dwell' data for a particular source in the ASM archive provides independent measurements from each 90 s exposure by one of the three ASM cameras. We select cameras 2 and 3 only for this exercise. Camera 1 is excluded because it has a secular gain drift, caused by a pinhole Xe leak discovered before *RXTE* launch, and it is rigidly calibrated to the other cameras for the specific spectral shape of the Crab Nebula. For other spectral shapes, the hardness ratios from camera 1 exhibit a time dependence that would add systematic noise in the present study.

Count rates for several sources observed by the ASM were calculated by Ron Remillard (private communication). For persistent sources (6 atolls, 6 Z sources, 4 classical X-ray
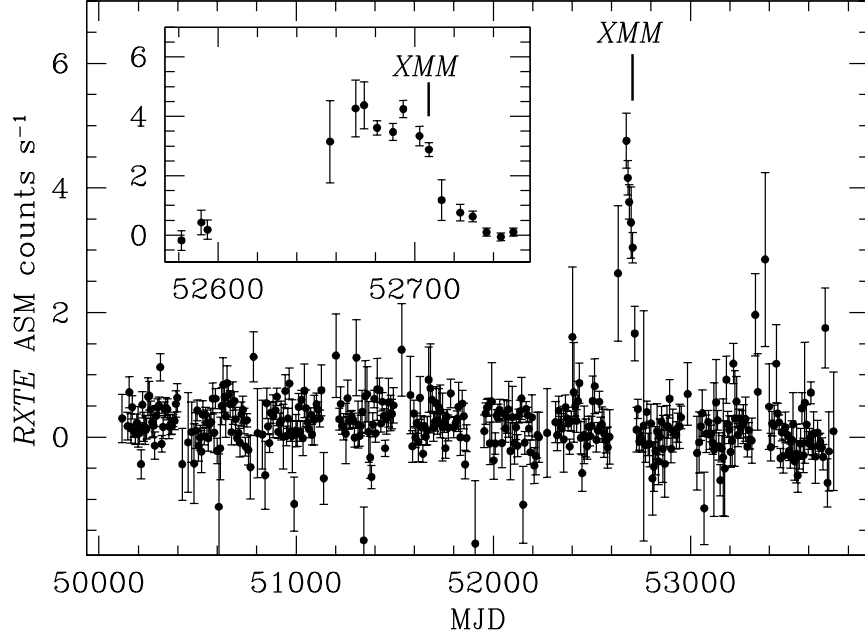
Figure 7.4: 7-day averaged *RXTE* ASM lightcurve for XMMU J181227.8−181234, with the time of the *XMM-Newton* observation marked. The inset shows the outburst in more detail, again with the time of the *XMM-Newton* observation marked. There is clearly only one outburst detected during the lifetime of *RXTE*.

pulsars, and the 2 LMC black holes), we compute the ASM count rates (weighted mean) in each energy band over a long time interval, arbitrarily chosen to be MJD 51000 – 52000. We also sample the persistent black hole binary Cyg X–1 in each of two X-ray states: soft (MJD 52250–52450) and hard (MJD 50720 – 50920). Count rates are determined for X-ray transients (8 atolls, 6 classical X-ray pulsars, and 7 black holes) for the 7-day time interval that captures the peak of the outburst. This is evaluated by finding the maximum flux in the weighted mean, while sliding a 7-day window along the light curve sampled in 1-day bins.

From this analysis, we find that a colour-colour diagram using these two ASM hardness ratios can give a good indication of source type (see Fig. 7.5). We note that HR1 is quite uncertain for this transient due to the low number of counts in the 1.5-3 keV band caused by the high absorption towards this object. The HR2 ratio, however, is less susceptible to interstellar absorption. We find that HR2 = 2.45, suggesting that this source is a high-mass X-ray binary pulsar.
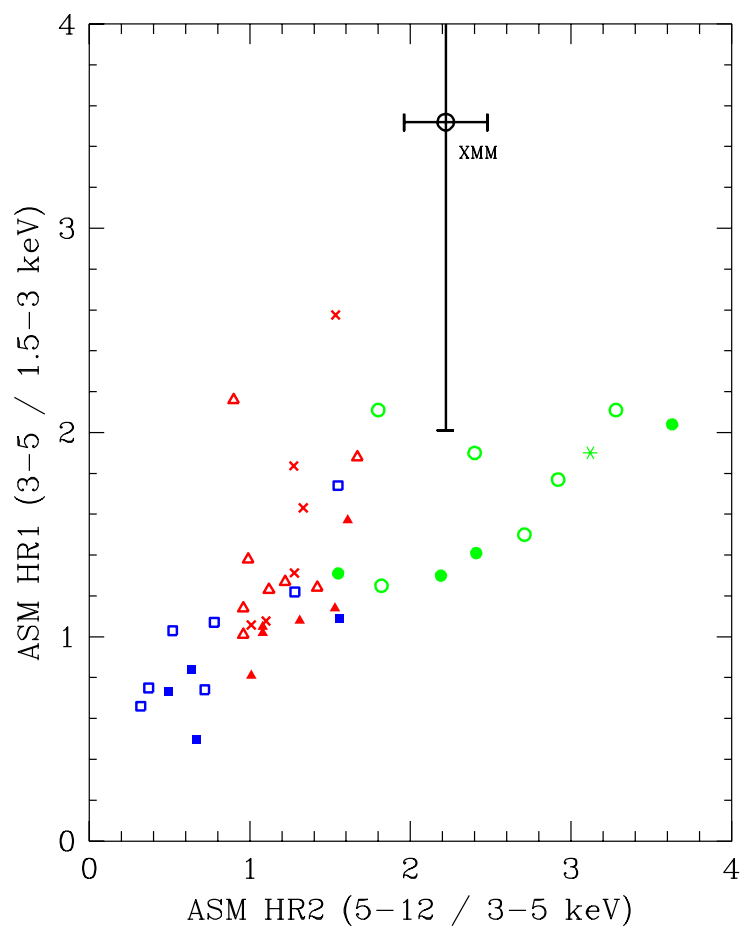
Figure 7.5: *RXTE* ASM colour-colour diagram. The shape (and also the colour) denote source types, an open symbol is a transient; filled symbols are persistent sources. The squares (blue) are black-hole binaries with two states for Cyg X-1. Triangles (red) denote the bursters. Crosses (red) denote the Z-sources (all of these are persistent). Circles (green) denote the pulsars. The green asterisk is the high-mass X-ray binary 4U 1700-377.

7.5 Discussion

7.5.1 The nature of XMMU J181227.8−181234

From our spectral fits to XMMU J181227.8−181234 we find a high absorption towards this source. Using the FTOOL nH (Dickey & Lockman, 1990), we get $N_H \sim 2 \times 10^{22}$ cm^{-2} in the direction of this source - a factor at least 5 different from the value from spectral fitting. This may suggest that the source has significant intrinsic absorption which would be indicative of a high-mass X-ray binary (HMXB). INTEGRAL observations of the Galactic plane have discovered sources with high intrinsic absorption that are likely HMXBs (e.g., Patel et al., 2004; Walter et al., 2004; Lutovinov et al., 2005a,b; Bodaghee et al., 2006). The intrinsic absorption is due to the accretion process in the majority of HMXBs in which the compact objects accrete matter from the stellar wind of a young companion star. The stellar wind can cause significant absorption. In low-mass X-ray binaries (LMXBs), however, accretion occurs via Roche-lobe overflow through the inner Lagrangian point, thus in the majority of cases no material is available to cause significant absorption. Only in high inclination systems significant internal absorption might be present. However, for this transient we do not find any of the characteristic count rate variations (i.e., dips and eclipses) which would indicate a high inclination.

HMXB pulsars typically show significant slow pulsations, however, there are notable exceptions, for instance the well known HMXB, 4U 1700-377 (marked in Fig. 7.5 as an asterisk), has no detectable pulsations. In addition, HMXBs can typically be fitted by an absorbed power-law with spectral index, $\Gamma \sim 1$. There are some lower-luminosity HMXBs that have spectra that are softer (with $\Gamma \sim 2 - 2.5$, see, e.g. Reig & Roche, 1999), though these sources are persistent and have $L_x \sim 10^{34}$ ergs s^{-1}, where as XMMU J181227.8−181234 is transient in nature and is significantly brighter (with L_x a few times 10^{37} ergs s^{-1}). XMMU J181227.8−181234 has no pulsations detected in the lightcurve and it is fit by a power-law spectral index of $\Gamma = 2.5$ which is far more typical of LMXBs. Thus, although the ASM colours and possible intrinsic absorption suggest that this source may be a HMXB, the power-law index is more suggestive of a LMXB. We are therefore unable to conclusively determine whether this transient is either a HMXB or a LMXB, and an IR follow-up is needed to search for a counterpart at this wavelength. As no optical or IR counterpart was found with USNO-B1.0 or 2MASS this suggests that the

source is not a nearby lower-luminosity object which is supported by the high measured N_H.

7.5.2 *ASCA* Galactic Plane Survey sources

The *ASCA* Galactic Plane Survey (Sugizaki et al., 2001) detected 163 discrete sources in the 0.7-10 keV energy band within the central region of the Galactic plane with a spatial resolution of $\sim3'$ and a positional error of $\sim1'$. The limiting flux of the survey in the 0.7-10 keV band was $\sim3 \times 10^{-13}$ ergs cm^{-2} s^{-1} which corresponds to a luminosity of $\sim2 \times 10^{33}$ ergs s^{-1} assuming a distance of 8 kpc. We use PIMMS to predict the EPIC-pn on-axis count rate assuming such a flux, a column density $N_H = 2 \times 10^{22}$ cm^{-2}, and with both a power-law with spectral index, $\Gamma = 0$ and spectral index, $\Gamma = 3$. We calculate the EPIC-pn on-axis count rate for this to be approximately 0.014 counts s^{-1} when $\Gamma = 0$ and 0.041 counts s^{-1} when $\Gamma = 3$. Thus, for an exposure time of 7 ks, the lower limit of *ASCA* Galactic Plane Survey corresponds roughly to between 100 and 290 counts on-axis (0.5-10 keV) for typical spectra. We note that off-axis the effective exposure time drops rapidly due to vignetting. By around $15'$ off-axis, the vignetting factor is about 0.3 (see Fig. 13 of the *XMM-Newton* User's Handbook[1]), thus the lower limit drops to between 30 and 90 counts. Thus we expect to detect any persistent point sources from the *ASCA* Galactic Plane Survey with this *XMM-Newton* observation.

Two of the sources (AX J1811.2−1828 and AX J1812.1−1835) from this survey lie within the field of view of this *XMM-Newton* observation and another of the sources (AX J1812.2−1842) is in an *XMM-Newton* observation of a nearby region. We discuss the *XMM-Newton* observation of these sources here.

7.5.3 AX J1811.2−1828

AX J1811.2−1828 was detected for the first time with *ASCA* (Sugizaki et al., 2001). No spectral model was fit to data from AX J1811.2−1828, though these authors quote a 2-10 keV count rate of 6.3 counts ks^{-1} GIS^{-1}. Depending on the spectral model, this converts to a 2-10 keV flux between $(4 - 11.5) \times 10^{-13}$ ergs cm^{-2} s^{-1}.

The majority of the error circle for this source falls off the edge of the MOS1 and

---

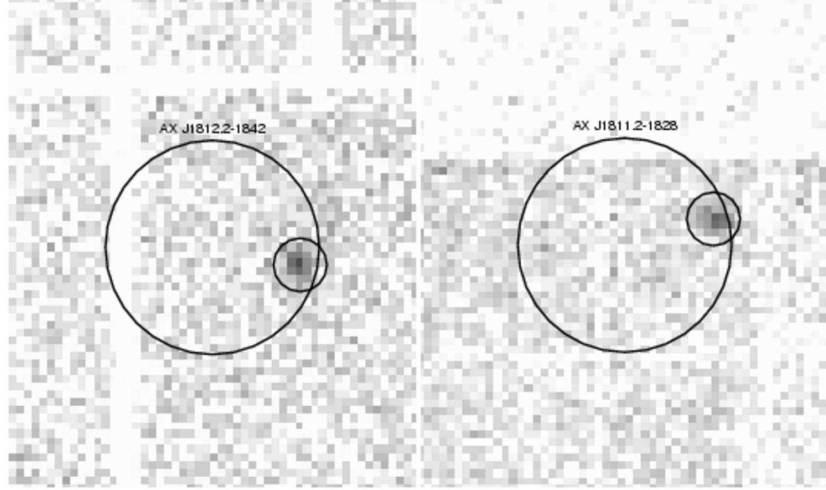[1]available from http://xmm.vilspa.esa.es

Figure 7.6: *XMM-Newton* image of the two *ASCA* sources AX J1812.2−1842 (left panel) and AX J1811.2−1828 (right panel), which are clearly detected with a much improved source position. The larger circles are the *ASCA* error circles for these sources, whilst the smaller circles are the 15″ source extraction regions we use here.

MOS2 detectors, and so we can only use the pn detector to search for a detection in this *XMM-Newton* observation. No bright source is detected within the error circle, however, we tentatively detect a possible faint source on the edge of the error circle for this source with 40 ± 9 net counts in the 0.2-12 keV range for the pn detector. To check whether this source is in fact real, we analyse two additional *XMM-Newton* archival observations (ObsID 0152834201 and 0152835401) in the region of this source. In both observations we detect a source with a position $\alpha = $ 18h11m13.3s, $\delta = -18°27'57''$ (J2000), and a positional error of 2″.2 (including both statistical and boresight errors). The position of the potential source in the original data is consistent with that of the source in the two extra data sets and thus the source is detected in all three *XMM-Newton* observations. In Fig. 7.6 the improved position of this source can be seen in a combined image from all 3 *XMM-Newton* observations. In ObsID 0152835401 the source is on the very edge of the field-of-view and so we only analyse the spectrum from the ObsID 0152834201 data, where the source is bright enough to bin the spectrum with enough counts to validly use χ^2 statistics in the spectral fitting.

We extract the spectrum from the MOS1, MOS2 and pn detectors using a circular source region with radius 15″, and we extract the background from an annulus around the source with inner and outer radii of 1′ and 2′ respectively. We bin the spectrum to 15

counts per bin, and fit the spectra simultaneously with an absorbed power-law model using XSPEC. The best-fitting model has parameters $N_H = 0.6^{+0.6}_{-0.3} \times 10^{22}$ cm^{-2} and $\Gamma = 1.5^{+0.7}_{-0.3}$. The reduced-$\chi^2$ for this fit is 0.8. For comparison with the *ASCA* detection we calculate the 2-10 keV flux, which we find to be $2.8^{+0.6}_{-0.4} \times 10^{-13}$ ergs cm^{-2} s^{-1} and the unabsorbed 2-10 keV flux is $2.9 \pm 0.6 \times 10^{-13}$ ergs cm^{-2} s^{-1}. This flux is slightly lower than the flux detected by *ASCA*. From the spectral fits this source has a reddening smaller than the interstellar absorption in this direction, thus it is likely closer than a distance of 8 kpc. As the distance to this source is unknown it is hard to determine what type of source this is with just this spectral fits, and the power-law index does not rule out a HMXB, LMXB or cataclysmic variable. We conclude that we have detected AX J1811.2$-$1828 with *XMM-Newton* with a 2-10 keV flux which was slightly lower than that seen by *ASCA*.

We find several possible optical and IR counterparts to this X-ray source in the USNO-B1.0 and 2MASS catalogues. The USNO-B1.0 source named USNO-B1.0 0715-0555562 is 1″.8 away and has a B2 magnitude of 19.8 and a R2 magnitude of 18.0. USNO-B1.0 0715-0555563 is 2″.6 away, and has B2 and R2 magnitudes of 19.3 and 16.5 respectively. USNO-B1.0 0715-0555571 is 2″.7 away and has B2 and R2 magnitudes of 19.11 and 15.35 respectively. The 2MASS source named 2MASS J18111351-1827565 is a distance of 3″.1 away from the X-ray source and has J, H and K magnitudes of 12.3, 11.2, and 10.9 respectively. Optical/IR follow-up spectroscopy of these sources is needed to determine the spectral type, and hence the likely nature of this source.

7.5.4 AX J1812.1$-$1835

Sugizaki et al. (2001) identify AX J1812.1$-$1835 with the supernova remnant G12.0-0.1 ($\alpha = $ 18h11m53.3s, $\delta = -18°35'54''$, Clark et al., 1975; Altenhoff et al., 1979; Kassim, 1992; Dubner et al., 1993; Green et al., 1997; Green, 2004). Their spectral fits to AX J1812.1$-$1835 lead to a flux for the source of $\sim 9 \times 10^{-13}$ ergs cm^{-2} s^{-1} in the 0.7-10 keV band. No source is detected within the error circle of AX J1812.1$-$1835. To determine an upper-limit for this source, we extract the count rate from the faintest source detected at a similar off-axis angle. Using an extraction radius of 15″ for a source located at $\alpha = $ 18h12m43.7s, $\delta = -18°31'58''$ (J2000) we get 51 ± 10 background-subtracted counts in the 0.2-12 keV range for the pn detector. A source-free annulus between 40″ and 100″ was used to determine the background counts. The average effective exposure in the source

extraction region is 2429s, giving a net count rate of 0.021 ± 0.004 counts s^{-1}. The average interstellar absorption in the direction of this source is 2×10^{22} cm^{-2}. Using PIMMS and assuming this value we get a 0.5-10 keV flux for the source in the range $(1.5 - 4.2) \times 10^{-13}$ ergs cm^{-2} s^{-1} depending on the power-law spectral index which we vary from 0 to 3. Thus, if AX J1812.1$-$1835 is a point source, and has not varied in flux since the *ASCA* observation it should be detected, which it is not.

There are several possible explanations for the lack of detection. Firstly, if this source is not associated with the supernova remnant (SNR), then the flux from this source has dropped by a factor of at least 2 between the *ASCA* and *XMM-Newton* observations, identifying the source as variable. However, it is likely that this source is associated with the SNR G12.0-0.1. Studying the VLA 1465 MHz radio observation of this SNR (see Fig. 3 from Dubner et al., 1993) we find that although the bright thermal source is located several arcminutes away from AX J1812.1$-$1835, the *ASCA* source does lie within the incomplete shell to the east. If AX J1812.1$-$1835 is associated with this SNR, then the emission will be diffuse, and therefore below our detection limit.

7.5.5   AX J1812.2$-$1842

AX J1812.2$-$1842 was first detected by the *ASCA* Galactic Plane Survey. No spectral model was fit to data from AX J1812.2$-$1842 by Sugizaki et al. (2001), though these authors quote a 2-10 keV count rate of 5.4 counts ks^{-1} GIS^{-1}. Depending on the spectral model, this converts to a 2-10 keV flux between $(3 - 10) \times 10^{-13}$ ergs cm^{-2} s^{-1}.

Although not in the field-of-view of the *XMM-Newton* observation containing the transient, it is in the data with ObsID 0152835401. The source is detected with a position $\alpha = 18h12m10.5s$, $\delta = -18°42'10''$ (J2000), and a positional error of $2''.3$ (including both statistical and boresight errors). The improved source position can be seen in a combined MOS1, MOS2 and pn image (Fig. 7.6, left panel).

We extract the spectrum from the MOS1, MOS2 and pn detectors using a circular source region with radius $15''$, and we extract the background from an annulus around the source with inner and outer radii of $1'$ and $2'$ respectively. We bin the spectrum to 15 counts per bin for the MOS1 and MOS2 data and 40 counts per bin for the pn data. The spectra are fit simultaneously with an absorbed power-law model using XSPEC. The best-

fitting model has parameters $N_H = 0.5^{+1.3}_{-0.5} \times 10^{22}$ cm^{-2} and $\Gamma = 0.0^{+0.7}_{-0.5}$. The reduced-$\chi^2$ for this fit is 0.7. For comparison with the *ASCA* detection we calculate the 2-10 keV flux, which we find to be $9.4^{+2.0}_{-1.7} \times 10^{-13}$ ergs cm^{-2} s^{-1} and the unabsorbed 2-10 keV flux is $9.6^{+1.8}_{-1.2} \times 10^{-13}$ ergs cm^{-2} s^{-1}. This flux is consistent with the source flux detected by *ASCA*. The low N_H suggests that the source maybe closer than 8 kpc, however, we note the large uncertainty in this parameter. The power-law spectral index suggests that this source could be a cataclysmic variable, though we cannot be conclusive.

A search for optical and IR counterparts finds no sources within the errors for the position. The nearest optical source, USNO-B1.0 0712-0536743, is a distance of $3\rlap{.}''5$ away, and has B2 and R2 magnitudes of 18.4 and 17.8 respectively. The nearest IR source, 2MASS J18121061-1842133, is a distance of $4\rlap{.}''3$, and has J, H and K magnitudes of 14.8, 12.3 and 10.9 respectively.

7.6 Conclusions

We have discovered an X-ray transient with position $\alpha = $ 18h12m27.8s, $\delta = -18°12'34''$ (J2000) detected by *XMM-Newton* and the *RXTE* ASM. This source was not previously detected by either *ROSAT* or *ASCA*, though it may be associated with 1H1812-182 detected by *HEAO 1* which has a large extended error box that is close to the transient source position. The X-ray spectrum of this transient is fitted equally well by an absorbed power-law or multi-colour disk blackbody model, where we find that the source is highly absorbed. We detect an unabsorbed 0.5-10 keV flux in the range $(2-5) \times 10^{-9}$ ergs cm^{-2} s^{-1}, which at a distance of 8 kpc corresponds to a 0.5-10 keV luminosity of $(1-4) \times 10^{37}$ ergs s^{-1}, quite typical of other Galactic X-ray binary transients in outburst. Using a periodogram analysis we searched for pulsations to help with source identification, but none were found. The high column density to the source and lack of optical/IR counterpart in the USNO-B1.0 and 2MASS catalogues suggests that the source is not a nearby source with lower luminosity. A colour-colour diagram from *RXTE* ASM data of different accreting objects suggests that the transient is a high-mass X-ray binary, as is also suggested by the high absorption compared to the average interstellar value in the direction of the source. However, the power-law spectral index is far more typical of a low-mass X-ray binary. Thus, we are unable to conclusively identify the nature of the transient. Follow-up

IR observations are required to help determine the nature of this source.

We also report on three sources first detected by the *ASCA* Galactic Plane Survey that lie within the field-of-view of this observation. We do not detect AX J1812.1−1835, though this is likely because it is associated with the supernova remnant G12.0-0.1 and so the diffuse emission would not be bright enough to be detected with this observation. For AX J1811.2−1828, we detect a source towards the edge of the error circle with a 2-10 keV flux of $2.8^{+0.6}_{-0.4} \times 10^{-13}$ ergs cm^{-2} s^{-1}, slightly lower than the *ASCA* observation of this source. The spectrum is fit with an absorbed power-law with $N_H = 0.6^{+0.6}_{-0.3} \times 10^{22}$ cm^{-2} and $\Gamma = 1.5^{+0.7}_{-0.3}$. We also detect AX J1812.2−1842 with a 2-10 keV flux of $9.4^{+2.0}_{-1.7} \times 10^{-13}$ ergs cm^{-2} s^{-1}, consistent with the *ASCA* observation of this source. The spectrum is fit with an absorbed power-law with $N_H = 0.5^{+1.3}_{-0.5} \times 10^{22}$ cm^{-2} and $\Gamma = 0.0^{+0.7}_{-0.5}$. We cannot conclusively determine the nature of AX J1811.2−1828 or AX J1812.2−1842 with these observations and optical/IR follow-ups are needed. Many sources from the *ASCA* Galactic Plane Survey remain unidentified in nature, and require further X-ray observations with *XMM-Newton* and *Chandra* to provide sub-arcsecond source positions allowing for optical/IR follow-up to aid with source identification as well as providing further X-ray temporal and spectral information.

CHAPTER 8

Conclusions and Future Work

8.1 Summary of the major findings

The first part of the thesis focused on reverberation mapping of the inner regions of AGN. Using emission line reverberations, over a 13-yr campaign, it was shown that the broad-line region changes in size as the luminosity of the source changes, and this was modelled in terms of a luminosity-dependent delay map. Secondly, using continuum reverberations, assumed to be from the accretion disc, distances to 14 AGN are measured. However, the distances measured imply a value for H_0 that is a factor of ~ 1.7 smaller than all other methods seem to be pointing towards.

In the second part of the thesis, quiescent neutron star X-ray transient sources were studied using the *Chandra* and *XMM-Newton* X-ray telescopes. The study of these quiescent sources was used to determine the required cooling mechanisms, which puts constraints on the internal structure of the neutron stars. Whilst the main findings of this thesis were summarised at the end of each chapter, they are also detailed below:

1. Using Hβ and optical continuum lightcurves from a 13-year monitoring campaign of the AGN NGC 5548, we find that the Hβ emitting region increases in size, and the Hβ response decreases, as the luminosity of the source increases. We use two methods to fit the observed lightcurves in detail: (i) parameterized models and, (ii) the `MEMECHO` reverberation mapping code. We model this by a delay map that allows the Hβ time delay and flux to depend on the continuum flux. The parameterized breathing models allow the time delay and the Hβ flux to depend on the continuum flux so that, $\tau \propto F_c^\beta$ and $F_{H\beta} \propto F_c^\alpha$. Our fits give $0.1 < \beta < 0.46$ and $0.57 < \alpha < 0.66$. α is consistent

with previous work by Gilbert & Peterson (2003) and Goad, Korista & Knigge (2004). Although we find β to be flatter than previously determined by Peterson et al. (2002) using cross-correlation methods, it is closer to the predicted values from recent theoretical work by Korista & Goad (2004).

2. Time delays between the continuum at different wavelengths and the SEDs of 14 AGN were modelled in terms of thermal disc reprocessing from an irradiating ionizing source. Such a model leads to a measurement of the nuclear extinction and the distances to these 14 AGN. However, when fitting the measured distances with a $\Omega_M = 0.3, \Omega_\Lambda = 0.7$ cosmology, we find $H_0 = 42 \pm 5$ km s^{-1} Mpc^{-1}, a factor of $\sim$1.7 smaller than the value of $H_0 = 72 \pm 8$ km s^{-1} Mpc^{-1} determined by the *HST* Key Project. This value either implies that the time delays measured via cross-correlation analysis are systematically biased too long, or that the assumptions of the thermal disc reprocessing model are incorrect, possibly suggesting that only part of surface of the disc is irradiated.

3. We observed the globular cluster NGC 6440 with *Chandra* on two occasions when the known bright transient in this cluster was in its quiescent state in July 2000 and June 2003 (both observations were made nearly 2 years after the end of their preceding outbursts). The quiescent spectrum during the first observation is well represented by a two component model (a neutron-star atmosphere model plus a power-law component which dominates at energies above 2 keV). During the second observation (which was roughly of equal duration to the first observation) we found that the power-law component could no longer be detected. Our spectral fits indicate that the effective temperature of the neutron-star surface was consistent between the two observations. We conclude that the effect of the change in power-law component caused the 0.5-10 keV flux to be a factor of $\sim$2 lower during the second observation compared to the first observation. This suggests that there may be on-going residual accretion during quiescence that was at a higher rate during the first observation. Additionally, we found that the quiescent flux from the transient in NGC 6440 was consistent with the neutron star cooling via standard processes only, without the requirement for enhanced levels of neutrino emission.

4. A $\sim$19 ks *Chandra* ACIS-S observation of the globular cluster Terzan 1 was presented. Fourteen sources are detected within 1.'4 of the cluster centre with 2 of these sources predicted to be not associated with the cluster (background AGN or foreground objects). The neutron star X-ray transient, X1732$-$304, has previously been observed in outburst

within this globular cluster with the outburst seen to last for at least 12 years. Here we find 4 sources that are consistent with the *ROSAT* position for this transient, but none of the sources are fully consistent with the position of a radio source detected with the VLA that is likely associated with the transient. The most likely candidate for the quiescent counterpart of the transient has a relatively soft spectrum and an unabsorbed 0.5-10 keV luminosity of 2.6×10^{32} ergs s^{-1}, quite typical of other quiescent neutron stars. Assuming standard core cooling, from the quiescent flux of this source we predict long (> 400 yr) quiescent episodes to allow the neutron star to cool. Alternatively, enhanced core cooling processes are needed to cool down the core. However, if we do not detect the quiescent counterpart of the transient this gives an unabsorbed 0.5-10 keV luminosity upper limit of 8×10^{31} ergs s^{-1}. From the estimated stellar encounter rate of this cluster we find that the number of sources we detect is significantly higher than expected by the relationship of Pooley et al. (2003). This is perhaps because the cluster was previously much larger and that most of the stars have been lost due to passages through the Galactic disk.

5. *Chandra* and *XMM-Newton* X-ray observations are presented that monitor the neutron star cooling of the quasi-persistent neutron star X-ray transients KS 1731−260 and MXB 1659−29 for approximately 4 years after these sources returned to quiescence from prolonged outbursts. In both sources the outbursts were long enough to significantly heat the neutron star crust out of thermal equilibrium with the core. We analyse the X-ray spectra by fitting absorbed neutron star atmosphere models to the observations. The results of our analysis strengthen the preliminary findings of Wijnands et al. that in both sources the neutron star crust cools down very rapidly suggesting it has a high heat conductivity and that the neutron star core requires enhanced core cooling processes. Importantly, we now detect the flattening of the cooling in both sources as the crust returns to thermal equilibrium with the core. We measure the thermal equilibrium flux and temperature in both sources by fitting a curve that decays exponentially to a constant level. The cooling curves cannot be fit with just a simple exponential decay without the constant offset. In addition, we find that the crust of KS 1731−260 cools faster than that of MXB 1659−29 by a factor of ∼2, likely due to different crustal properties. This is the first time that the cooling of a neutron star crust into thermal equilibrium with the core has been observed in such detail.

6. The discovery of an X-ray transient, observed in outburst with *XMM-Newton* was reported. No known source is present at this position and the source was not detected

during published *ROSAT* or *ASCA* observations of that region. However, the source may be associated with 1H1812-182 detected by *HEAO 1*, although the error bars on the *HEAO 1* position are very large and the two sources could also be unrelated. The X-ray spectrum of this transient is fitted equally well by an absorbed power-law (with a spectral index of 2.5) or multi-colour disk blackbody model (with kT~2 keV), where we find that the source is highly absorbed. We detect an unabsorbed 0.5-10 keV flux in the range $(2 - 5) \times 10^{-9}$ ergs cm^{-2} s^{-1}, which at a distance of 8 kpc corresponds to a 0.5-10 keV luminosity of $(1 - 4) \times 10^{37}$ ergs s^{-1}. No pulsations were detected by timing analysis. A colour-colour diagram from ASM data of different accreting objects suggests that the transient is a high-mass X-ray binary, as is also suggested by the high absorption compared to the average interstellar value in the direction of the source. However, the power-law spectral index is far more typical of a low-mass X-ray binary. Thus, we were unable to conclusively identify the nature of the transient.

7. The transient was discovered during an archival search of sources first detected by the *ASCA* Galactic Plane Survey. In *XMM-Newton* observations of the region close to the transient there are 3 sources from this *ASCA* survey. Two of these sources were detected by *XMM-Newton*, significantly improving the accuracy of the source positions, now allowing for further optical/IR follow-up that can help identify the nature of the sources. The other source was not detected, though this is because it is likely associated with a supernova remnant, and hence the emission with be diffuse and thus require a higher sensitivity limit than the archival observations had.

8.2   Future Work

There are several possible areas of future research that follow on from the work presented here in this thesis. They are summarised here:

1. Line profile changes in NGC 5548. The residuals detected when modelling the long-term lightcurves in NGC 5548 may be associated with changes in the structure of the broad-line region over timescales of a couple of years. One way to check for this would be to study and characterise the line profile shape over the full campaign. Whilst this has been looked at for the first 5 years of the monitoring campaign, it has not been done in a consistent way for the full 13-year campaign. Such a project will lead to more

understanding of the dynamics of the BLR and what implications this might have for future reverberation mapping experiments.

2. Luminosity-dependent delay maps in AGN Watch objects. The AGN Watch collaboration monitored a handful of AGN throughout the 1990s. Whilst the campaign to monitor NGC 5548 was the longest, there are other data sets within the AGN Watch public archive that may be suitable to try and measure the 'breathing' effect within, allowing us to look at whether all AGN show the same luminosity dependence.

3. Continuum reverberations in the low luminosity AGNs. The optical continuum in typical Seyfert galaxies, such as those used in the Sergeev et al. sample presented in this thesis, vary most significantly on timescales of weeks to months. Monitoring campaigns to measure interband time delays in these objects therefore need to last at least a month, with daily monitoring to ensure that the interband delays, which are typically less than a couple of days, can be measured. The situation is worse for more luminous AGN that vary on longer timescales, requiring longer monitoring campaigns. However, the lowest luminosity AGNs vary significantly during one night, with interband delays predicted to be around 10 minutes. For example, in the lowest luminosity AGN, NGC 4395, the CIV emitting region is about 1 light-hour in size (Peterson et al., 2005). An experiment to measure the interband lags in this object could easily be done in one night of observing time using an instrument such as ULTRACAM, which can monitor in 3 filters simultaneously. Such an experiment can test the thermal disc reprocessing hypothesis and accretion disc models with significantly less observing time than required for the typical Seyferts.

4. Observational requirements for continuum reverberation mapping experiments. The observational requirements for a continuum reverberation mapping campaign depends highly on the luminosity and black hole mass of the objects, as this determines the variability characteristics and predicted interband time delays. By simulating the driving lightcurves in the AGN using realistic power-density spectra, and then calculating the observed lightcurves through convolution with an accretion disc transfer function, the required campaign length and sampling rate can be determined for a successful campaign. We plan to run these types of simulations for a range of black hole mass and luminosity to provide an easy 'look-up' table for the observational requirements to measure interband delays.

5. Continuum reverberations in quasars. If the continuum reverberation method for

measuring distances to AGN is ever going to be used as a cosmological probe, the thermal disc reprocessing hypothesis needs testing, for example by using low luminosity AGN (as mentioned above), and additionally, it needs to be shown that interband delays can also easily be detected in quasars at higher redshifts (e.g., $z \geq 0.5$). Though these quasars will need to be more luminous than at lower redshifts to get the required signal-to-noise, the wavelength of the optical region in the emitted-frame will be more towards the UV, and hence more variable, and time-dilation effects will lengthen the time delays. This would allow for a less intensive monitoring campaign than in the lower-luminosity objects, which may be more practical with drop-outs due to weather having more of a significant affect on campaigns that require daily monitoring. Such an experiment can also test whether the temperature profile of the accretion disc in the more-luminous quasars is the same as in the Seyferts.

6. X-ray sources within the globular cluster NGC 6440. Whilst the variability of the neutron star transient in the globular cluster NGC 6440 has been studied in this thesis, the other globular cluster sources from that observation have yet to be analysed. Variability can be searched for in any of the objects, as the 2001 and 2003 *Chandra* observations of this cluster both detect the same sources.

7. Monitoring of KS 1731-260 and MXB 1659-29. From X-ray monitoring of these two sources, we showed that the cooling of the crust in both sources had now flattened. However, continued monitoring is required to further understand the emission during quiescence in these objects. For instance, if any variability is observed in the source flux over the next few years, this would indicate that there is on-going residual accretion during quiescence. Additionally, if these sources continue to cool, at a much slower rate than previously, this would test a new theory predicting that the crust should continue to cool but at a slower rate (Ed Brown, private communication).

8. Low-luminosity accreting X-ray sources in the galaxies. As mentioned in Chp. 7 the *ASCA* Galactic Plane Survey detected around 150 X-ray sources within the luminosity range 10^{34} - 10^{36} erg s^{-1}. This luminosity range is particularly interesting as it is lower than the majority of the actively accreting neutron star or black hole binaries, yet higher than their quiescent counterparts or CVs also. The vast majority of the sources detected by *ASCA* remain unidentified due to the poor positional accuracy (1-3 arcmin) which would hamper any attempt at a follow-up at any other wavelength. *Chandra* and *XMM-Newton*

can significantly improve the source positions, finally allowing for optical/IR follow-ups to identify their nature. We want to determine whether these sources are isolated or in binaries, what type of compact object is present, whether exotic accretion processes are needed to explain their luminosity, and, whether binary and galactic evolution models can explain their number and distribution.

Bibliography

Aldcroft T. L., Karovska M., Cresitello-Dittmar M. L., Cameron R. A., Markevitch M. L., 2000, in Proc. SPIE Vol. 4012, p. 650-657, X-Ray Optics, Instruments, and Missions III, Joachim E. Truemper; Bernd Aschenbach; Eds. Initial performance of the aspect system on the Chandra Observatory: postfacto aspect reconstruction. pp 650–657

Altenhoff W. J., Downes D., Pauls T., Schraml J., 1979, A&AS, 35, 23

Antonucci R., 1993, ARA&A, 31, 473

Antonucci R. R. J., Miller J. S., 1985, ApJ, 297, 621

Arnaud K. A., 1996, in ASP Conf. Ser. 101: Astronomical Data Analysis Software and Systems V XSPEC: The First Ten Years. p. 17

Aschenbach B., 1985, Reports of Progress in Physics, 48, 579

Baldwin J., Ferland G., Korista K., Verner D., 1995, ApJ, 455, L119

Baldwin J. A., 1977, ApJ, 214, 679

Barret D., et al., 1992, ApJ, 394, 615

Barret D., Motch C., Predehl P., 1998, A&A, 329, 965

Bassa C., Pooley D., Homer L., Verbunt F., Gaensler B. M., Lewin W. H. G., Anderson S. F., Margon B., Kaspi V. M., van der Klis M., 2004, ApJ, 609, 755

Bentz M. C., Peterson B. M., Pogge R. W., Vestergaard M., Onken C. A., 2006, ApJ, 644, 133

Bhattacharya D., Srinivasan G., 1995, in Lewin W. H. G., van Paradijs J., van den Heuvel E. P. J., eds, X-ray Binaries. The magnetic fields of neutron stars and their evolution. p. 495

Bildsten L., 1998, in Buccheri R., van Paradijs J., Alpar A., eds, NATO ASIC Proc. 515: The Many Faces of Neutron Stars. Thermonuclear Burning on Rapidly Accreting Neutron Stars. pp 419–+

Bildsten L., et al., 1997, ApJS, 113, 367

Blandford R. D., McKee C. F., 1982, ApJ, 255, 419

Bodaghee A., Walter R., Zurita Heras J. A., Bird A. J., Courvoisier T. J.-L., Malizia A., Terrier R., Ubertini P., 2006, A&A, 447, 1027

Bonamente M., Joy M., La Roque S., Carlstrom J., Reese E., Dawson K., 2005, ApJ, in press, astro-ph/0512349

Borrel V., et al., 1996a, A&AS, 120, 249

Borrel V., et al., 1996b, ApJ, 462, 754

Broos P., Townsley L., Getman K., Bauer F., 2002, ACIS Extract, An ACIS Point Source Extraction Package. Pennsylvania State University

Brown E. F., 2000, ApJ, 531, 988

Brown E. F., Bildsten L., Chang P., 2002, ApJ, 574, 920

Brown E. F., Bildsten L., Rutledge R. E., 1998, ApJ, 504, L95

Burderi L., et al., 2002, ApJ, 574, 930

Campana S., Colpi M., Mereghetti S., Stella L., Tavani M., 1998a, A&AR, 8, 279

Campana S., Ferrari N., Stella L., Israel G. L., 2005, A&A, 434, L9

Campana S., Israel G. L., Stella L., Gastaldello F., Mereghetti S., 2004, ApJ, 601, 474

Campana S., Stella L., 2000, ApJ, 541, 849

Campana S., Stella L., 2003, ApJ, 597, 474

Campana S., Stella L., Gastaldello F., Mereghetti S., Colpi M., Israel G. L., Burderi L., Di Salvo T., Robba R. N., 2002, ApJ, 575, L15

Campana S., Stella L., Mereghetti S., Colpi M., Tavani M., Ricci D., Fiume D. D., Belloni T., 1998b, ApJ, 499, L65

Carroll S. M., Press W. H., Turner E. L., 1992, ARA&A, 30, 499

Cash W., 1979, ApJ, 228, 939

Chen W., Shrader C. R., Livio M., 1997, ApJ, 491, 312

Chiang J., 2002, ApJ, 572, 79

Chiang J., Blaes O., 2003, ApJ, 586, 97

Clark D. H., Caswell J. L., Green A. J., 1975, Australian Journal of Physics Astrophysical
    Supplement, pp 1–38

Clark G. W., 1975, ApJ, 199, L143

Clavel J., et al., 1991, ApJ, 366, 64

Clavel J., Nandra K., Makino F., Pounds K. A., Reichert G. A., Urry C. M., Wamsteker
    W., Peracaula-Bosch M., Stewart G. C., Otani C., 1992, ApJ, 393, 113

Collier S., et al., 2001, ApJ, 561, 146

Collier S., Horne K., Wanders I., Peterson B. M., 1999, MNRAS, 302, L24

Collier S. J., 1998, PhD thesis, University of St Andrews, p. 96

Collier S. J., et al., 1998, ApJ, 500, 162

Collin S., Coupé S., Dumont A.-M., Petrucci P.-O., Różańska A., 2003, A&A, 400, 437

Collin-Souffrin S., 1991, A&A, 249, 344

Colpi M., Geppert U., Page D., Possenti A., 2001, ApJ, 548, L175

Cominsky L., Ossmann W., Lewin W. H. G., 1983, ApJ, 270, 226

Cominsky L. R., Wood K. S., 1984, ApJ, 283, 765

Cominsky L. R., Wood K. S., 1989, ApJ, 337, 485

Courbin F., 2003, in Valls-Gabaud D., Kneib J. P., eds, ASP Conf. Ser. 326: Gravitational
    Lensing: a unique tool for cosmology, Quasar Lensing: the Observer's Point of View,
    astro-ph/0304497

Cutri R. M., et al., 2003, VizieR Online Data Catalog, 2246

Dickey J. M., Lockman F. J., 1990, ARA&A, 28, 215

Dietrich M., Kollatschny W., 1995, A&A, 303, 405

Djorgovski S., 1993, in ASP Conf. Ser. 50: Structure and Dynamics of Globular Clusters
    Physical Parameters of Galactic Globular Clusters. p. 373

Doroshenko V. T., Sergeev S. G., Merkulova N. I., Sergeeva E. A., Golubinsky Y. V., Pronik V. I., Okhmat N. N., 2005a, Astrophysics, 48, 156

Doroshenko V. T., Sergeev S. G., Merkulova N. I., Sergeeva E. A., Golubinsky Y. V., Pronik V. I., Okhmat N. N., 2005b, Astrophysics, 48, 304

Doxsey R., Bradt H., Johnston M., Griffiths R., Leach R., Schwartz D., Schwarz J., Grindlay J., 1979, ApJ, 228, L67

Dubner G. M., Moffett D. A., Goss W. M., Winkler P. F., 1993, AJ, 105, 2251

Dubus G., Hameury J.-M., Lasota J.-P., 2001, A&A, 373, 251

Edelson R., et al., 2000, ApJ, 534, 180

Edelson R. A., Krolik J. H., 1988, ApJ, 333, 646

Fabian A. C., Pringle J. E., Rees M. J., 1975, MNRAS, 172, 15P

Fabian A. C., Vaughan S., Nandra K., Iwasawa K., Ballantyne D. R., Lee J. C., De Rosa A., Turner A., Young A. J., 2002, MNRAS, 335, L1

Fender R. P., Gallo E., Jonker P. G., 2003, MNRAS, 343, L99

Ferrarese L., Merritt D., 2000, ApJ, 539, L9

Flowers E., Ruderman M., Sutherland P., 1976, ApJ, 205, 541

Forman W., Jones C., Tananbaum H., 1976, ApJ, 207, L25

Frank J., King A., Raine D. J., 2002, Accretion Power in Astrophysics: Third Edition. Cambridge University Press

Freedman W. L., et al., 2001, ApJ, 553, 47

Freeman P. E., Kashyap V., Rosner R., Lamb D. Q., 2002, ApJS, 138, 185

Fryer C. L., 1999, ApJ, 522, 413

Fryer C. L., Hungerford A., 2005, in Baykal A., Yerli S. K., Inam S. C., Grebenev S., eds, The Electromagnetic Spectrum of Neutron Stars. Neutron star formation: constraints from/on neutron star populations. p. 3

Fukugita M., Shimasaku K., Ichikawa T., 1995, PASP, 107, 945

Gamow G., Schoenberg M., 1941, Phys. Rev., 59, 539

Garcia M. R., McClintock J. E., Narayan R., Callanan P., Barret D., Murray S. S., 2001, ApJ, 553, L47

Gaskell C. M., Ferland G. J., 1984, PASP, 96, 393

Gaskell C. M., Goosmann R. W., Antonucci R. R. J., Whysong D. H., 2004, ApJ, 616, 147

Gaskell C. M., Peterson B. M., 1987, ApJS, 65, 1

Gaskell C. M., Sparke L. S., 1986, ApJ, 305, 175

Gebhardt K., et al., 2000, ApJ, 539, L13

Giacconi R., et al., 2001, ApJ, 551, 624

Giacconi R., Gursky H., Paolini F. R., Rossi B. B., 1962, Physical Review Letters, 9, 439

Gilbert K. M., Peterson B. M., 2003, ApJ, 587, 123

Glass I. S., 2004, MNRAS, 350, 1049

Goad M. R., Korista K. T., Knigge C., 2004, MNRAS, 352, 277

Green A. J., Frail D. A., Goss W. M., Otrupcek R., 1997, AJ, 114, 2058

Green D. A., 2004, Bulletin of the Astronomical Society of India, 32, 335

Griffiths R., Johnston M., Bradt H., Doxsey R., Gursky H., Schwartz D., Schwarz J., 1978, IAU Circ., 3190

Grimm H.-J., Gilfanov M., Sunyaev R., 2002, A&A, 391, 923

Grindlay J. E., Heinke C., Edmonds P. D., Murray S. S., 2001a, Sci, 292, 2290

Grindlay J. E., Heinke C. O., Edmonds P. D., Murray S. S., Cool A. M., 2001b, ApJ, 563, L53

Guainazzi M., Parmar A. N., Oosterbroek T., 1999, A&A, 349, 819

Gudmundsson E. H., Pethick C. J., Epstein R. I., 1983, ApJ, 272, 286

Gunn J. E., Stryker L. L., 1983, ApJS, 52, 121

Gusakov M. E., Kaminker A. D., Yakovlev D. G., Gnedin O. Y., 2004, A&A, 423, 1063

Haensel P., 2003, in Motch C., Hameury J.-M., eds, EAS Publications Series Equation of State of Dense Matter and Maximum Mass of Neutron Stars. pp 249–+

Harris W. E., 1996, AJ, 112, 1487

Heinke C. O., Edmonds P. D., Grindlay J. E., Lloyd D. A., Cohn H. N., Lugger P. M., 2003a, ApJ, 590, 809

Heinke C. O., Grindlay J. E., Edmonds P. D., Cohn H. N., Lugger P. M., Camilo F., Bogdanov S., Freire P. C., 2005, ApJ, 625, 796

Heinke C. O., Grindlay J. E., Edmonds P. D., Lloyd D. A., Murray S. S., Cohn H. N., Lugger P. M., 2003, ApJ, 598, 516

Heinke C. O., Grindlay J. E., Lugger P. M., Cohn H. N., Edmonds P. D., Lloyd D. A., Cool A. M., 2003b, ApJ, 598, 501

Horne K., 1994, in ASP Conf. Ser. 69: Reverberation Mapping of the Broad-Line Region in Active Galactic Nuclei Echo Mapping Problems Maximum Entropy solutions. pp 23–25

Horne K., Welsh W. F., Peterson B. M., 1991, ApJ, 367, L5

Hut P., Murphy B. W., Verbunt F., 1991, aap, 241, 137

Idiart T. P., Barbuy B., Perrin M.-N., Ortolani S., Bica E., Renzini A., 2002, A&A, 381, 472

in 't Zand J., Heise J., Bazzano A., Ubertini P., Smith M. J. S., Muller J. M., Torroni V., 1998, IAU Circ., 6997, 3

in 't Zand J., Heise J., Smith M. J. S., Cocchi M., Natalucci L., Celidonio G., 1999a, IAU Circ., 7138

in 't Zand J. J. M., van Kerkwijk M. H., Pooley D., Verbunt F., Wijnands R., Lewin W. H. G., 2001, ApJ, 563, L41

in 't Zand J. J. M., Verbunt F., Strohmayer T. E., Bazzano A., Cocchi M., Heise J., van Kerkwijk M. H., Muller J. M., Natalucci L., Smith M. J. S., Ubertini P., 1999b, A&A, 345, 100

Inoue H., Koyama K., Makishima K., Matsuoka M., Murakami T., Oda M., Ogawara Y., Ohashi T., Shibazaki N., Tanaka Y., 1981, ApJ, 250, L71

Ivanova N., Rasio F. A., Lombardi J. C., Dooley K. L., Proulx Z. F., 2005, apj, 621, L109

Janka H.-T., 2004, in Camilo F., Gaensler B. M., eds, IAU Symposium Neutron Star Formation and Birth Properties. pp 3–+

Jansen F., et al., 2001, A&A, 365, L1

Johnston H. M., Verbunt F., Hasinger G., 1995, A&A, 298, L21

Jonker P. G., Bassa C. G., Nelemans G., Juett A. M., Brown E. F., Chakrabarty D., 2006, MNRAS, p. 395

Jonker P. G., Galloway D. K., McClintock J. E., Buxton M., Garcia M., Murray S., 2004b, MNRAS, 354, 666

Jonker P. G., Méndez M., Nelemans G., Wijnands R., van der Klis M., 2003, MNRAS, 341, 823

Jonker P. G., Wijnands R., van der Klis M., 2004a, MNRAS, 349, 94

Kaspi S., Maoz D., Netzer H., Peterson B. M., Vestergaard M., Jannuzi B. T., 2005, ApJ, 629, 61

Kaspi S., Smith P. S., Netzer H., Maoz D., Jannuzi B. T., Giveon U., 2000, ApJ, 533, 631

Kassim N. E., 1992, AJ, 103, 943

Khachikian E. Y., Weedman D. W., 1974, ApJ, 192, 581

Kinney A. L., Rivolo A. R., Koratkar A. P., 1990, ApJ, 357, 338

Kirsch M., 2006, XMM-EPIC status of calibration and data analysis, http://xmm.vilspa.esa.es/docs/documents/CAL-TN-0018.pdf

Kishimoto M., Antonucci R., Blaes O., 2003, MNRAS, 345, 253

Kishimoto M., Antonucci R., Boisson C., Blaes O., 2004, MNRAS, 354, 1065

Kollatschny W., 2003, A&A, 407, 461

Kong A. K. H., McClintock J. E., Garcia M. R., Murray S. S., Barret D., 2002, ApJ, 570, 277

Koratkar A. P., Gaskell C. M., 1991, ApJ, 370, L61

Korista K. T., et al., 1995, ApJS, 97, 285

Korista K. T., Goad M. R., 2004, ApJ, 606, 749

Kormendy J., Richstone D., 1995, ARA&A, 33, 581

Krolik J. H., Begelman M. C., 1988, ApJ, 329, 702

Krolik J. H., Done C., 1995, ApJ, 440, 166

Krolik J. H., Horne K., Kallman T. R., Malkan M. A., Edelson R. A., Kriss G. A., 1991, ApJ, 371, 541

Kuulkers E., et al., 2002, A&A, 382, 503

Lamb F. K., Pethick C. J., Pines D., 1973, ApJ, 184, 271

Lasota J.-P., 2001, New Astronomy Review, 45, 449

Lattimer J. M., Prakash M., 2001, ApJ, 550, 426

Lattimer J. M., Prakash M., 2004, Science, 304, 536

Lewin W., Marshall H., Primini F., Wheaton W., Cominsky L., Jernigan G., Ossman W., 1978, IAU Circ., 3190

Lewin W. H. G., Hoffman J. A., Doty J., 1976, IAU Circ., 2994

Lewin W. H. G., van der Klis M., 2006, Compact stellar X-ray sources. Compact stellar X-ray sources, Cambridge, UK: Cambridge University Press, 2006 Cambridge astrophysics series, Vol. 39. Edited by Walter H.G. Lewin and Michiel Van der Klis. ISBN 0521826594.

Lewin W. H. G., van Paradijs J., Taam R. E., 1995, in Lewin W. H. G., van Paradijs J., van den Heuvel E. P. J., eds, X-ray Binaries. X-ray bursts. p. 175

Lomb N. R., 1976, Ap&SS, 39, 447

Lutovinov A., Revnivtsev M., Gilfanov M., Shtykovskiy P., Molkov S., Sunyaev R., 2005b, A&A, 444, 821

Lutovinov A., Rodriguez J., Revnivtsev M., Shtykovskiy P., 2005a, A&A, 433, L41

Makishima K., et al., 1981, ApJ, 247, L23

Malkan M. A., Sargent W. L. W., 1982, ApJ, 254, 22

Maoz D., Markowitz A., Edelson R., Nandra K., 2002, AJ, 124, 1988

Markert T. H., Backman D. E., Canizares C. R., Clark G. W., Levine A. M., 1975, Nat, 257, 32

Markowitz A., et al., 2003, ApJ, 593, 96

Marti J., Mirabel I. F., Rodriguez L. F., Chaty S., 1998, A&A, 332, L45

Mason K. O., et al., 2002, ApJ, 580, L117

McHardy I. M., Gunn K. F., Uttley P., Goad M. R., 2005, MNRAS, 359, 1469

McHardy I. M., Papadakis I. E., Uttley P., Page M. J., Mason K. O., 2004, MNRAS, 348, 783

McLure R. J., Jarvis M. J., 2002, MNRAS, 337, 109

Menou K., Esin A. A., Narayan R., Garcia M. R., Lasota J.-P., McClintock J. E., 1999, ApJ, 520, 276

Menou K., McClintock J. E., 2001, ApJ, 557, 304

Miller J. S., Goodrich R. W., 1990, ApJ, 355, 456

Miller J. S., Goodrich R. W., Mathews W. G., 1991, ApJ, 378, 47

Minezaki T., Yoshii Y., Kobayashi Y., Enya K., Suganuma M., Tomita H., Aoki T., Peterson B. A., 2004, ApJ, 600, L35

Miyoshi M., Moran J., Herrnstein J., Greenhill L., Nakai N., Diamond P., Inoue M., 1995, Nat, 373, 127

Molendi S., Sembay S., 2003, *XMM-Newton* Calibration Presentations (CAL-TN-0036-1-0)

Monet D. G., et al., 2003, AJ, 125, 984

Muno M. P., Arabadjis J. S., Baganoff F. K., Bautz M. W., Brandt W. N., Broos P. S., Feigelson E. D., Garmire G. P., Morris M. R., Ricker G. R., 2004, ApJ, 613, 1179

Muno M. P., Chakrabarty D., Galloway D. K., Savov P., 2001, ApJ, 553, L157

Muno M. P., et al., 2006, ApJ, 636, L41

Muno M. P., Fox D. W., Morgan E. H., Bildsten L., 2000, ApJ, 542, 1016

Nandra K., Clavel J., Edelson R. A., George I. M., Malkan M. A., Mushotzky R. F., Peterson B. M., Turner T. J., 1998, ApJ, 505, 594

Nandy K., Thompson G. I., Jamar C., Monfils A., Wilson R., 1975, A&A, 44, 195

Narayan R., Garcia M. R., McClintock J. E., 1997, ApJ, 478, L79+

Narita T., Grindlay J. E., Barret D., 2001, ApJ, 547, 420

Netzer H., Maoz D., 1990, ApJ, 365, L5

O'Brien P. T., Goad M. R., Gondhalekar P. M., 1995, MNRAS, 275, 1125

Onken C. A., Ferrarese L., Merritt D., Peterson B. M., Pogge R. W., Vestergaard M., Wandel A., 2004, ApJ, 615, 645

Onken C. A., Peterson B. M., 2002, ApJ, 572, 746

Onken C. A., Peterson B. M., Dietrich M., Robinson A., Salamanca I. M., 2003, ApJ, 585, 121

Oosterbroek T., Parmar A. N., Sidoli L., in't Zand J. J. M., Heise J., 2001, A&A, 376, 532

Ortolani S., Barbuy B., Bica E., 1994, A&AS, 108, 653

Ortolani S., Barbuy B., Bica E., Renzini A., Marconi G., Gilmozzi R., 1999, A&A, 350, 840

Osmer P. S., Porter A. C., Green R. F., 1994, ApJ, 436, 678

Parmar A. N., Stella L., Giommi P., 1989, A&A, 222, 96

Patel S. K., Kouveliotou C., Tennant A., Woods P. M., King A., Finger M. H., Ubertini P., Winkler C., Courvoisier T. J.-L., van der Klis M., Wachter S., Gaensler B. M., Phillips C. J., 2004, ApJ, 602, L45

Pavlinsky M., Grebenev S., Finogenov A., Sunyaev R., 1995, Advances in Space Research, 16, 95

Pavlov G. G., Shibanov I. A., 1978, Soviet Astronomy, 22, 214

Pavlov G. G., Shibanov I. A., Zavlin V. E., 1991, MNRAS, 253, 193

Pereyra N. A., Vanden Berk D. E., Turnshek D. A., Hillier D. J., Wilhite B. C., Kron R. G., Schneider D. P., Brinkmann J., 2006, ApJ, 642, 87

Perez E., Robinson A., de La Fuente L., 1992, MNRAS, 255, 502

Perlmutter S., et al., 1999, ApJ, 517, 565

Peterson B. M., 1993, PASP, 105, 247

Peterson B. M., 2001, in Advanced Lectures on the Starburst-AGN Variability of Active Galactic Nuclei. pp 3–67

Peterson B. M., 2004, to appear in "The Interplay Among Black Holes, Stars, and ISM in Galactic Nuclei," IAU Coll. 222, eds. Storchi-Bergmann, Ho, and Schmitt, astro-ph/0404539

Peterson B. M., et al., 1999, ApJ, 510, 659

Peterson B. M., et al., 2000, ApJ, 542, 161

Peterson B. M., et al., 2002, ApJ, 581, 197

Peterson B. M., et al., 2004, ApJ, 613, 682

Peterson B. M., et al., 2005, ApJ, 632, 799

Peterson B. M., Wandel A., 1999, ApJ, 521, L95

Peterson B. M., Wandel A., 2000, ApJ, 540, L13

Peterson B. M., Wanders I., Horne K., Collier S., Alexander T., Kaspi S., Maoz D., 1998, PASP, 110, 660

Pier E. A., Krolik J. H., 1992a, ApJ, 401, 99

Pier E. A., Krolik J. H., 1992b, ApJ, 399, L23

Pier E. A., Krolik J. H., 1993, ApJ, 418, 673

Pijpers F. P., Wanders I., 1994, MNRAS, 271, 183

Pogge R. W., 1988, ApJ, 328, 519

Pogge R. W., Peterson B. M., 1992, AJ, 103, 1084

Pooley D., et al., 2003, ApJ, 591, L131

Pooley D., Hut P., 2006, ApJ, in press, astro-ph/0605048

Pooley D., Lewin W. H. G., Homer L., Verbunt F., Anderson S. F., Gaensler B. M., Margon B., Miller J. M., Fox D. W., Kaspi V. M., van der Klis M., 2002a, ApJ, 569, 405

Pooley D., Lewin W. H. G., Verbunt F., Homer L., Margon B., Gaensler B. M., Kaspi V. M., Miller J. M., Fox D. W., van der Klis M., 2002b, ApJ, 573, 184

Potekhin A. Y., Chabrier G., Yakovlev D. G., 1997, A&A, 323, 415

Predehl P., Schmitt J. H. M. M., 1995, A&A, 293, 889

Press W. H., Teukolsky S. A., Vetterling W. T., Flannery B. P., 1992, Numerical recipes in FORTRAN. The art of scientific computing. Cambridge: University Press, —c1992, 2nd ed.

Pringle J. E., Rees M. J., 1972, A&A, 21, 1

Rajagopal M., Romani R. W., 1996, ApJ, 461, 327

Rasio F. A., Shapiro S. L., 1991, ApJ, 377, 559

Rees M. J., 1984, ARA&A, 22, 471

Refsdal S., 1964, MNRAS, 128, 307

Reig P., Roche P., 1999, MNRAS, 306, 100

Rengstorf A. W., et al., 2004, ApJ, 606, 741

Reynolds C. S., Nowak M. A., 2003, Phys. Rep., 377, 389

Reynolds C. S., Ward M. J., Fabian A. C., Celotti A., 1997, MNRAS, 291, 403

Riess A. G., et al., 1998, AJ, 116, 1009

Riess A. G., et al., 2004, ApJ, 607, 665

Robinson A., Perez E., 1990, MNRAS, 244, 138

Rokaki E., Magnan C., 1992, A&A, 261, 41

Romanishin W., et al., 1995, ApJ, 455, 516

Rutledge R. E., Bildsten L., Brown E. F., Pavlov G. G., Zavlin V. E., 1999, ApJ, 514, 945

Rutledge R. E., Bildsten L., Brown E. F., Pavlov G. G., Zavlin V. E., 2000, ApJ, 529, 985

Rutledge R. E., Bildsten L., Brown E. F., Pavlov G. G., Zavlin V. E., 2001a, ApJ, 559, 1054

Rutledge R. E., Bildsten L., Brown E. F., Pavlov G. G., Zavlin V. E., 2001b, ApJ, 551, 921

Rutledge R. E., Bildsten L., Brown E. F., Pavlov G. G., Zavlin V. E., 2002a, ApJ, 577, 346

Rutledge R. E., Bildsten L., Brown E. F., Pavlov G. G., Zavlin V. E., Ushomirsky G., 2002b, ApJ, 580, 413

Sakano M., Koyama K., Murakami H., Maeda Y., Yamauchi S., 2002, ApJS, 138, 19

Sanders D. B., Phinney E. S., Neugebauer G., Soifer B. T., Matthews K., 1989, ApJ, 347, 29

Scargle J. D., 1982, ApJ, 263, 835

Schechter P. L., 2005, in Mellier Y., Meylan G., eds, IAU Symposium The Hubble Constant from Gravitational Lens Time Delays. pp 281–296

Schlegel D. J., Finkbeiner D. P., Davis M., 1998, ApJ, 500, 525

Schmidt R. W., Allen S. W., Fabian A. C., 2004, MNRAS, 352, 1413

Seaton M. J., 1979, MNRAS, 187, 73P

Sergeev S. G., Doroshenko V. T., Golubinskiy Y. V., Merkulova N. I., Sergeeva E. A., 2005, ApJ, 622, 129

Seyfert C. K., 1943, ApJ, 97, 28

Share G., et al., 1978, IAU Circ., 3190

Shemmer O., et al., 2001, ApJ, 561, 162

Sidoli L., Belloni T., Mereghetti S., 2001, A&A, 368, 835

Sidoli L., Oosterbroek T., Parmar A. N., Lumb D., Erd C., 2001, A&A, 379, 540

Silk J., White S. D. M., 1978, ApJ, 226, L103

Skinner G. K., Willmore A. P., Eyles C. J., Bertram D., Church M. J., 1987, Nat, 330, 544

Smith D. A., Morgan E. H., Bradt H., 1997, ApJ, 479, L137+

Srinivasan G., 2002, ARA&A, 11, 67

Strüder L., et al., 2001, A&A, 365, L18

Suganuma M., Yoshii Y., Kobayashi Y., Minezaki T., Enya K., Tomita H., Aoki T., Koshida S., Peterson B. A., 2004, ApJ, 612, L113

Suganuma M., Yoshii Y., Kobayashi Y., Minezaki T., Enya K., Tomita H., Aoki T., Koshida S., Peterson B. A., 2006, ApJ, 639, 46

Sugizaki M., Mitsuda K., Kaneda H., Matsuzaki K., Yamauchi S., Koyama K., 2001, ApJS, 134, 77

Sunyaev R., 1989, IAU Circ., 4839, 1

Sunyaev R., 1990b, IAU Circ., 5104, 1

Sunyaev R., et al., 1990a, Soviet Astronomy Letters, 16, 59

Sunyaev R. A., Zeldovich I. B., 1980, ARA&A, 18, 537

Sunyaev R. A., Zeldovich Y. B., 1972, Comments on Astrophysics and Space Physics, 4, 173

Sutantyo W., 1975, A&A, 44, 227

Swank J., Markwardt C., 2001, in ASP Conf. Ser. 251: New Century of X-ray Astronomy Populations of Transient Galactic Bulge X-ray Sources. p. 94

Tadhunter C., Tsvetanov Z., 1989, Nat, 341, 422

Tanaka Y., et al., 1995, Nat, 375, 659

Tavani M., 1991, ApJ, 379, L69

Terzan A., 1966, C.R. Acad. Sci. Ser. B1, 263, 221

Tomsick J. A., Gelino D. M., Halpern J. P., Kaaret P., 2004, ApJ, 610, 933

Tomsick J. A., Gelino D. M., Kaaret P., 2005, ApJ, 635, 1233

Trager S. C., King I. R., Djorgovski S., 1995, AJ, 109, 218

Treister E., et al., 2004, ApJ, 616, 123

Treister E., et al., 2006, ApJ, 640, 603

Turner M. J. L., et al., 2001, A&A, 365, L27

Urry C. M., Padovani P., 1995, PASP, 107, 803

Ushomirsky G., Rutledge R. E., 2001, MNRAS, 325, 1157

Uttley P., Edelson R., McHardy I. M., Peterson B. M., Markowitz A., 2003, ApJ, 584, L53

van Paradijs J., 1996, ApJ, 464, L139+

van Paradijs J., 1998, in Buccheri R., van Paradijs J., Alpar A., eds, NATO ASIC Proc. 515: The Many Faces of Neutron Stars. Neutron Stars and Black Holes in X-Ray Binaries. pp 279–+

van Paradijs J., McClintock J. E., 1995, in Lewin W. H. G., van Paradijs J., van den Heuvel E. P. J., eds, X-ray Binaries. Optical and ultraviolet observations of X-ray binaries. p. 58

van Paradijs J., Verbunt F., Shafer R. A., Arnaud K. A., 1987, A&A, 182, 47

Vanden Berk D. E., et al., 2004, ApJ, 601, 692

Verbunt F., 2001, A&A, 368, 137

Verbunt F., 2003, in ASP Conf. Ser. 296: New Horizons in Globular Cluster Astronomy Binary Evolution and Neutron Stars in Globular Clusters. p. 245

Verbunt F., 2005, in AIP Conf. Proc. 797: Interacting Binaries: Accretion, Evolution, and Outcomes X-ray sources in globular clusters. pp 30–39

Verbunt F., Bunk W., Hasinger G., Johnston H. M., 1995, A&A, 300, 732

Verbunt F., Hut P., 1987, in IAU Symp. 125: The Origin and Evolution of Neutron Stars, ed. D .J Helfand & J. H. Huang (Dordrecht: Reidel) p. 187

Verbunt F., van den Heuvel E. P. J., 1995, in Lewin W. H. G., van Paradijs J., van den Heuvel E. P. J., eds, X-ray Binaries. Formation and evolution of neutron stars and black holes in binaries. p. 457

Verbunt F., van Kerkwijk M. H., in't Zand J. J. M., Heise J., 2000, A&A, 359, 960

Vestergaard M., 2002, ApJ, 571, 733

Vestergaard M., 2004, ApJ, 601, 676

Vestergaard M., Peterson B. M., 2006, ApJ, 641, 689

Vio R., Horne K., Wamsteker W., 1994, PASP, 106, 1091

Wachter K., Leach R., Kellogg E., 1979, ApJ, 230, 274

Wachter S., Smale A. P., Bailyn C., 2000, ApJ, 534, 367

Walter R., Courvoisier T. J.-L., Foschini L., Lebrun F., Lund N., Parmar A., Rodriguez J., Tomsick J. A., Ubertini P., 2004, in Schoenfelder V., Lichti G., Winkler C., eds, ESA SP-552: 5th INTEGRAL Workshop on the INTEGRAL Universe IGR J16318-4848 & Co.: a new population of hidden high-mass X-ray binaries in the Norma Arm of the Galaxy. pp 417–422

Wandel A., Peterson B. M., Malkan M. A., 1999, ApJ, 526, 579

Wanders I., et al., 1997, ApJS, 113, 69

Wanders I., Peterson B. M., 1996, ApJ, 466, 174

Warwick R. S., Norton A. J., Turner M. J. L., Watson M. G., Willingale R., 1988, MNRAS, 232, 551

Welsh W. F., 1999, PASP, 111, 1347

Welsh W. F., Horne K., 1991, ApJ, 379, 586

White R. J., Peterson B. M., 1994, PASP, 106, 879

Wijnands R., 2002, in Schlegel E. M., Vrtilek S. D., eds, ASP Conf. Ser. 262: The High Energy Universe at Sharp Focus: Chandra Science Long-duration Neutron Star X-ray Transients in quiescence: the Chandra Observation of KS 1731-260. p. 235

Wijnands R., 2004, in Tovmassian G., Sion E., eds, Revista Mexicana de Astronomia y Astrofisica Conference Series The crust cooling curve of the neutron star in MXB 1659-29. pp 7–9

Wijnands R., 2005, in Wass A. P., ed., Progress in Neutron Star Research (Nova Science Publishers: Hauppauge NY), astro-ph/0405089 Crust Cooling Curves of Accretion-heated Neutron Stars

Wijnands R., et al., 2006, A&A, 449, 1117

Wijnands R., Guainazzi M., van der Klis M., Méndez M., 2002a, ApJ, 573, L45

Wijnands R., Heinke C. O., Grindlay J. E., 2002b, ApJ, 572, 1002

Wijnands R., Heinke C. O., Pooley D., Edmonds P. D., Lewin W. H. G., Grindlay J. E., Jonker P. G., Miller J. M., 2005a, ApJ, 618, 883

Wijnands R., Homan J., Heinke C. O., Miller J. M., Lewin W. H. G., 2005b, ApJ, 619, 492

Wijnands R., Homan J., Miller J. M., Lewin W. H. G., 2004, ApJ, 606, L61

Wijnands R., Miller J. M., Markwardt C., Lewin W. H. G., van der Klis M., 2001a, ApJ, 560, L159

Wijnands R., Muno M. P., Miller J. M., Franco L. M., Strohmayer T., Galloway D., Chakrabarty D., 2002c, ApJ, 566, 1060

Wijnands R., Nowak M., Miller J. M., Homan J., Wachter S., Lewin W. H. G., 2003, ApJ, 594, 952

Wijnands R., Strohmayer T., Franco L. M., 2001b, ApJ, 549, L71

Wijnands R., van der Klis M., 1998, Nat, 394, 344

Wijnands R. A. D., van der Klis M., 1997, ApJ, 482, L65+

Winkler H., 1997, MNRAS, 292, 273

Winkler H., Glass I. S., van Wyk F., Marang F., Jones J. H. S., Buckley D. A. H., Sekiguchi K., 1992, MNRAS, 257, 659

Wood K. S., Meekins J. F., Yentis D. J., Smathers H. W., McNutt D. P., Bleach R. D., Friedman H., Byram E. T., Chubb T. A., Meidav M., 1984, ApJS, 56, 507

Yakovlev D. G., Kaminker A. D., Levenfish K. P., 1999, A&A, 343, 650

Yakovlev D. G., Pethick C. J., 2004, ARA&A, 42, 169

Yamauchi S., Koyama K., 1990, PASJ, 42, L83

Zampieri L., Turolla R., Zane S., Treves A., 1995, ApJ, 439, 849

Zavlin V. E., Pavlov G. G., Shibanov Y. A., 1996, A&A, 315, 141